Indium Phosphide based Integrated Photonic Devices for Telecommunications and Sensing Applications

by

Ta-Ming Shih

M.S. Electrical Engineering
Massachusetts Institute of Technology 2007

B.S. Electrical Engineering and Computer Science
University of California, Berkeley 2006

Submitted to the Department of Electrical Engineering and Computer Science in partial fulfillment of the requirements for the degree of

Doctor of Philosophy in Electrical Engineering

at the
MASSACHUSETTS INSTITUTE OF TECHNOLOGY

June 2012

Author .....
Department of Electrical Engineering and Computer Science
May 18, 2012

Certified by .....
Leslie A. Kolodziejski
Professor of Electrical Engineering
Thesis Supervisor

Accepted by .....
Leslie A. Kolodziejski
Chair, Committee on Graduate Students

Indium Phosphide based Integrated Photonic Devices for Telecommunications and Sensing Applications

by

Ta-Ming Shih

Submitted to the Department of Electrical Engineering and Computer Science
on May 18, 2012, in partial fulfillment of the
requirements for the degree of
Doctor of Philosophy in Electrical Engineering

Abstract

Photonics is an exciting area of study that is situated at the cross-section of physics, material science, and electrical engineering. The integration of photonic devices serves to reduce the size, weight, power consumption, and cost of the photonics-based systems, whose applications can be as disparate in nature as communications and medicine. In particular, an integrated all-optical logic gate and wavelength converter for fiber-optic telecommunications and an integrated tunable laser for trace-gas sensing are investigated in this thesis. These devices are fabricated in the indium phosphide (InP) material system, which includes InP and the ternary/quaternary III-V semiconductors that can be grown closely lattice-matched on the InP substrate.

The all-optical logic gate is designed as a Mach-Zehnder interferometer with semiconductor optical amplifiers as active nonlinear elements that are optically coupled to the passive waveguides using the asymmetric twin waveguide technique. The device is grown and fabricated monolithically and carrier-dependent optical interference is demonstrated at the 1.55 μm wavelength. The tunable diode laser is designed to operate in the wavelength range of 1.55 μm – 2 μm for trace-gas spectroscopic sensing and comprises of strained InGaAs quantum wells. The laser is monolithically fabricated using mask-less lithography techniques and tuning is demonstrated in Fabry-Perot cavity lasers under continuous-wave operation. A ring-coupled 2 μm wavelength laser is designed that will exhibit a tuning range of tens of nanometers.

Thesis Supervisor: Leslie A. Kolodziejski
Title: Professor of Electrical Engineering

Acknowledgments

I am honored to have had the opportunity to work with and learn from so many talented people during the course of my PhD. It has been an unforgettable experience that I will cherish for the rest of my life. My wonderful time could not have been possible without all of the people I worked with at MIT.

I am extremely grateful to my advisor, Professor Leslie Kolodziejski, for all of her guidance throughout the years. Leslie gave me the freedom to chart my own way, while she provided a light for the path. She has taught me the value of teamwork and collaboration, along with the importance of patience. Through all of the ups and downs of the past 6 years, Leslie has demonstrated to me what it means to stay focused on the big picture and smile through it all. And finally, she has shown me how to have fun: I will always remember the parties at her house, at MIT, and even aboard the Spirit of Boston!

The great thing about being a graduate student in the Integrated Photonic Devices and Materials group is that one automatically gets to have another advisor: Dr. Gale Petrich. Gale has always been there to help me get to the bottom of anything that was suspicious, broken, or missing. I cannot count the number of times that I knocked on his door with a random question that I knew only he would know. I am thankful to Gale for all of the explanations, advice, and rides to Lincoln Laboratory!

I would like to express my sincere gratitude toward my committee members, Professors Erich Ippen and Rajeev Ram, for their valuable insights and generous guidance. Professor Ippen has been a great source of knowledge and advice since I started my studies at MIT. He has always been more than happy to make time for any questions that I had. Rajeev has been a role model for me throughout my PhD. Having taken two of his classes and helped to TA another, I have a lot of respect for his modesty and charisma. The people in the groups of Professors Ippen and Ram have been wonderful to collaborate with, especially Dr. Marcus Dahlem (now Professor), Dr. Ali Motamedi, Dr. Jason Orcutt, and Dr. Joseph Summers.

Professor Jaime Viegas has become a true mentor and friend during his stay at

MIT and the continued collaboration between our group at MIT and his at the Masdar Institute of Science and Technology. Jaime's humor has never failed to lighten the mood of a meeting, and his candor is something that I admire. I want to thank him for all of the times he sat down with me to help me with my research.

No amount of thanks would be enough to give to the folks at the Nanostructures Laboratory (NSL) for all of their help and advice. Professor Henry Smith has always been able to set aside time for me to meet with him. Mark Mondol has been extremely patient with me as I tried my best not to break the e-beam lithography tool. Dr. Tim Savas has never failed to put a smile on my face with his humor. A medal of honor should go to James Daley, who has always been there to answer questions, fix equipment, perform evaporations, or just talk to in the cleanroom. Jim has been a mentor in the lab and has become a good friend.

Similarly I need to offer my appreciation to the people at the Microsystems Technology Laboratories (MTL), where a large fraction of my fabrication work was performed. I want to thank Vicky Diadiuk for her understanding and all of the technical staff for their patient instruction. Finally, I want to offer a warm "Thank you" to Debroah Hodges-Pabon for giving me the opportunity to work as a session chair for the Microsystems Annual Research Conference.

The Integrated Photonics Initiative has been a great joint effort between the MIT campus and Lincoln Laboratory. The wonderful people at Lincoln have been a matchless source of guidance and encouragement. It has been tremendous to have had the opportunity to work with Dr. Paul Juodawlkis, Dr. Reuel Swint, Dr. Jade Wang, and William Loh. Infinite thanks to Jason Plant for all of the fabrication assistance and wisdom that he has imparted on me.

I also need to thank all of the staff from 6.007 who have made my two semesters as TA and one semester as instructor some of the best experiences I had at MIT. Thank you to Professor James Kirtley and Dr. Yu Gu (now Professor) for being so supportive. Thank you to Professor Kenneth Wong for trusting me and inviting me to Hong Kong, and for treating me as a friend. And a million thanks to Professor Vladimir Bulović, for his encouragement and counsel throughout it all, and for giving

me the opportunity to lecture as a graduate student. His humble attitude toward teaching will stick with me for the entirety of my career.

I want to thank Orit Shamir, with whom I shared an office for 5 years, for being such a great friend and colleague. From the gumball trophy, to the taped-shut mini-fridge, to the carpet-less floor, Orit and I have really made 36-295 an office to call our own. She has been a great person to discuss ideas with, not all of which pertained to research. I will always remember the April fool's day of 2008 when we hacked our group's website and replaced it with "Leslie's Daily Journal," and our never-published research paper, "Analysis of Optimized and Quantized Performance and the Results Obtained."

It has been a true pleasure to work with Dr. Sheila Nabanja, a fellow groupmate and next door neighbor. The long days that we spent upstairs in the optics lab as we took pages of data were tolerable because of her optimism and humor. I also need to express my gratitude for her shared interest of taking exercise classes at the gym!

During the IAPs of 2009 and 2010 I organized a three-unit seminar class called "Hooked on Photonics" for MIT undergrads. I want to thank everyone who participated for their selflessness and enthusiasm, especially Dr. Vanessa Wood (now Professor), Dr. Tim Heidel, and Dr. Zheng Wang (now Professor). Course 6.095 could not have been possible without you.

There are many other friends at MIT whom I will not be able to mention here. But I absolutely need to express my gratitude to everyone in my group for their fellowship: Pei Chun Amy Chi, Mohammad Araghchini, Dr. Ryan Williams, and Dr. Reginald Bryant. My experience at MIT would not have been the same without the kindness from my friends Adrian YiXiang Yeng, Dr. Sidney Tsai, Allen Hsu, David He, Dr. Amil Patel, Dr. Donald Winston, and Dr. Mahmut Ersin Sinangil.

Finally, I want to thank my family for always being there for me. My parents have been unrelentingly supportive of my education, applying just the right amount of pressure here and there to help me along the way. A special thanks goes to my sister, Hui-Wen, who has been a blessing in my life. And words cannot describe the gratitude I have for my wife Angela, who, starting from day one has been behind my

graduate goals one hundred percent.

Cambridge, 2012 TM S

Contents

List of Figures

List of Tables

Chapter 1

Introduction

Today's technological advancements in electronics often go hand-in-hand with advancements in optics. For example, as recent developments in low-power electronics for mobile devices are announced, new designs for liquid crystal display (LCD) and light emitting diode (LED) technologies for the screens of those same devices are implemented. As lighter-weight, higher-capacity batteries are created and deployed, higher-efficiency photovoltaic modules are being invented and manufactured. As computers acquire better graphics processors for video and gaming, fiber-optic telecommunications research keeps global network bit-rates ahead of the growing bandwidth requirements.

Silicon's versatility and low cost has made it the material of choice for many electronic and optical devices. However, there are other semiconductors that have advantages over silicon in certain respects. For example, III-V semiconductors, such as gallium arsenide (GaAs) and indium phosphide (InP), have a much higher electron mobility than silicon, and have been used to make high-power and high-frequency electronics. Furthermore, unlike silicon, III-V semiconductors have a direct bandgap, allowing them to efficiently emit and absorb photons with energies slightly above their respective bandgaps. In fact, there are no commercial optical emitters today that are silicon-based. While a lot of photovoltaics today are silicon-based, the highest-efficiency solar panels are still the ones fabricated out of III-V semiconductors.

III-V semiconductors also have the added potential of monolithic integration that

many other optical materials do not possess. The rapid pace of advancement for electronic circuits has been largely due to scaling, which could not have been possible without integration. Integration refers to the placement of all of the components of a system on the same chip. Monolithic integration describes the fabrication of the entire chip out of a single wafer. In contrast, hybrid integration describes the fabrication of certain components of a chip out of different wafers and then assembling the pieces together in the form of a single chip. Not only does monolithic integration allow complex systems to have a smaller footprint (and therefore lower costs), it also greatly simplifies the assembly process that would be required if all of the components were discrete, or if hybrid integration is employed. The fact that III-V semiconductors are well-suited to monolithic integration make III-V photonics an exciting area of research.

Integration is necessary, but not sufficient, for scaling to take place. Integrated photonics, or photonic integrated circuits (PICs), have remained approximately the same size over the past ten years. The dimensions for optical devices have not been limited by lithography, but rather by geometries suitable for low-loss light propagation. One of the hurdles that integrated photonics still faces is the lack of a universally-accepted building block that is comparable in functionality and versatility to the transistor for ICs. The integrated photonic equivalent of an electronic wire, however, is widely accepted to be the ridge waveguide.

This thesis explores devices constructed in the indium phosphide material system, which is an important subset of III-V semiconductors. The InP material system includes ternary and quaternary III-V semiconductors that are lattice-matched to InP, such as InGaAs, InGaAsP, InGaAlAs, and InAlAsP. Devices operating at different wavelengths, from the primary fiber-optic telecommunications wavelength of 1.55 μm up to 2 μm are investigated. Along the way, three different waveguide-based building blocks for integrated photonics will be examined: (1) the Fabry-Perot resonator, (2) the Mach-Zehnder interferometer, and (3) the microring resonator.

1.1 The Indium Phosphide Material System

Indium phosphide is a binary III-V semiconductor that has a crystal structure of two overlapping face-centered cubic lattices with a lattice constant of 5.87 Å [103]. While not as cheap as Si, InP is available as large wafers at moderate prices, making it attractive for the study and, in some cases, production of electrical and photonic devices. Because its electron mobility is much higher than that of silicon, InP can be found in communications devices where high speed is a necessity. Indium phosphide has a direct bandgap of 1.344 eV at room temperature, which corresponds to the near-infrared wavelength of 923 nm. One of the advantages of InP is that it can be used as a substrate for the epitaxial growth of other III-V semiconductors. By combining one or more binary compounds (*e.g* GaAs, InP, InAs), it is possible to create ternary (*e.g.* InGaAs, InAlAs) and quaternary (*e.g* InGaAsP, InGaAlAs) compounds [103]. For the purposes of this thesis, all of these materials will be considered as part of the InP material system. In three-dimensional bulk form, these materials are limited to emission wavelengths corresponding to their bandgap energies. In reduced-dimensionality forms, such as quantum wells and quantum dots, the emission/absorption wavelengths can be even more precisely tailored. If strained materials are also introduced, the InP material system has the ability to cover the wavelength range of 0.9 μm to 2 μm [135]. Fortunately, the bandgap energy has an inverse relationship with refractice index, which allows the use of the larger-bandgap materials, such as InP itself, as the cladding of a waveguide, and the smaller-bandgap material, such as InGaAs, as the core of a waveguide [22].

Figure 1-1 shows the lattice constant versus the bandgap energy of important III-V materials. The lines correspond to ternary compounds and they bound areas that represent quaternary compounds. Five and even six constituent compounds are possible, but are difficult to render graphically. Knowledge about the lattice constants of these semiconductors is important for epitaxial growth. If the lattices of the grown semiconductor and the substrate are not equal, or mismatched, defects and dislocations can be introduced into the semiconductor and degrade the quality of the

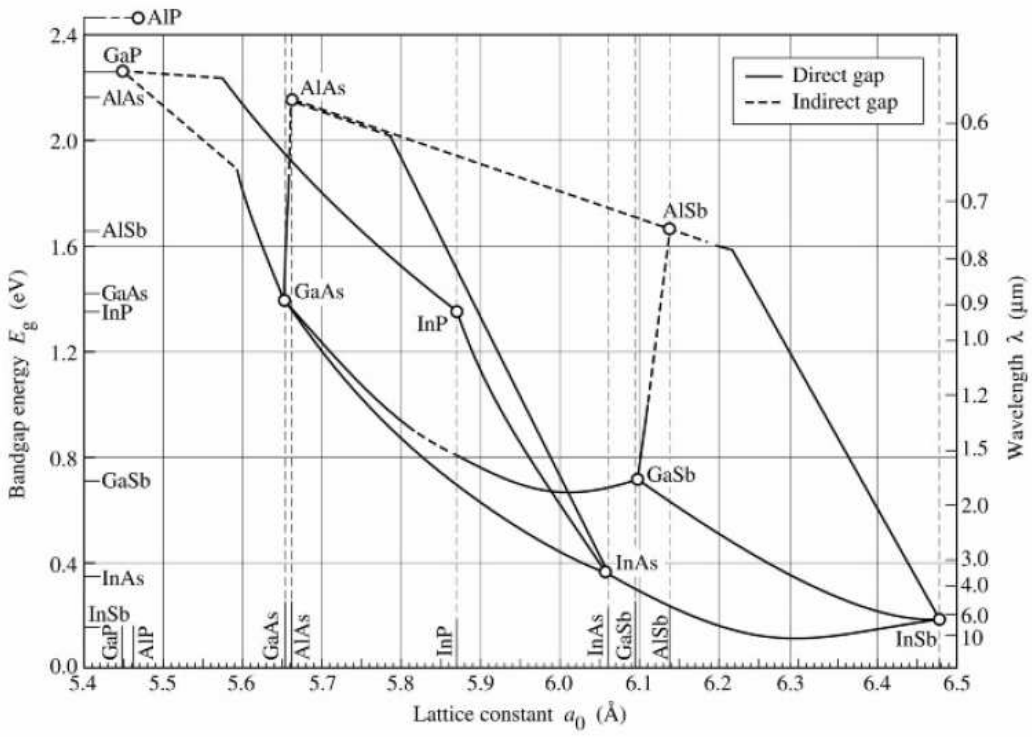

Figure 1-1: The bandgap energy versus the lattice constant of III-V semiconductors [103]. The lines connecting the binary semiconductors represent ternary semiconductors.

film. The vertical lines represent the epitaxial constraints of growing on a particular substrate. In certain situations, however, lattice mismatches are desired, such as for the growth of strained materials or quantum dot materials as will be discussed in Chapter 3.

1.2 Integrated Photonic Waveguide Building Blocks

This thesis will explore three major waveguide-based building blocks of integrated photonics, including: the Fabry-Perot (FP) resonator, the Mach-Zehnder interferometer (MZI), and the microring resonator. They are shown in plan view in Figure 1-2. The Fabry-Perot resonator, consisting of a straight waveguide with cleaved facets, is the simplest type of waveguide-based resonator. Light propagates along the waveguide and is partially reflected at the facets, which determines the round-trip length of the

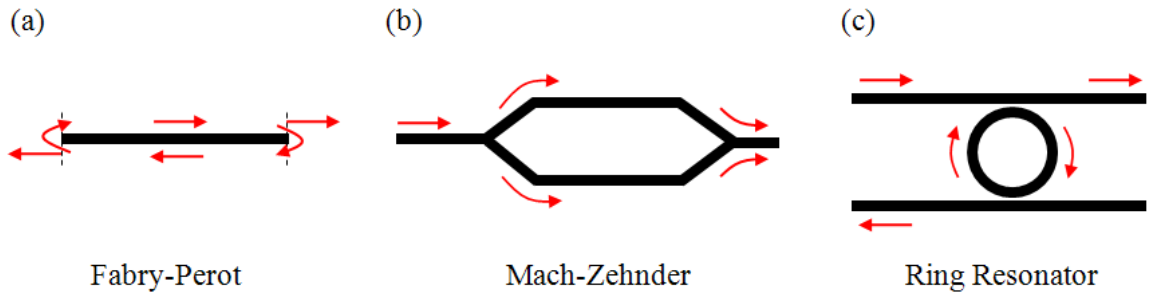

Figure 1-2: (a) A Fabry-Perot cavity: light propagates along the waveguide and is partially reflected and partially transmitted at the mirror facets. Only wavelengths that interfere constructively in the cavity will receive positive feedback if there is gain. (b) A Mach-Zehnder interferometer (MZI): light that propagates within the MZI experiences a 50-50 power split. After traveling through the respective arms of the Mach-Zehnder, the light is recombined (interfered) as the two arms meet at the output waveguide. The output is zero when destructive interference occurs. (c) A microring resonator: input light is evanescently coupled to the ring only if an integer number of wavelengths fit in a round trip of the ring resonator. The light in the ring can be coupled back out to another waveguide.

cavity, or etalon. If gain is introduced, the wavelengths that interfere constructively in the cavity will experience positive feedback [22].

Mach-Zehnder interferometers are very versatile interferometric structures that are well-suited to integration. In many free-space optical interferometric structures, the light paths overlap. However, in integrated waveguide structures, crossing lightpaths without crosstalk is difficult, and the integrated MZI is able to eliminate them. In an MZI, the light first experiences a 50-50 power split. Then, after traveling through the respective arms of the Mach-Zehnder, the light is interfered at the output waveguide [100].

A microring resonator is a wavelength selective device, much like a Fabry-Perot resonator, but the feedback mechanism is inherent in the geometry of the rings. The rings can be made to have round-trip lengths that are generally smaller than that of ridge FP resonators due to cleaving constraints, making the free-spectral range (FSR) of the rings larger than that of FP resonators [90].

1.3 Thesis Organization

In Chapter 2, integrated all-optical logic (AOL) gates operating at the wavelength of 1550 nm will be investigated. All-optical logic has the potential to transform telecommunications and beyond. In this chapter, I present the design of an integrated AOL unit cell based on an MZI structure with electrically-pumped semiconductor optical amplifiers (SOAs) as nonlinear elements. The operation of dilute waveguides and asymmetric twin waveguides for coupling between the passive waveguides and SOAs is demonstrated. The carrier-dependent interference of the MZI is visualized by performing a static bias scan, which allows the DC operating point for the AOL unit cell to be successfully determined.

Chapter 3 delves into Fabry-Perot ridge diode lasers with gain from active material layers in which lattice mismatches are intentionally introduced. InAs quantum dots with gain near the wavelength of 1.55 μm and strained InGaAs quantum wells with gain in the wavelength range of 1.55 μm to 2 μm are characterized.

Chapter 4 examines tunable ring resonator-coupled lasers emitting at 1.78 μm, 1.88μm, and 1.98 μm. Tunable long-wavelength lasers have applications in tunable diode laser absorption spectroscopy (TDLAS) for trace-gas sensing. An assortment of gases have absorption lines in the 1.55 μm to 2 μm wavelength range. The ring resonator-coupled lasers are designed so that wavelength tuning can be achieved with carrier injection into the rings. Double ring resonator-coupled lasers are designed with a slight detuning in the FSR of the two rings, which gives rise to wide tunability due to the Vernier effect.

In Chapter 5, conclusions and future work are presented.

Chapter 2

Integrated All-Optical Logic and Wavelength Conversion

The fast-paced improvement in technology over the past three decades has been largely due to the advancement of digital logic in the form of electronic integrated circuits (ICs). As the workhorse of the digital IC industry, complementary metal-oxide-semiconductor (CMOS) technology has been extremely amenable to scaling: the density of transistors in microprocessors has doubled approximately every 18 months [102]. While electronics are well-suited to performing dense information processing, information transmission may be better accomplished in the optical domain [3]. With the advent of fiber-optic communications and, more recently, integrated photonics, copper has been gradually replaced by optical components. Recent developments in fiber-to-the-home and on-chip optical interconnects depict the on-going switch from electronic to optical signal transmission [32, 72]. Many believe that it is possible for integrated circuits to be replaced by so-called photonic integrated circuits (PICs) that perform digital logic with photons rather than electrons. As Moore's Law slows down, PICs are beginning to emerge as a promising technology with advantages over electronic ICs in speed and power consumption [22].

One of the success stories of modern-day technological innovation is the Internet. From its advent in the 1980s to the present, the Internet has revolutionized both communications and the media. Since 1990, a vast network of intercity and transoceanic

fiber-optic cables has been installed to increase Internet capacity. Today, the state-of-the-art long-distance broadband Internet is relayed through these fiber cables at bit rates of up to 40 Gb/s per channel, transmitting thousands of petabytes a day. Using wavelength division multiplexing (WDM), over 100 different channels are transmitted through a single fiber [41]. This seemingly large capacity is being consumed rapidly however, as international Internet traffic rises at an average rate of 75% a year [127]. Between 2004 and 2006 alone, U.S. broadband access increased by almost 65% [107]. Unfortunately, during the same time frame, Internet capacity has only increased by an annual rate of 45%. Furthermore, the increase in Voice over Internet Protocol (VoIP) applications, video and music streaming websites, and peer-to-peer file transfer programs put a significant additional strain on Internet bandwidth. Without an acceleration in the expansion of Internet capacity, Internet congestion can become a problem with large-scale economic consequences.

The solutions to the Internet capacity problem can be categorized as either parallel or series approaches. For example, a parallel approach would be to lay more fiber-optic cables into the ground, creating more parallel channels for transmission. A series approach would be to increase the capacity of the existing fiber infrastructure by swapping out bandwidth-limiting components for faster technologies. As it turns out, the series approach is more attractive than the parallel approach, since laying down more fiber-optic cables is a very expensive effort. In this chapter, ways to increase the bit rates transmitted through the existing fiber cables are investigated.

Routers play an important role in optical fiber telecommunication networks today, directing transmitted data to their correct destinations. Wavelength conversion is an important component of routing in current circuit-switched WDM networks. In packet-switched networks, header processing is necessary for routing. Regenerators are used along with routers to perform reamplification, reshaping, and retiming (3R-regeneration) on optical data. 3R-regeneration is also used to eliminate the added noise from amplifiers in long-distance transmissions. Routing and regeneration of optical signals require electronic logic operations, and therefore conversions between the optical and electronic domains. These optical-to-electronic-to-optical (O/E/O) con-

versions take place at each regenerator and router node, putting limits on the speed, cost, and power consumption of the regenerating and routing operations. To increase bit rates and transmission channels, the O/E/O bottleneck must be addressed.

One of the ways to address the cost of O/E/O conversions is integration. The company Infinera has developed ten-channel 10 Gb/s and 40 Gb/s transmitter and receiver chips for O/E/O conversion that are monolithically integrated in indium phosphide [77]. By integrating lasers, modulators, detectors, multiplexers, and attenuators onto a single PIC, they have reduced the costs of manufacturing and packaging, thus making O/E/O conversions less of a bottleneck than before.

We propose to eliminate O/E/O conversions altogether. That is, to perform routing, 3R-regeneration, and wavelength conversion directly in the optical domain. In fact, electronic processing, when compared to all-optical processing, underperforms in the areas of latency (and therefore buffering requirements) and power consumption [65]. Furthermore, if the all-optical processor is monolithically integrated, the cost can be driven down to a price-point that is competitive for large-scale deployment.

To perform digital processing on a PIC, the first step is to create photonic equivalents of electronic processing building blocks. The two fundamental building blocks of digital ICs are the logic gate and the flip-flop, or more broadly, the processing unit and the memory unit. In this chapter, all-optical logic is investigated, although all-optical memory, or buffering, is a very interesting area of research as well.

The most rudimentary all-optical buffers consist of delay lines or recirculating loops [137]. A recirculating loop is a loop in which the optical data is made to circulate until it is coupled out when needed. Often, a regenerator is placed in the loop to compensate for fiber losses and distortions. Delay lines and recirculating loops can be designed to provide variable delays [137]. Variable delays have also been achieved using fiber dispersion by taking advantage of the different group delays that different wavelengths experience [19]. Data can be converted to the wavelength corresponding to the desired delay, transmitted through the delay line, and converted back to its original wavelength at the output [138]. Another promising method for providing all-optical buffers is "slow light," although most demonstrations show only

about a pulse-width of delay [80, 144]. "Slow light" is achieved by exploiting peaks in the dispersion relation of either the material or the waveguide that a signal propagates in. The group velocity of a pulse can be made to be hundreds of times slower than the speed of light.

2.1 All-Optical Logic

All-optical logic (AOL) provides a framework for eliminating the expensive O/E/O conversions in fiber-optic networks. Routing and regeneration performed completely in the optical domain can reduce power consumption, latency, and complexity. An AOL gate is a device with optical input and output ports, where the outputs are causally dependent on the inputs. Because the optical signals must interact with each other, an AOL gate is inherently optically nonlinear. Demonstrations of all-optical logic have been achieved by exploiting the nonlinearities in passive materials such as silica (SiO_2) fiber, passive semiconductors, and even organic molecules [28, 143, 146]. Actively pumped semiconductors, such as semiconductor optical amplifiers (SOAs), have been successfully demonstrated to exhibit even larger nonlinearities [115].

The nonlinear interaction of optical signals can cause changes in phase, and to a lesser degree, power. Because of this, all-optical switching techniques most often utilize some sort of interference to take advantage of the phase change. All-optical switches have been demonstrated utilizing cross-phase modulation in resonating structures [143]. All-optical demultiplexing of 160 Gb/s data streams has been demonstrated using nonlinear optical loop mirrors [123]. Up to 100 Gb/s logic operation has been demonstrated with the ultrafast nonlinear interferometer (UNI), as well as 40 Gb/s packet routing [36, 136]. The UNI was the first high-speed all-optical logic gate to be demonstrated in a single-arm interferometer [85, 86]. All-optical logic has also been demonstrated with Mach-Zehnder interferometers (MZIs) that have semiconductor optical amplifiers (SOAs) in each arm [25]. These MZI structures have also shown wavelength conversion at bit rates of 168 Gb/s, along with demultiplexing at 336 Gb/s [129, 78].

The SOA is a very interesting device because it is not only capable of achieving large nonlinearities, but is also well-suited for integration. For all-optical logic to become a viable part of telecommunication networks, it needs to be integrated. The majority of the all-optical logic demonstrations (including those described above) have been performed with configurations set up on an optical bench. Discrete SOAs and fibers, however, present size, cost, and packaging issues that can be solved by monolithic integration. The challenges of designing and building an integrated device are quite different from that of making the device out of fiber and discrete components.

2.2 Semiconductor Optical Amplifiers

Semiconductor optical amplifiers (SOAs), also often called semiconductor laser amplifiers, were first developed as amplifiers in optical transmission networks. However, the SOA possessed poor noise performance, recovery-time-induced patterning effects, and lower saturated output power than its fiber-based counterpart, the erbium-doped fiber amplifier (EDFA), which became the amplifier of choice in optical networks. The SOA does have some advantages over the EDFA, however, such as being electrically pumped, rather than optically pumped. Furthermore, SOAs are well-suited for integration because semiconductor materials can be epitaxially grown on semiconductor wafers. These qualities make the SOA a very useful building block in PIC applications.

A SOA is structurally a laser diode without mirrors. Like a laser diode, carrier injection inverts the carrier population and creates gain. With no mirrors, any photon traveling in the SOA will make a single pass through the device. Because of this, the electroluminescence of the SOA, called amplified spontaneous emission (ASE), is representative of the gain spectrum of the device [22]. SOAs provide gain and exhibit large nonlinearities for wavelengths with photon energies that are slightly above the bandgap of the gain material that is used [115].

The nonlinearity in a SOA arises due to stimulated emission, which depletes the free carriers and decreases the gain. This creates a change in the refractive index of

the SOA, as governed by the Kramers-Kronig relation. Only a small number of free carriers are needed to be depleted in order to create a nonlinear index change that is useful in integrated waveguide structures. The active injection of carriers, allows for relatively fast recovery times, on the nanosecond time scale down to hundreds of picoseconds, for high injection levels [64].

Quantum dot (QD) SOAs have been measured to have recovery times as short as 15 ps [148]. Quantum dots confine electrons in three dimensions, creating a 3D potential well that "squeezes" the electronic energy levels into atomic-like quantized steps. The energy level spacings depend on the size of the QD; the smaller the QD, the fewer the bound states the QD will possess. One of the benefits of having only a handful of energy levels is that fewer carriers are required to achieve population inversion. Typically, a QD found in an SOA will have two bound states, a "ground" state and an "excited" state [130]. The QD layers are grown with very high lattice mismatch, the stress of which causes the layer to self-assemble into small islands, the quantum "dots," rather than form a continuous layer. Beneath the QD layer is the wetting layer, which can be considered a reservoir of carriers for the QDs because of its large number of carriers compared to the bound electrons and holes of the QDs. Thus, when stimulated emission depletes the carriers of the QDs, this reservoir of carriers quickly replenishes the supply, leading to very fast recovery times [74].

2.3 Integrated All-Optical Logic Gate and Wavelength Converter Design

Utilizing the large nonlinearities of SOAs and their compatibility with integration, along with the performance of MZI structures for AOL, the integrated all-optical logic gate that is depicted in Figure 2-1, was designed [65, 137, 141]. The device, called the all-optical logic unit cell, consists of a MZI with SOAs in both arms. The MZI has three input ports. A signal sent into the top or bottom port will travel through the top or bottom arm of the MZI, respectively. A signal sent into the middle port will

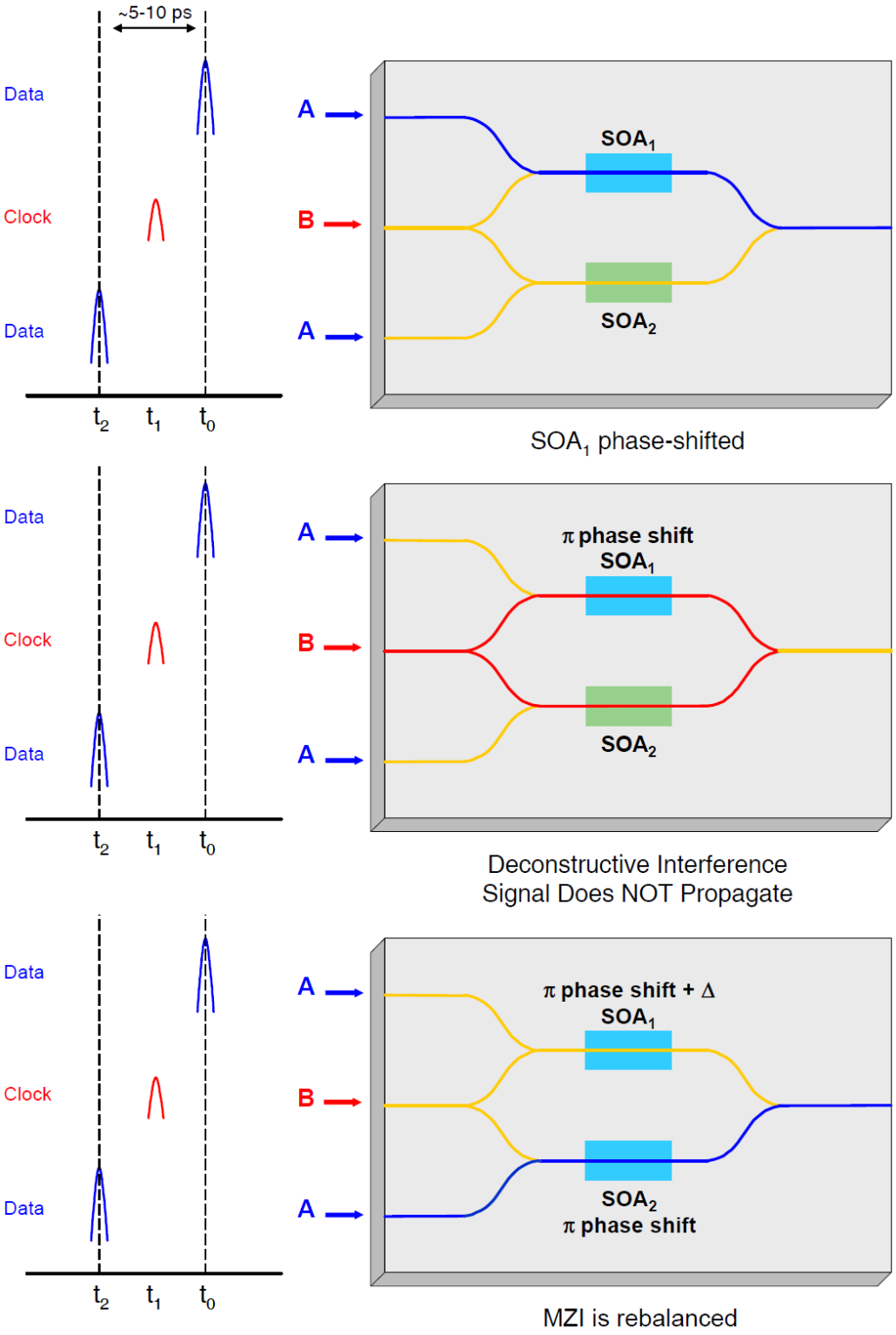

Figure 2-1: Operation of the all-optical logic unit cell [141].

encounter a 50-50 power split and travel through both arms of the MZI. The input signals do not have to be at the same wavelength; at the output a wavelength filter can be placed to select for the desired output wavelength. The AOL unit cell can be cascaded to perform any logic operation and is inherently a wavelength conversion device. While the general design is wavelength-independent, the target wavelength of operation for the AOL chip was 1550 nm, the primary wavelength that is used in fiber-optic telecommunications.

To understand the operation of the AOL unit cell, consider the example that is illustrated in Figure 2-1. At time $t = t_0$, the signal "A" at a wavelength λ_A, which consists of a data pulse (representing a logical 1), is transmitted into the top input port. As the pulse travels through the top arm of the MZI, the pulse nonlinearly changes the refractive index of SOA_1, causing the optical phase delay in SOA_1 to be π-phase shifted with respect to that in SOA_2. The DC bias of the SOAs and the intensity of the pulse must be calibrated to achieve the desired π phase shift. For the time being, assume that the calibration has been achieved. Less than 10 ps later, at time $t = t_1$, signal "B", which also consists of a data pulse (representing a logical 1), arrives in the middle input port. In this example, signal "B" is at a different wavelength, λ_B. At the output, there is a filter selecting for λ_B. Because the two SOAs are out of phase, destructive interference occurs at the output for signal "B." The output is a logical 0. If signal "A" had been a logical 0, then the output would have been a logical 1. If signal "B" is made to be a Clock signal, then the logical output is equivalent to $\neg$A or $\bar{A}$ (boolean operation NOT A). Notice that a wavelength conversion has taken place as a result of the logic operation, from λ_A to λ_B.

At this point, the AOL unit cell is unbalanced. One can wait for the carriers in SOA_1 to recover, or alternatively, another signal "A" can be transmitted into the bottom input port to rebalance the MZI arms as shown in the bottom of Figure 2-1. If rebalancing is not performed, AOL unit cells employing bulk or quantum well SOAs would only be able to achieve operating rates of low tens of Gb/s. On the other hand, QD SOAs, with their fast recovery times, can achieve theoretical operating bit rates

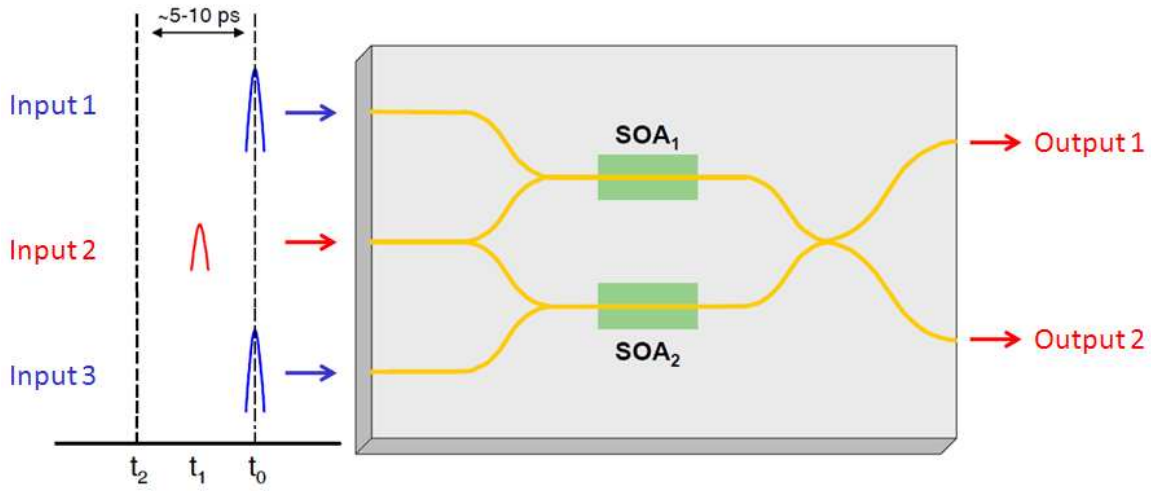

Figure 2-2: An alternative form of the all-optical logic unit cell.

Table 2.1: Example Boolean operations of the all-optical logic unit cell.

Signal 1	Signal 2	Signal 3	Output 1	Output 2
A	CLK	-	$\neg$A	A
A	B	CLK	A$\cdot$B	-
A	CLK	B	A$\odot$B	A$\oplus$B

of 160 Gb/s without rebalancing [120].

Rebalancing considerations aside, Figure 2-2 depicts the AOL unit cell under operation with three different inputs and two outputs. Under this configuration, the signals of both Input1 and Input3 are used to switch the signal at Input2. Once again, at the outputs there are filters selecting for the wavelength of the middle input port (Input2). At the output there is a 2$\times$2 coupler, which has the property that Output1 and Output2 can be adjusted to be Boolean negatives of each other as long as Input2 is a CLK signal. Table 2.1 lists a few combinations of input signals and the resulting operations performed, including NOT ($\neg$), AND ($\cdot$), XOR ($\oplus$), and XNOR ($\odot$). The AND and NOT gates can be cascaded to make a NAND gate, which can theoretically be used to create any other logical function that cannot be achieved with a single gate. Table 2.1 also shows that a wavelength converter can be created by using the identity operation, since the input and output wavelengths are different.

2.4 Active-passive Integration

The AOL unit cell that is depicted in Figure 2-2 can be broken down into active and passive components. The active components are the SOAs. The passive components include the waveguides and the splitters/combiners in the MZI. The active SOAs need to be fabricated out of semiconductor material that has a bandgap near the wavelength of operation to provide a large nonlinearity. A potential material is $In_xGa_{1-x}As_yP_{1-y}$, which can have a bandgap close to the photon energy of 1550 nm light for $x = 0.56$ and $y = 0.94$. During operation, the SOAs need to be electrically pumped above transparency. The passive components need to be fabricated out of material with a bandgap that is much larger than the photon energy of 0.8 eV corresponding to 1550 nm light, so that it remains transparent during operation. A potential material is InP, which has a bandgap energy of 1.34 eV.

The integration of the active and passive components can be achieved in a number of ways. One method is to epitaxially grow the passive material first, then selectively etch away regions where the active material is desired and perform another growth selectively in the etched areas. This method, called regrowth, creates a structure in which the active and passive sections are butt-coupled and lie on the same plane on the chip. An alternative is to epitaxially grow the passive material first, and then grow the active material above. Using a vertical coupling technique, the light can be made to couple between the lower passive components and the upper active components [118]. The structure, no longer planar, allows for a relatively straightforward growth process, but has a challenging fabrication process. The regrowth method has a more challenging epitaxy process, but a relatively easy fabrication process.

We chose to use a vertical coupling technique known as the asymmetric twin waveguide (ATW) [70, 118, 142]. The twin waveguide technique was first developed as index-matched (symmetric) waveguides with directional coupling, however, coupling efficiencies were low (25%) [16, 119]. The asymmetric twin waveguide technique utilizes an adiabatic taper to increase the coupling efficiency [73, 116, 117]. With the adiabatic taper, the top and bottom waveguides do not need to be index-matched.

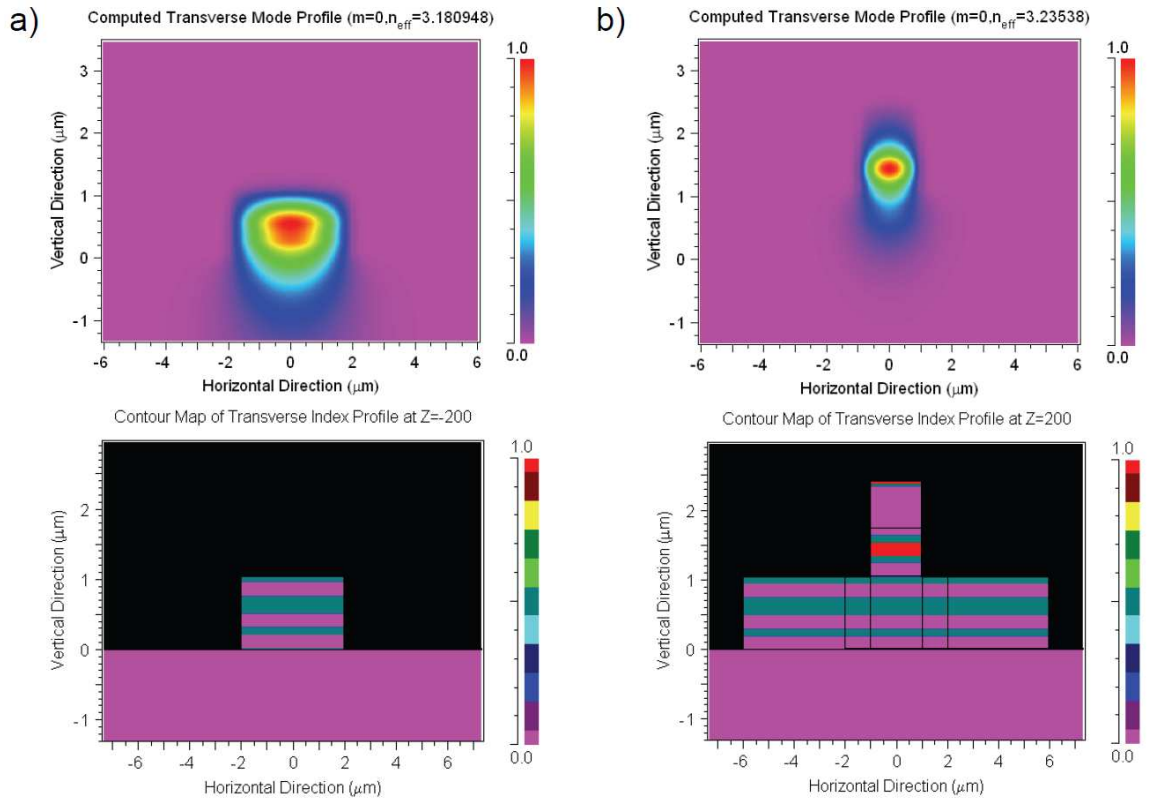

Figure 2-3: BPM simulations of the passive and active waveguide modes. (a) The fundamental mode profile and cross-section of the passive waveguide as simulated in BPM. (b) The fundamental mode profile and cross-section of the active waveguide as simulated in BPM [65].

The passive and the active waveguides were designed to be dilute waveguides, which allows the effective indices of the waveguides to be "tuned" by changing the epitaxial layers. "Diluting" the waveguide by adding low-index layers enabled the width of the waveguide to be designed to be wider while maintaining single-mode operation. A wider waveguide was desired for a simpler fabrication process (see Section 2.6) and easier optical coupling into and out of the device. In addition, dilute waveguides allowed for the use of strain-reducing layers in the growth process, which can reduce the number of defects in the semiconductor [65].

Figure 2-3 shows the structure of the passive and active waveguide sections, along with the transverse electric (TE) modes as simulated using the beam propagation method (BPM). Details about BPM can be found in Appendix A. The epitaxial layers

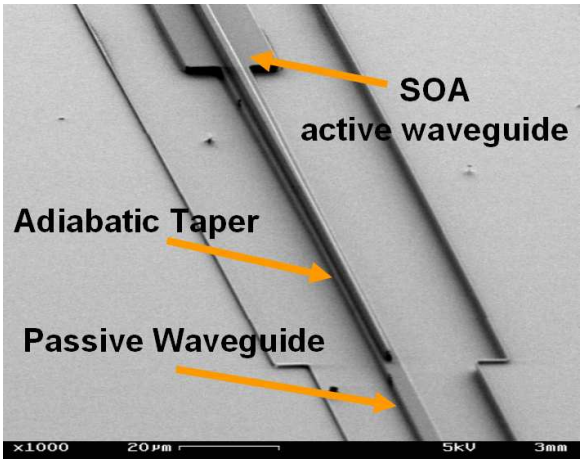

Figure 2-4: Scanning electron micrograph of the asymmetric twin waveguide taper for coupling between the active SOA waveguide to the passive waveguide situated in the lower plane [141].

of the dilute waveguides are given in detail in Section C.1. The InP/InGaAsP material system is used to achieve the operating wavelength of 1550 nm. The fundamental modes of the passive and active waveguides have effective indices of $n_{passive} = 3.18$ and $n_{active} = 3.24$, respectively. The passive waveguide is designed to be single mode. Because the active waveguide is actually an SOA, it can provide either gain or loss depending on the level of carrier injection. The active and passive waveguides are coupled to each other via the ATW technique. The scanning electron micrograph (SEM) of Figure 2-4 shows that the SOA active waveguide is tapered adiabatically, while the bottom passive portion also gradually becomes narrower until it reaches the passive waveguide.

2.5 Optical Modeling

Prior to fabrication, simulations are used to calculate the dimensions of the different components of the AOL unit cell to optimize the device performance. Table 2.2 shows the different structures that compose the AOL unit cell, along with their dimensions [65]. Each component was designed separately and then combined together to form the entire AOL unit cell.

Table 2.2: The dimensions of the waveguide components that make up the AOL unit cell.

Structure	Width [μm]	Height [μm]	Length [μm]
Passive WG	4	0.85	-
Active SOA Narrow	2	1.39	0.4, 0.5, 0.6, 0.75, 0.85, 1.0
Active SOA Wide	4	1.39	0.4, 0.5, 0.6, 0.75, 0.85
Taper Narrow	$2 \rightarrow 0.5$	1.39	175
Taper Wide	$4 \rightarrow 0.5$	1.39	175
MMI 1×2	12	0.85	159
MMI 2×2	18	0.85	480

2.5.1 Passive and Active Waveguides

The waveguide dimensions were designed concurrently with the epitaxial layer structure [65]. The goal was to have a single-mode passive waveguide that could be defined using contact lithography, which has a resolution of $\approx$1 μm. The effective index of the dilute waveguide was assessed with respect to variations arising from epitaxial growth and fabrication. The intensity of material composition variation was determined from material specifications provided by IQE, the commercial supplier of the epitaxial wafers. For example, the bandgap wavelength for the $In_{0.79}Ga_{0.21}As_{0.45}P_{0.55}$ layers are quoted to be $\lambda = 1180 \pm 20$ nm. The error margin corresponds to an arsenic content between 0.413 and 0.473 and an approximate effective index variation of about $\pm$0.011. At the high end of the arsenic concentration range, the passive waveguide supports a higher-order TE mode. This can lead to potentially undesirable behavior, but can be easily remedied by fabricating narrower passive waveguides. The effective index of the waveguide is also affected by the etch depth. An etch depth of 1.05 μm is designed. A deviation of $\pm$100 nm results in an effective index variation of 10^{-4}, as modeled with BPM.

The ATG structure is designed to optimize coupling of the passive waveguide mode to the fundamental mode of the active waveguide. The dimensions of the ATG structure, as designed using BPM, are shown in Figure 2-5. The active waveguide layers are shown in yellow and the passive waveguide layers are shown in red. A

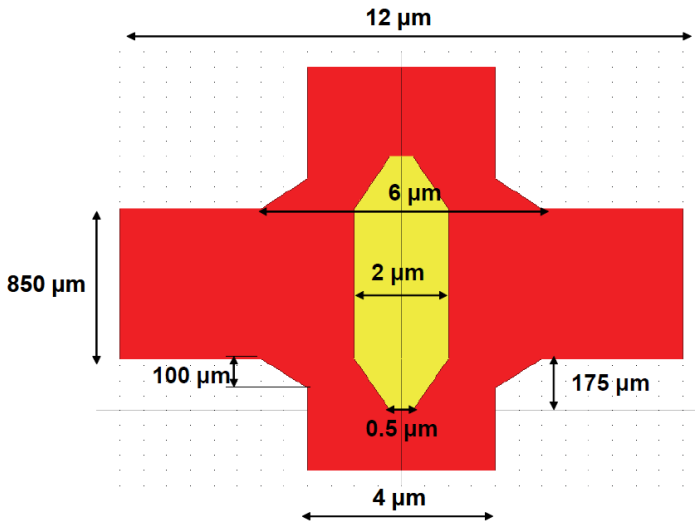

Figure 2-5: The layout of the tapered ATG structure as seen from the RSoft BPM CAD window. The active waveguide layers are shown in yellow and the passive waveguide layers are shown in red. Notice that the horizontal dimension is exaggerated to show detail.

taper that starts from a point would be ideal, but is impossible to fabricate using the processing equipment at MIT. Thus, a taper that starts from a width of 0.5 μm is designed. The taper expands to a width of 2 μm (or 4 μm, depending on the width of the particular SOA), at which point it joins with the active SOA. In the absence of tapers, optical power can be partially transferred from the passive waveguide to the active portion of the ATG due to the higher effective index of the active device. However, calculations indicate that less than 10% of the optical power is transferred from the passive waveguide to the active waveguide, corresponding to loss of over 10 dB. With the taper, a coupling efficiency of larger than 95% can be achieved theoretically, as shown in Figure 2-6(a).

The trade-offs associated with the taper length are as follows. A gradual change in the width minimizes scattering of optical power from the fundamental mode into higher-order modes. On the other hand, compact couplers are essential for reducing the footprint of PICs, and therefore the tapers should be designed to be as short as possible while preserving high efficiency. The taper length is designed to be 175 μm [65].

In the first generation of the all-optical logic chip, the tapers, although composed of the active waveguide material, were not designed to have carriers directly injected from above [118]. Structurally speaking, this meant that the tapers did not have metal contact pads fabricated above them [141]. BPM simulations indicated that the coupling was ineffective, as shown in Figure 2-6(b), if the taper was not electrically pumped, and therefore absorptive. The simulation suggests that direct carrier injection into the taper can be a crucial aspect of device operation.

The BPM simulations of Figure 2-6 do not include the effects of carrier diffusion, however. Experimentally, researchers have reported that InGaAsP contact layers doped to $p = 5 \times 10^{18}$ cm^{-3} were able to facilitate carrier diffusion over distances of hundreds of microns and bias regions that were not directly pumped above transparency [118]. In the final design, however, the metal contact pads were expanded to cover the tapers, providing direct carrier injection to the taper sections, because

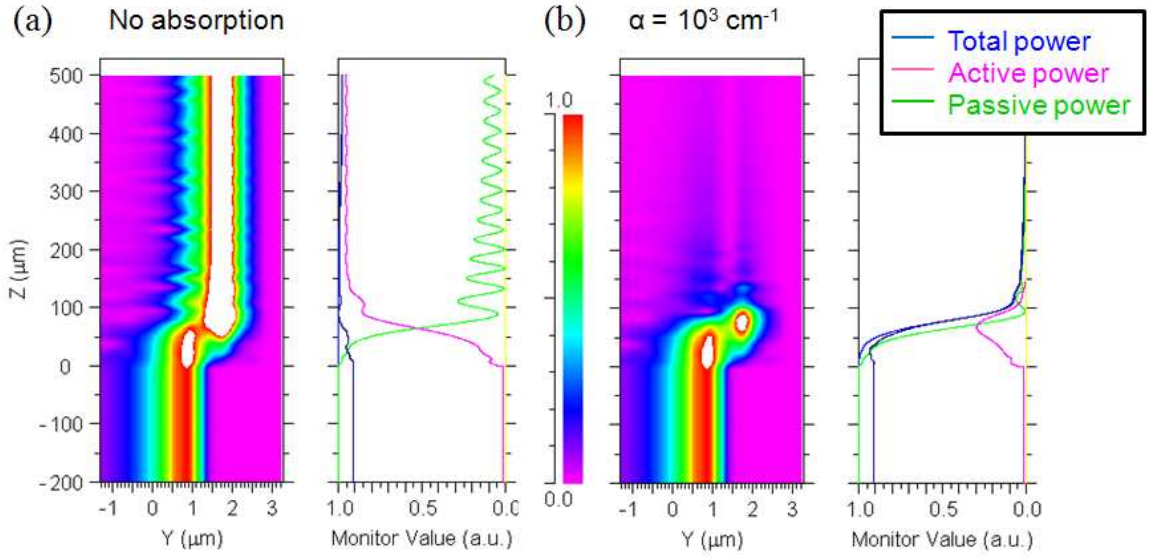

Figure 2-6: BPM simulations of coupling between the passive and active waveguides, (a) assuming no losses in the tapers, and (b) assuming an active material loss of 1000 cm^{-1}, corresponding to the lower bound on the active material loss [2]. The direction of propagation is in the z direction and the y axis denotes the vertical direction. The mode propagates in the passive waveguide from $z = -200$ μm until $z = 0$ μm, at which point the tip of the active taper begins and the mode is coupled vertically upward into the active waveguide.

there are other benefits to having larger contacts, such as heat dissipation and ease of probing.

2.5.2 Multimode Interference Couplers

For splitting and combining optical signals, multimode interference (MMI) couplers were used because they offer better polarization and fabrication tolerances than directional couplers or Y-splitters [111]. The MMI coupler is actually a multimode waveguide, so its dimensions will always be larger than any single-mode passive waveguide, making the MMI easy to fabricate using contact lithography. The MMI coupler takes advantage of specific relationships between the propagation constants of the different waveguide modes to obtain self-imaging of the input field at particular distances along the length of the MMI waveguide. Light can be launched into and recovered from a multimode waveguide by means of single-mode passive waveguides. The design of 1×2 and 2×2 MMI couplers are shown in Figures 2-7 and 2-8, respectively. The input and output waveguides are 2 μm apart from each other.

The 1×2 MMI, when used as a combiner, will only operate as desired if the two

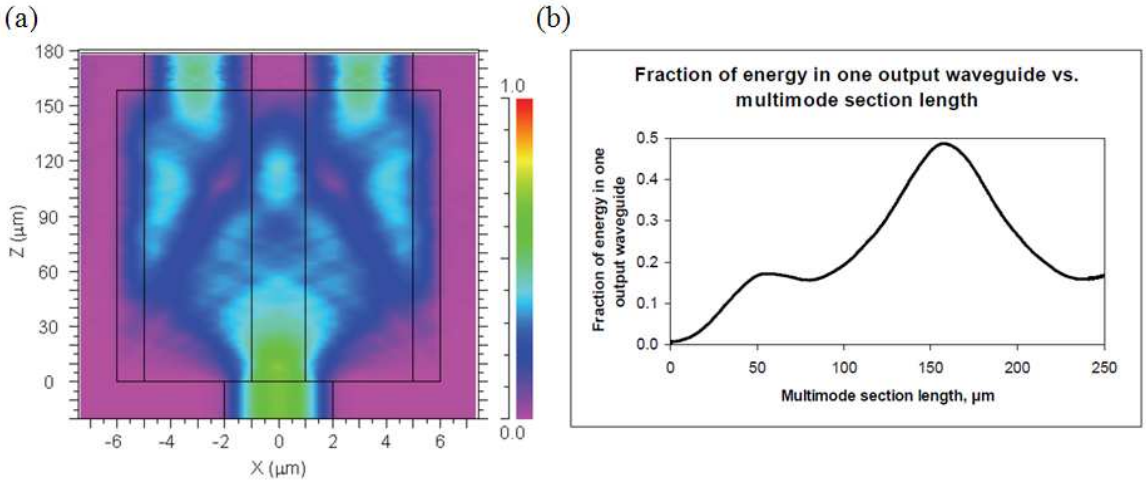

Figure 2-7: BPM simulation of a 1×2 MMI coupler producing a 50-50 splitting ratio. (a) Plan view BPM simulation depicting the cross-section of the optical field. (b) Graph of the normalized energy in one output waveguide as a function of the length of the MMI. The optimum length for 50-50 splitting is seen to be 159 μm.

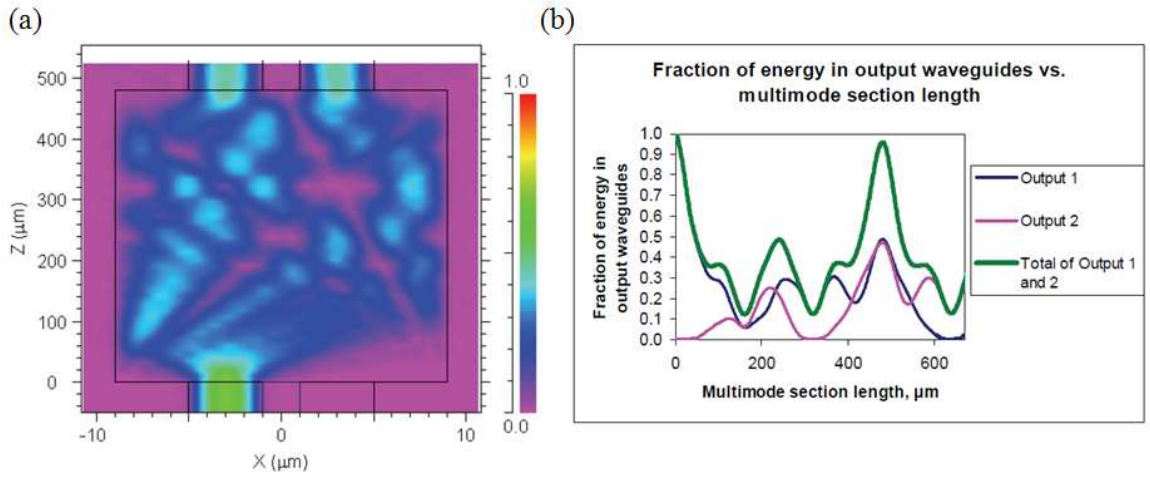

Figure 2-8: BPM simulation of a 2×2 MMI coupler producing a 50-50 splitting ratio. (a) Plan view BPM simulation depicting the cross-section of the optical field. (b) Graph of the normalized energy in the output waveguides as a function of the length of the MMI. The optimum length for 50-50 splitting is seen to be 480 μm.

inputs are in phase. When the two inputs are out of phase (π phase shifted), they destructively interfere at the output, meaning that the power will be reflected back toward the inputs. With the 2×2 MMI coupler, the MZI arms can be biased so that when destructive interference occurs at one output, the other output exhibits constructive interference ($\pi/2$ and $3\pi/2$ phase shifts) [65]. Using the 2×2 MMI coupler, no counter-propagating modes exist in the all-optical unit cell.

2.6 Fabrication

The fabrication process of the AOL unit cell is challenging because the structure has passive and active layers that must be patterned separately while maintaining perfectly alignment with each other. The process flow is depicted in Figure 2-9. Quantitative details of the fabrication process can be found in Appendix Section C.4.

2.6.1 Mask Design

The fabrication process requires a total of three contact lithography steps using three different masks, one for each of the following layers: the active layer (Mask 1), the

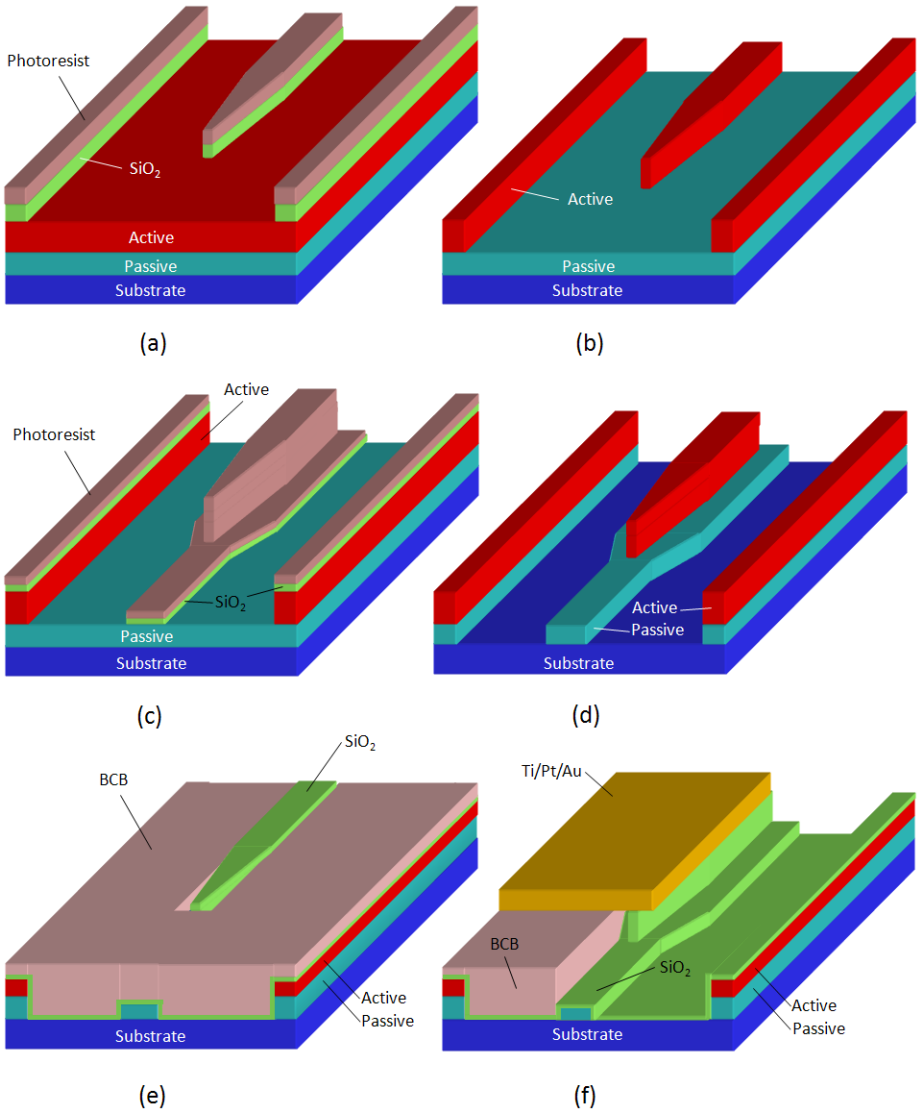

Figure 2-9: Process flow for the all-optical logic gates investigated in Chapter 2. (a) 200 nm of SiO_2 is deposited (PECVD), followed by a photolithography step to define the active waveguides and trenches. (b) The resist is removed and the active region is etched using ICP RIE. (c) A layer of 200 nm SiO_2 is deposited (PECVD), followed by a 2nd photolithography step to define the passive waveguides. (d) The resist is removed and the passive waveguides are etched using ICP RIE. (e) BCB is applied and etched back in RIE to expose the SiO_2 on the active ridge. (f) The SiO_2 is removed in HF. A photolithography step is implemented to define the contact pads, and Ti/Pt/Au contacts are deposited by e-beam evaporation, followed by lift-off. The wafer is lapped to 160 μm, followed by backside e-beam evaporation of Ge/Au/Ni/Au. The metal is annealed at 450°C for 30 s to obtain ohmic contacts.

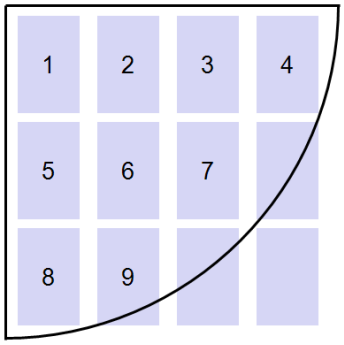

Figure 2-10: The arrangement of dies on a quarter 2-inch wafer. Only 9 of the 12 dies on the mask can be fit in their entirety onto the quarter wafer. Each die contains 35 devices as shown in Figure C-10 in Appendix C.

passive layer (Mask 2), and the metal layer (Mask 3).[1] The smallest feature on the masks is the tapered waveguide on Mask 1, which starts from 2 or 4 μm (depending on the width of the SOA) and decreases to a point at the tip. Contact lithography systems are generally only capable of achieving a resolution of $\approx$1 μm. With some experimentation, a taper tip that was approximately 0.5 μm in width was achieved with consistency and in many instances down to 0.1 μm wide tip widths were observed.

Each die was designed to have 35 devices, including passive waveguides with bends, single SOAs coupled to passive waveguides, MZI structures, and AOL unit cells. Each mask had 12 identical dies arranged in a 3-by-4 grid. The devices were fabricated on quarters of 2-inch wafers, which could only accommodate 9 of the 12 dies, as shown in Figure 2-10. The axes of the dies were aligned to the crystalline cleave axes of the wafer, which were grown by metal-organic chemical vapor deposition (MOCVD) on (100) InP substrates by a commercial wafer supplier, IQE.

In general, contact masks are patterned using a direct-write method such as electron-beam lithography or laser direct-write lithography on a glass plate. In the simplest case, a metal such as chromium is deposited onto the plate after lithography and a lift-off process is used to pattern the metal. However, this makes the surface of the mask uneven, since the metal ends up sitting on the glass plate. Some masks are manufactured by first etching trenches in the glass, and then filling them with

[1]The fabrication sequence has been modified from the initial four-mask process presented in [141].

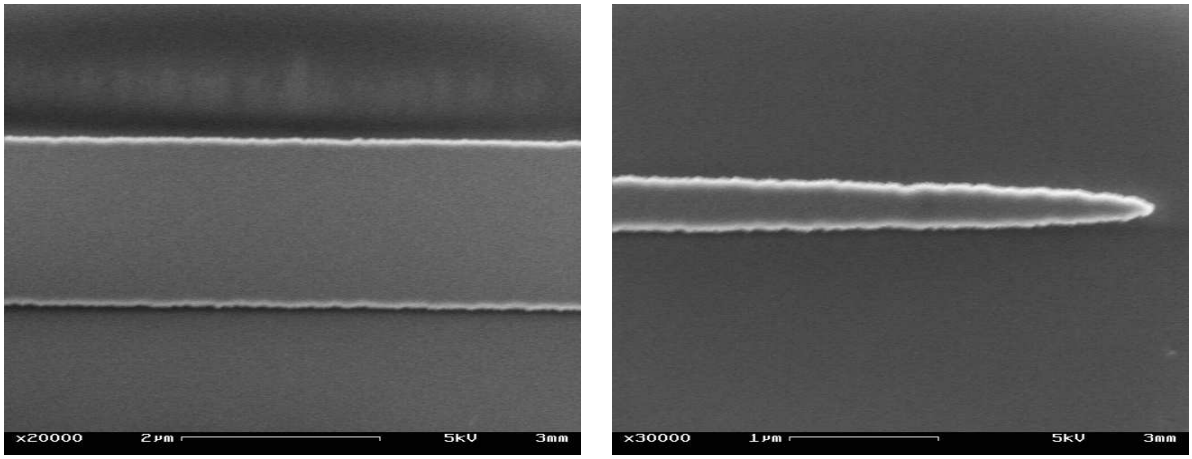

Figure 2-11: Side-edge roughness of the metal on the mask of a straight waveguide and a taper.

metal, leaving the surface smooth. For contact lithography, the quality of the contact between the mask and the substrate determines the quality of the pattern to a large extent. More details about contact lithography can be found in Appendix B.

The fidelity of the mask is another important point to consider, because the mask is the mold from which all of the patterns on the chips are made. If there is a mistake on the mask, then that mistake will be propagated through the various process steps onto the final device. For example, the AOL masks exhibited non-negligible side-edge roughness, as shown in Figure 2-11, most likely due to the use of a laser direct-write process. A significant fraction of the total waveguide side-wall roughness is likely due to the mask itself. The roughness could probably have been reduced if the mask were written using electron-beam lithography.

Aside from devices and test structures, the dies had alignment marks to facilitate the alignment of the different mask patterns to each other. The most crucial alignment is between Mask 1 and Mask 2, since any offset of the active waveguide to the passive waveguide can degrade the active-passive coupling efficiency. Figure 2-12 is a SEM of a taper that is misaligned to the passive section underneath. Well-designed fabrication processes try to minimize or eliminate critical alignment steps and replace them with non-critical or self-aligned strategies. Furthermore, dark-field masks (negative masks) are much more difficult to align than clear-field masks (positive masks) and should

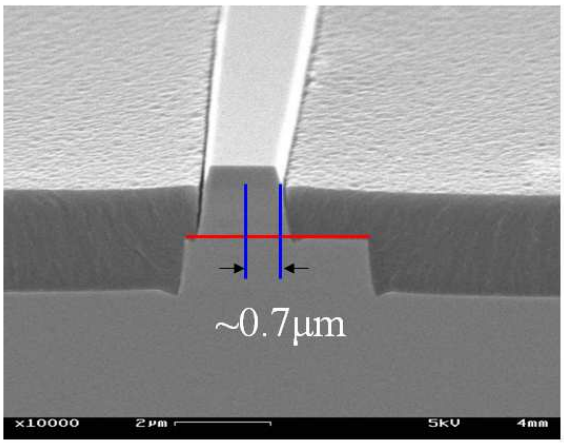

Figure 2-12: Part of a taper that is misaligned to the passive waveguide below.

be avoided. Alignments in this thesis were performed on a Electronic Visions EV620 Mask Aligner.

2.6.2 Photoresists

The first mask (Mask 1) defines the active layer and is a positive mask, meaning that the metal pattern on the mask is the same as the desired resist pattern when a positive resist is used. For this lithography step, AZ5214 (manufactured by AZ Electronic Materials) was used initially, but was later replaced by PR1-4000A (manufactured by Futurrex) because the AZ5214 was discovered to leave a residue during reactive ion etching with fluorine-based chemistries. A series of calibration experiments were performed for PR1-4000A and all of the other resists used in this thesis. The details can be found in Appendix Section C.4.

The two important parameters of a photolithography step are the exposure dose and the development time. These two parameters are not independent, so determining the proper dose and development time is often an iterative process. Figure 2-13 shows the PR1-4000A resist profiles of the same pattern that was defined using two different exposure doses and developed for the same amount of time (50 s). The resist profile in Figure 2-13(a) exhibits footing, suggesting that the resist is underexposed, which the residue in the trench confirms. The resist profile in Figure 2-13(b) exhibits a slight

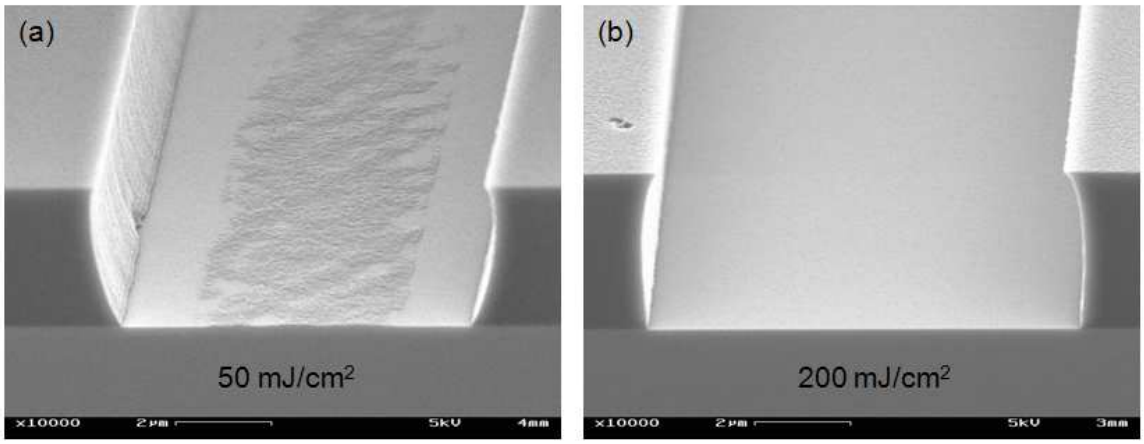

Figure 2-13: Photoresist profiles of PR1-4000A for different exposures. (a) An underexposed resist profile, as seen from the footing and the resist residue in the trench. (b) An overexposed resist profile, as seen from the T-topping or undercut of the resist profile.

T-topping (undercut), suggesting that it is slightly overexposed. Through a series of experiments, the correct dose is found to be 125 mJ/cm^2 for a resist thickness of 2.8 μm.

Figure 2-14 shows the PR1-4000A resist profiles of the same pattern exposed at the same dose (125 mJ/cm^2) but developed for different lengths of time. The resist in Figure 2-14(a) is underdeveloped judging from the curved resist profile, while the development time used for Figure 2-14(b) is closer to ideal. Practically speaking, many parameters that affect a photolithography step can change over time, such as the power of the lamp of the contact aligner, the age of the photoresist, and the humidity in the lab. Performing exposure calibrations intermittently is important because of this drifting of process parameters over time.

One challenge with contact lithography is obtaining good contact between the mask and the sample. As mentioned above, if the surface of the mask is not flat, that can translate into a non-uniform contact. The same occurs if the surface of the sample is not flat. Dust particles that land on the surface of the sample can create gaps between the mask and the substrate. Another issue can cause non-uniform contact is non-uniform spin coating of the photoresist. This is a disadvantage of using quarter-

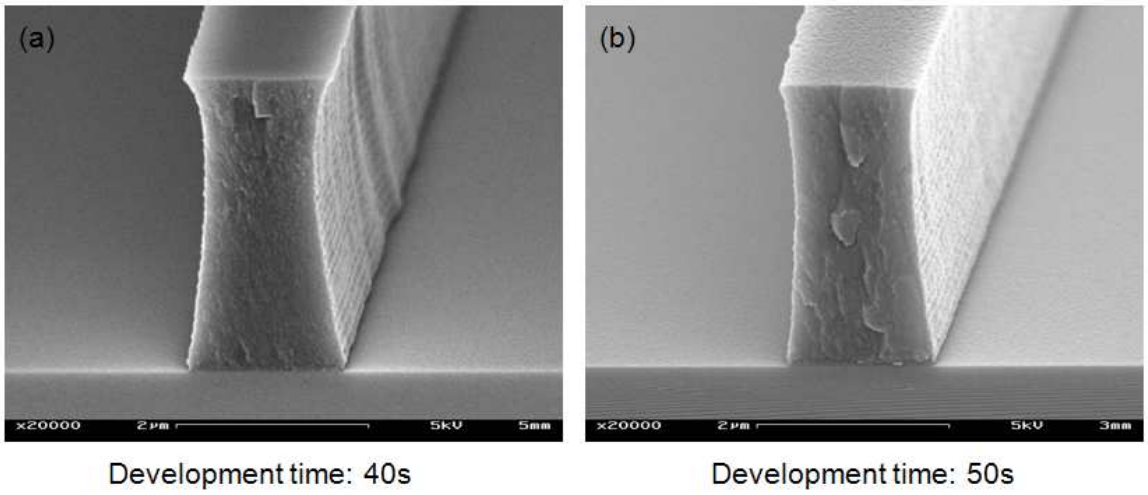

Figure 2-14: (a) An underdeveloped resist profile, as seen from the wider top and bottom of the ridge. (b) A resist profile that experienced the proper development time, as seen from the straighter sidewalls.

wafer samples instead of full-wafer samples, because quarter-wafer samples do not spin as uniformly as full wafers.

An experiment that was performed on a square sample is shown in Figure 2-15. The same pattern was exposed on the mask at different positions on the sample. Away from the center of the sample, the resist profile is degraded, due to the worsened quality of contact achieved. Different methods can be used to minimize the amount of non-uniformity across a sample, such as cleaning the sample and mask before exposure. However, as a fabrication process is carried out, the sample surface will almost certainly accumulate height variations due to etching. One can employ the use of flexible masks that conform to the sample surface to alleviate this problem [97].

By optimizing the contact lithography step for the tapers, taper tip widths well below 1 μm were achieved. As mentioned above, the ideal taper would end at a point. However, due to fabrication constraints, the taper tip was designed to be 0.5 μm. The mask was made so that the taper did shrink to a point, as seen in Figure 2-11. In the experiments though, a sharp point could not be achieved. Surprisingly, the limiting factor was not the optics, but rather the rigidity of the photoresist. As shown in Figure 2-16, the resist at the tip was so thin that it could no longer remain

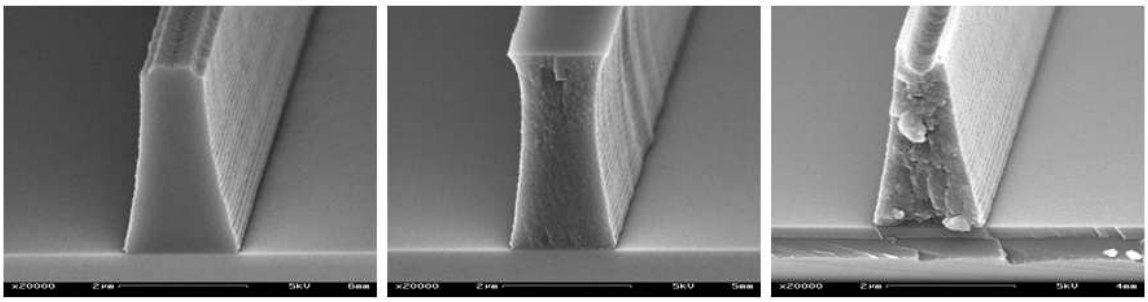

Figure 2-15: An experiment is performed where the same pattern is exposed on different regions of a square sample. The resist profile one centimeter to the left or the right of the center of the sample is degraded due to poor contact between the mask and the wafer.

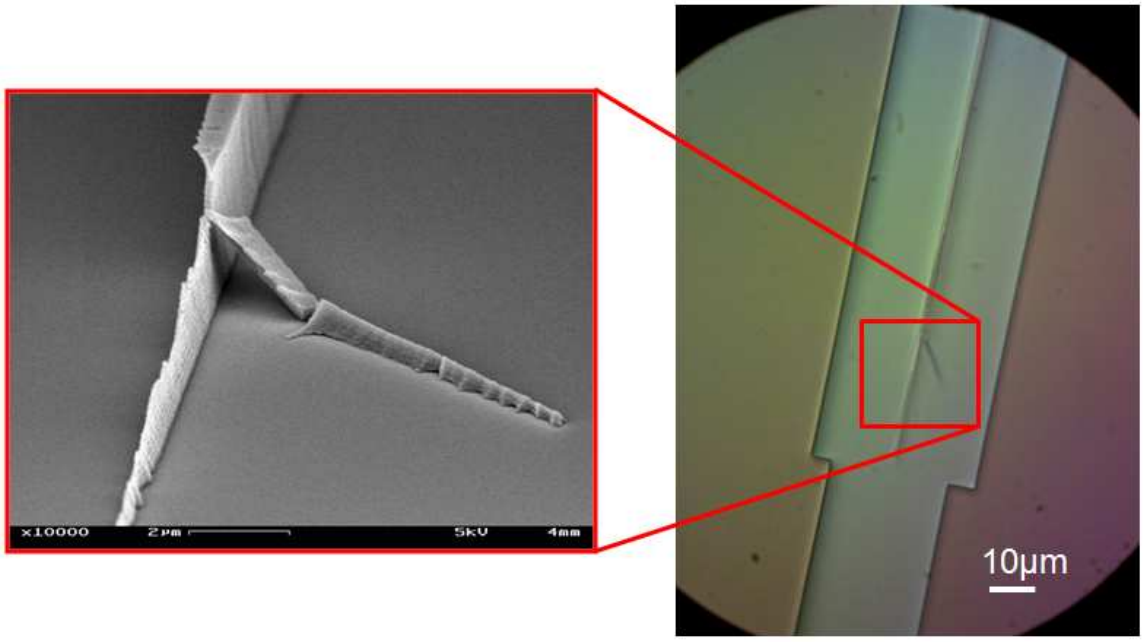

Figure 2-16: SEM of a taper defined in photoresist (PR1-4000A) that has fallen over. The taper is unable to be fabricated such that it shrinks to a sharp tip, as designed. If the taper tip is made too thin, the photoresist cannot stand upright.

upright. By fabricating tips that were approximately 0.5 μm wide, this was no longer an issue.

The final consideration of a photolithography step is the removal of the resist after the pattern has been transferred to the underlaying layers. In most circumstances,

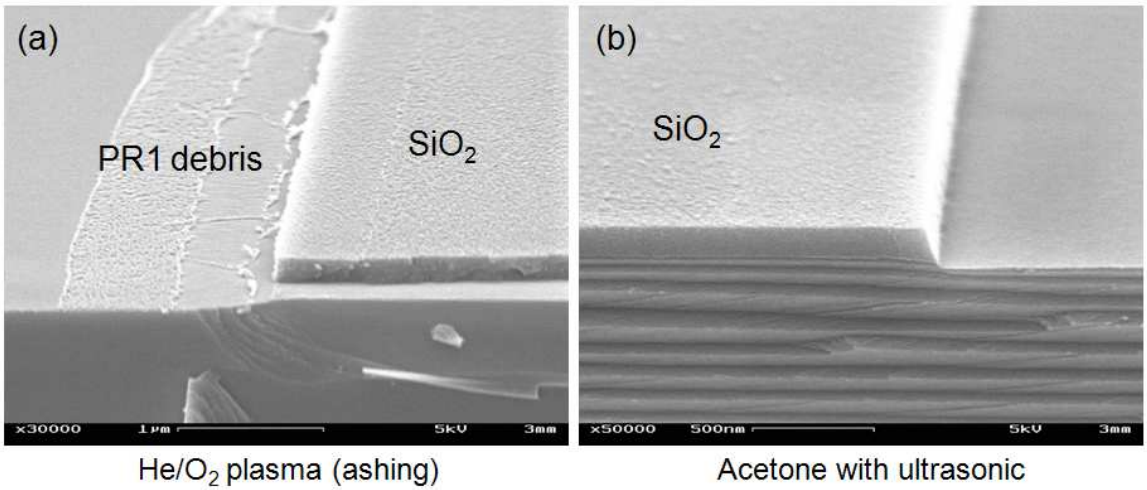

Figure 2-17: Photoresist (PR1-4000A) removal experiments. (a) Removing the PR1-4000A resist with acetone or RR4 left debris on the surface of the sample that was unable to be ashed off. (b) Removing the PR1-4000A resist with acetone in an ultrasonic bath was seen to consistently remove the resist without leaving debris.

a solvent such as acetone or a commercially available resist remover such as RR4 (manufactured by Futurrex for Futurrex resists) is adequate. However, in the case of PR1-4000A, the resist could not be completely removed, as shown in Figure 2-17(a). A common technique for removing leftover resist debris is to ash the resist in a He/O_2 plasma. However, 20 minutes of ashing did not remove the debris left on the surface of the wafer either. After some experimentation, the most reliable method for removing the resist without leaving debris was to use acetone with ultrasonic agitation, the results of which are shown in Figure 2-17(b).

The second mask (Mask 2) defines the passive layer and is a dark-field mask that requires the use of a negative resist. AZ5214 was used as a negative resist by first performing the exposure at a lower intensity, then adding a post-exposure bake, and finally a flood exposure. The third mask (Mask 3) for the metal contacts is a clear-field mask, and requires the use of a negative resist. The reason a clear-field mask is paired with a negative resist is because the resist is used to perform a lift-off to define the metal contact pads, which is another image-reversal process. AZ5214 and NR9-1000PY (manufactured by Futurrex) were used, both of which facilitate the lift-off process by having an undercut profile as shown in Figure 2-18.

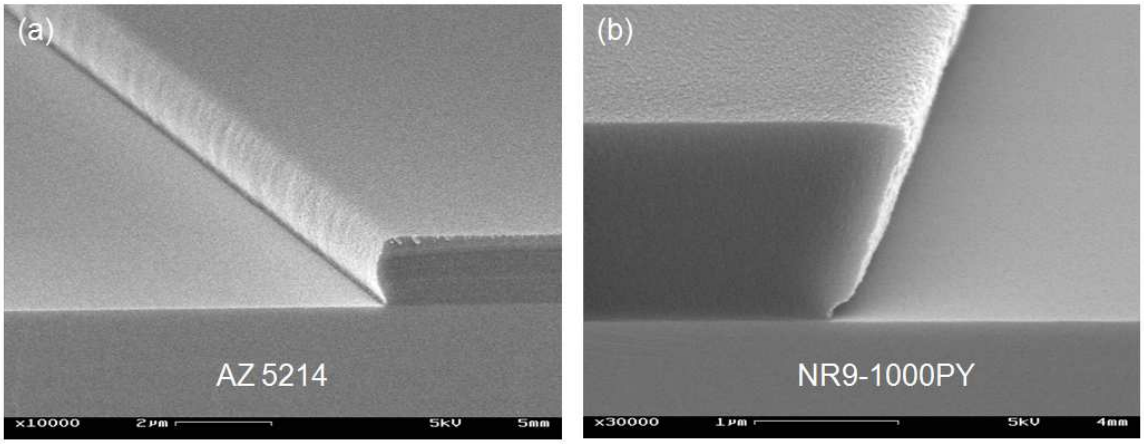

Figure 2-18: Cross-sectional profiles of some negative photoresists. (a) AZ5214 resist exhibits an undercut that facilitates the lift-off process. (b) NR9-1000PY resist exhibits an undercut that is even more conducive to lift-off.

2.6.3 Reactive Ion Etching

After the photolithography steps, reactive ion etching (RIE) is used to transfer the photoresist pattern into the SiO_2 and the semiconductor. Using the photoresist as an etchmask, the SiO_2 layer below the photoresist is etched in a Plasma-Therm 790 RIE system. Then the resist is removed and the SiO_2 is used as an RIE etchmask for the etching of the semiconductor layers below. The semiconductor etch is performed with the SAMCO Model 200iP Inductively-coupled Plasma (ICP) RIE system. For a more detailed treatment of RIE, please refer to Appendix Section B.3.

There are many characteristics associated with the profile of an RIE-etched ridge. The "anisotropy" describes the degree of directional (vertical) etching that is achieved (as opposed to "isotropic," or omnidirectional, etching). "Trenching" occurs when there is a small region of deeper etching on the sides of the etched ridge, forming what looks like a gutter around the ridge. The opposite of trenching is "footing," or a region of shallower etching on the sides of the etched ridge. Side-wall roughness, often transferred from the etchmask, is also known to be intensified by RIE processes [10]. Surface roughness, often referred to as "grass," is another undesirable characteristic.

The calibration of an RIE step requires the consideration of all of the above aspects. Etch calibration is an iterative process involving many parameters, as described

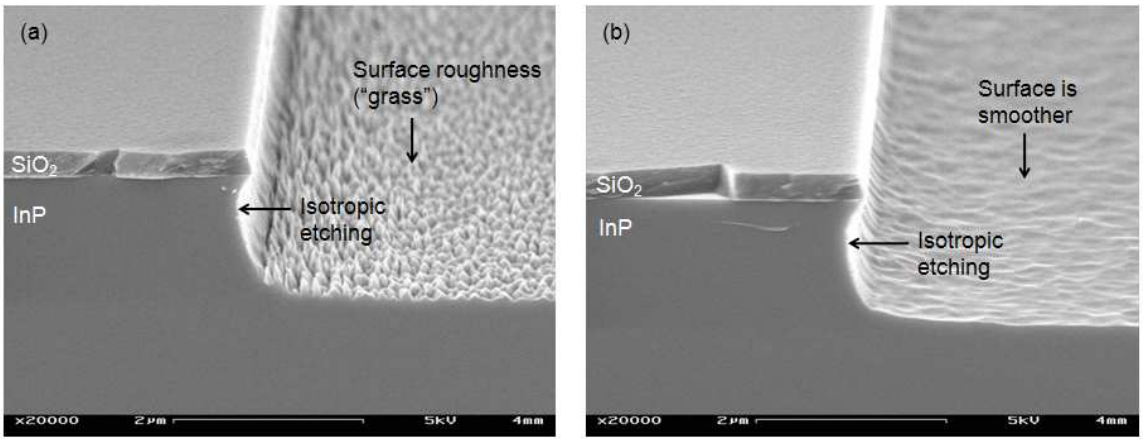

Figure 2-19: The etch profiles of 90-second InP etches with SiO_2 etchmasks on ceramic carriers and the following shared parameters: Bias power = 100W; ICP power = 250W; Cl_2 flow = 0.5 sccm; Ar flow = 10 sccm; Pressure = 0.6 Pa; Temperature = 220°C. (a) The $SiCl_4$ flow = 1 sccm (b) The $SiCl_4$ flow = 2 sccm.

in Appendix Section B.3: (1) gas flow, (2) RF power, (3) DC bias voltage or power, (4) chamber pressure, (5) temperature, and (6) etch time. These parameters are often not independent from each other. Another point of consideration is the state of the etching chamber—whether it has been cleaned and/or conditioned. A chamber that needs to be cleaned can manifest itself in an etch as surface roughness. The particulates on the chamber walls can land on the sample surface and act as micromasks. However, as shown in Figure 2-19(a) for the etching of InP, surface roughness can occur even when the chamber has been cleaned. The micromasking that is occuring in this case is due to sputtering of the SiO_2 etchmask. The surface roughness is found to be reduced by increasing the isotropy of the etch (in this case, increasing the flow rate of the $SiCl_4$ etch gas), as shown in Figure 2-19(b).

Figure 2-19 (a) and (b) are representative of the calibration etches performed for the InP material system in the SAMCO Model 200iP ICP RIE system. The final InP etch, shown in Figure 2-20, uses a higher bias power than the etches in Figure 2-19, which increases the anisotropy of the etch.

The carrier that is used to hold the III-V semiconductor samples in the Samco ICP RIE is ceramic. Other researchers have found that using a silicon carrier works

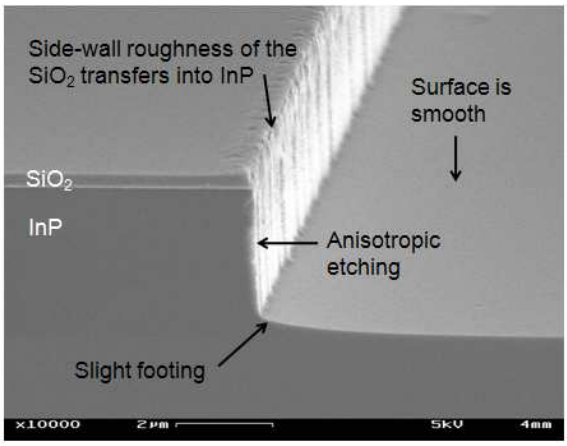

Figure 2-20: The optimized InP etch profile using an SiO_2 etchmask: a 90-second etch with a ceramic carrier and the following parameters: Bias power = 160W; ICP power = 250W; Cl_2 flow = 0.5 sccm; $SiCl_4$ flow = 2 sccm, Ar flow = 10 sccm; Pressure = 0.6 Pa; Temperature = 220°C.

for etching III-V semiconductors as well. One of the differences is that a silicon carrier will "load" the chamber and slow down the etch rate, because the chlorine-based plasma will etch silicon along with III-V semiconductors. Vacuum grease is often used between the carrier and the sample to create a good thermal contact that allows for better heat transfer from the carrier to the sample. For the RIE of most III-V semiconductors, the substrate needs to be at an elevated temperature because the resultant species from the etch are not sufficiently volatile at room temperature. If vacuum grease is not applied, there will be large gaps between the substrate and carrier, because neither is entirely flat, meaning that they will only make contact at a few points. One would expect the sample to take a very long time to reach thermal steady state with the carrier in a vacuum chamber. However, experimentally, etching is successful without vacuum grease, suggesting that the grease-less thermal contact is sufficient to achieve steady state within the time the sample is loaded into the chamber and the plasma is turned on. Avoiding vacuum grease makes the RIE step a cleaner process. Figure 2-21 shows etches of the taper tip and the active waveguide performed in an InP wafer, using the final calibrated etch parameters.

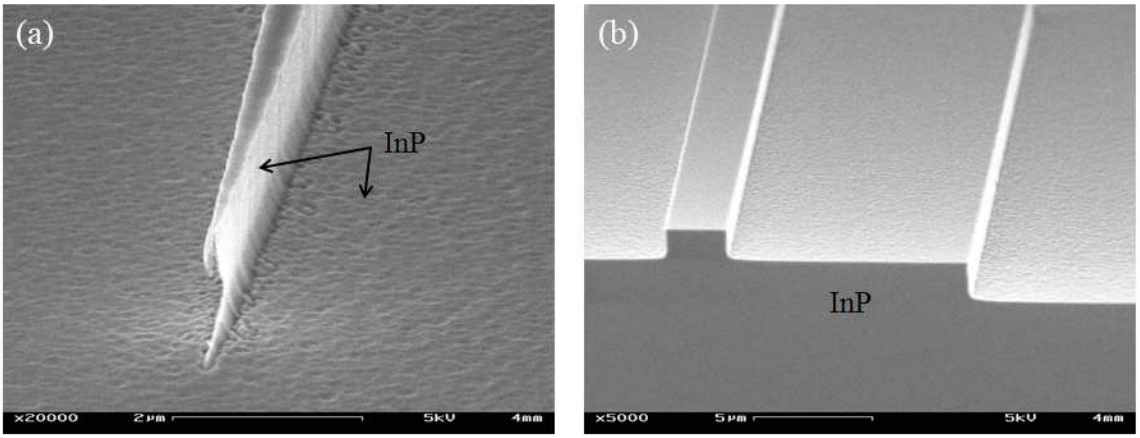

Figure 2-21: Scanning electron micrographs of the AOL unit cell during fabrication. (a) The tip of a taper etched in InP. (b) The active waveguide (SOA) structure etched into InP. Two photolithography and ICP RIE steps are required.

2.6.4 Planarization

After the photolithography and RIE steps that define the active and passive layers, the quarter-wafer is planarized to facilitate the application of contact metal pads. Planarization is achieved with benzocyclobutene (BCB), also called Cyclotene Advanced Electronic Resin (manufactured by Dow Chemical). BCB is a dielectric that is applied using spin-coating and then etched back using RIE. The planarization process is described in more detail in Appendix Section B.4. The refractive index of BCB at $\lambda = 1.55$ μm is close to 1.5, making it a an appropriate waveguide cladding material optically similar to SiO_2.

There are an assortment of BCB dilutions available that spin to different thicknesses. A thicker-spinning BCB increases the planarity, but requires a longer etch-back process. Depending on the topography of the sample surface prior to planarization, multiple layers of BCB can be applied to increase the planarity, but the BCB profile will always follow the underlying surface profile to some degree. For the purposes of the AOL chips, planarization is made to be better than 50 nm. After spin-coating, BCB is cured in a nitrogen environment at 250°C. After curing, the BCB is etched back using a CF_4/O_2 RIE chemistry. Due to the relatively fast etch-back rate, the exact point when the waveguides have cleared is difficult to determine. Fig-

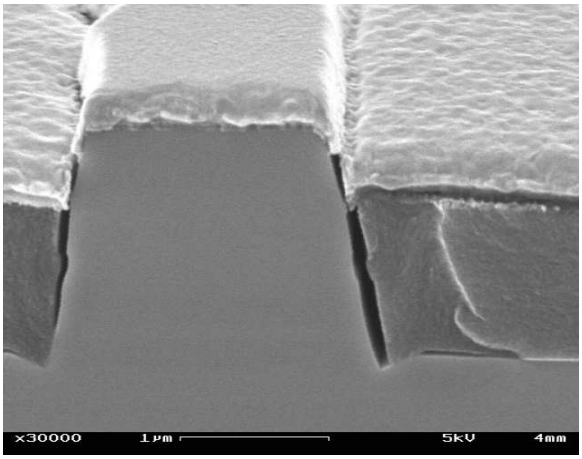

Figure 2-22: Poor BCB planarization causes the metal contact to be disconnected.

ure 2-22 shows BCB that was over-etched, along with the fabricated metal contact pads. When the height mismatch of the exposed waveguide to the BCB is larger than the thickness of the contact metal layer, the metal can become disconnected. The etch-back process needs to be monitored carefully using optical microscopy as well as profilometry to determine the position of the BCB relative to the ridges. Details of the BCB planarization process can be found in Appendix Section C.4.

Poor planarization was a primary cause of initial devices not being capable of supporting the requisite current injection levels that were needed to bring the active region into transparency or gain. Above 100 mA, the devices "burned out," with further probing resulting in open circuit responses. In conjunction with better planarization, the thickness of the metal layers were increased, so that even if there was a step between the semiconductor ridge and the BCB, as shown in Figure 2-22, the metal would have a greater likelihood of remaining connected.

In order to protect the semiconductor surface from damage due to ion bombardment in the RIE when the top of the ridge is exposed, a 100 nm layer of conformal high-frequency SiO_2 was deposited before the BCB was applied. The SiO_2 also facilitated the adhesion of BCB to the surface. The SiO_2 is removed with wet etching using buffered HF. Figure 2-23 shows an experiment of BCB planarization with SiO_2. As can be seen, the etch-back process introduces surface roughness to the BCB, which

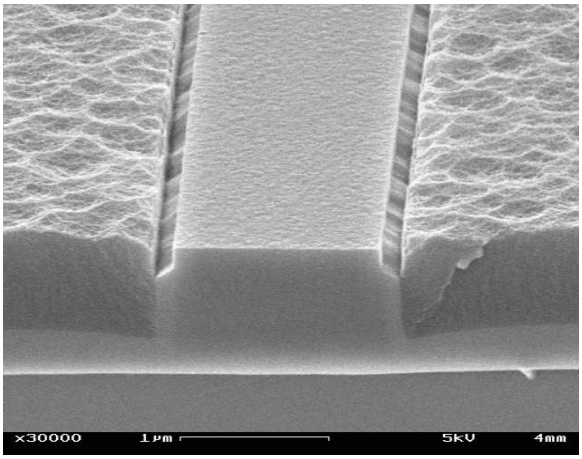

Figure 2-23: BCB planarization process on a silicon nitride ridge with a conformal layer of 100 nm SiO_2. After the SiO_2 is exposed, it is removed using buffered HF to expose the ridge.

is desired to enhance the adhesion of the contact metal layer to the BCB.

2.6.5 Metalization

The typical metal stack that is used to make contact to p-type InGaAsP is Ti/Pt/Au that is annealed at 450° for 30 s.[2] A contact resistance on the order of $10^{-6}\ \Omega \cdot \text{cm}^2$ is desired, and can be achieved if the p-doping of the InGaAsP top contact layer is on the order of $10^{19}\ \text{cm}^{-3}$ [44]. Unfortunately, the wafers had been doped to a level of approximately $2 \times 10^{18}\ \text{cm}^{-3}$. Correspondingly, the contact resistances of the devices were on the order of $10^{-4}\ \Omega \cdot \text{cm}^2$, estimated from the diode characteristics. This large contact resistance can generate a large amount of resistive heating that can compromise the performance of the AOL devices. A discussion on metalization can be found in Appendix Section B.5.

Zinc-based metal stacks were investigated, as they have been shown to achieve contact resistances of $10^{-6}\ \Omega \cdot \text{cm}^2$ at the doping level of the existing InGaAsP contact layer, $2 \times 10^{18}\ \text{cm}^{-3}$ [9, 95]. Experiments using the metal stack Pd/Zn/Pd/Ge were performed. A two-mask set of contact resistance test structures was designed,

[2] A note on convention: the metal layers are listed in the order of the deposition. Therefore, a "Ti/Pt/Au" structure consists of Au that is physically at the top of the metal stack.

Table 2.3: The mean and standard deviation of the implants, as obtained from Transport of Ions in Matter (TRIM) simulations of the ion energy. The two implants were designed so that the average ion concentration over $\pm\sigma$ was $1.1 \times 10^{19}\text{cm}^{-3}$.

Dose (cm^{-3})	E (keV)	μ (nm)	σ (nm)
5.7×10^{13}	8	24.3	13.0
2.1×10^{13}	2	8.8	5.1

as shown in Appendix Section C.3. A detailed treatment of contact resistance measurements can be found Appendix D. After the test structures were fabricated, the electrical measurements were performed using a two-probe station connected to a Tektronix Type 576 Curve Tracer. The studies suggested that for the metal stack Pd/Zn/Pd/Ge, the Zn diffused beyond the immediate contact layer into the semiconductor nearby, which was undesirable. Other groups have also observed similar effects [82].

Next, other methods of increasing the doping level of the p-type InGaAsP contact layer were investigated to obtain a lower contact resistance with the Ti/Pt/Au metal stack. Common p-dopants of InP are zinc and carbon. Among these, carbon has the capability of ion implantation. Two carbon (C+) ion implantations were designed to bring the doping level of the 50 nm thick InGaAsP contact layer from 2×10^{18} cm^{-3} to 1×10^{19} cm^{-3}. The dose and acceleration energies of the two implantations are presented in Table 2.3.

Table 2.3 also shows the mean and standard deviation of the implantation profile, as calculated from Transport of Ions in Matter (TRIM) simulations. The ion density profiles after implant can be assumed to be near Gaussian in shape, as described by Equation 2.1.

$$\text{Dose} = \int \frac{\text{Dose}}{\sigma\sqrt{2\pi}} \exp\left(\frac{(x-\mu)^2}{2\sigma^2}\right) dx \tag{2.1}$$

where the integral is over all of space. The implants were performed by Innovion Corporation.

After ion implantation, an anneal must be performed to minimize the damage

due to the ion bombardment of the substrate via recrystallization. If left unannealed, the dangling bonds produced by the ion bombardment can introduce mid-gap states that would degrade the efficiency of the device by providing nonradiative pathways for recombination. The anneal process will also allow the carbon atoms to diffuse beyond the Gaussian density profiles described by Equation 2.1, creating a more uniform distribution. After experimenting with the anneal process, a final anneal of 750°C for 60 s was seen to exhibit the lowest contact resistance. However, after the fabrication of the devices, measurements were unsuccessful, most likely due to damage still left in the contact layer even after the anneal was performed. At this time, effort was shifted towards fabricating and characterizing devices with the original contact layer doping and the Ti/Pt/Au metal stack. Despite the higher contact resistance, the devices operated properly as long as they received adequate cooling.

To facilitate heat dissipation, thick metal (on the order of 1 μm) was used for the contact pads. Thicker metal also eases the electrical probing process and enhances metal continuity across non-planar regions of the wafer. The initial method of metal deposition was electron beam (e-beam) evaporation. While electron beam evaporation can be used to deposit thick metal, it is expensive because it coats the entire evaporation chamber with metal, most of which is wasted. Layers thicker than 200 nm were seldom deposited using e-beam evaporation. The more economical alternative is electroplating, which only deposits metal at the desired locations of the contact pads.

Electron beam evaporation of 900 nm of metal was performed. The total metal stack consisted of Ti/Pt/Au with thickness of 30/20/850 nm. A lift-off process was performed using AZ5214 photoresist. A good rule of thumb for lift-off is that the thickness of the metal should be at most 1/3 that of the photoresist. Thus, multiple lift-off steps were required to create 900 nm thick metal pads. A technique for multiple lift-off steps of the same metal contact pattern was developed. As shown in Figure, 2-24, consecutive lift-off patterns should be intentionally misaligned so that at the photoresist-metal boundary, the thickness of the metal is not augmented by the previous deposition. Three liftoff steps of thicknesses 300 nm each were performed,

with intentional misalignments of approximately 15 μm.

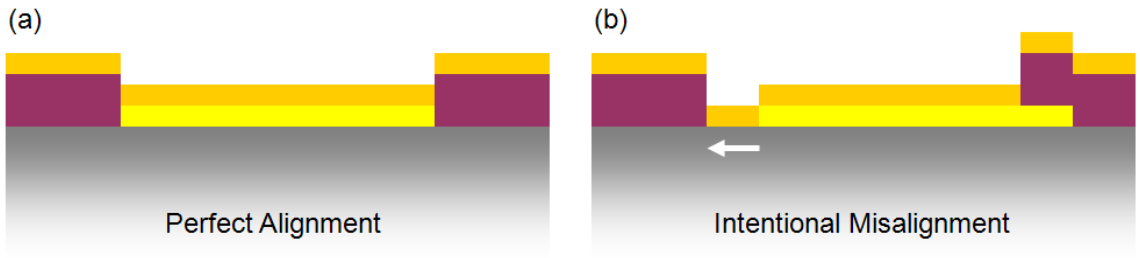

Figure 2-24: Technique for the lift-off of multiple metal layers. (a) A perfectly aligned resist profile can create difficulty in the lift-off step because the solvent has difficulty accessing the edge of the photoresist. (b) An intentionally misaligned resist profile does not have the difficulty with lift-off.

Electroplating was also performed on certain samples to create metal pads that were 2 μm in thickness. Electroplating is a process in which the sample is immersed in a solution of metal ions. The metal (in this case, Au) is moved by an electric field to coat areas of the sample that are electrically conductive. Prior to electroplating, metal pads consisting of Ti/Pt/Au at thicknesses of 30/20/70 nm were fabricated using e-beam evaporation and a lift-off step. Next 80 nm of Au was e-beam evaporated over the entire sample. Finally, a photolithography step was used to define the contact pads once again. The thin (80 nm) Au seed layer ensures that all of the contact pads are electrically connected. Next, electroplating is performed. The Au accumulates in areas that are not covered by photoresist. Finally, the photoresist is removed (this is not a lift-off step) and a short wet-etch removes the thin layer of Au that connects the contact pads to make them electrically isolated. Figure 2-25 shows the results of contacts created using electroplating.

2.6.6 Post-processing

One of the challenges of fabricating an integrated photonic circuit is the input and output coupling of optical signals. Because the waveguides run along the plane of the wafer, the most natural inputs and outputs occur at the edges of the chip. However, even when cleaving along a crystalline plane of the semiconductor, smooth facets

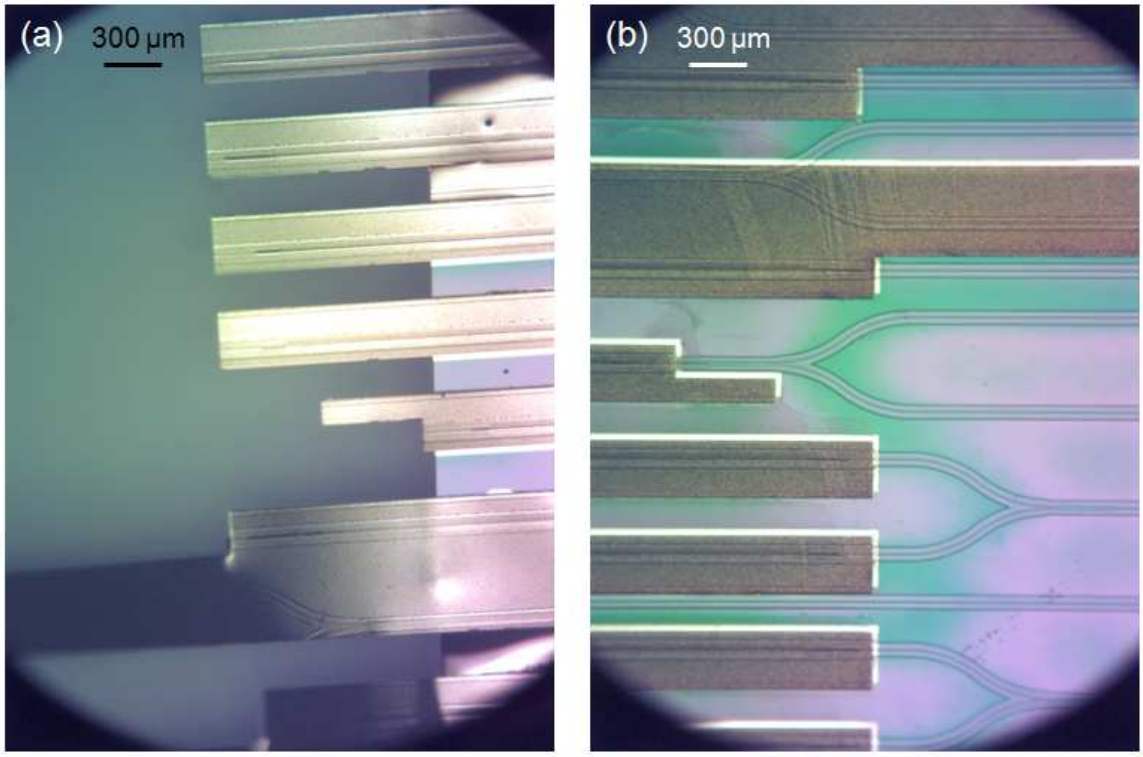

Figure 2-25: Contact pads formed by Au electroplating. (a) Electroplated metal contact pads (2 μm thick) are seen to hang off the edge of a cleaved sample. (b) Electroplated metal contact pads on a sample facilitated electrical probing because the probe tip can be pressed into the thick metal.

can be difficult to achieve. If a facet is scalloped or otherwise not smooth, input and output coupling will be compromised by excess scattering. Vertical couplers have been developed as a way to avoid this problem [131]. One of the methods that is used to obtain consistently smooth facets is wafer thinning, or lapping. Typical commercial III-V semiconductor wafers are approximately 350 μm thick. When the wafer is reduced to 200 μm or thinner, cleaving along crystalline planes results in consistently smooth facets. Thinning the wafer also reduces the resistance of the substrate and provides better heat dissipation through the substrate.

The samples were lapped by hand using aluminum oxide grit to a thickness of 160 μm. For the lapping process, the samples were mounted top-side down with wax to a cylindrically-shaped piece of glass, whose top surface is an optical flat. Details of the lapping process can be found in Appendix Section C.4.

After lapping, with the sample still mounted to the optical flat, 20/60/30/200 nm of Ge/Au/Ni/Au was evaporated onto the backside of the sample with a BOC Coating Technology Temescal FCE-2500. Then 50/70/50 nm of Ti/Pt/Au was sputter-coated onto the sample. A rapid thermal anneal (RTA) was then performed in a RTP-600XP at approximately 440°C for 30 s. Afterwards, the samples were unmounted and rinsed with trichloroethylene (TCE).

The thinned quarter-wafers were cleaved using a Loomis LSD-100 scriber into the individual dies. Then the dies were soldered onto a "dogbone" copper carrier using indium foil. Prior to soldering, the copper carrier was also coated with Ti/Pt/Au (thicknesses 50/70/50 nm) for matching the thermal coefficient of expansion to the Ti/Pt/Au sputtered onto the backside of the device. If materials that are soldered together have mismatched thermal coefficients of expansion, the connection can break due to thermal cycling (operation) of the device [141].

2.7 Measurement

The 35 devices on each die include (1) passive waveguides, (2) passive waveguides with bends, (3) passive waveguides with 50:50-split MMIs, (4) single SOAs coupled to passive waveguides, (5) Mach-Zehnder interferometers (MZIs) with SOAs in each arm, and (6) AOL unit cells. In this section, the characterization of each type of structure is described, in order of complexity.

The AOL chips were soldered onto a copper "dog-bone" shaped mount, which was then affixed to an actively-cooled copper block in the testing setup. The thermoelectric (TE) cooler is set to a temperature of 15°C as measured by a thermistor inserted into a hole that is drilled into the copper block. When cooling to temperatures below 18°C, one must be careful about condensation on the sample, which occurs when the temperature of the device is lower than the dew point of the laboratory environment.[3] Figure 2-26 is a photograph of an AOL chip under testing. Light is coupled into and out of the device using tapered fibers that have a 4 μm spot size. Depending on the

[3]The dew point is directly related to the humidity and is reported by most weather sources.

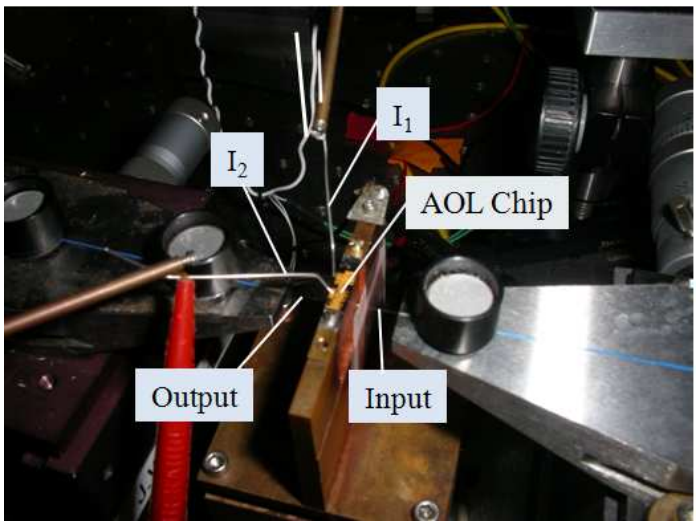

Figure 2-26: Schematic of the optical setup used for making measurements of the AOL chip. Current (I_1, I_2) is injected into the devices through probes brought from above the chip into contact with the metal pads. Light is coupled into and out of the device with tapered fibers. A coupling loss of 7.6 dB is experienced per facet. The single-mode SMF-28 output fiber is either connected to an InGaAs detector or an OSA, and the input fiber is connected to a tunable laser source.

type of measurement, the current probes, I_1 and I_2, may or may not be turned on.

2.7.1 Passive Waveguides and Bends

The most important metric that describes the passive waveguide structures is the propagation loss. One common method that is used to determine waveguide loss is the cut-back method. However, as the cut-back method is irreversibly destructive, a more gentle technique, the Hakki-Paoli method, was used [35]. The Hakki-Paoli method can be used to measure propagation losses independent of coupling losses into and out of the waveguide. The Hakki-Paoli method involves coupling light into the waveguide and varying its wavelength while measuring the transmission through the waveguide. As a function of wavelength, the transmission is oscillatory, corresponding to constructive and destructive interference between the reflected waves in the resonator created by the cleaved mirror facets. The values of the maximum and minimum transmitted powers depend only on the loss, reflectivities, and length of the waveguide. Thus, the total loss of the waveguide can be determined from the output

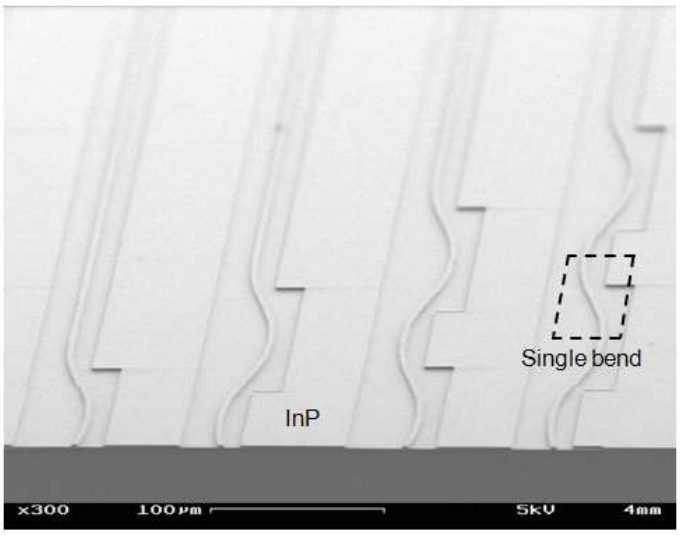

Figure 2-27: SEM of passive waveguide structures with different numbers of bends. A single bend is defined as a single "S" shape.

powers, reflectivities, and length:

$$\alpha = \frac{1}{L} \ln \left(\frac{\sqrt{P_{max}} + \sqrt{P_{min}}}{\sqrt{P_{max}} - \sqrt{P_{min}}} \right) + \frac{1}{2L} \ln(R_1 R_2) \tag{2.2}$$

where α is the power loss coefficient. In the measurements, P_{max} and P_{min} are values averaged over $\lambda = 1549$ and 1550.5 nm, $R_1 = R_2 = 0.272$ (calculated assuming an effective index of 3.18), and $L \approx 3.5$ mm for the particular chip. The passive waveguides were designed to have outputs that are at a 7° angle with respect to the cleaved facets to minimize reflections. However, because of initial difficulties coupling light into and out of angled facets, the dies were cleaved with straight facets. The passive waveguide loss was found to be 0.95 cm^{-1} or 4.1 dB/cm [137].

The AOL unit cell employs the use of passive waveguide bends. The larger bends have radii of roughly 330 μm and the smaller bends have radii of roughly 296 μm. On the dies, there are passive waveguides that have 2, 4, 6, and 8 bends that are designed to help characterize the bending losses. The bends for the test structures, depicted in Figure 2-27, have radii of roughly 285 μm, which means that any bending loss values obtained from these devices will be an upper bound on the loss of the actual bends that are used in the AOL unit cell. Using the Hakki-Paoli method, a bending loss of

1.17 dB per bend, or 0.75 dB per radian, was measured for the test structures. The definition of a single bend is shown in Figure 2-27.

2.7.2 Single SOAs

With straight cleaved facets, the single SOAs that were coupled to passive waveguides behaved as diode lasers. Figure 2-28(a) shows the lasing spectrum of an SOA (with dimensions 850 μm $\times$ 4 μm) for different levels of current injection. The lasing peak is seen to be red-shifted for increased current levels due to heating. The lasing wavelength is between 1575 and 1580 nm. Figure 2-28(b) shows the I-L curve for the same device. The threshold current is 210 mA and a peak output power of 2.5 mW is achieved at 400 mA. For higher current levels, the power decreases due to heating.

To make the device into a single-pass SOA rather than a laser, the straight-cleaved facets were anti-reflective (AR) coated. The fact that the same device was characterized with and without reflective facets yielded a unique opportunity to determine the tapered fiber coupling losses. Figure 2-29(a) depicts the laser structure, which consists of an active waveguide (SOA) coupled via the adiabatic taper to passive

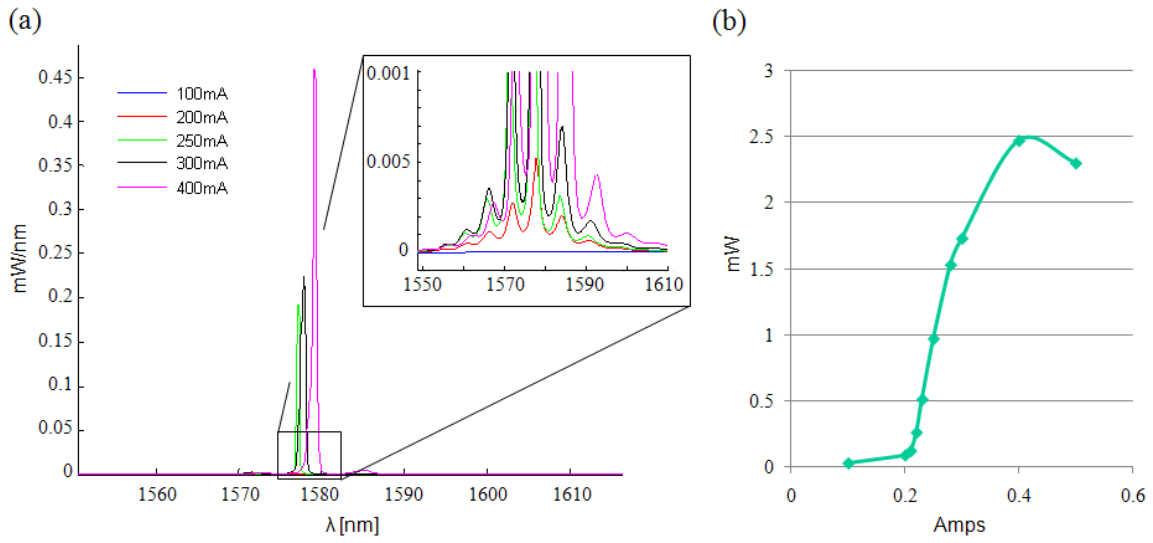

Figure 2-28: Measurements of a straight-cleaved 850 μm $\times$ 4 μm laser (before the facets are AR coated). (a) The lasing spectrum for different current injection levels. (b) The I-L curve for the same device. The threshold current is 210 mA.

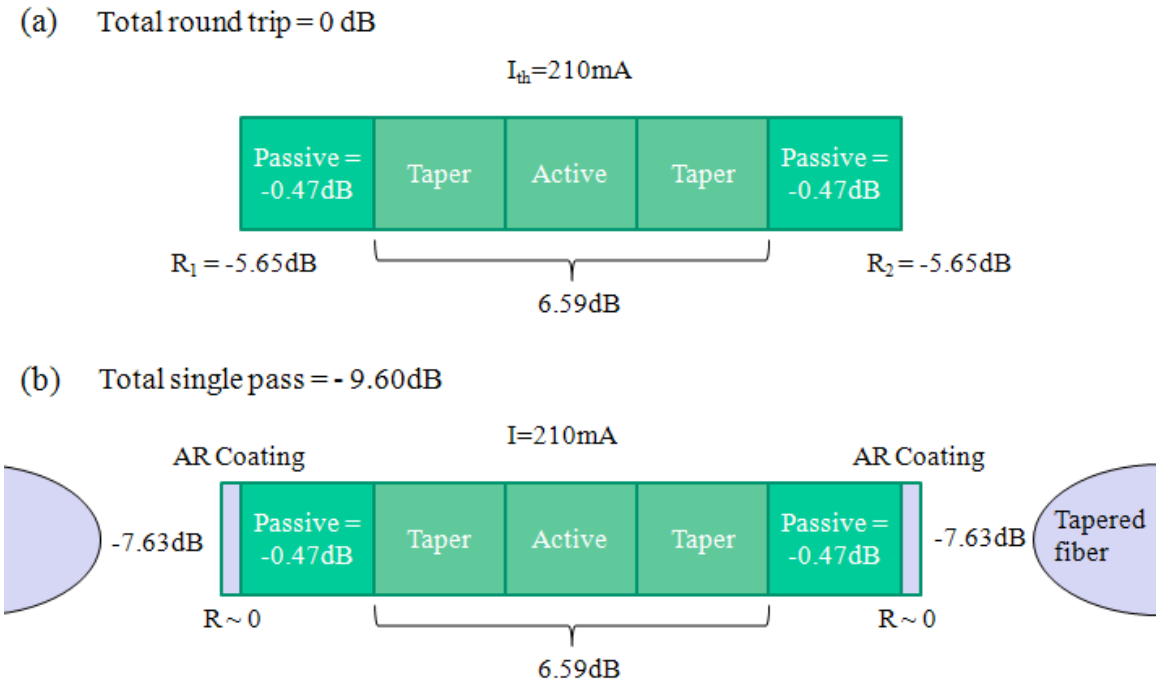

Figure 2-29: Schematic of the measurement of tapered fiber coupling losses. (a) Before AR coating: the taper-active-taper gain at I_{th} = 210 mA can be calculated since the round trip gain is known to be 0 dB. (b) After AR coating: the tapered fiber coupling loss can be calculated from a single-pass measurement since the taper-active-taper gain at I = 210 mA is unchanged.

waveguides on either end. The passive waveguide loss and the as-cleaved facet losses are known. Thus, at threshold (210 mA), the gain of the taper-active-taper region can be calculated, because the round-trip gain is known to be 0 dB.

After the application of the AR coating, a single-pass measurement can be made at a wavelength of 1575 nm with I = 210 mA using the tapered fibers, as shown in Figure 2-29(b). AR coating the facets does not affect the taper-active-taper gain of the device. Thus, at I = 210 mA, the taper-active-taper gain is the same as before AR coating took place. With all other losses known, the tapered fiber coupling loss is calculated to be 7.6 dB per facet. This value is large due to the mismatch between the passive waveguide mode, which is elongated (the passive waveguide is 4 μm wide and 1 μm tall), and the symmetric focal spot of the tapered fiber.

Once the tapered fiber coupling losses were determined, the total taper-active-

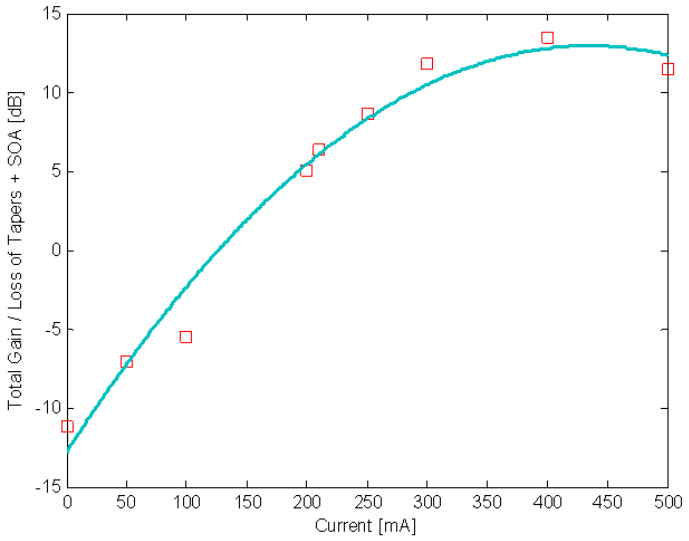

Figure 2-30: Total gain or loss of the taper-active-taper region as a function of current for a wavelength of 1575 nm. The line is drawn to guide the eye.

taper gain at $\lambda = 1575$ nm could be found for different levels of current injection, as shown in Figure 2-30. The gain region is seen to achieve transparency at $I = 130$ mA. The lasing threshold occurs at $I = 210$ mA when the gain is able to offset the passive waveguide and mirror losses.

The same device is measured for its amplified spontaneous emission (ASE) spectrum. As shown in Figure 2-31, the ASE peak blueshifts for increasing current injection up to approximately 300 mA. This blueshift is due to the bandfilling with increased carrier concentration levels. Above 300 mA, the ASE peak redshifts due to heating. The ASE spectrum is directly related to the gain spectrum of the active materials [22].

2.7.3 Mach-Zehnder Interferometers

After characterizing single SOAs, the double SOAs arranged in the MZIs were characterized. First, the MMI splitters were visually determined to provide close to 50-50 splitting [137]. The exact insertion loss of the MMI splitters were not measured because the important aspect of the MMI is to provide balanced splitting. Any losses due to the MMI can be compensated for by the gain of the device.

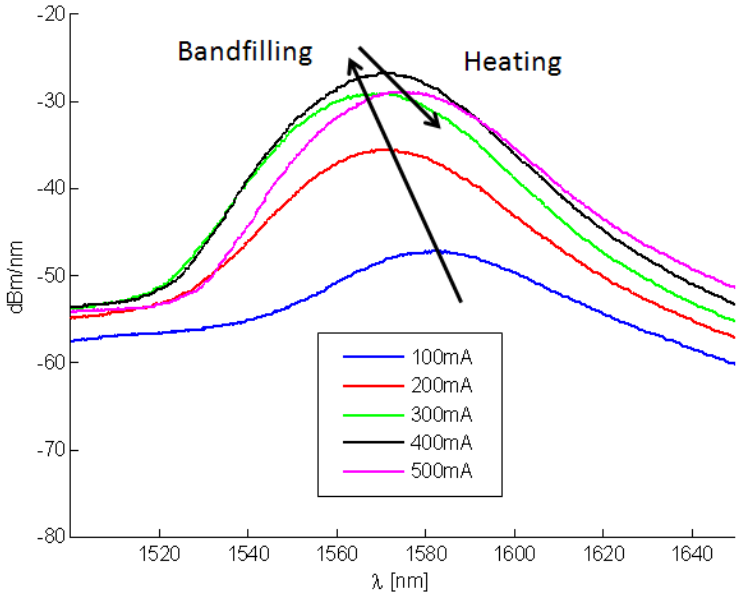

Figure 2-31: The ASE spectrum of the 850 μm $\times$ 4 μm SOA for different current injection levels. For lower current levels, bandfilling causes the ASE peak to blueshift, and for high current levels, the ASE peak is redshifted due to heating.

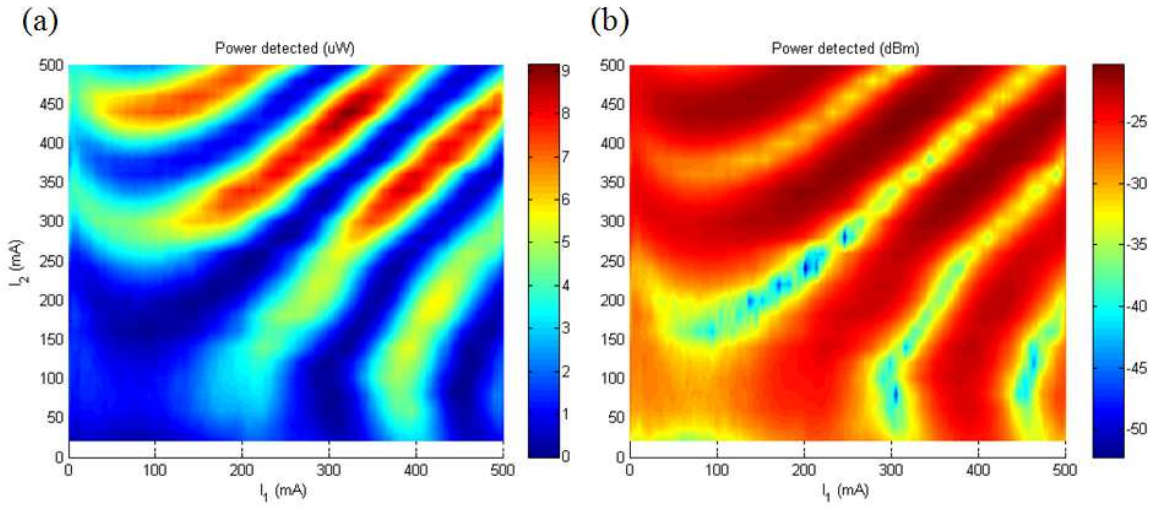

Figure 2-32: The 2D bias scan in which the constructive and destructive interference of the MZI can be observed. (a) The 2D bias scan on a linear scale of throughput power. (b) The 2D bias scan on a log scale.

Next, a bias scan is performed on the MZI to characterize the interference between the two arms. A bias scan is a two-dimensional sweep of the DC current that is injected into each SOA arm of the MZI while measuring the power throughput. A great

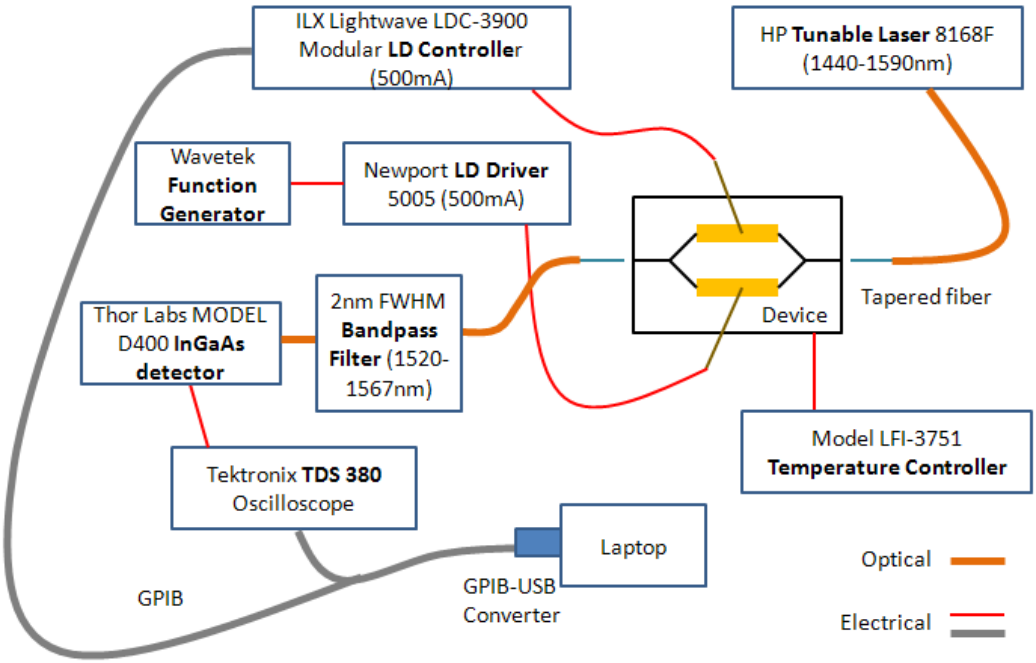

Figure 2-33: Measurement setup for the bias scan.

method for visualizing the bias scan is a 2D color plot that depicts the interference between the two MZI arms, as shown in Figure 2-32. The bias scan derives its name from the information that it provides on how to DC-bias the MZI arms for all-optical logic operation.

Figure 2-33 shows a schematic of the measurement setup that was used to perform the bias scan. The measurement system employs much of the same testing equipment that was used to make the other measurements. The ILX current driver is controlled by a Labview program to step the current from 0 to 500 mA in increments of 10 mA. The signal generator produces a sawtooth modulation signal that modulates the Newport current driver output from 0 to 500 mA and back down in a sawtooth fashion. The output is bandpass filtered to remove unwanted ASE before it is detected by the InGaAs detector. The detector output voltage signal is fed into the oscilloscope and is captured by the Labview program. The voltage is converted to optical power via a conversion that was calibrated using an optical spectrum analyzer (OSA). Lowpass filtering is performed in software to remove high frequency noise.

The resulting bias scan for a MZI with 850 μm $\times$ 4 μm SOAs is shown in Fig-

ure 2-32. The fringes correspond to bias points where constructive and destructive interference occurs between the arms of the MZI. The dark region in the lower left of the plot represents current levels that are inadequate to bring the SOAs past transparency. For AOL operation, the SOAs should be biased for constructive interference. For example, $(I_1, I_2) = (300\text{ mA}, 400\text{ mA})$ could be a potentially optimal point to bias the SOAs. If used as a carrier injection modulator, the device exhibits an "I_π" (analogous to V_π) of approximately 50 mA at bias levels near the diode threshold. The extinction ratio is approximately 20 dB.

2.8 Conclusion

All-optical logic has the potential to transform telecommunications and beyond. One key component to the widespread adoption of AOL technology is integration. In this chapter, the design of an integrated AOL unit cell that is based on an MZI structure with electrically-pumped SOAs as nonlinear elements was presented. Targeted for operation at the primary telecommunications wavelength of 1550 nm, the device was modeled and fabricated in the InP-based material system. The fabricated devices were then characterized. The operation of dilute active and passive waveguides, bends, and MMIs were successfully demonstrated. Vertical passive-active coupling via the asymmetric twin waveguide technique was also achieved. Finally, the static bias scan was used to characterize the MZI, successfully demonstrating carrier-dependent optical interference.

Future work includes the successful fabrication of AOL unit cells using quantum dot active materials. Quantum dot materials can provide faster carrier recovery, which could allow the current AOL unit cell design to achieve bit rates of 100 Gb/s or higher. Demonstrations of pulsed signal switching with the AOL unit cells as well as cascaded AOL unit cells performing different logic functions will also be investigated.

Chapter 3

Ridge Lasers

Ridge lasers are widely used in industry and research because they are one of the most basic integrated semiconductor devices to design, fabricate, and characterize. Consisting simply of a straight ridge waveguide with cleaved facet mirrors and a metal contact, ridge lasers are quite tolerant to fabrication nonidealities such as alignment and etching errors, making them an excellent proof-of-concept or diagnostic for novel materials and more complicated devices. In addition, the packaging of ridge lasers has become an industry standard, because III-V semiconductor diode lasers are preferred nowadays to gas or solid state lasers in a variety of applications mainly due to their being more compact, efficient, reliable and potentially inexpensive. In this chapter, ridge lasers are utilized to investigate two material systems: InAs quantum dots emitting at 1.5 μm, and strained InGaAs quantum wells (QWs) emitting at 1.6–2.0 μm.

3.1 Quantum Dot Lasers

Quantum dot (QD) lasers and amplifiers at 1.5μm have a broad range of potential benefits for fiber-optic telecommunications applications. Quantum dots confine electrons in three dimensions, creating a 3D potential well that "squeezes" the electronic energy levels into atomic-like quantized steps. The energy level spacings depend on the size of the QD, which can be made to have only a few bound energy levels. One

of the benefits of having only a few energy levels (sometimes only one or two) is that fewer carriers are required to achieve population inversion, thus providing a lower I_{th} than quantum well or bulk structures. Furthermore, the emission wavelength is more stable to temperature changes, thus providing a higher T_0 than quantum well or bulk structures [13]. Other benefits of QD lasers include lower chirp and broader gain spectrum for wavelength tuning or mode-locking. Quantum dot SOAs are also expected to have lower noise figure and faster dynamic response times [55].

Self-assembled quantum dots that are grown by molecular beam epitaxy (MBE) or metal-organic chemical vapor deposition (MOCVD) have been studied for the fiber-optic telecommunications wavelengths of 1.3 μm and 1.55 μm. The term "self-assembled" is used because a lattice mismatch is intentionally introduced between the QD layer and the semiconductor it is residing on (often called the wetting layer) so that the QD layer will form islands rather than become a continuous film, in order to minimize the energy. Although called quantum dots, they are usually not round, but are wider than they are tall as shown in Figure 3-1. Chemically synthesized QDs on the other hand, such as CdSe QDs, often do resemble dots [17].

Indium Arsenide is a common semiconductor that is used to make QDs for the telecommunications wavelengths. InAs has a bandgap of 0.354 eV, which translates into a wavelength of 3.5 μm. However, in the form of a QD, the InAs energy levels provide gain at 1.3 - 1.5 μm. In fact, 1.3 μm wavelength InAs-on-GaAs QD lasers and SOAs are already quite mature [56, 121]. On the other hand, the operating wavelength of 1.55 μm has been a more challenging domain. Some of the first 1.55-μm-emitting QDs were also grown on GaAs. InGaAs and GaInNAs QDs on GaAs, as well as InAs QDs on GaAs with an InGaAs strain-reducing layer were achieved towards the last few years of the millennium [98, 112, 126]. Later, InAs QDs that were grown on (311)B InP substrates that emitted at 1.55 μm were successfully measured [99]. However, the (311)B InP substrate is less economical and fabrication-friendly than the (100) InP substrate, and 1.5-μm-emitting InAs QDs that are grown on (100) InP have been successfully grown on InGaAsP wetting layers or in InGaAsP QWs (also called dots-in-a-well or DWELL) [55, 148, 7, 57]. Others have used InGaAlAs

wetting layers or grown InAs QDs directly on InP to achieve 1.5 μm emission [47, 71].

Our goal was to make a first pass on growing InAs QDs on (100) InP substrates, and to characterize the emission of the QDs by fabrication of ridge lasers and by measuring their electroluminescence. Two heterostructures were grown using MBE: one consisting of quantum dots and the other of quantum dashes, which are effectively just elongated quantum dots. A quantum well heterostructure was also grown for diagnostic purposes. The photoluminescence of the gain materials for each heterostructure was confirmed to have an emission range near 1.5 μm.

3.1.1 Epitaxial Structure

The epitaxial structure of the quantum dot, quantum dash, and quantum well heterostructures can be found in Appendix Section C.1. The QD heterostructure (VA117) consists of four layers of 0.75 nm InAs on 2 nm of $In_{0.5}Ga_{0.4}Al_{0.1}As$ wetting layer, on top of $In_{0.75}Ga_{0.25}As_{0.55}P_{0.45}$, and capped with 8 nm of $In_{0.5}Ga_{0.4}Al_{0.1}As$. The quantum dash heterostructure (VA118) consists of four layers of 0.9 nm InAs on 20 nm of $In_{0.8}Ga_{0.2}As_{0.46}P_{0.54}$. The quantum well heterostructure (VA96) was grown with four $In_{0.54}Ga_{0.46}As$ quantum wells. A capping layer of 700 nm of InP was placed on top of the gain layers to separate the mode from the metal contact, which is placed on the very top of the structure. For VA117 and VA118, a thin layer of InGaAlAs was grown in the middle of the InP cap layer to serve as a wet etch stop.

An atomic force microscope (AFM) image of the InAs quantum dot layer is shown in Figure 3-1. The quantum dot density is measured to be 6 dots/μm^2 per layer. A total of four layers was grown, resulting in an effective dot density of 24 dots/μm^2. This dot density is too low to provide the requisite gain for lasing; in general the density for room-temperature continuous-wave (CW) lasing needs to be at least $\approx 10^2$ μm^2 [55]. These results were later confirmed by the devices that we fabricated at MIT as well as devices fabricated by Thorlabs Quantum Electronics (formerly Covega Technology). In fact, the dot density of VA117 is in the range for which single-dot experiments have been reported [6].

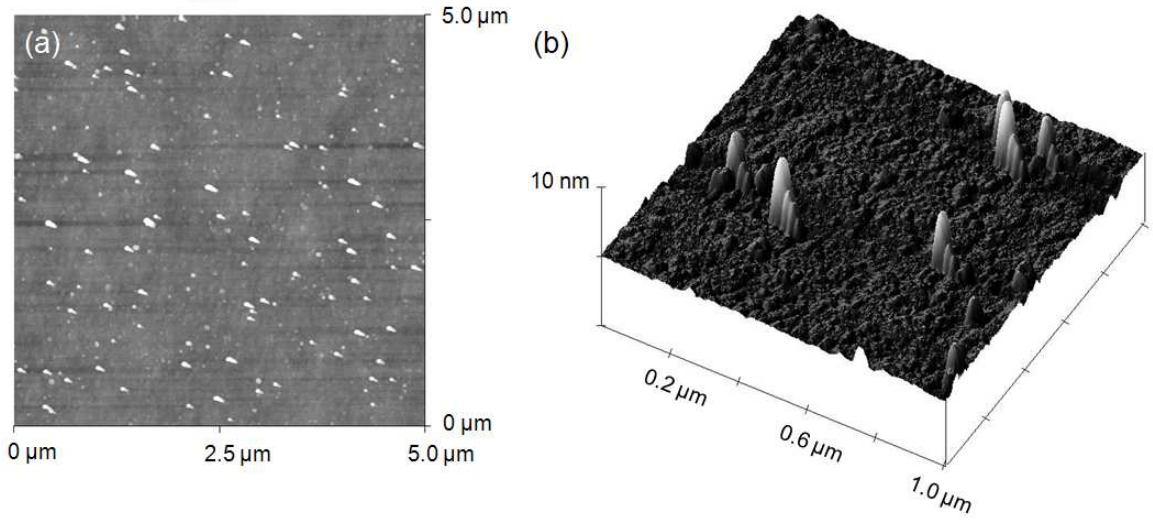

Figure 3-1: Atomic force microscope images of InAs quantum dots. (a) AFM image of a 5 by 5 μm portion of the surface of VA159. The density is 6 dots/μm^2, which is too low to provide the gain required for lasing but can be utilized for single-dot emission experiments. (b) Angled AFM image of a magnified portion of the surface, showing the shape of the dots. The dots are about 10 nm tall on average and take an elongated shape of approximately 30 nm in width and 80 nm in length on average.

3.1.2 Fabrication

Ridge waveguides were fabricated using the quantum dot, quantum dash, and quantum well heterostructures. The fabrication procedure for the ridge waveguides is given in Figure 3-2. The methods that are used are mostly identical to the fabrication steps found in the all-optical logic process of Section 2.6. The only difference is in the etching of the semiconductor layers.

Due to laboratory constraints, we were unable to utilize the $SiCl_4$-based ICP RIE process that was developed in Section 2.6 for the fabrication of these ridge waveguides. Two methods of etching were investigated: (1) wet etching and (2) ICP reactive ion etching with BCl_3.

Wet etching of III-V semiconductors in the fabrication of photonic devices is generally avoided because the isotropic nature of the wet etch results in structures that have curved sidewalls, which are difficult to model and introduces extra variables into processes that are generally very complicated already. However, there are methods of

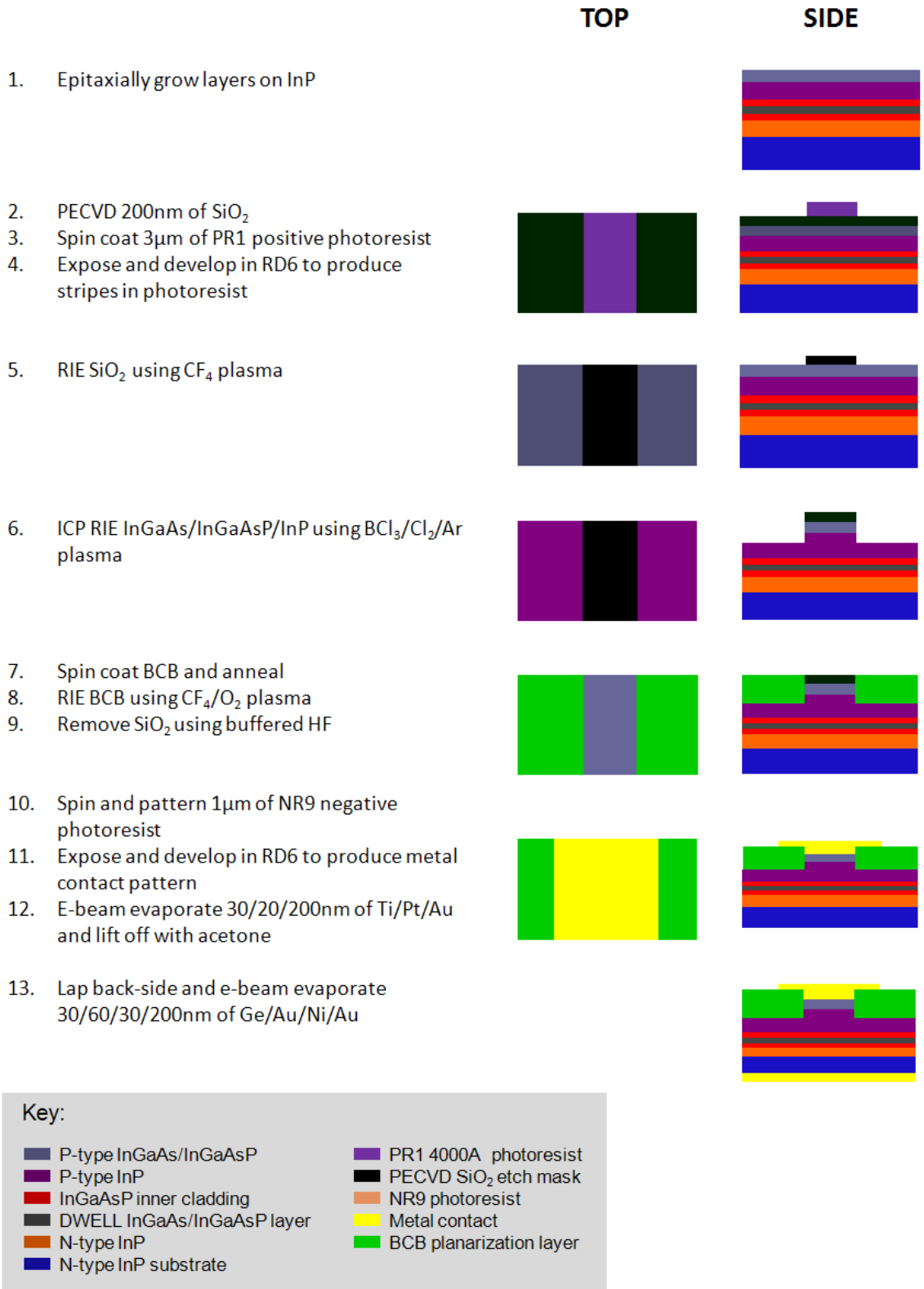

Figure 3-2: Process flow for the quantum dot and quantum dash ridge lasers.

making wet etches more anisotropic. In etch systems using HCl (which etches InP, for example), weak acids such as phosphoric acid or acetic acid can be used to make the etch more anisotopic [38]. Furthermore, one of the advantages of wet etch systems for III-V semiconductors is that there are many options for selective etching. Continuing with the example of HCl, scientists have discovered that the etch has selectivity greater than 10^6 to $In_{0.53}Ga_{0.47}As$ with respect to InP [104]. The InGaAlAs etch stop layer found in VA117 and VA118 has low Al content and was seen to perform as an effective etch stop in an etch consisting of $HCl:H_3PO_4:H_2O$ (1:1:10). On the other hand, if one wanted to selectively etch $In_{0.53}Ga_{0.47}As$, while using InP as an etch stop, a combination of citric acid and hydrogen peroxide has been shown to exhibit a selectivity of 470 [27].

Experiments were also performed in the ICP RIE using BCl_3 as the primary etch gas. Figure 3-3 shows the most optimal BCl_3 etch achieved. The surface is seen to exhibit some roughness. However, because the waveguide mode is situated relatively far from the surface, the roughness should contribute negligibly to the scattering loss of the waveguide. Finally, the dry-etch method was chosen for its superior anisotropy and ability of obtaining a deeper etch.

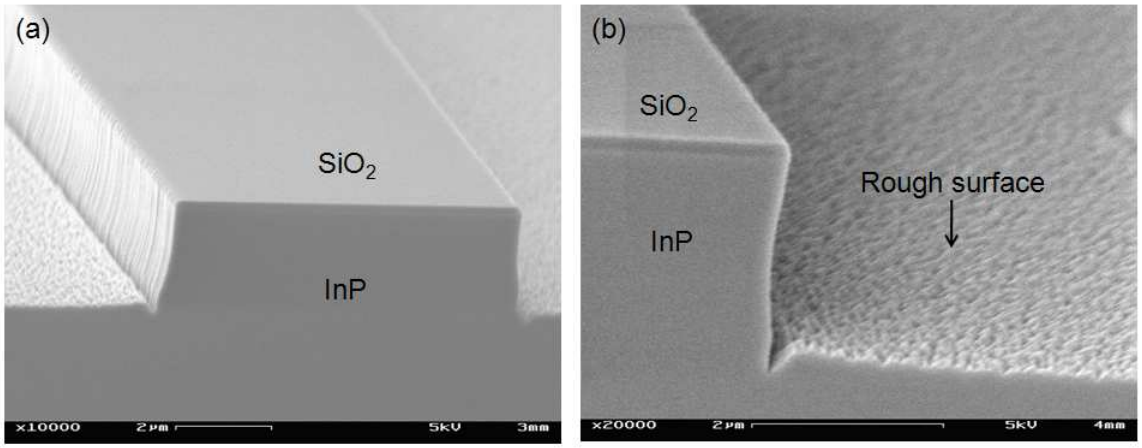

Figure 3-3: ICP RIE etching of InP using a BCl_3 etch recipe. (a) 3-minute etch of InP (details of the etch can be found in Section C.4). (b) At greater magnification, the surface exhibits roughness and there is a trench along the side of the ridge. Because the mode is expected to be situated below the surface, these features will not cause excessive scattering losses.

Ridge waveguides ranging from 1 μm to 30 μm in width, arranged parallel to each other with a period of 160 μm were fabricated using contact lithography. With a resolution of $\approx$1 μm, contact lithography was empirically observed to reliably pattern waveguides that were wider than 2 μm. Waveguides narrower than 2 μm were too close to the resolution limit to be patterned reliably in practice. The ridges were etched to a depth of 2.2 μm, making them multimode waveguides. The top Ti/Pt/Au metal contact pads were 128 μm wide and separated by 32 μm.

3.1.3 Measurement and Conclusion

Electroluminescence (EL) spectra were measured from the fabricated waveguides, as depicted in Figure 3-4. Both the quantum dot and quantum dash lasers exhibited gain in the 1.4 μm to 1.5 μm range. The emission spectrum can be seen to be quite broad, a feature of a QD gain region that results from the nonuniform dot sizes. The measurements were performed with the thermoelectric (TE) temperature controller set to 15°C.

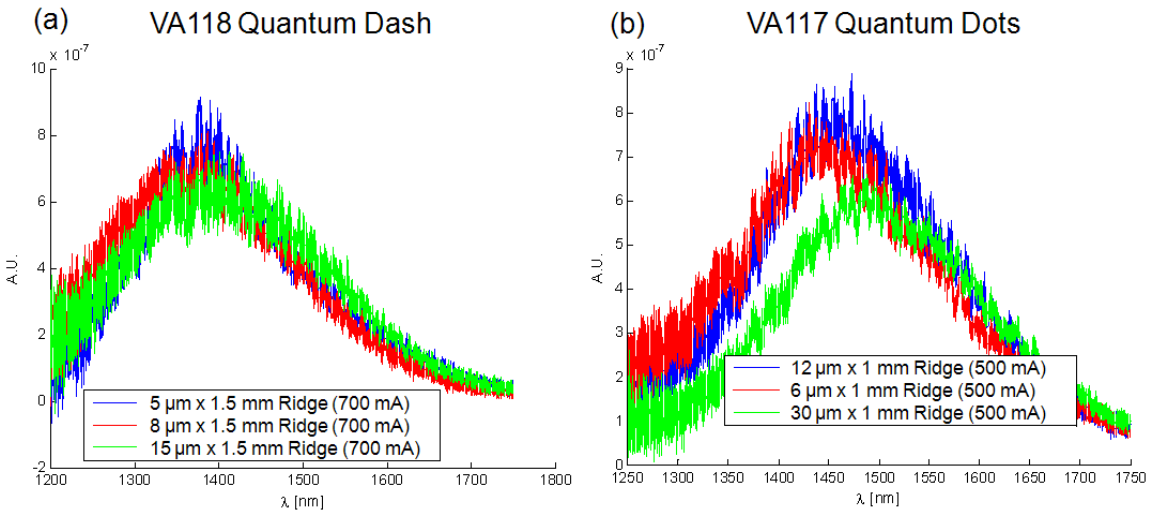

Figure 3-4: The electroluminescence spectra of InAs quantum dash and quantum dot materials. (a) The EL spectrum of the quantum dash material from waveguides with different ridge dimensions. The emission is seen to be centered around 1400 nm. (b) The EL spectrum of the quantum dot material from waveguides with different ridge dimensions. The emission is seen to be centered around 1450 nm.

The densities of the dots and dashes were not high enough to provide enough gain to offset the losses of the ridge waveguide and cleaved-facet mirrors. However, the ridges fabricated from the quantum well heterostructure (VA96) by Thorlabs Quantum Electronics did achieve CW lasing at 1.655 μm with 10 mW (at 500 mA) output power, $I_{th} = 110$ mA, and differential efficiency $\eta = 0.03$ mW/mA.

These experiments provide an understanding of the QD material characteristics from our MBE system. Future work includes the growth of higher-density QD material by changing the MBE growth conditions, as well as increasing the number of QD layers that are grown in a single device. Additionally, investigations into single-dot emission can be performed on the lower-density QD material. Quantum dot gain materials can also be used in all-optical logic gates to provide faster recovery times, and hence, faster bit-rates (>100 Gbit/s). Quantum dot gain material at 1.5 μm will continue to be an interesting area of research due to its wide range of applications.

3.2 Mid-infrared Lasers

The wavelength range between 1.7 μm and 5 μm is an important part of the infrared spectrum that is not well-investigated. Unlike 1.3 μm and 1.5 μm wavelengths, the study of which has been driven by fiber-optic telecommunications applications, the longer wavelengths currently do not have readily available commercial laser sources, amplifiers, or detectors. This part of the infrared spectrum lies at the tenuous boundary between what most scientists classify as "near-infrared" and "mid-infrared" (mid-IR). Part of this wavelength range is also often referred to as "short-wave infrared". Without dwelling too much on semantics, for the remainder of this thesis, the 1.7–5 μm wavelengths will be referred to as "mid-infrared" or simply as "long" wavelengths. A few important applications of these long wavelengths include (1) free-space communications, (2) laser ablation for medical procedures, and (3) trace gas sensing.

There are atmospheric transmission windows between 2.1 and 2.4 μm as well as between 3.5 and 4.2 μm, making optical free-space telecommunications possible in these wavelength ranges [30]. Additionally, the transmission windows can be used

to facilitate infrared countermeasures to protect aircraft, ships, and other vehicles against heat-seeking missiles. High output power, usually exceeding 1 W, is needed for these countermeasure applications.

Medical applications for mid-IR wavelength include laser ablation and laser surgery. Mid-IR lasers emitting in the 2–3 μm spectral range (generally Er:YAG solid-state lasers) are used in dental and dermatological applications. Other 2 μm solid-state lasers, such as Ho:YAG and Tm:YAG, are beginning to find niche applications for minimal invasive surgery, particularly in urology [114].

The absorption lines of several crucial trace gases (CH_4, CO_2, CO, HCl) are situated in the spectral region spanning from 2 to 4 μm [53]. Mid-infrared absorption by hydrocarbons is strong near 3 μm due to the C-H stretching vibration [76]. Tunable diode laser absorption spectroscopy is a suitable method for portable low-cost trace gas analysis [133]. Leak detection, chemical process control, and atmospheric pollutant sensing are all applications made viable by advancements in trace gas detection with semiconductor and solid-state lasers [113, 128]. Trace gas sensing also has applications in medicine, including very sensitive and time-resolved exhaled breath monitoring [76].

Portable low-cost trace gas sensing laser sources need to have a few tens of milliwatts of output power, good spectral purity, and tunability. Because of this, semiconductor lasers are great candidates for trace gas sensing sources. In this section, we investigate laser material with long-wavelength emission. The fabrication and characterization of ridge lasers will be presented.

The material of choice for emission wavelengths between 2–5 μm is the GaSb material system. Strained InGaAsSb/AlGaAsSb quantum wells have achieved gain between 2–3 μm [46, 58]. With the so-called "W" energy band line-up heterostructure, wavelengths in the range of 3–5 μm have been achieved [48, 12]. On the shorter wavelength side, high-indium-content strained InGaAs quantum wells with AlGaInAs barriers on InP substrates have been shown to emit in the range of 1.7–2.2 μm. Emission wavelengths near 2 μm can be achieved if more than 1.5% strain is incorporated into the InGaAs quantum wells: a 2.2% strained $In_{0.86}Ga_{0.14}As$-$In_{0.48}Ga_{0.42}Al_{0.1}As$-

InP QW diode laser with a 2.2 μm emission wavelength has been successfully grown using solid-source MBE [54]. With this as a starting point, ridge laser sources with strained-InGaAs multiple quantum wells for long-wavelength emission were designed.

3.2.1 Laser Design

Multiple long-wavelength laser heterostructures were grown by solid-source MBE. By increasing the indium content of the quantum well layer, the gain peak was tuned to longer wavelengths [20]. Table 3.1 lists the heterostructures that were grown, along with the indium content of their QW layers and the number of quantum wells within the gain region. Emission wavelengths in the range of 1.5 μm to 2 μm was achieved, as shown in Figure 3-5; the figure shows the photoluminescence (PL) originating from the different wafers.

The epitaxial structure of VA159 is shown in Figure C-5 in Appendix Section C.1 as a representative heterostructure. The gain region consists of three quantum wells with InGaAlAs cladding layers. There is a low-index InP cap layer that is designed to push the mode downward, away from where the metal contact resides. The top InGaAs contact layer is doped p+ to minimize the metal-semiconductor contact resistance. The rest of the heterostructures listed in Table 3.1 are similar except for the QW layers.

Table 3.1: Long wavelength laser heterostructures grown by MBE at MIT. The threshold current, laser wavelength, and output power are quoted for the lasers fabricated by Thorlabs Quantum Electronics.

Epi Growth	QW Composition	Number of QWs	CW I_{th} [mA]	Laser λ [nm]	CW Output Power [mW]
VA152	$In_{0.53}Ga_{0.47}As$	3	120	1502	11
VA153	$In_{0.66}Ga_{0.34}As$	2	67	1777	14
VA154	$In_{0.66}Ga_{0.34}As$	3	120	1814	7
VA158	$In_{0.71}Ga_{0.29}As$	2	58	1879	14
VA159	$In_{0.71}Ga_{0.29}As$	3	49	1893	16
VA162	$In_{0.74}Ga_{0.26}As$	2	80	1978	7.5
VA163	$In_{0.75}Ga_{0.25}As$	3	240	1990	3.5

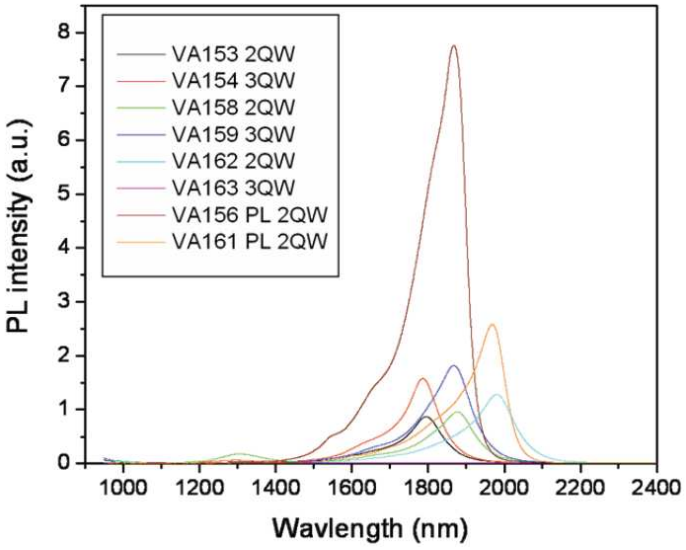

Figure 3-5: The PL spectra of different epitaxial structures of strained InGaAs QWs. As the indium content is increased, the PL peak is red-shifted. VA156 and VA161 were not laser structures; they were structures grown for PL analysis only [20].

3.2.2 Measurement

The heterstructures listed in Table 3.1 were fabricated into ridge lasers by Thorlabs Quantum Electronics and then packaged onto a C-mount. The fabrication process is largely proprietary, however the cross-section of the finished device, shown in Figure 3-6, suggests that the fabrication process was very similar to the one employed in Section 3.1.2. The ridges were 3 μm in width and etched 2 μm deep. The metal contact to the p-type semiconductor was 930 nm of Ti/Pt/Au, and the n-type metal contact was 880 nm of Au/Ge/Ni/Pt/Au.

A C-mount is a specialized mount for bar lasers that is designed to be mounted to a platform on its side. This provides better cooling because the TE cooler can be placed closer to the device. Figure 3-7 is a photograph of a C-mounted 1.9 μm laser during testing. A drawback of the C-mount is that the vertical platform blocks one of the facets and also limits probe access to the top of the device.

When performing a measurement with the C-mounted device, output light can be coupled via tapered fiber. However, due to the relatively small NA of the tapered fiber, higher collection efficiency can be achieved by using a two-lens system, as shown

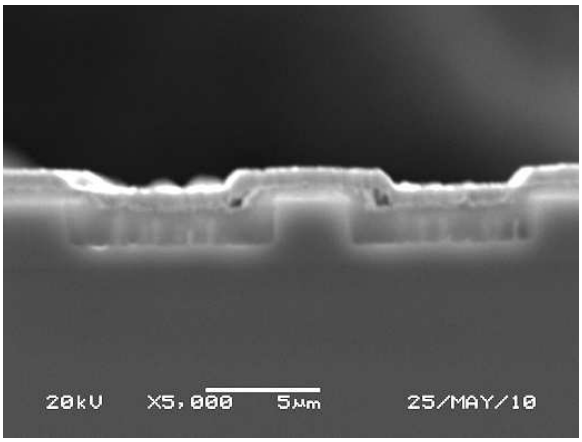

Figure 3-6: Scanning electron micrograph (SEM) of the long-wavelength ridge lasers fabricated by Thorlabs Quantum Electronics, showing the ridge etched into the epitaxially grown wafer, along with the planarization and metal contact layers.

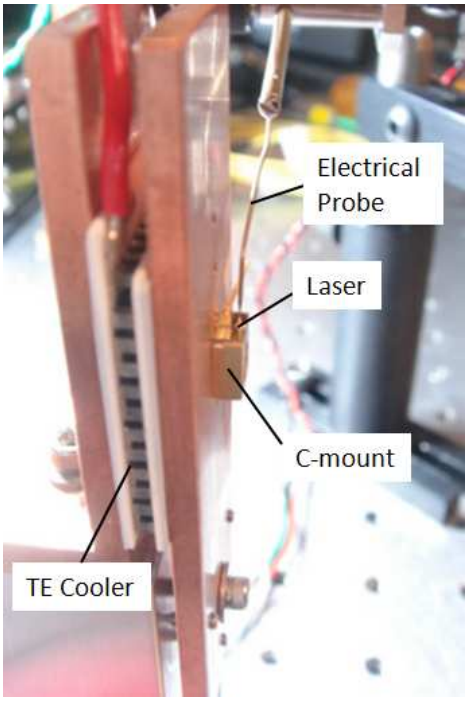

Figure 3-7: The test setup that was custom-made for C-mounted lasers. The TE cooler is placed very close to the C-mount to provide low thermal resistance.

in Figure 3-8. The first lens used is a high-NA (NA = 0.68) lens that collects and collimates the light. The second lens is a small-NA lens that is used to focus the light onto the end of a fiber.

The lasing characteristics, as well as wavelength tuning characteristics, were measured. Table 3.1 shows the lasing characteristics of all of the heterostructures. Measurements were made with the TE temperature controller set to 20°C.

Tuning the CW wavelength of the ridge lasers can be achieved with carrier injection. The injection of carriers, in turn, will change the effective index of the waveguide via two mechanisms. The first is by increasing the carrier concentration and thus the gain of the QW active regions. This effect will tend to blue-shift the gain peak. The Kramers-Kronig relation dictates that this change in gain will also change the index of refraction of the material. The second mechanism is through an increase in the temperature from Joule heating, which will also change the index of refraction. An increase in temperature will affect the cavity length via thermal expansion. The temperature increase will also spread out the Fermi distribution of carriers, which will serve to red-shift the gain peak. The material bandgap is also reduced with temperature. The mechanism that dominates the tuning of ridge lasers can be shown to be the temperature, and the general effect is that the lasing peak is red-shifted with

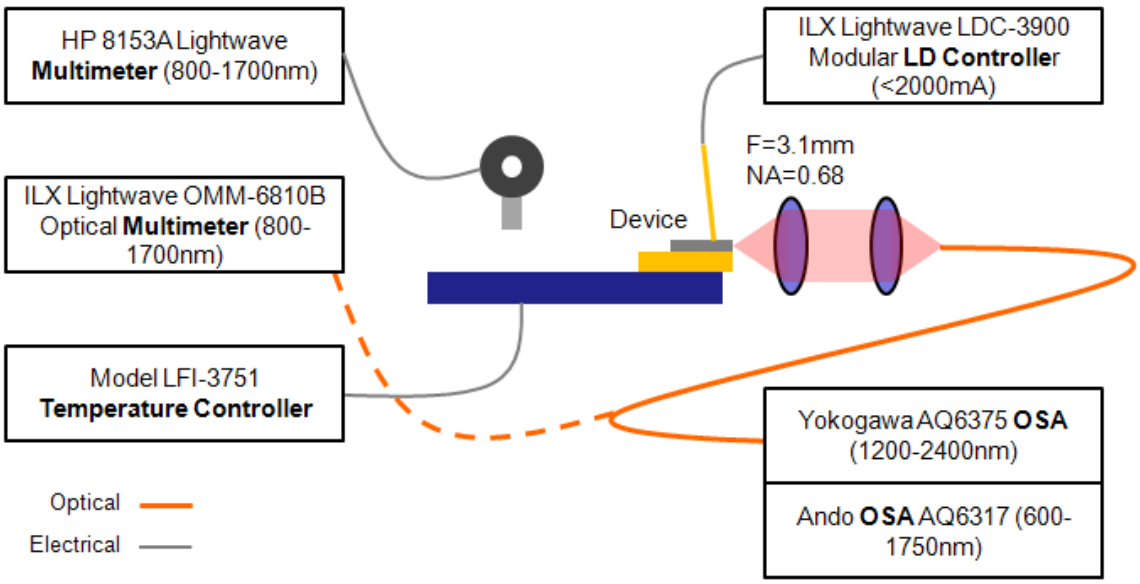

Figure 3-8: The optical test setup used to measure ridge laser devices mounted on a copper holder. Power is measured by the large area power meter. To measure the spectrum, a high-NA two-lens system is used to capture the light from the waveguide onto a multimode fiber, which is fed into the optical spectrum analyzer (OSA).

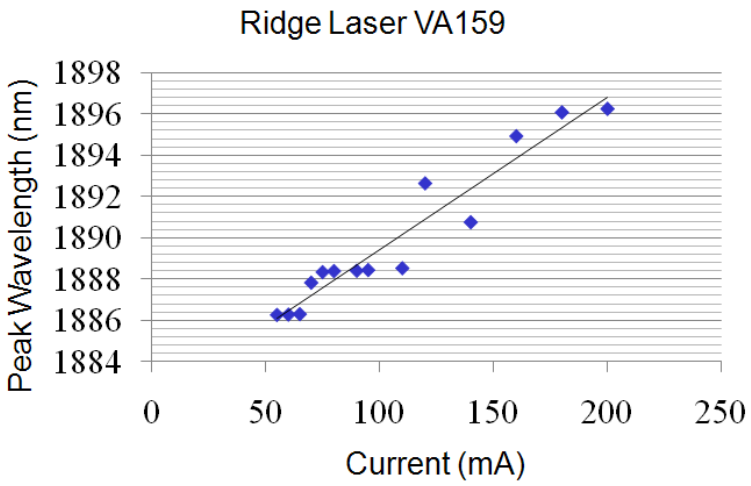

Figure 3-9: The shift of the peak lasing wavelength as a function of injected current, measured for the VA159 ridge laser. Mode hopping can be observed, and the tuning rate is seen to be approximately 0.07 nm/mA.

increased carrier injection [133]. One can write

$$\frac{d\lambda}{dI} = \frac{d\lambda}{dT}\frac{dT}{dI} \tag{3.1}$$

where λ is the wavelength, I is the injected current, and T is the temperature. Figure 3-9 shows the wavelength tuning as a function of current, measured from a VA159 ridge laser. The tuning rate $\frac{d\lambda}{dI}$ is 0.07 nm/mA near an 80 mA bias point. Mode hopping is observed, which suggests that the temperature-induced cavity length expansion is not playing a large role in wavelength tuning. Mode hopping also limits the tunability of the ridge laser; continuous tuning cannot be achieved using this method.

The term $\frac{d\lambda}{dT}$ was measured by pulsing the current at 200 kHz with a duty cycle of 0.1. This particular pulse width and repetition rate was chosen to ensure that no roll-off was observed in the LI curve of the laser up to 200 mA, indicating that the pulses were inducing no noticeable temperature increase. The temperature of the device is then solely determined by the temperature of the TE cooler, which was run in reverse as a heater. The value of $\frac{d\lambda}{dT}$ is measured to be 1 nm/K near an 80 mA bias point for VA159.

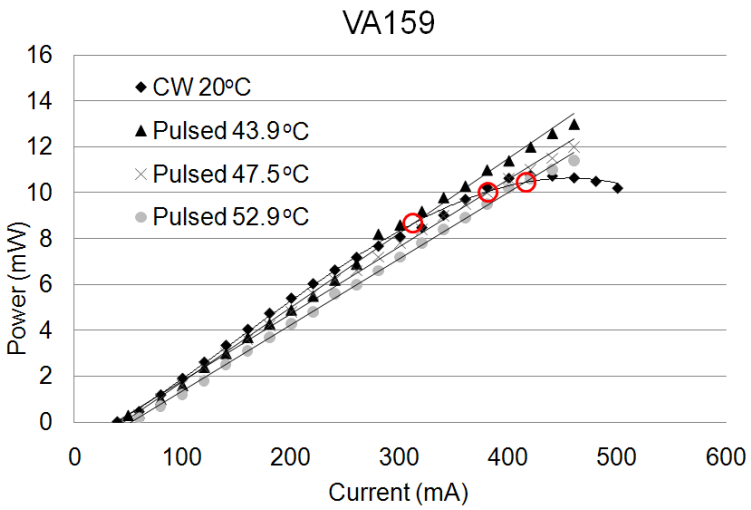

Figure 3-10: The LI curves for the VA159 ridge laser for CW operation and pulsed operation at three different temperatures. In CW operation, the LI curve is seen to deviate from linear for high currents, indicating heating. The circles indicate the three intersection points the LI curve in CW makes with the LI curves in pulsed operation. From these intersection points, the laser temperature for the particular current value can be determined.

There are two methods that can be used to determine the final term, $\frac{dT}{dI}$, which is difficult to measure directly. The first method simply takes the first term, $\frac{d\lambda}{dI}$ of Equation 3.1, and divides it by the second term $\frac{d\lambda}{dT}$, as is done in Figure 3-11(b). The second method involves fitting the LI curve for CW operation with the LI curves for pulsed operation. The intersection points portray the temperature of the laser in CW operation for a particular current level. Figure 3-10 shows the intersection points of the LI curves measured for CW and pulsed operation. The relationship of T to I is given by

$$T(I) = R_{th}P_{th}(I) \tag{3.2}$$

$$= R_{th}(IV - P_{optical}) \tag{3.3}$$

$$\approx R_{th}IV \tag{3.4}$$

where R_{th} is the thermal resistance and $P_{th}(I)$ is the electrical power that is converted

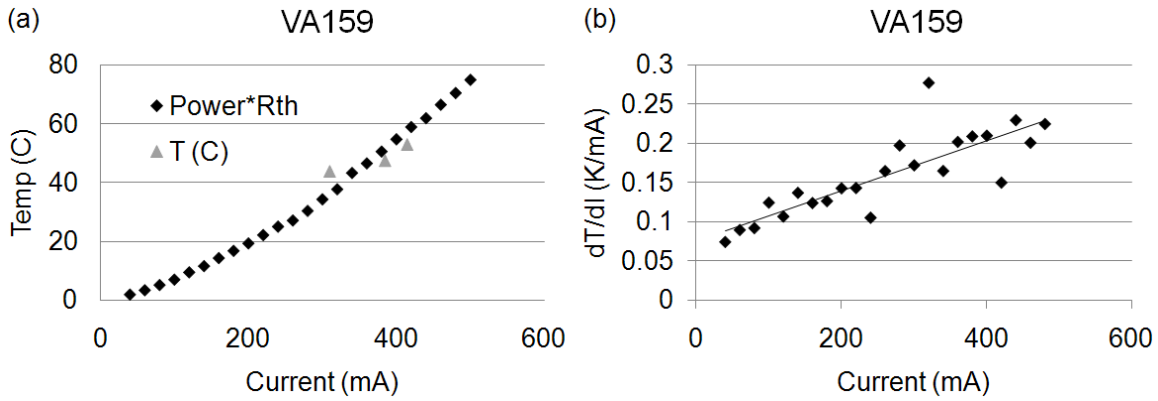

Figure 3-11: Determination of the thermal resistance of the long-wavelength C-mounted laser. (a) A plot of Equation 3.4 with R_{th} fit to the intersection points of Figure 3-10. The fit value of R_{th} is 38 K/W. (b) A linear fit to $\frac{dT}{dI}$ calculated by using Equation 3.1. The values of $\frac{dT}{dI}$ are consistent to experimental error with the derivative of $T(I)$ in part (a).

to heat. The thermal resistance is a function of the mounting and heat sinking of the device. Given this form of $T(I)$, a value of $R_{th} = 38K/W$ can be fitted to the intersection points, as shown in Figure 3-11(a). Next, $\frac{dT}{dI}$ is calculated by differentiating Equation 3.4. The value of $\frac{dT}{dI}$ was found to be 0.09 K/mA near 80 mA for VA159, which is consistent with the data presented in Figure 3-11(b). The measured thermal resistance is too small to achieve a wide tuning range. However, the small thermal resistance is precisely what is necessary to achieve a wavelength stable laser. To maintain the wavelength to within 1 nm, the current would need to be maintained within a 15 mA range or the temperature within 1°C, which are easy to achieve with the appropriate equipment.

Two of the typical metrics used to characterize the temperature stability of a diode laser are the characteristic temperatures T_0 and T_1. The threshold current of a laser diode is exponentially related to the temperature: $I_{th} \propto e^{T/T_0}$, where T_0 is called the characteristic temperature of the laser. For VA159, a characteristic temperature $T_0 \approx 50$°C was obtained. The differential efficiency of a laser diode also tends to vary exponentially with temperature: $\eta_d \propto e^{T/T_1}$. T_1 was measured to be ≈400°C.

3.3 Conclusion

Ridge lasers are easy to design and fabricate, making them common diode lasers in industry and academia alike. As great prototyping and diagnostic devices, they can be used to quickly gain knowledge about novel material systems. In this chapter, research was presented on using ridges to characterize quantum dot and quantum dash material at 1.55 μm, as well as strained InGaAs QW material at 1.5–2.0 μm. Due to the ridge lasers' robustness to fabrication non-idealities, key properties of these materials were assessed without having to perform multiple fabrication and design iterations.

In Section 3.2, a successful long-wavelength diode laser was created, but wavelength tuning that was both continuous and wide-bandwidth was not achieved. In the next chapter, widely-tunable long-wavelength lasers are described. Knowledge about the different laser heterostructures discussed in this section will provide an excellent starting point for designing devices to meet more complicated specifications.

Chapter 4

Widely-tunable Long-wavelength Lasers

Tunable lasers are of interest for a wide range of applications, from fiber-optic telecommunications to broadband sensing [23]. Around the early part of the millennium, the telecommunications industry began to drive the research and development of tunable lasers for wavelength division multiplexing (WDM) systems [24]. The desire was to build a monolithically-integrated full-band tunable laser with good spectral purity. Designs that were proposed include, among others, (1) sampled-grating distributed Bragg reflector (SG-DBR) lasers, (2) double ring resonator-coupled lasers, and (3) micro-electro-mechanical system (MEMS) lasers [67, 61, 18]. The lasers were designed to operate at the 1550 nm telecommunications wavelength. However, the designs can be adapted to longer wavelengths without major modifications.

The distributed Bragg reflector (DBR) laser is similar to the Fabry-Perot ridge laser that was discussed in Chapter 3, except that the DBR laser has an index grating that is formed near or on the waveguide that serves as both a reflector for the cavity and a mode selection filter [52]. Specifically, the so-called sampled-grating DBR laser provides a wide tuning range because the filtering is due to two differently spaced and independently-tuned reflection gratings that achieve the Vernier effect [67]. The tuning can be performed electronically through heating or carrier injection. Tunable vertical-cavity surface-emitting lasers (VCSELs) have been designed with one mirror

mounted on a flexible arm. When the mirror is moved up/down electrostatically, the emission wavelength of the VCSEL is tuned by changing the length of the cavity [51].

Double ring resonator-coupled lasers also employ the Vernier effect to select modes for wide-range tunability. For details about mode selection, please refer to Appendex Section A.2. Double ring resonator-coupled lasers can considerably extend the effective cavity length and photon lifetime, allowing these lasers to offering high side-mode suppression ratios (SMSRs) and narrow linewidths for better spectral purity [61]. Furthermore, because these lasers do not require gratings, they are also potentially simpler and cheaper to manufacture. In recent years, ring resonators have been used as stand-alone filters due to their compact size [11].

One of the first demonstrations of a semiconductor ring resonator-coupled laser was performed using a single ring made out of active material biased at transparency [84]. Directional couplers were employed to couple the waveguide gain sections to the passive ring and a lasing wavelength of 1.55 μm was achieved. Rabus *et al.* then demonstrated a monolithically-integrated double ring resonator-coupled laser with a SMSR of $>$ 35 dB and a modest tuning range of 6 nm, which was later improved to 17 nm. [91, 92]. The rings were tuned with heaters and were coupled to the straight waveguides using multimode interference (MMI) structures. A regrowth procedure was used to fabricate different active and passive waveguide materials. Ring resonator-coupled lasers in which the active and passive waveguides were wafer-bonded together have been successfully demonstrated as well, requiring the optical mode to be vertically coupled between the active and passive waveguides [43].

Recently, full C-band tuning (50 nm) using double ring resonator-coupled lasers with a SMSR of 30 dB has been achieved at NTT Photonics Laboratories [69]. Tuning was achieved with carrier injection. Once again, a regrowth procedure was used to fabricate different active and passive waveguide materials [105]. NEC Corporation demonstrated a tuning range of 96 nm across the L-band using three ring resonators and an off-chip gain section [26]. Researchers at NEC have also demonstrated full C-band tuning with SMSR $>$ 45 dB using an air-bridge ring structure [68]. Kim *et al.* recently demonstrated 16 nm of tuning range and 20-30 dB SMSR using square

rings instead of circular rings [49].

This chapter describes the design, modeling, fabrication, and characterization of widely-tunable lasers, building on the long-wavelength (1.5–2.2 μm) laser heterostructures that were developed in Section 3.2. The absorption lines of several crucial trace gases (CH_4, CO_2, CO, HCl) are situated in the spectral region spanning from 2 to 4 μm [53]. Mid-infrared absorption by hydrocarbons is strong near 3 μm due to the C-H stretching vibration [76]. Tunable diode laser absorption spectroscopy is a suitable method for portable low-cost trace gas analysis [133]. Leak detection, chemical process control, and atmospheric pollutant sensing are all applications made viable by advancements in trace gas detection with semiconductor and solid-state lasers [113, 128]. Trace gas sensing also has applications in medicine, including very sensitive and time-resolved exhaled breath monitoring [76].

The epitaxial structure of VA159 is shown in Appendix Section C.1 as a representative heterostructure; aside from the quantum wells (QWs), the rest of the heterostructure layers and thicknesses are all nearly identical between the different growths shown in Table 3.1, reproduced below as Table 4.1. These heterostructures contain high-indium-content strained InGaAs quantum wells with AlGaInAs barriers on InP substrates, which have been shown to emit in the range of 1.5–2.2 μm. Grown by solid-source molecular beam epitaxy (MBE), emission wavelengths near 2 μm can be achieved if more than 1.5% strain is incorporated into the InGaAs quantum wells.

Table 4.1: Long wavelength laser heterostructures grown by MBE at MIT.

Epi Growth	QW Composition	Number of QWs	CW I_{th} [mA]	Laser λ [nm]	CW Output Power [mW]
VA152	$In_{0.53}Ga_{0.47}As$	3	120	1502	11
VA153	$In_{0.66}Ga_{0.34}As$	2	67	1777	14
VA154	$In_{0.66}Ga_{0.34}As$	3	120	1814	7
VA158	$In_{0.71}Ga_{0.29}As$	2	58	1879	14
VA159	$In_{0.71}Ga_{0.29}As$	3	49	1893	16
VA162	$In_{0.74}Ga_{0.26}As$	2	80	1978	7.5
VA163	$In_{0.75}Ga_{0.25}As$	3	240	1990	3.5

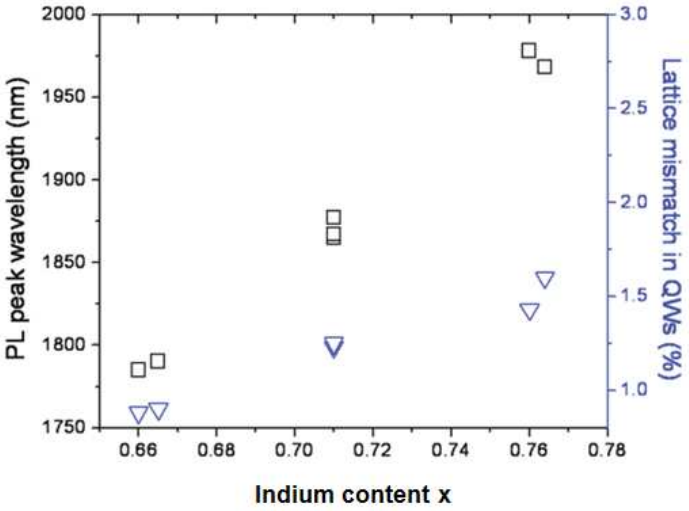

Figure 4-1: The photoluminescence (PL) peak and the lattice mismatch (%) as a function of the indium content of the InGaAs QWs. As the indium content x is increased from 0.66 to 0.77, the PL peak is correspondingly shifted from 1750 nm to 1975 nm [20].

There is a low-index InP cap layer that is designed to push the mode downward, away from the upper metal contact. The top InGaAs contact layer is doped p+ to minimize the metal-semiconductor contact resistance. By changing the indium content of the quantum well layer, emission wavelengths in the range of 1.5 μm to 2 μm were achieved, as shown in Figure 4-1, which plots the peak wavelength of the photoluminescence originating from the different wafers and the lattice mismatch (%) as a function of the indium content x.

4.1 Design

Utilizing the long-wavelength laser heterostructures, the same semiconductor is used for both the active and the passive waveguides. As such, different active and passive waveguide sections will be differentiated post-fabrication by their respective levels of DC carrier injection, as in [84]. The design of the tunable double ring resonator-coupled laser is shown in plan view in Figure 4-2, along with the approximate "zones" of gain, transparency, and absorption that are set by the DC biases.

As shown in Figure 4-2, the laser consists of two rings, or racetracks, of different circumferences, biased at transparency. Racetracks are equivalent to rings, except that they have a straight section to increase the coupling length between the ring and the straight waveguide. The racetracks can be coupled to the waveguide using directional couplers or MMIs. The tunable laser in this chapter is designed using directional couplers (see Section 4.2.2). The gain region is immediately adjacent to the chip facet, which serves as the two end mirrors of the cavity. Having both mirrors on the same side of the chip allows for ease of cleaving, mounting, and testing. At the other end of the device are absorptive waveguides that end in a small-radius, high-loss bend. The purpose of this section is to minimize reflection and operate as a detector for diagnostics.

The two racetracks can be tuned near transparency independently via carrier

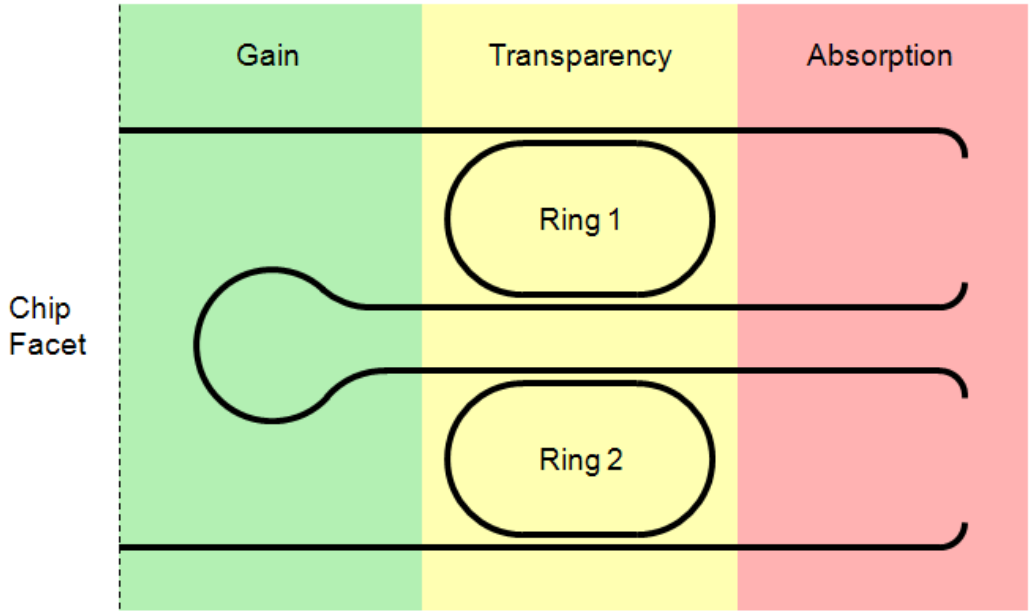

Figure 4-2: Schematic of the double ring resonator-coupled laser. The two mirrors of the lasing cavity share the same chip facet. The regions of gain, transparency, and absorption are shown. The two rings, or more descriptively, racetracks, are designed to have slightly different circumference, and are tuned independently, to obtain wide-tunability through the Vernier effect. The absorption region of the waveguide can also be used for detection diagnostics. The chip facet serves as the two mirrors of the laser cavity. Having both mirrors on the same side of the chip allows for ease of cleaving, mounting, and testing.

injection, and act as wavelength filters employing the Vernier effect, allowing for wide tunability. The single-pass transmission through the double ring resonator-coupled laser can be described by Equations A.41 and A.42, which are derived using coupled-mode theory in Appendix Section A.2. A more intuitive way to understand the Vernier mode selection mechanism of the double ring resonator-coupled laser is presented below.

Let FSR_1 and FSR_2 be the free spectral ranges (FSRs) of the larger and smaller racetracks with circumferences L_1 and L_2, respectively. Suppose the operating wavelength was centered around λ_o and the waveguides had an effective index of n_{eff}. Then $\mathrm{FSR}_2 > \mathrm{FSR}_1$, where

$$\mathrm{FSR}_k = \frac{\lambda_o^2}{n_{eff} L_k} \tag{4.1}$$

for $k = 1, 2$. Figure 4-3 is a diagram illustrating the Vernier effect: the modes of the two racetracks are depicted with their respective FSRs. For now, the FSR of the cavity formed by the cleaved facets of the laser will be ignored since it will be an order of magnitude smaller in general. The modes of the cavity formed by the cleaved facets will limit the wavelength tuning resolution. The modes of the double ring structure can be thought of as the product of the two; in other words, modes exist only where the modes of the individual racetracks line up. The total FSR is given by

$$\mathrm{FSR}_{total} = M \cdot \mathrm{FSR}_1 = N \cdot \mathrm{FSR}_2 \tag{4.2}$$

where M and N are natural and coprime numbers. Figure 4-3 juxtaposes the modes of the two racetracks. Observe that for each successive mode away from the first aligned mode, the modes from the two racetracks become more and more misaligned. Each successive mode has an extra $\Delta = \mathrm{FSR}_2 - \mathrm{FSR}_1$ of misalignment. Assuming that Equation 4.3 holds, then M is equal to the number of Δ required to become misaligned by FSR_2, which is equivalent to being aligned once again. Therefore,

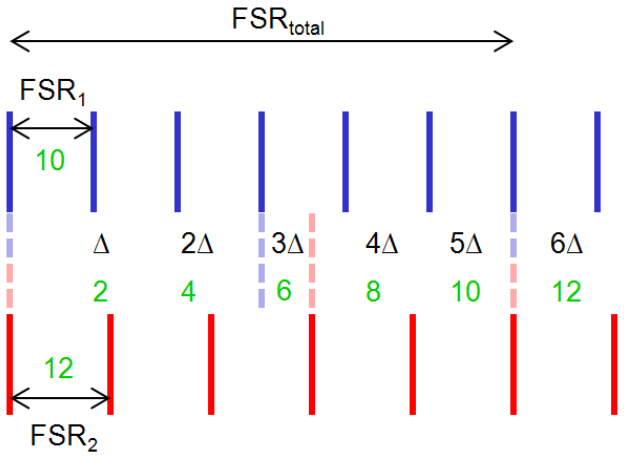

Figure 4-3: Modes of two rings demonstrating the Vernier effect. Suppose that two rings have FSR of 10 and 12 "units." Assume also that their modes are aligned somewhere along the spectrum, as shown for the left-most modes. For each successive mode away from the aligned modes, the relative modes of the two rings pick up an offset Δ of 2 "units" from each other. Only have $12/2 = 6$ successive modes do the realign. The total FSR is 6 $\mathrm{FSR}_1 = (\mathrm{FSR}_1)(\mathrm{FSR}_2)/(\mathrm{FSR}_2\text{-}\mathrm{FSR}_1)$ by inspection.

$$M = \frac{\mathrm{FSR}_2}{\mathrm{FSR}_2 - \mathrm{FSR}_1} \tag{4.3}$$

M is also called the wavelength tuning enhancement factor, because the total FSR of the system is increased from FSR_1 to $M \cdot \mathrm{FSR}_1$ by the insertion of the second racetrack.

Figure 4-4(a) depicts the transmission spectrum through a double ring resonator-coupled laser as shown in Figure 4-2, for the special case where $\kappa = 0.5$ and $n_{eff} = 3.6$. The propagation loss is assumed to be 10 dB/cm. The racetracks have different circumferences with corresponding to FSRs: $\mathrm{FSR}_1 = 5.6$ nm and $\mathrm{FSR}_2 = 6.2$ nm. The circumference C of a racetrack can be broken down into its straight coupling region and its curved regions:

$$C_n = 2L_{\text{coupler}} + 2\pi r_n \tag{4.4}$$

where $n = 1, 2$ is the racetrack number. For the double ring resonator-coupled laser

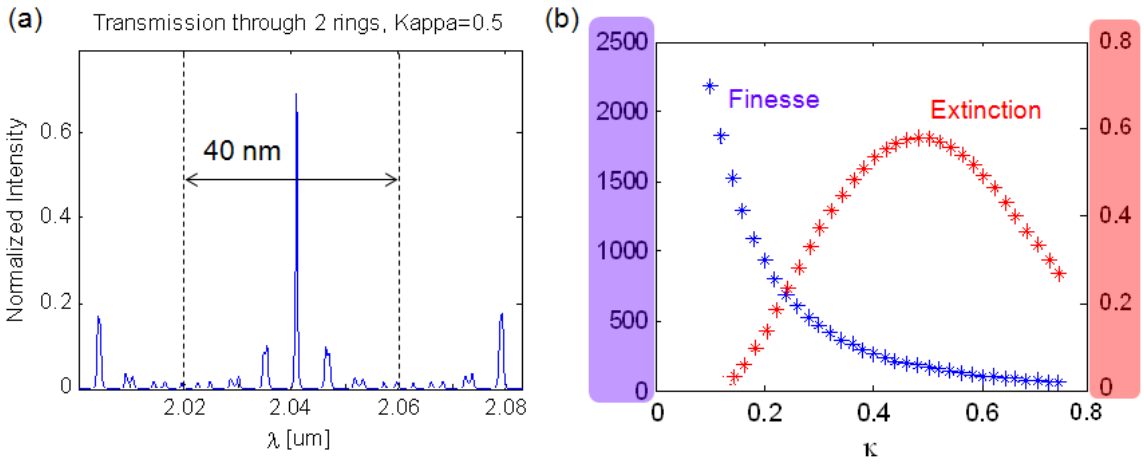

Figure 4-4: (a) Single-pass transmission through two racetracks with $\kappa = 0.5$. The other parameters of the device are as follows: $n_{eff} = 3.6$, $L_{\text{coupler}} = 15$ μm, $r_1 = 29.5$ μm, and $r_2 = 25$ μm. The total FSR is ≈ 40 nm, and the extinction ratio (ER) is 0.6. (b) The extinction ratio and finesse plotted as a function of κ. The finesse is maximized for small κ while the extinction ratio is maximized when $\kappa = 0.5$.

whose spectrum is shown in Figure 4-4(a), $L_{\text{coupler}} = 15$ μm, $r_1 = 29.5$ μm, and $r_2 = 25$ μm. The details of the directional coupler dimensions and the bending losses are presented in Section 4.2.

The racetracks individually have only ≈6 nm of free spectral range. However, the total combined FSR of the two rings is 40 nm. As long as the gain spectrum is narrower than 40 nm in this particular case, the tuning range of the laser is determined by the bandwidth of the gain. If one of the racetracks is tuned while the other is kept constant, then the laser will be able to achieve emission at discrete wavelengths that are separated by the FSR of the constant racetrack. Semi-continuous tuning, down to a resolution determined by the cleaved-facet cavity mode spacing, can be achieved if both racetracks are tuned individually and simultaneously.

The single-pass analysis that is presented in Figure 4-4(a) does not reveal the actual SMSR of the laser. Under lasing operation, the SMSR is expected to be improved due to the multiple passes of the light through the laser cavity. Even so, a high SMSR will be obtained by having a high extinction ratio (ER), defined as the difference between the values of the highest and second highest single-pass

transmission peaks [45]. Assuming that the coupling coefficient κ can be changed by altering the gap dimensions and coupling lengths of the directional couplers, the ER is plotted versus κ in Figure 4-4(b). For more on κ, please refer to Appendix Section A.2.

If κ is small, not enough light is being coupled to the ring resonators, meaning that the selected peak is small, leading to a small ER. If κ is large, more of the side peaks will be transmitted, leading to a small ER as well. Thus, to maximize the SMSR, an optimal coupling coefficient of $\kappa = 0.5$ is required; the power coupling coefficient is 25% (recall that κ^2 is the power coupling coefficient).

Aside from the ER, which corresponds to the SMSR of the lasing peak, the finesse of the cavity is also of interest, because it corresponds to the linewidth of the lasing spectrum. A narrow linewidth is desired, especially because the modes of the cavity formed by the cleaved facets will have an FSR that is an order of magnitude smaller than the FSR of the rings. To obtain single longitudinal mode lasing, the filtering linewidth is desired to be smaller than the FSR of the cleaved-facet cavity modes. Figure 4-4(b) also plots the finesse as a function of κ, where high finesse occurs for low values of κ. A significant part of the laser design is balancing the trade-offs associated with κ.

4.2 Modeling

To better understand the dimensions and associated trade-offs in performance and fabrication tolerances, optical modeling of the waveguides is performed. In the next sections, the analysis of the design is described for a double ring resonator-coupled laser operating at 1.88 μm. The qualitative design considerations are summarized below:

- Waveguides: single mode TE
- Waveguide bends: losses < 10 dB/cm
- Directional couplers: $\kappa = 0.44$.

4.2.1 Waveguides

One of the difficulties associated with designing devices that operate at long-wavelengths is the fact that the indices of refraction n for many materials are not accurately known at wavelengths beyond 1.55 μm. Interpolation is a good method for double checking a literature n value, or calculating an n value if none exists in the literature. For example, to estimate the refractive index of $In_{0.53}Ga_{0.32}Al_{0.15}As$, a linear interpolation can be performed with $Al_{0.68}Ga_{0.32}As$ and $In_{0.68}Ga_{0.32}As$.

For modeling, a simplification was made to the heterostructure shown in Appendix Section C.1. Table 4.2 shows the layer structure that was used to model the waveguides at $\lambda = 1.88$ μm using the beam propagation method (BPM) (see Appendex Section A.1) and 2D mode solving as described in [88]. The refractive index of $In_{0.53}Ga_{0.32}Al_{0.15}As$ at 1.88 μm is not well known; Table 4.2 shows both a value found in the literature and a value obtained via linear interpolation of $Al_{0.68}Ga_{0.32}As$ (from literature) and $In_{0.68}Ga_{0.32}As$ obtained by applying the Sellmeier equation in the energy range slightly above the fundamental absorption edge[1] [31, 106].

[1]The Sellmeier equation is most accurate in the transparent wavelength range.

Table 4.2: The simplified heterostructure for optical modeling ($\lambda = 1.88$ μm).

Layer	Material	Thickness (μm)	Literature n	Interpolated n
p+ Contact	$In_{0.53}Ga_{0.47}As$	0.1 μm	3.57 [42]	3.57 [42]
Cladding	InP	2.2 μm	3.132 [1]	3.132 [1]
Core	$In_{0.52}Ga_{0.33}Al_{0.15}As$	0.46 μm	3.4 [81]	3.62 [31, 106]
Substrate	InP	-	3.132 [1]	3.132 [1]

Table 4.3: The simplified heterostructure for optical modeling ($\lambda = 1.78$ μm).

Layer	Material	Thickness	Literature n	Measured n
p+ Contact	$In_{0.53}Ga_{0.47}As$	0.1 μm	3.61 [42]	3.61 [42]
Cladding	InP	2.2 μm	3.136 [1]	3.136 [1]
Core	$In_{0.52}Ga_{0.33}Al_{0.15}As$	0.46 μm	3.412 [81]	3.8
Substrate	InP	-	3.136 [1]	3.136 [1]

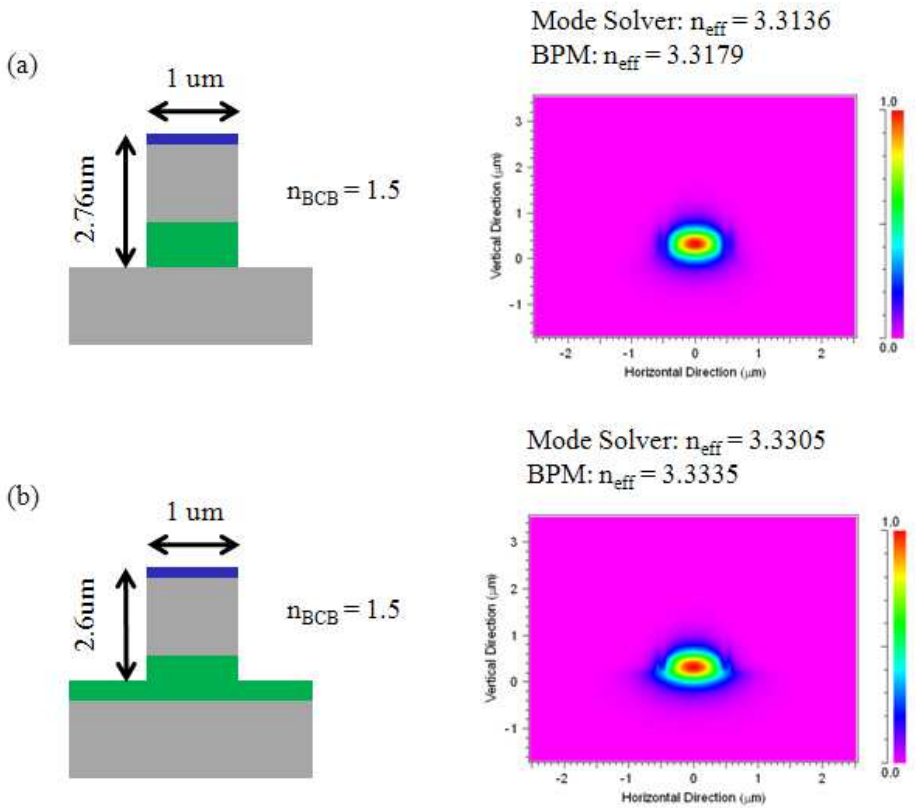

Figure 4-5: BPM mode simulations for waveguides with different etch depths ($\lambda = 1.88$ μm). (a) A side-view diagram of a 1 μm wide waveguide etched down to 2.76 μm (all the way through the entire high index core), and the corresponding TE mode profile. (b) A side-view diagram of a 1 μm wide waveguide etched down to 2.6 μm, and the corresponding TE mode profile. For these simulations the interpolated values of n from Table 4.2 are used.

In Section 3.2, the long-wavelength laser structures listed in Table 4.1 were fabricated into lasers emitting at close to 1.78 μm, 1.88 μm, and 1.98 μm. Table 4.3 lists the layer structure that was used to model the waveguides at $\lambda = 1.78$ μm. The last column of the table shows a value of the refractive index of $In_{0.53}Ga_{0.32}Al_{0.15}As$ obtained by measuring the longitudinal mode spacing of a fabricated Fabry-Perot laser and back-calculating the refractive index. This value of n was obtained post-design, but should be incorporated into the models for future designs.

In Section 4.2.3, calculations will show that the waveguide must be etched deeper than the high index core in order to exhibit a manageable bending loss. Due to the high index contrast, this constrains the waveguide width to be ≤ 1 μm to satisfy

the single-mode requirement. Figure 4-5 shows the mode profile at $\lambda = 1.88$ μm, as simulated by BPM, and the effective indices as simulated by BPM and the mode solver, for a 1 μm wide waveguide that is etched to two different depths. BPM has the tendency to calculate higher values of effective index by 0.1%, which is small compared to the uncertainties of the refractive index estimates at $\lambda = 1.88$ μm. For these simulations the interpolated values of n from Table 4.2 are used.

4.2.2 Directional Couplers versus MMIs

Both directional couplers and MMIs have been used for double ring resonator-coupled laser designs. Table 4.4 compares the two structures, showing that the main advantage of MMIs is that they have larger feature sizes and therefore can potentially be fabricated more easily with contact lithography. Directional couplers are more difficult to fabricate but they are more versatile in operation. For this reason, directional couplers were chosen as the coupling method from racetrack to straight waveguide and vice versa.

One important advantage of directional couplers over MMIs is that they can be fabricated to have an arbitrary κ. With MMIs, non-symmetric splitting is more difficult to achieve without significant reflections. MMIs perform well with 50:50 splitting, but that translates into a κ of 0.71, which results in a low extinction ratio according to Figure 4-4(b). Some initial work was performed to obtain a non-symmetric splitting. Figure 4-6 depicts a BPM simulation of a 50:50-splitting MMI. The waveguides in this simulation are 2 μm (not single-mode). The length of the MMI is $L_{3dB} \approx 230$

Table 4.4: Comparison of MMIs and directional couplers.

Attribute	MMI	Directional Coupler
Smallest Feature	Micron	Sub-micron
Reflections	Yes	No
Splitting Ratio	50:50	Arbitrary
Larger Bandwidth		✓
Smaller Footprint		✓

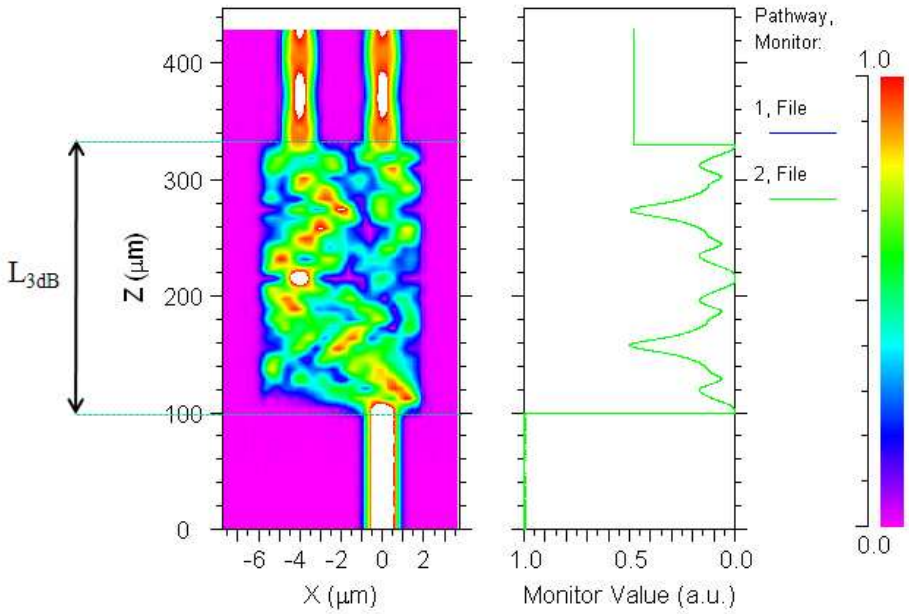

Figure 4-6: BPM simulation of a 50:50-splitting MMI structure ($\lambda = 1.88$ μm) modeled to be etched down 2.76 μm as in Figure 4-5(a). The waveguides are 2 μm (multimode) to allow for definition with contact lithography. $L_{3dB} \approx 230$ μm. For this simulation the interpolated values of n from Table 4.2 are used.

μm. If the MMI is extended in length to $1.5L_{3dB}$ as in Figure 4-7, the splitting is 14.3:83.7 with $\kappa = 0.378$, which translates into an extinction ratio that is close to the optimum, with only a 2% insertion loss. The desire to create single-mode waveguides however, as discussed in Section 4.2.1, limits the width of the waveguides to 1 μm, making pattern definition with contact lithography a challenge. Instead, electron beam lithography was used, which can define directional couplers capably. In the future, a dilute waveguide heterostructure can allow for larger-width single-mode waveguides to be defined using contact lithography. In such a scenario, the MMI design of Figure 4-7 may aid in maintaining a high ER.

4.2.3 Etch Depth

The design of the etch depth of the waveguide is complicated. First, there is the tradeoff between coupling and bending loss. A shallower depth is desired to decrease the length of the directional couplers, while at the same time, a deeper depth is desired

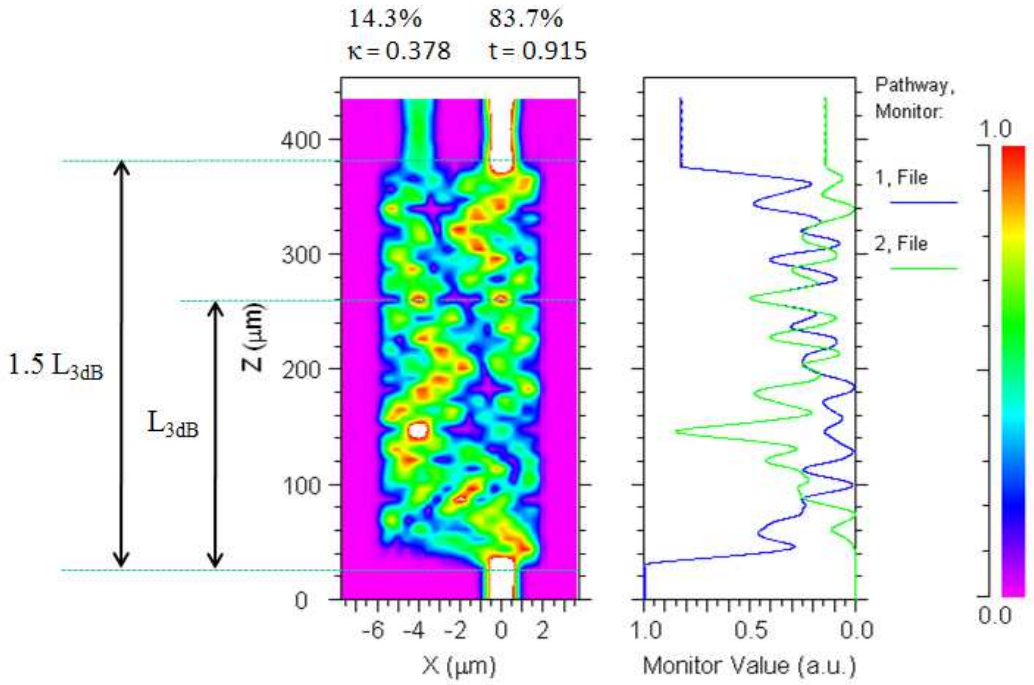

Figure 4-7: BPM simulation of a 14.3:83.7-splitting MMI structure ($\lambda = 1.88$ μm) modeled to be etched down 2.76 μm as in Figure 4-5(a). The waveguides are 2 μm (multimode) to allow for definition with contact lithography. The length is $1.5L_{3dB} \approx$ 345 μm. For this simulation the interpolated values of n from Table 4.2 are used.

to minimize the bending losses from the racetracks and other waveguide bends. For the best pattern fidelity, both of these dimensions should be confined to the field size of the electron beam lithography tool. In other words, the racetracks of these devices must fit into the 100 μm^2 field of the Raith 150 scanning electron beam lithography tool.

One method used to decouple the etch depth trade-off between coupling length and bending loss is bi-level etching. Bi-level etching is generally performed by etching the directional couplers and the bends separately to different depths, which requires two etch steps and an extra lithography step [33]. Semi-bi-level etching can be achieved by utilizing the dependence of the etch rate on feature size [84]. More details about this method will be discussed in Section 4.3.2.

Beyond the theoretical considerations, there is also the fabrication issue of depth control. In other words, the reproducibility of the etch in the reactive ion etcher (RIE)

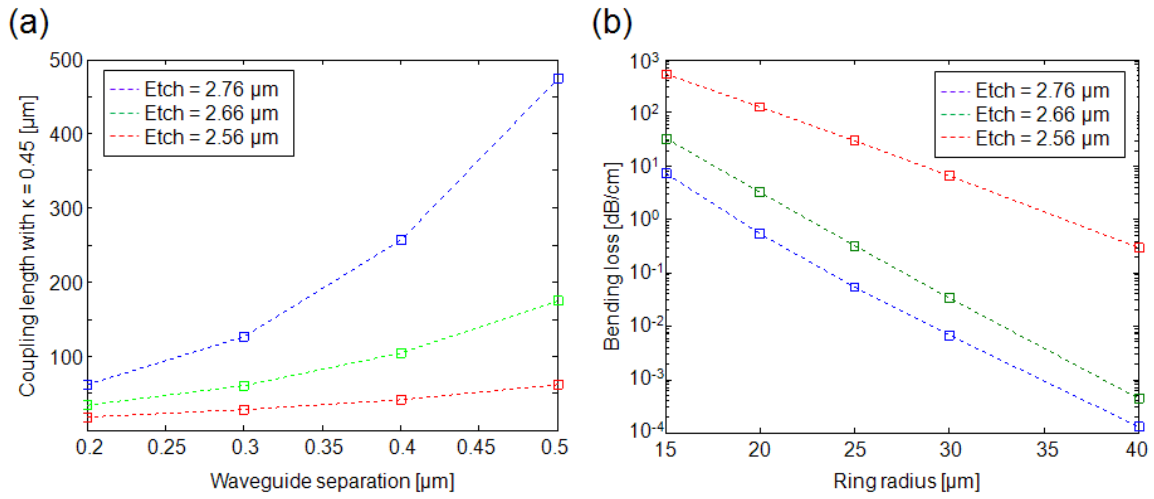

Figure 4-8: Coupler length and bending loss trade-off for different waveguide etch depths ($\lambda = 1.88$ μm). (a) The directional coupler length L that is required to achieve a $\kappa = 0.45$ as a function of the waveguide separation for different values of etch depths. (b) The bending loss as a function of the bend radius for different values of etch depth. For these simulations the interpolated values of n from Table 4.2 are used.

must be taken into account. Given an experimentally-observed etch rate in excess of 1 μm/min, and observing that the etch rate can be controlled to $\pm 5\%$, the uncertainty in the etch depth is 100 nm. Efforts to slow down the etch rate by decreasing the etching temperature have resulted in surface roughness. Figure 4-8 depicts (a) the coupling length of the directional coupler that is required to achieve $\kappa = 0.45$ as a function of the waveguide separation and (b) the bending loss as a function of the radius of curvature for etch depths that differ by 100 nm.

4.3 Fabrication

The fabrication process of the double ring resonator-coupled laser is challenging partially due to the high aspect ratios of the waveguides and the narrow spacings between them that are required for effective coupling. The process flow is depicted in Figure 4-9. Quantitative details of the fabrication process can be found in Appendix Section C.4.

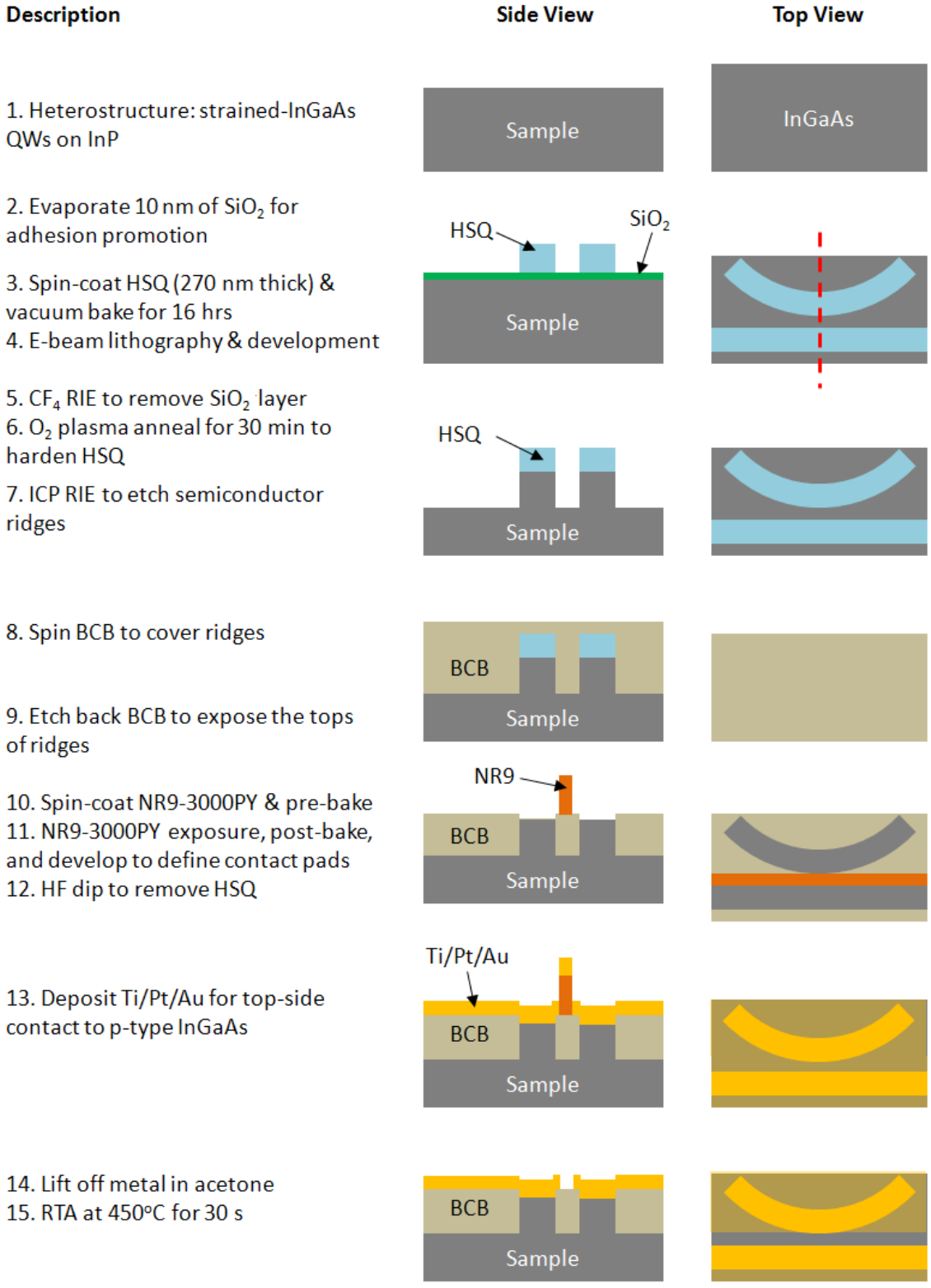

Figure 4-9: Process flow for the double ring resonator-coupled tunable lasers.

4.3.1 Electron Beam Lithography

Electron beam (e-beam) lithography is used to define the waveguide pattern. One of the benefits of e-beam lithography, and other direct-write lithography systems, is that the device patterns can be altered between writes, unlike using the pre-defined patterns on contact masks, as was done in the previous chapters. The double ring resonator-coupled laser device layouts can be found in Appendix Section C.3.

Nominally, the Raith 150 e-beam lithography tool exposes features using an x-y rastering of the electron beam. Curved waveguides, such as rings and racetracks, that are written using x-y rastering have been observed to exhibit pixellated edges [10, 39]. Thus, the x-y rastering was modified to an exposure method in which the electron beam traces specific paths according to a list of coordinates. Each arc is typically divided into 1000 line segments. In this way, the racetracks of the double ring resonator-coupled laser were exposed by the electron beam tracing paths of concentric racetrack shapes that were separated by 12 nm.

As in any lithography process, the first step was to select a resist and identify the appropriate dose for pattern definition. The resist that was chosen for pattern definition was Hydrogen SilsesQuioxane (HSQ). HSQ is a spin-on dielectric that is also a negative e-beam resist. HSQ can be used as the etch mask itself for the III-V semiconductor reactive ion etch, since it resembles SiO_2, especially after annealing [145]. HSQ was empirically observed to not adhere well to InP-based substrates however, so a thin 10 nm thick layer of SiO_2 is evaporated onto the substrate for adhesion promotion before the application of the HSQ. After spin-coating at 3 krpm to obtain a 300 nm thick layer of HSQ, the carrier solvent is removed with a 16 hour room-temperature vacuum bake prior to exposure. Two specific formulations of HSQ were used: Dow Corning FOx-14 and FOx-22 ("Flowable Oxides"). The Dow FOx 10-series uses methyl isobutyl ketone (MIBK) as its carrier solvent, whereas the second-generation FOx (20-series) uses a volatile methyl siloxane (VMS) fluid blend as the carrier solvent.

The dose that is required for stand-alone well-separated waveguides is 450 $\mu C/cm^2$

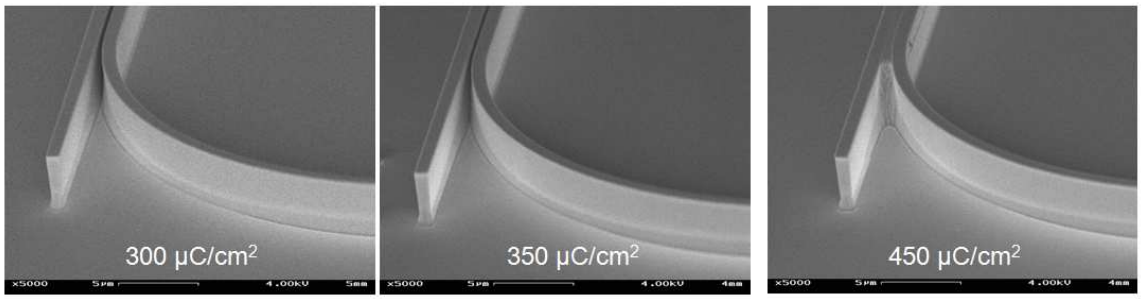

Figure 4-10: SEMs demonstrating the effect of e-beam dose on the gap of the directional coupler. The same structure is exposed at different doses and developed for 90 s, then etched in the Samco ICP RIE for 150 s. Etch parameters: 250W ICP RF power, 160W Bias RF power, 0.6 Pa, 0.5 sccm Cl_2, 2 sccm $SiCl_4$, 10 sccm Ar, using the ceramic carrier heated to 220°C.

for FOx-14 and 600 μC/cm^2 for FOx-22 at an acceleration energy of 30 keV on InP substrates. The point spread function of exposure for an electron beam is larger than the actual beam size due to the proximity effect (see Appendix Section B.2). The smaller atomic size of silicon causes a silicon substrate to exhibit a smaller amount of the proximity effect and therefore to require a higher exposure dose than an indium phosphide substrate. Figure 4-10 shows HSQ patterns on InP exposed at different doses and etched using the HSQ as a hardmask. The gap spacing of the directional coupler between the racetracks and the straight waveguides was defined to be 200 nm. However, the gap narrows for increasing dose until the gap no longer exists. The waveguides in the directional coupler region of the pattern requires a lower dose than the stand-alone waveguides.

In order to address the proximity effect issue, a method of exposure was developed to provide different doses in different regions of the pattern. Depicted in Figure 4-11, the method divides the total exposure into two steps. First, the entire pattern is exposed at the lower dose that is suitable for the directional coupler where the waveguides are closer together. Next the e-beam traces paths along the areas that require the higher dose that is suitable for stand-alone waveguides. Because the transition from stand-alone waveguides to the directional coupler is gradual, the traces of the e-beam in the second step are designed to gradually decrease in density to

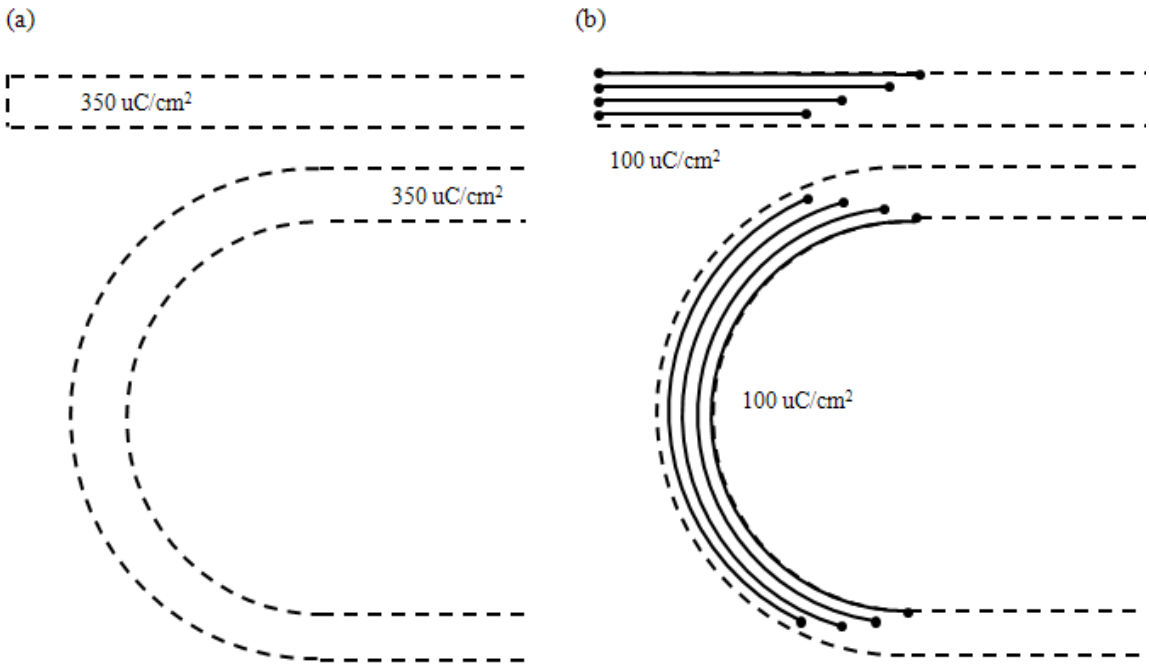

Figure 4-11: A method of writing a racetrack coupled with a straight waveguide in the presence of the proximity effect. (a) First, the entire structure is written at the dose corresponding to the coupling region. (b) Next, the electron beam is programmed to trace paths to increase the dose for the stand-alone waveguides.

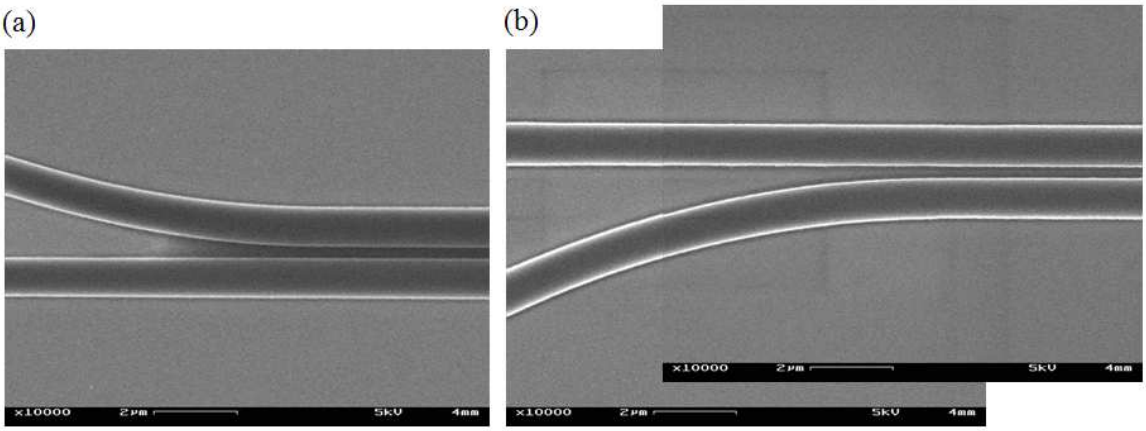

Figure 4-12: A demonstration of the proximity effect method for patterning the directional coupler. (a) The coupling region is written with a dose of 450 μC/cm^2 and developed for 140 s. The region is overexposed and the gap has not cleared. (b) Using the proximity effect method described in Figure 4-11 allows both the coupling region and the stand-alone waveguides to receive the proper doses.

accommodate the transition.

Figure 4-12(a) is a plan-view SEM of the directional coupler that was exposed at the higher dose that is suitable for stand-alone waveguides, in which the HSQ inside the gap has not been removed after development. Figure 4-12(b) shows the same structure written using the two-step exposure method, in which the HSQ in the gap has been removed and the waveguides maintain a 1 μm width throughout the structure.

Aside from the proximity effect, electron beam lithography presents another unique non-ideality: unlike photons, electrons are charged particles. HSQ is not conductive and it can accumulate electrons and "charge up" in the exposed areas, causing poor reproducibility and write errors due to the accumulated charge deflecting the electron beam (also called pattern-dependent beam errors).

For a typical e-beam lithography system, the write field is often smaller than the total pattern to be written. A write field is the area over which the electron beam is deflected to expose the desired areas. For the Raith 150 system, a write field of 100 μm $\times$ 100 μm was used. An e-beam lithography system will break down the total pattern into many fields. During an exposure, the stage will translate the sample beneath the beam in order for each write field to be exposed. Write errors can often be observed between fields. These errors are called stitching errors, and can be due to many factors, such as the accuracy of the translation stage, the size of the field (and therefore the amount of pattern distortion at the field edges), and the charging that can cause pattern-dependent errors. Figure 4-13 shows the stitching errors that were observed in a waveguide pattern that was written in HSQ on an InP substrate.

Large stitching errors can contribute to propagation loss in the waveguide. Experiments indicated that most of the stitching error could be attributed to the pattern-dependent charging of HSQ. When a conductive layer that serves as a ground plane was deposited above the HSQ, the stitching errors were reduced. Figure 4-14(a) shows the stitching errors between fields of a sample without any conductive coating, and Figure 4-14(b) shows the stitching errors between fields of a sample that was coated with 10 nm of evaporated aluminum on top of the HSQ. With the conductive

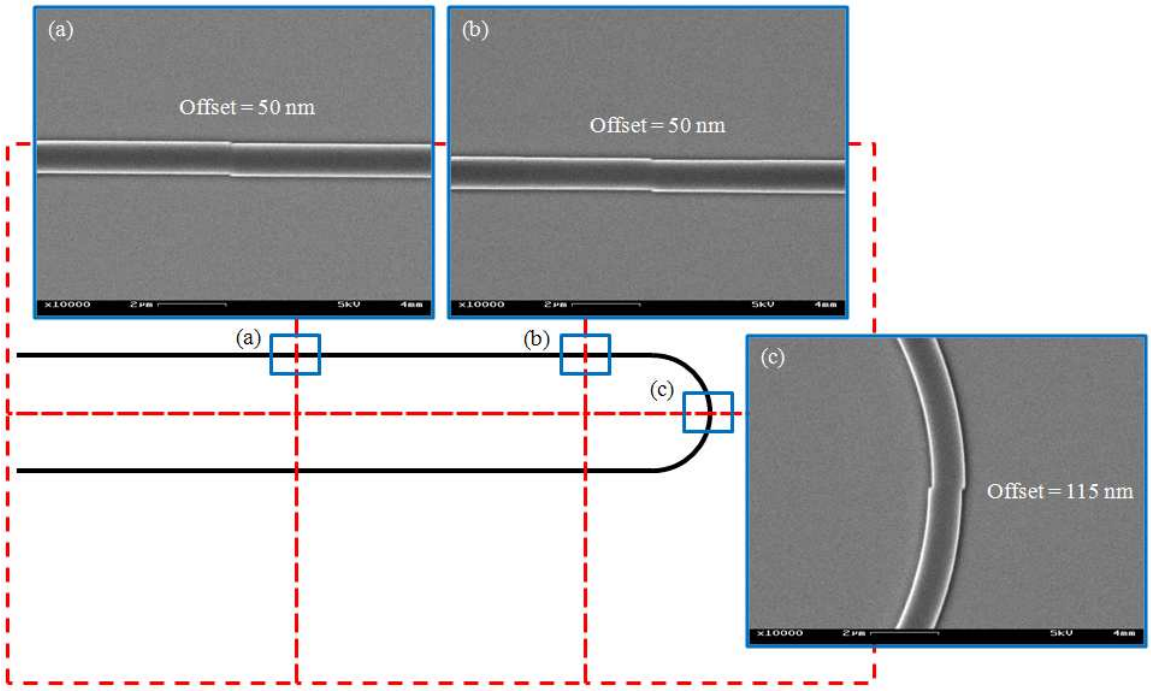

Figure 4-13: Stiching errors at the boundaries of the 100 × 100 μm^2 fields of the Raith 150, that are depicted as dashed-line squares. The insets show SEMs of the waveguide write errors.

coating, there is a drastic improvement in the stitching error, as measured from the Verniers that were written at the boundaries of the write fields, an example of which is shown in Figure 4-14(c). Aluminum is chosen as a conductive layer because it can be etched and hence removed by the developer for HSQ, tetramethylammonium hydroxide (TMAH).

E-spacer, a commercially available spin-on conductive polymer, has been shown to provide improvements in stitching as well, but not at the level of the aluminum layer. However, because E-spacer can be applied simply by spin-coating and is water soluble, the devices in this chapter were ultimately fabricated using E-spacer as the conductive coating above the HSQ.

After exposure with the e-beam, the E-spacer is removed with a DI water rinse, and the HSQ is developed in 25% (by weight) TMAH for 40 seconds. TMAH will etch SiO_2, so the development time needs to be calibrated such that the SiO_2 adhesion layer is not etched completely. SiO_2 can be observed to peel off the substrate when

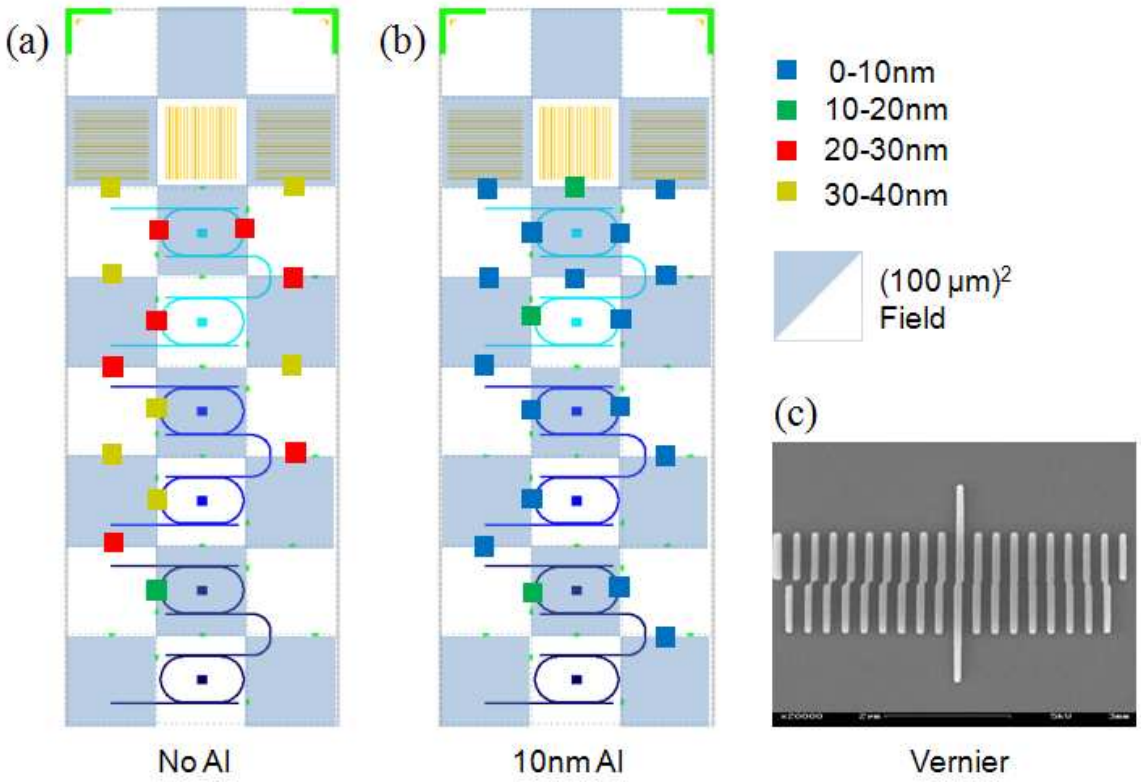

Figure 4-14: Adding a conductive layer above the HSQ is shown to reduce the stitching error. (a) The stitching errors of the chip exposed in HSQ on InP. (b) A clear reduction of stitching errors is observed when 10 nm of Al is evaporated above the HSQ on InP. (c) SEM of a Vernier with the third bar from the center aligned, indicating a 30 nm stitching error (10 nm per bar).

the resist is over-developed. After development, the SiO_2 adhesion layer is removed using a 35 second CF_4 reactive ion etch. A 30 minute O_2 plasma anneal is performed to harden the HSQ prior to its use as an etch mask in the subsequent dry etch that is used to define the ridge waveguides [145].

4.3.2 Inductively-coupled Plasma Reactive Ion Etching

The waveguide ridges are defined using inductively-coupled plasma (ICP) reactive ion etching (RIE). The sample temperature is elevated to 220°C to improve the volatility of the etch by-products so that the residue can be pumped out of the etch chamber during the etch. A general description of dry etching can be found in Appendix Sec-

tion B.3, and the detailed parameters for ICP RIE etching can be found in Appendix Section C.4.

As discussed in Section 4.2.3, a deeper etch is desired to reduce the bending loss, while a shallower etch is desired to reduce the coupling length. For directional couplers, bi-level etching has been utilized to achieve a deep outside etch with a shallow inside etch, but requires an extra lithography and etch step [33]. Figure 4-15(a) shows a cross-sectional SEM of an etched directional coupler with different etch depths on the inner and outer edges of the ridges. Achieved with a single etch, the structure in Figure 4-15(a) exploits the feature-size-dependent etch rate of reactive ion etching [84]. The semiconductor in the gap etches at a slower rate than the semiconductor on the outside, most likely due to the transport-limited flow of the etch species into and out of the gap.

The depth of the gap can be controlled by adjusting the gap opening, or the as-defined separation of the waveguides in the directional coupler. As shown in Figure 4-16, the etch rate inside the gap increases as the gap opening is increased until the the etch rate inside the gap reaches the etch rate outside the gap. Figure 4-

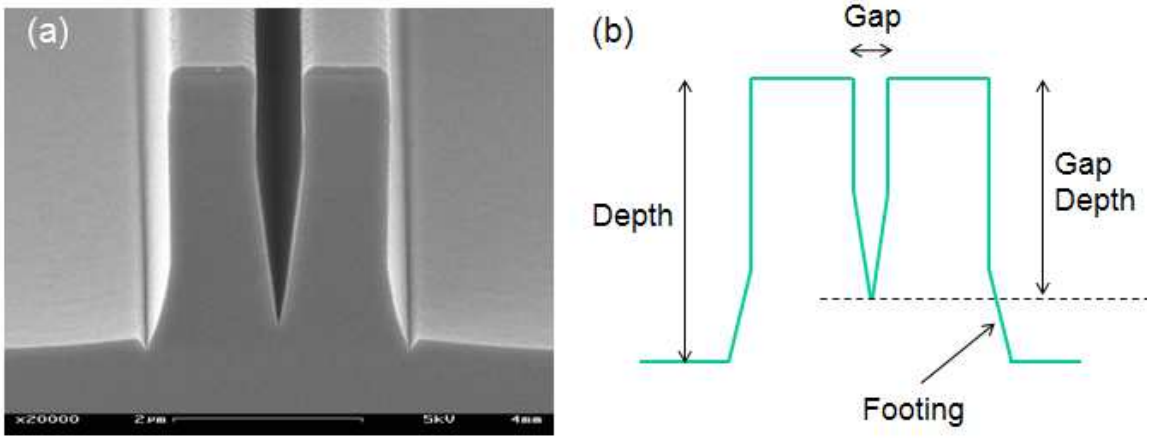

Figure 4-15: The cross section of two adjacent waveguides of a directional coupler. (a) SEM of the directional coupler in InP etched with the ICP RIE. (b) Simplified analytical cross-section of the directional coupler, depicting the most important feature: the gap opening between the waveguides at the top that draws to a point at the bottom, the difference in height between the "depth" and the "gap depth," and the footing that occurs near the bottom of the etch.

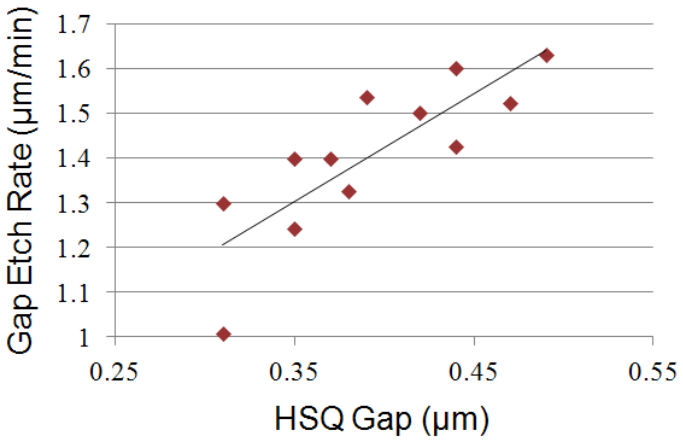

Figure 4-16: The etch rate of the semiconductor inside the gap as a function of the HSQ gap opening. The etch rate inside the gap increases as the gap opening is increased until the the etch rate inside the gap reaches the etch rate outside the gap.

15(b) depicts a model of the cross-section of the directional coupler, with the most important features of the etch defined. Most importantly, to minimize bending losses, the so-called "depth" should be deeper than the high index core of the waveguides, *i.e.* deeper than 2.76 μm. To decrease the coupling length, the so-called "gap depth" should be as shallow as possible without introducing problematic higher-order modes.

Modeling was performed to confirm that the directional coupler would function appropriately with the slanted waveguide sidewalls in the gap. From a fabrication point of view, however, the relevant parameters for the gap are the exposure dose and waveguide spacing. Thus, these two parameters were varied, along with the coupling length, to empirically obtain the appropriate gap for the devices.

4.3.3 Planarization

Another issue with the narrowness of the gap presents itself right after the ICP RIE etch: planarization. For a general description of planarization, please refer to Appendix Section B.4. Figure 4-17 shows a planarization experiment that was performed using benzocyclobutene (BCB), a spin-on dielectric. The BCB was spun on, annealed, and etched back. The BCB was able to fill the narrow gap completely as desired, and provides a planar surface for metalization that has some roughness, which enhances

the metal adhesion.

The adhesion of BCB to III-V semiconductors is stated to be poor in the processing recommendations by Dow Corning. As a result, silicon dioxide and silicon nitride have been investigated as adhesion layers between the indium phosphide substrate and the BCB. The BCB was observed to have very good adhesion to both materials, but later steps in the fabrication process prevented their use. Thus the BCB was applied without the use of an adhesion layer. For the purposes of these devices, the adhesion of BCB to indium phosphide was sufficient to obtain functional devices, especially if the BCB is restricted to confined areas.

Silicon dioxide is non-ideal as an adhesion layer because its etch rate is extremely high in HF (in excess of 6 nm/s). The HSQ on the top of the ridge waveguides needs to be removed with buffered HF before the top-side metal deposition can be performed. In experiments, the timing accuracy that was required to ensure that the SiO_2 adhesion layer was not etched significantly during the HF wet etch of HSQ was too short to be reproducible. In the case of silicon nitride, BCB peeling was observed when the sample was exposed to TMAH during the development of the photoresist that was used to define the metal contact pads, as shown in Figure 4-18. The TMAH

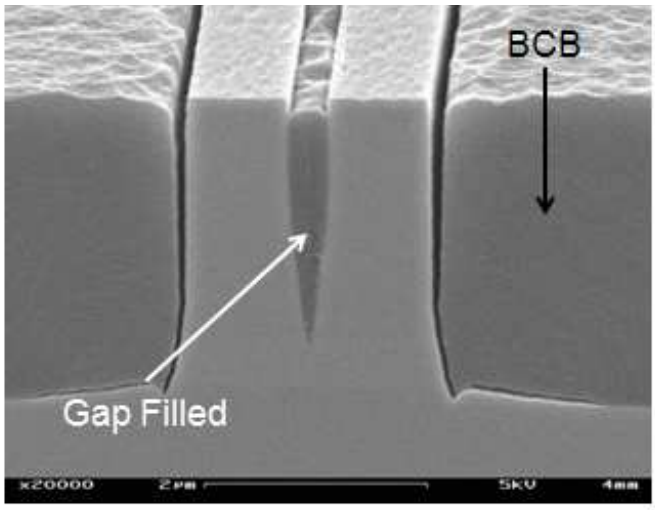

Figure 4-17: The planarization achieved with BCB successfully fills in the space between the waveguides in the directional coupler.

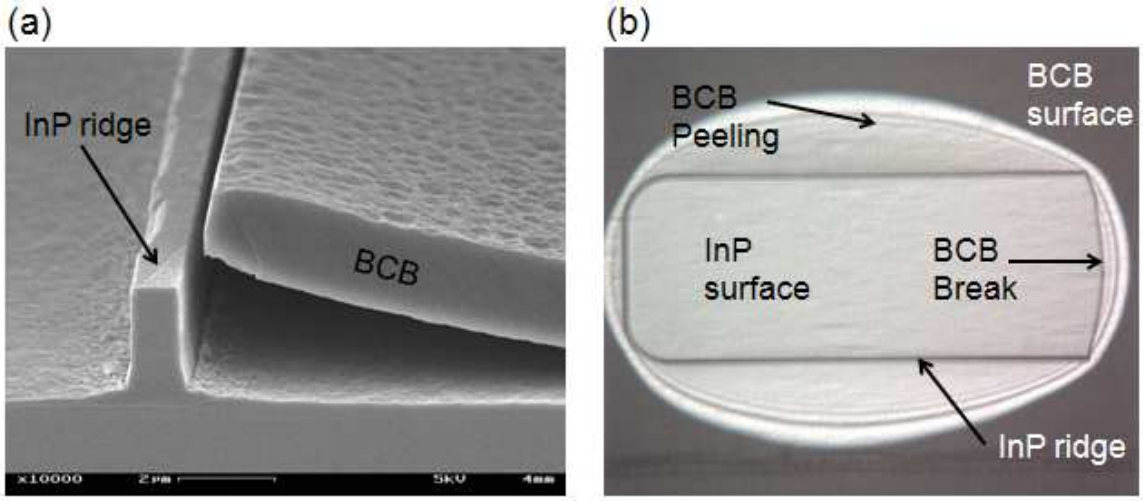

Figure 4-18: BCB peeling from the surface of the substrate when a 10 nm silicon nitride adhesion layer is used. (a) SEM of the BCB peeling away from the ridge waveguide after immersion in RD6, a TMAH-based developer. (b) Plan-view microscope image showing the BCB peeling away from the substrate starting from the where the ridge waveguide is located. The interference fringes around the edges of the light-colored area can be seen, indicating the height variation of the BCB lifting from the surface.

most likely attacked the interface between silicon nitride and the III-V semiconductor.

When applied without an adhesion promotion layer, the BCB was observed in many cases to accumulate enough stress to separate from the semiconductor, especially when exposed to the trauma of cleaving. Figure 4-19(a) shows the BCB separating from the semiconductor ridge after cleaving. The total stress of the BCB can be reduced if it is confined to a small area. To this end, ridge-like structures were fabricated to behave as "fences" to confine the BCB, as shown in Figure 4-19(c). Figure 4-19(b) shows the improvement in BCB adhesion as a result of the fencing.

4.3.4 Laser Direct-write Lithography

The BCB etch-back process is halted once the tops of the waveguides are exposed. The metal contact pad pattern is defined using laser direct-write lithography with a Heidelberg μPG tool. The resolution of the μPG is 1 μm, with an alignment accuracy of 3 μm. Due to the low level of accuracy required for the lift-off process,

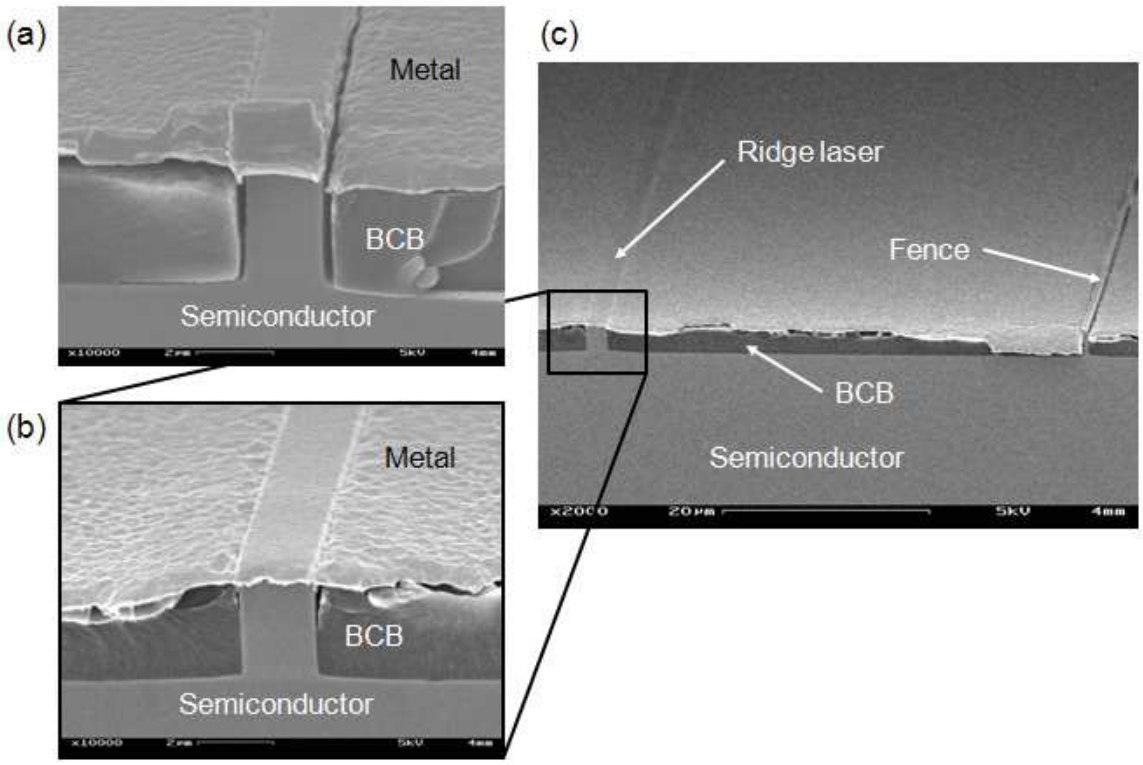

Figure 4-19: Confining the BCB layer to small areas facilitates adhesion to InP. (a) A large area of BCB is seen to separate from the ridge laser after cleaving. (b) When the BCB is confined to a small area, the stress in the BCB is not large enough to separate it from the ridge when cleaving. (c) The "fence" situated 40 μm away from the waveguide ridge serves to confine the BCB to a small area.

this was adequate. After the resist pattern had been obtained, the top-side metal was deposited and a lift-off process was used to fabricate the contact pads. Two types of negative photoresists were utilized: NR9-1000PY and NR9-3000PY. As shown in Figure 4-20, the rastering of the direct-write laser beam causes the top of photoresist to be scalloped. This, however, did not effect the metal contact pads. The undercut of the resist profile helps to facilitate the lift-off process. NR9-3000PY, the thicker of the two negative resists, was used for the fabrication.

A cross-sectional view of the photoresist, which was cleaved at the indicated location as shown in Figure 4-21(a), is shown in Figure 4-21(b). To minimize the exposure time, rectangles corresponding to the edges of the contact pads were patterned in the negative photoresist. The resulting wafer is covered completely in metal, with 10 μm

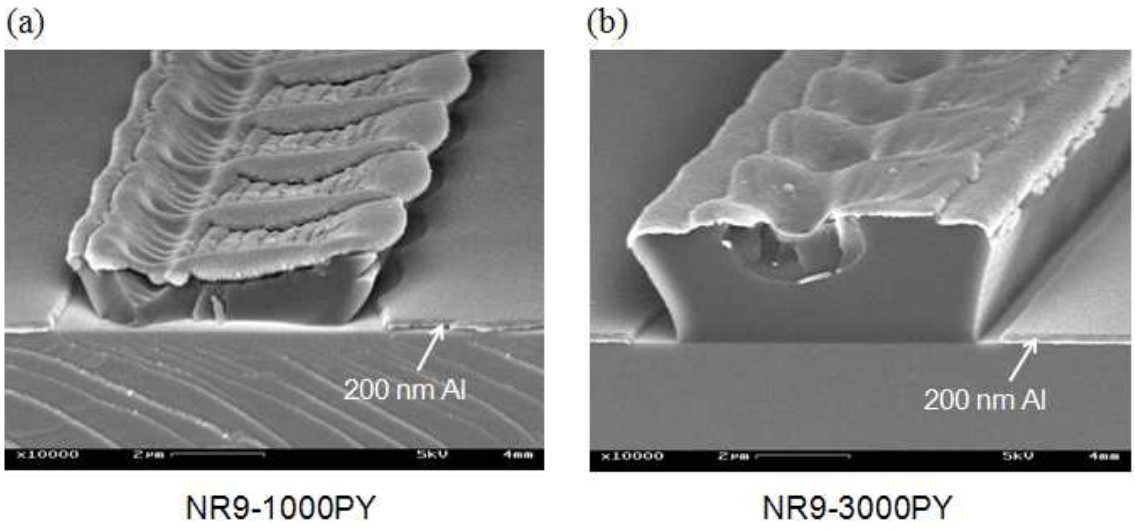

Figure 4-20: Cross-sectional SEMs of NR9 photoresists. (a) A NR9-1000PY pattern on Si substrate with 200 nm of Al evaporated prior to lift-off. The undercut facilitates the lift-off process. Scalloping of the resist is observed to correspond to the direct-write raster. (b) A NR9-3000PY pattern on Si substrate with 200 nm of Al evaporated prior to lift-off.

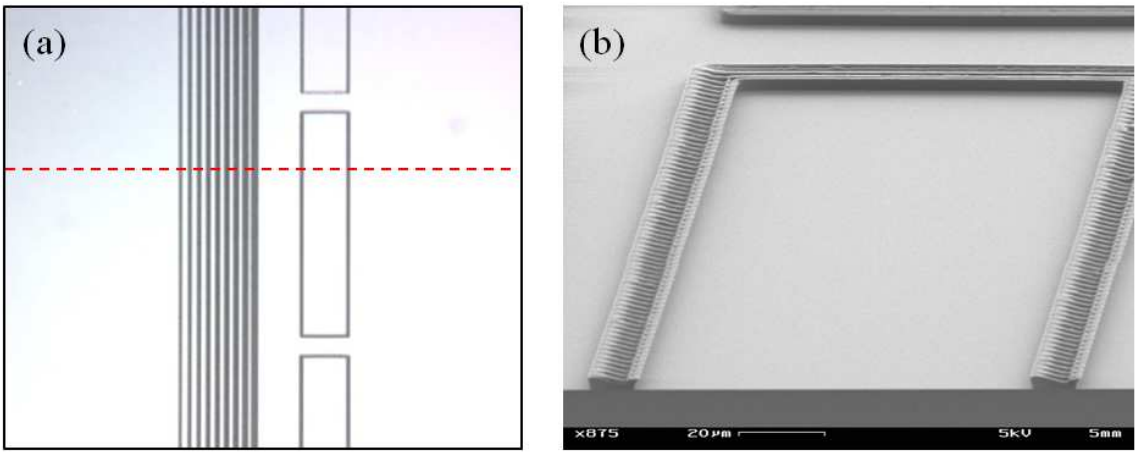

Figure 4-21: Experimental pattern defined in NR9-3000 using the Heidelberg direct write lithography tool. (a) Plan view of a test pattern written on a Si substrate. The lines are ≈ 10 μm wide. (b) A side view cross at the cross section labeled in part (a).

spaces between different contact pads. The locations of the "fences" also need to be covered by the photoresist so that the metal only makes contact to the waveguide ridge. To allow the metal pads to be large enough for electrical probing, the fences

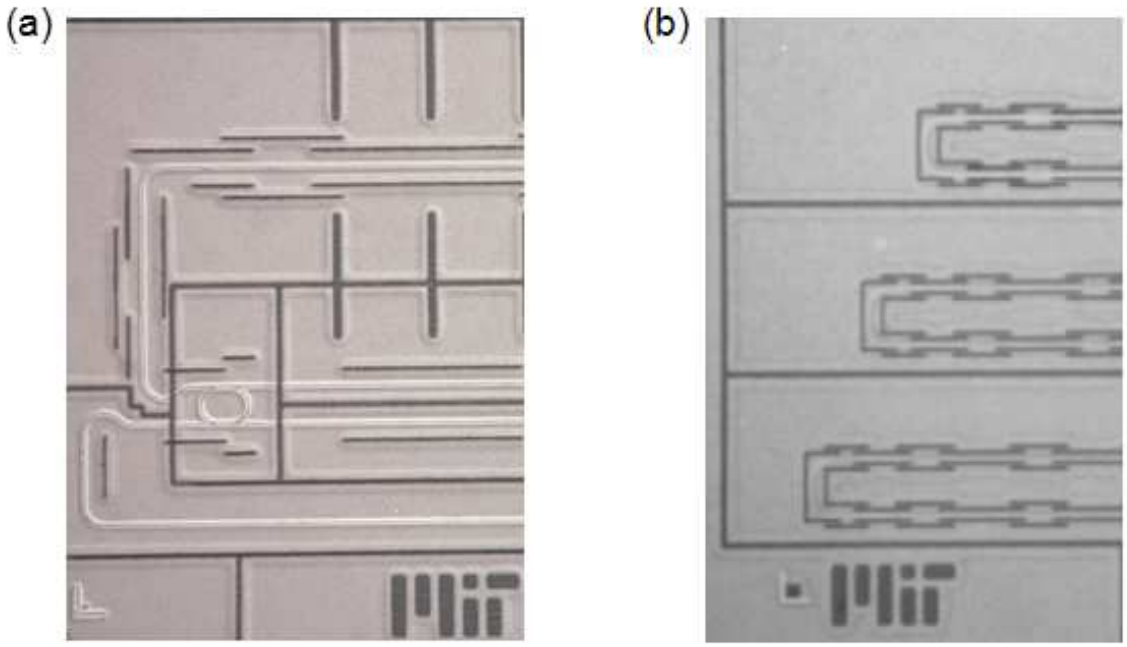

Figure 4-22: Plan-view microscope images of long-wavelength laser dies after fabrication of the metal pads. (a) A single-ring coupled laser. (b) Three single-facet lasers. The dark lines correspond to locations without metal. The form of the waveguides are visible in part (a). In part (b), the waveguide is bound by the staggered fences.

are staggered as shown in Figure 4-22. Figure 4-22(a) shows a single ring resonator-coupled laser. Multiple contacts were fabricated to bias different sections of the laser with different injection currents. In particular, the ring was designed to be biased separately from the straight waveguide sections. Figure 4-22(b) shows 3 single-facet lasers. The waveguides are bound by the staggered fences, but are not visible in the image. Single-facet lasers have both mirrors sharing the same facet, allowing for the cleaving and mounting of these devices to be simplified as compared to the straight Fabry-Perot ridge lasers. The layouts of the devices are shown in Appendix Section C.3. The laser layouts are functionally the same as that shown in Figure 4-2.

4.3.5 Post-processing

After the direct-write lithography step that was used to define the contact pads, buffered HF is used to remove the HSQ above the ridges as well as the native oxide

on the surface of the p-doped InGaAs contact layer. HCl is another acid often used to remove the surface oxide of InGaAs [122].

Next, a metal stack of Ti/Pt/Au, with thicknesses of 20/30/450 nm, is deposited with e-beam evaporation. The lift-off is performed with acetone at room temperature. Often, ultrasonic agitation may be needed to remove the entirety of the photoresist. The metal is annealed at 450°C for 30 s to obtain ohmic contacts for the top-side contact to p-type InGaAs. Figure 4-22 shows plan-view microscope images of a single ring resonator-coupled laser and single-facet lasers after fabrication and before cleaving.

If electroplating is required, then a seed layer of 80 nm of gold is evaporated and another direct-write lithography step is used to define the contact pad pattern above the seed layer. About 1 μm of Au is electroplated, after which the photoresist is removed in acetone and the Au seed layer is removed with Au etchant. Details of electroplating can be found in Appendix Section C.4.

After top-side metalization, the sample is then bonded upside-down to a lapping chuck using wax. Lapping is performed with a South Bay Technology Model 910 lapping tool using silicon-carbide lapping paper. The wafer is thinned from its original thickness of 340 μm down to 160 μm.

The lapping residue from the backside of the wafer is removed before the n-type contact metal of Ge/Au/Ni/Au with thicknesses of 30/60/30/200 nm is e-beam evaporated onto the backside of the wafer. Then, in another evaporation step, Ti/Pt/Au with thicknesses of 50/70/50 nm is evaporated onto the backside of the wafer and the copper mounts to which the chips will be attached after cleaving. These final metal layers are used to match the thermal coefficient of expansion (TCE) of the mount, indium solder, and substrate. TCE matching is important for device longevity. The thermal cycling of devices that are not TCE-matched can lead to fracture and delamination of the device from its mounting [141].

After backside metalization, the sample is then removed from the lapping chuck and cleaned with trichloroethylene (commonly also abbreviated as "TCE"). A 350°C rapid thermal anneal for 30 s is performed for the backside n-type contact. The

sample is cleaved using a Loomis LSD-100 scriber into individual chips. The chips are mounted on the copper mounts with indium film. A "sandwich" is made from the copper mount (bottom), the indium foil (middle), and the cleaved die (top). A probe is used to press the chip downward as the sample is heated above the melting point of indium (156.6°C). The devices are ready for testing once the assembly has cooled.

4.4 Measurement

The setup used to characterize the long-wavelength lasers in this Chapter employed the lens system from Figure 3-8. Multiple Signatone current probes and ILX current drivers were utilized as necessary.

4.4.1 Electrical Characterization

The laser diodes were electrically characterized. Figure 4-23(a) shows the IV curve of a laser diode with dimensions 1 μm $\times$ 100 μm. The laser diode can be electrically modeled as a perfect diode in series with a resistor R_d, as shown in Figure 4-23(b). R_{dA} will be used to denote the area-normalized resistance of R_d in units of $\Omega \cdot \mu m^2$. The diode equation is often written as

$$I_d = I_o \left(e^{(V_d - R_d I_d)/V_T} - 1 \right) \tag{4.5}$$

where I_d and V_d are the diode current and voltage, I_o is the reverse saturation current, R_d is the diode resistance, and $V_T = \frac{kT}{q}$ is the thermal voltage, which is 26 mV at room temperature. The diode equation can be written in the same form with current densities J_d and J_o (corresponding to I_d and I_o), and the area-normalized resistance R_{dA}.

$$J_d A = J_o A \left(e^{(V_d - (R_d A) J_d)/V_T} - 1 \right) \tag{4.6}$$

$$J_d = J_o \left(e^{(V_d - R_{dA} J_d)/V_T} - 1 \right) \tag{4.7}$$

$$\tag{4.8}$$

The laser diode whose IV characteristic in depicted in Figure 4-23(a) has a series resistance of $R_d = 156\ \Omega$ and $R_{dA} = 1.56 \times 10^{-4}\ \Omega \cdot \text{cm}^2$. Measurement of the area-independent diode characteristic allows for the electrical modeling of laser diodes with different areas. Furthermore, the value of R_{dA} gives some indication of the contact resistance of the top-side p-type ohmic contact. Knowledge about the area-normalized diode parameters further allows one to model the carrier density as a function of position for a laser that has multiple contacts where each contact may be biased at a different voltage/current level. For example, this diode model was used to quantify the carrier density in the sections of the lasers that were not directly covered by metal pads. These gaps in the metal occur in lasers that have multiple contacts and are generally 10 μm in length. The calculations indicated that the p+ doping level of the InGaAs top contact semiconductor layer was adequate for the layer to be

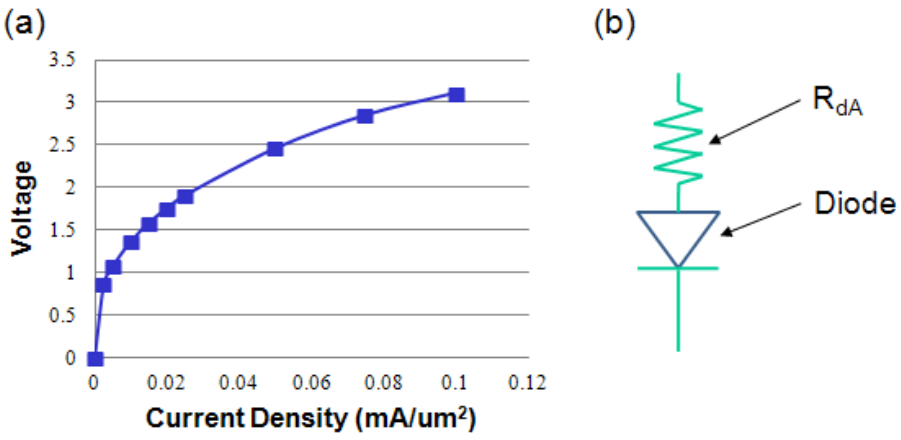

Figure 4-23: Electrical characterization of the laser diode. (a) Current-voltage characteristic of a 1 μm wide waveguide that is 100 μm long. (b) The diode can be modeled as a perfect diode in series with a resistor.

conductive enough to allow fringe currents to spread to the non-contacted waveguide regions. The current density was high enough in these regions such that absorption was not a concern.

4.4.2 Single-facet Lasers

The characterization of a 3 μm wide single-facet laser is depicted in Figure 4-24. Part (a) shows a single-facet laser without fences. Both mirrors of the ridge laser share the same facet, allowing for the cleaving and mounting of these devices to be simplified as compared to the straight Fabry-Perot ridge lasers. Figure 4-24(b) shows the IL curve of the 3-μm-wide single-facet laser operating at 1780 nm, which has a threshold current $I_{th} = 55$ mA or $J_{th} = 1900$ A/cm^2. Figure 4-24(c) shows the lasing spectrum for different values of injected current. The peak wavelength red-shifts as the injection current is increased. The tuning rate is observed to be 0.05 nm/mA. Figure 4-24(d) shows the red-shift and decrease in output power as a result of an increase in the temperature of the TE temperature controller.

One of the challenges mentioned in Section 4.2.1 associated with designing devices at long-wavelengths was estimating the refractive index of the quaternary semiconductor layers. From the emission spectrum of Figure 4-24(c), the mode spacing of the ridge laser is measured to be 0.456 nm. From Equation 4.1, the effective index of the waveguide can be calculated to be 3.62, and the refractive index of $In_{0.53}Ga_{0.32}Al_{0.15}As$, which constitutes the majority of the high index waveguide core, can be back-calculated by mode-solving to be 3.8 at $\lambda = 1780$ nm, documented in Table 4.3.

The above-threshold optical output power P of a Fabry-Perot laser can be described to be linear with the input current I, if higher-order effects, such as heating, are neglected.

$$P(I) = \frac{\hbar\omega}{q}\frac{\eta_i\alpha_m}{\alpha_i + \alpha_m}(I - I_{th}) = \frac{\hbar\omega}{q}\frac{\eta_i\frac{1}{L}\ln(\frac{1}{R})}{\alpha_i + \frac{1}{L}\ln(\frac{1}{R})}(I - I_{th}) \tag{4.9}$$

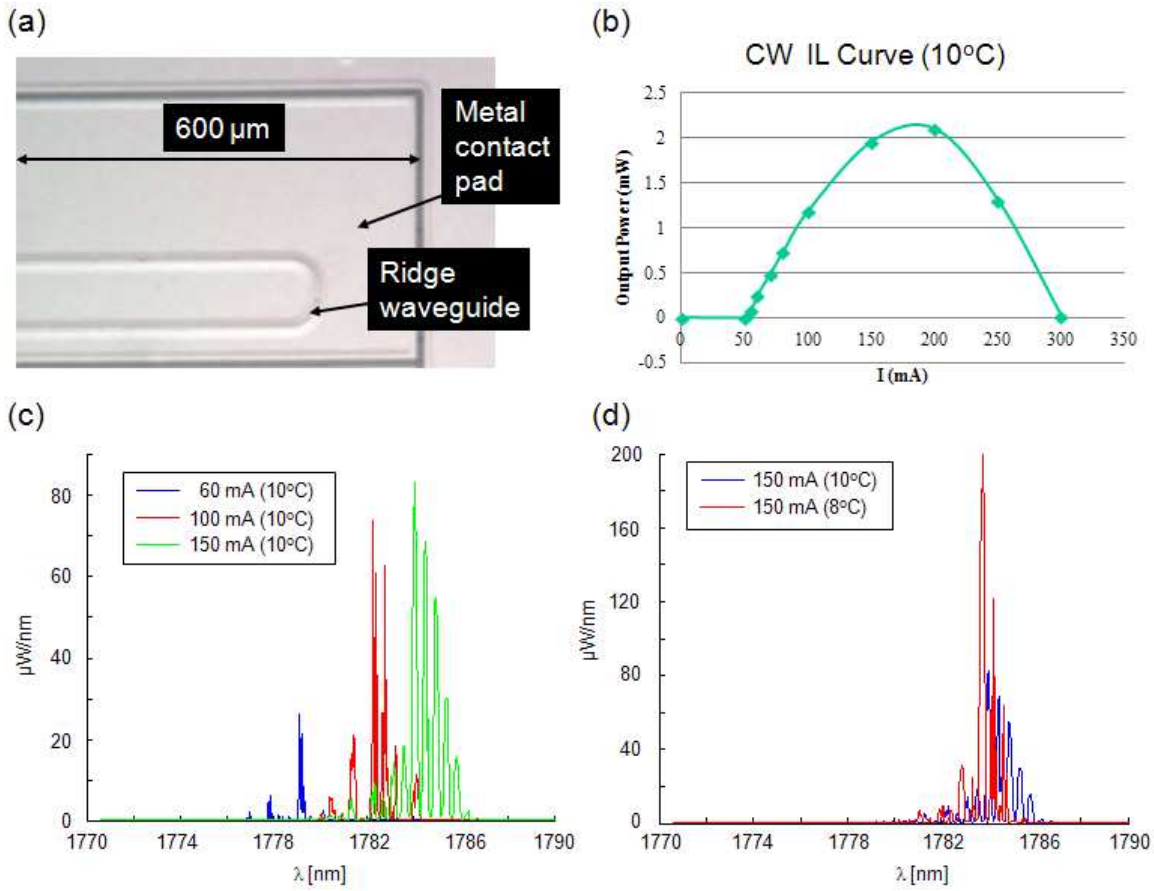

Figure 4-24: A 3 μm wide $\times$ 965 μm single-facet laser on the chip "D2A" emitting at $\approx$1.785 nm. (a) Plan-view optical microscope image of the single-facet laser. The bending radius is 40 μm. (b) IL curve of the single-facet laser at the TE cooler set temperature $T_{\mathrm{TE}} = 10°\mathrm{C}$, depicting a threshold current of 55 mA, peak power of 2.1 mW, and significant heating above 150 mA. (c) The lasing spectrum for different injection currents at $T_{\mathrm{TE}} = 10°\mathrm{C}$. For higher current levels, the wavelength is red-shifted due to heating. (d) The lasing spectrum for $I = 150$ mA with different TE cooler temperatures.

where I_{th} is the threshold current, η_i is the quantum efficiency, α_i is the waveguide loss, $\alpha_m = \frac{1}{L}\ln(\frac{1}{R})$ is the effective mirror loss, $R \approx 0.32$ is the power reflectance of the facet mirror, and L is the single-pass length of the cavity.

Figure 4-25(a) shows the IL characteristic of a 2 μm wide single-facet laser that is 1565 μm in length, operating at 10°C under CW and pulsed (0.5 μs pulses at 200 kHz) operations. The measured L-I curve under pulsed current operation of the laser does exhibit the linear characteristic described by Equation 4.9. However, under CW oper-

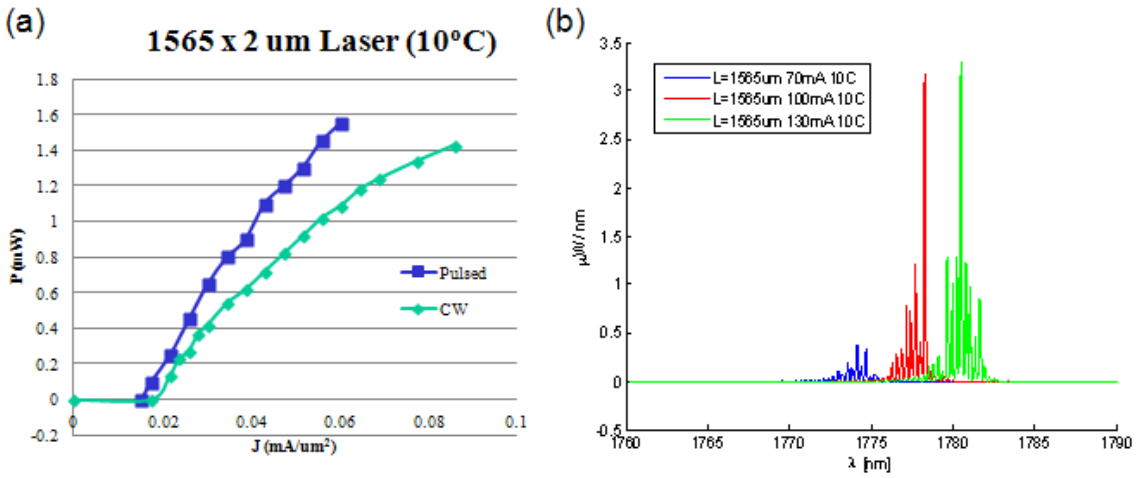

Figure 4-25: A 2 μm wide $\times$ 1565 μm single-facet laser emitting at $\approx$1.780 nm. (a) IL characteristics under CW and pulsed operation (0.5 μs pulses at 200 kHz). (b) The lasing spectrum for different levels of current injection.

ation, the laser diode self-heating causes the output power to decrease for high levels of input current [87]. The temperature affects a number of key mechanisms in laser diodes, including spreading the Fermi distribution of carriers, which decreases and red-shifts the gain peak, and increasing nonradiative recombination rates, especially the Auger coefficient. It also reduces the bandgap, which takes a part in red-shifting the output spectrum. Figure 4-25(b) shows the lasing spectrum for different levels of current injection and a tuning rate of the lasing peak of 0.1 nm/mA. The peak wavelength red-shifts as the injection current is increased. Lasing has been observed in other 2 μm wide single-facet lasers at $\lambda = 1.88$ μm and $\lambda = 1.98$ μm with the more highly strained laser materials described in Table 4.1.

The differential quantum efficiency η_d is often defined to be the slope of the L-I curve, normalized by $\frac{\hbar\omega}{q}$.

$$\eta_d = \frac{\eta_i \alpha_m}{\alpha_i + \alpha_m} = \frac{\eta_i \frac{1}{L}\ln(\frac{1}{R})}{\alpha_i + \frac{1}{L}\ln(\frac{1}{R})} \tag{4.10}$$

The differential quantum efficiency η_d of the device in Figure 4-25(a) can be calculated for the pulsed operation to be $\frac{q}{\hbar\omega}\cdot(0.011$ mW/mA). A simple manipulation of

Equation 4.10 provides:

$$\frac{1}{\eta_d} = \frac{\alpha_i}{\eta_i \ln(\frac{1}{R})} L + \frac{1}{\eta_i} \tag{4.11}$$

A typical method for determining the waveguide propagation loss α_i is to measure η_d for lasers of different length L and plot η_d^{-1} versus L. The resulting linear fit should allow for the determination of the quantum efficiency η_i from the y-intercept and then α_i from the slope.

For the single-facet lasers there are waveguide bending losses, which can be incorporated into Equation 4.10 if an effective bending loss α_b is defined, similar to the mirror loss

$$\alpha_b = \frac{1}{L} \ln(\frac{1}{T_b}) \tag{4.12}$$

$$\tag{4.13}$$

where T_b is the power transmission at the waveguide bends for a single pass through the cavity. Then Equation 4.10 becomes

$$\eta_d = \frac{\eta_i \alpha_m}{\alpha_i + \alpha_m + \alpha_b} = \frac{\eta_i \frac{1}{L} \ln(\frac{1}{R})}{\alpha_i + \frac{1}{L} \ln(\frac{1}{R}) + \frac{1}{L} \ln(\frac{1}{T_b})} \tag{4.14}$$

However, plotting η_d^{-1} versus L will not be as helpful in this case to determine η_i and α_i, as illustrated by Equation 4.15. Bending losses are best characterized using passive waveguide measurements of devices with different numbers of bends.

$$\frac{1}{\eta_d} = \frac{\alpha_i}{\eta_i \ln(\frac{1}{R})} L + \frac{1}{\eta_i} \left(1 + \frac{\ln(\frac{1}{R})}{\ln(\frac{1}{T_b})} \right) \tag{4.15}$$

Multiple attempts to graph $1/\eta_d$ versus L for the single-facet lasers resulted in

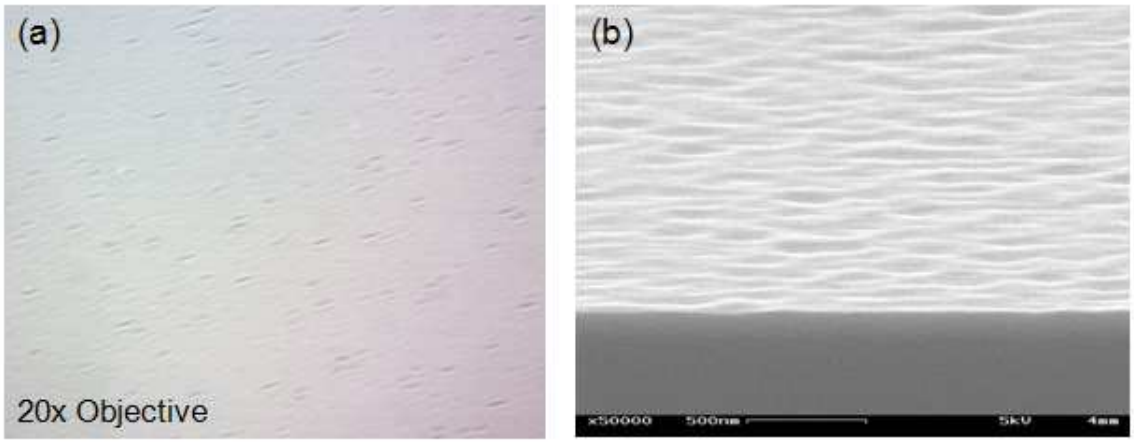

Figure 4-26: The surface topology of the VA159 wafer, a strained InGaAs laser heterostructure. (a) A plan-view optical microscope image taken with a 20 x objective lens. (b) The side-view SEM image shows that the roughness on the surface is directional.

nonlinear plots, which indicated that there was a significant amount of variation between the fabricated devices. By assuming that the injection efficiency η_i is in the range of 10%–90%, a corresponding range for the propagation loss α_i can be calculated from η_d. The propagation losses α_i for the various single-facet lasers were observed to be in the regime of 100s of dB/cm. This high loss is most likely due to crystal defects in the p-type cladding layers due to non-optimized epitaxial growth conditions, or non-optimized crystal quality in the active region. The broad FWHM in the PL emission shown in Figure 3-5 indicates structural imperfections may be present in the active region [20]. The single and double ring resonator-coupled lasers exhibited output powers on the order of tens of μW that were too low to successfully couple into the OSA for spectral analysis. Figure 4-26 shows the surface of one of the strained InGaAs wafers before fabrication and is representative of the other strained InGaAs growths. The non-optimized growth of the semiconductor layers is manifested in the surface topology of the wafer.

4.5 Conclusion

Tunable diode laser absorption spectroscopy (TDLAS) is a suitable method for portable low-cost trace gas analysis [133]. Leak detection, chemical process control, and atmospheric pollutant sensing are all applications made viable by advancements in trace gas detection with semiconductor and solid-state lasers [113, 128]. Trace gas sensing also has applications in medicine, including very sensitive and time-resolved exhaled breath monitoring [76].

In this chapter, the design, modeling, and fabrication of long-wavelength single-facet and ring resonator-coupled tunable lasers were presented. Utilizing the Vernier effect, the double ring resonator-coupled lasers are simulated to be able to achieve a 40 nm tuning range through carrier injection. The challenges associated with fabricating the ring resonator-coupled lasers were investigated, and the single ring and double ring resonator-coupled lasers were fabricated using mask-less lithography methods. Single-facet Fabry-Perot ridge lasers were also fabricated and characterized. A tuning rate of 0.1 nm/mA was demonstrated in these devices.

The propagation losses α_i for the various single-facet lasers were observed to be in the regime of 100s of dB/cm. This high loss is most likely due to crystal defects in the p-type cladding layers due to non-optimized epitaxial growth conditions, or non-optimized crystal quality in the active region. The broad FWHM in the PL emission shown in Figure 3-5 indicates structural imperfections may be present in the active region [20]. The single and double ring resonator-coupled lasers exhibited output powers on the order of tens of μW that were too low to successfully couple into the OSA for spectral analysis.

Future work includes the characterization of single ring and double ring resonator-coupled lasers. The integration of a chip-based TDLAS system is also desired, and will require the development of a detector and hybrid integration of a gas-handling system. Furthermore, to access the absorption lines from 2 μm to 5 μm, the GaSb material system, which will be discussed in Chapter 5, can be employed.

Chapter 5

Future Work

III-V photonics is an exciting field of study because there are so many directions to explore. In the previous chapters, various devices were investigated, each based on different waveguide building blocks. All of the devices were fabricated in the InP material system. A natural extension of this work includes the exploration of new III-V materials and new waveguide structures. In this chapter, the antimonide material system and waveguide-based vertical couplers are presented as potential research avenues.

5.1 Antimonide-based Long-wavelength Materials

In Chapters 3 and 4, laser sources ranging from 1.55 μm (the primary telecommunications wavelength) to 2 μm were explored. As discussed, there are many useful applications for wavelengths beyond 2 μm. For example, the absorption lines of several important trace gases (CH_4, CO_2, CO, HCl) are situated in the spectral region spanning from 2 to 4 μm [53]. However, due to issues related to lattice mismatch, the InP material system cannot provide sources with operating wavelengths far beyond 2 μm.

The GaSb material system is suitable for emission wavelengths between 2–5 μm. Antimony-based III-V lasers are commonly categorized by their energy band alignments: Type I, Type II, or Type III (broken type II) [20]. Lasers with Type I band

offsets are most common in the 2 to 3 μm region, especially for InGaAsSb/AlGaAsSb strained quantum well lasers that are commonly used in TDLAS [46, 58]. Some of the advantages of Type I band alignment include: (1) the improved carrier confinement, (2) the convenient tuning of the operating wavelength by altering QW dimensions, and (3) the lower threshold current due to decreased in-plane heavy hole effective mass as a result of compressive strain. On the longer-wavelength end of the spectrum, the larger Auger coefficient in Type I lasers has proved to be a problematic barrier. For some time, the longest wavelength achieved for CW lasing at room temperature was 3.04 μm [59]. Very recently, a CW lasing wavelength of 3.7 μm was achieved at room-temperature [134]. Using the so-called "W" band line-up heterostructure that exhibits lower Auger recombination rates, wavelengths in the range of 3–5 μm have been achieved [48, 12]. One of the longest emission wavelengths reported thus far under CW and room-temperature operation is a single stage "W" laser emitting at 4.02 μm [12].

5.1.1 Heterostructure Growth and Modeling

To take a first step into developing Sb-based lasers, the Type I heterostructure that is shown in Figure 5-1(a) was grown with solid-source molecular beam epitaxy (MBE). Figure 5-1(b) depicts the photoluminescence (PL) spectrum with a gain peak at 1.8 μm. The heterostructure that is used for the PL measurement has a thinner upper $Al_{0.8}Ga_{0.2}As_{0.07}Sb_{0.93}$ cladding layer and a thinner GaSb contact layer than shown in Figure 5-1(a), to minimize the absorption of the pump light in these large-bandgap layers.

One of the issues with designing photonic devices at long wavelengths is the dearth of published refractive index data that is needed for optical modeling. A good first step would be to fabricate simple single-facet lasers to determine more accurately the refractive indices of the III-V layers at the operating wavelength. Figure 5-2 shows the refractive indices for $Al_xGa_{1-x}As_ySb_{1-y}$ at $\lambda = 1.8$ μm as a function of x, using a few different interpolation methods.

Using Figure 5-2, optical modeling indicates that for waveguides etched deeper

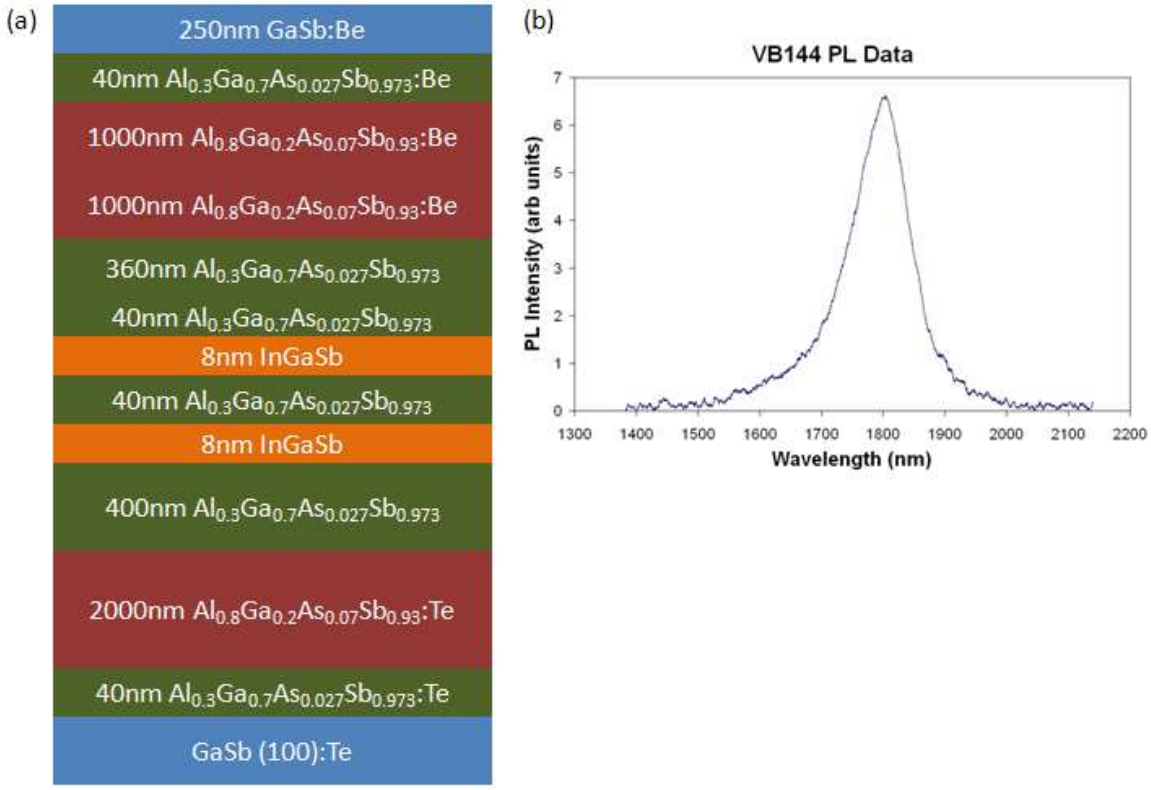

Figure 5-1: An antimonide-based quantum well laser heterostructure that was grown by MBE. (a) The detailed epitaxial heterostructure. (b) Photoluminescence spectrum from the quantum well structure, which shows a gain peak at 1.8 μm. The heterostructure that is used for the PL measurement has a thinner upper $Al_{0.8}Ga_{0.2}As_{0.07}Sb_{0.93}$ cladding layer and a thinner GaSb contact layer than shown in part (a), to minimize the absorption of the pump light in these large-bandgap layers.

than the location of the high-index core, single-mode operation will occur for waveguide widths ≤ 1 μm. At a width of 1 μm, the effective index n_{eff} of the waveguide is modeled to be 3.4. The laser structures in Chapter 4 can be adapted to the GaSb material system with the modification of n_{eff}. The fabrication process can also be adapted with slight modifications, such as changes in the ICP reactive ion etch and the e-beam lithography dose. The requisite e-beam dose for a GaSb substrate is given in Appendix Section C.4.

Early experiments with etching GaSb bulk substrates indicated that high anisotropy can be achieved with the $Cl_2/SiCl_4/Ar$ etch chemistry at a plate temperature of 100°C and a pressure of 0.4 Pa, with $P_{\mathrm{ICP}} = 100$ W and $P_{\mathrm{Bias}} = 50$ W. A negligible amount

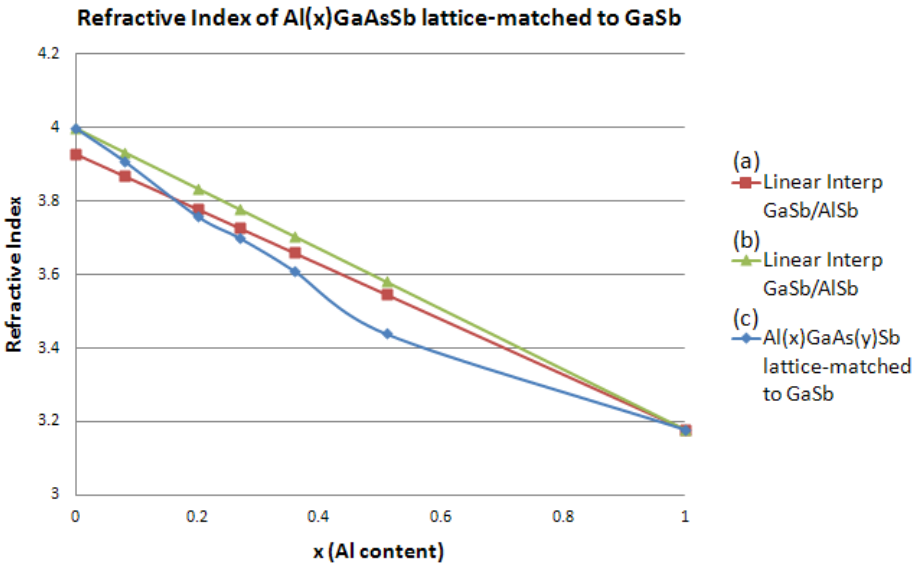

Figure 5-2: The refractive index of AlGaAsSb lattice-matched to GaSb and AlGaSb as a function of Al content. (a) Linear interpolation of GaSb and AlSb [75]. (b) Another linear interpolation of GaSb and AlSb [5]. (c) AlGaAsSb lattice-matched to GaSb [5].

of surface roughness was observed for gas flow rates of 0.5–5 sccm for Cl_2, 10 sccm for $SiCl_4$, and 50 sccm for Ar. The etch rate ranged from 1.7–2.1 μm/min, varying linearly with the Cl_2 flow rate. Figure 5-3 shows the profile of various GaSb etching using the ICP RIE.

The laser structure shown in Figure 5-1(a) contains GaSb as well as AlGaAsSb layers. If the etch shown in Figure 5-3 (etching bulk GaSb) is used to etch the laser structure, a difference in etch rate between the GaSb and AlGaAsSb layers is observed, contributing to a rough sidewall (see Figure 5-4(a)). As shown in Figure 5-4(b), increasing the anisotrophy of the etch by increasing the bias power P_{Bias} forces the GaSb and AlGaAsSb layers to etch at more similar rates, resulting in a smoother sidewall. (The sample etched in Figure 5-4 is a PL heterostructure and not the real laser heterostructure.)

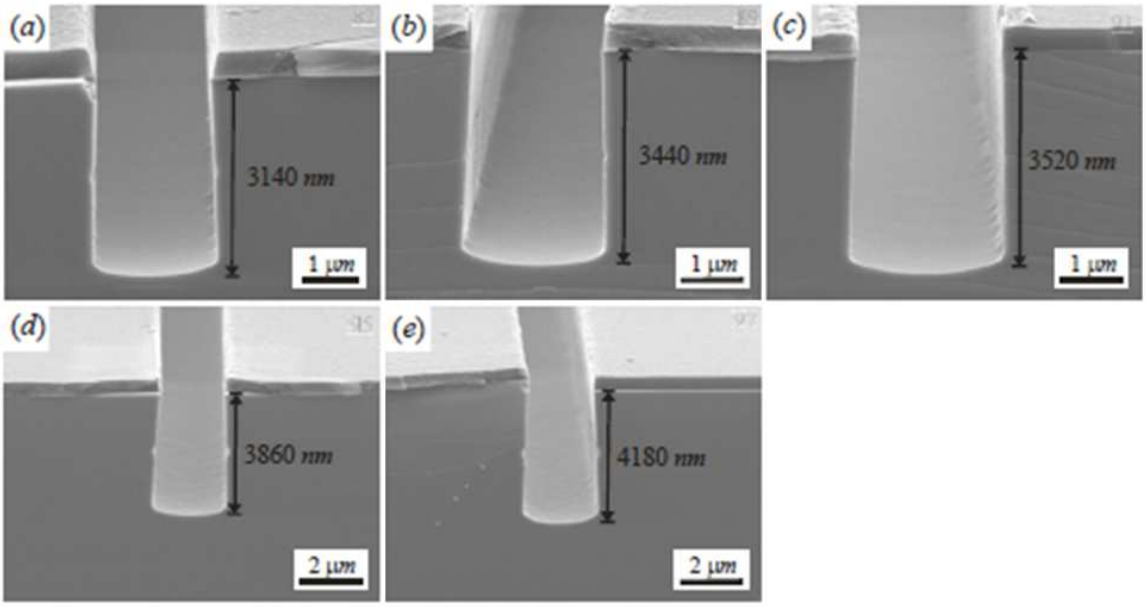

Figure 5-3: SEM images of GaSb(001) etched using ICP RIE with $Cl_2/SiCl_4/Ar$ chemistry at 100°C, a pressure of 0.4 Pa, with $P_{ICP} = 100$ W and $P_{Bias} = 50$ W. An SiO_2 hardmask was used. Gas flow was 10 sccm for $SiCl_4$, 50 sccm for Ar, and (a) 0 sccm, (b) 0.5 sccm, (c) 1 sccm, (d) 3 sccm, (e) 5 sccm for Cl_2 [4].

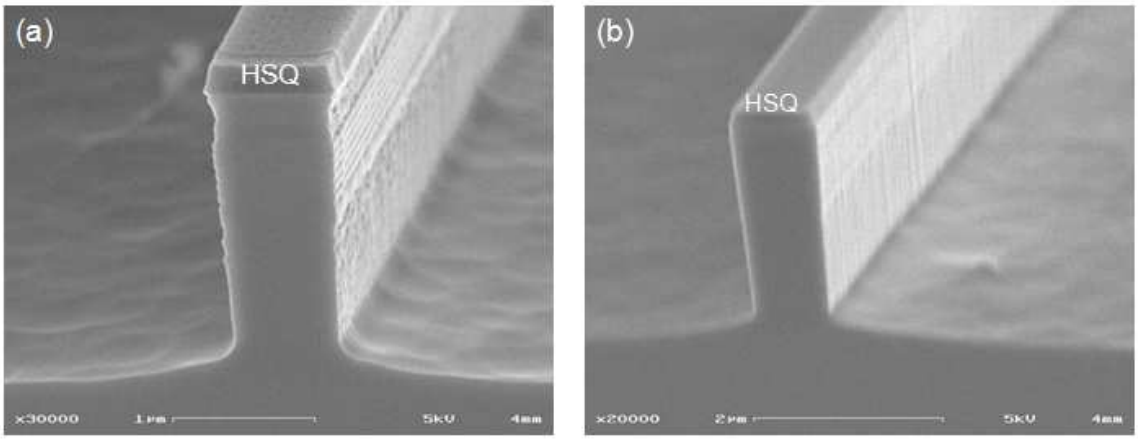

Figure 5-4: SEM images of GaSb-based VB145 PL structure etched by ICP RIE. The temperature was 100°C, the pressure was 0.4 Pa, and P_{ICP} was 100 W. Gas flow was 10 sccm for $SiCl_4$, 50 sccm for Ar, and 0.5 sccm for Cl_2. (a) When P_{Bias} is set to 50 W as in Figure 5-3, scalloping is seen on the sidewall due to the difference in etch rate between the GaSb and the AlGaAsSb. (b) By increasing P_{Bias} to 80 W, the etch is made to be more anisotropic and less chemical, forcing the GaSb and AlGaAsSb layers to etch at more similar rates, which creates a smoother sidewall.

5.2 Vertical Coupling

5.2.1 Asymmetric Twin Waveguides in Long-wavelength Lasers

The asymmetric twin waveguide (ATW) technique that was described in Section 2.4 can be incorporated into the design of the long-wavelength double ring resonator-coupled lasers. The tunable lasers that are discussed in this thesis have consisted completely of active material. Fabricating the racetracks as passive waveguides would allow for better decoupling of the tuning elements and the gain elements in the laser structure. Furthermore, higher levels of integration can be achieved with passive waveguides because they allow for signals to be routed to different areas of a chip. In the ATW scheme, the passive material is epitaxially grown first, followed by the active material, which is grown above the passive material.

Leveraging the knowledge of the ATW structure that was developed in this thesis, a tunable laser can be designed as depicted in Figure 5-5, where the laser modes are coupled upward to a semiconductor optical amplifier (SOA) for gain, and then coupled downward to the passive waveguides and racetracks for filtering. In Figure 5-5, the black waveguides are passive waveguides situated in the lower waveguide plane, while the grey waveguides are active waveguides that are located in the upper waveguide plane, similar to the all-optical logic chip in Chapter 2. Racetrack tuning could be achieved by using heaters that are situated above the racetracks, or by employing the electro-optic effect with a DC bias voltage applied across the waveguide. If carrier injection is desired for tuning, the racetracks can be fabricated as active waveguides as well. In either design, the laser light could be tapped out at a passive waveguide region to be routed to a different area of the chip, perhaps with the use of an integrated isolator.

5.2.2 Vertical Grating Couplers

In this thesis, most of the design choices were made based on device functionality, with only slight modifications to the designs based on fabrication issues. Even less

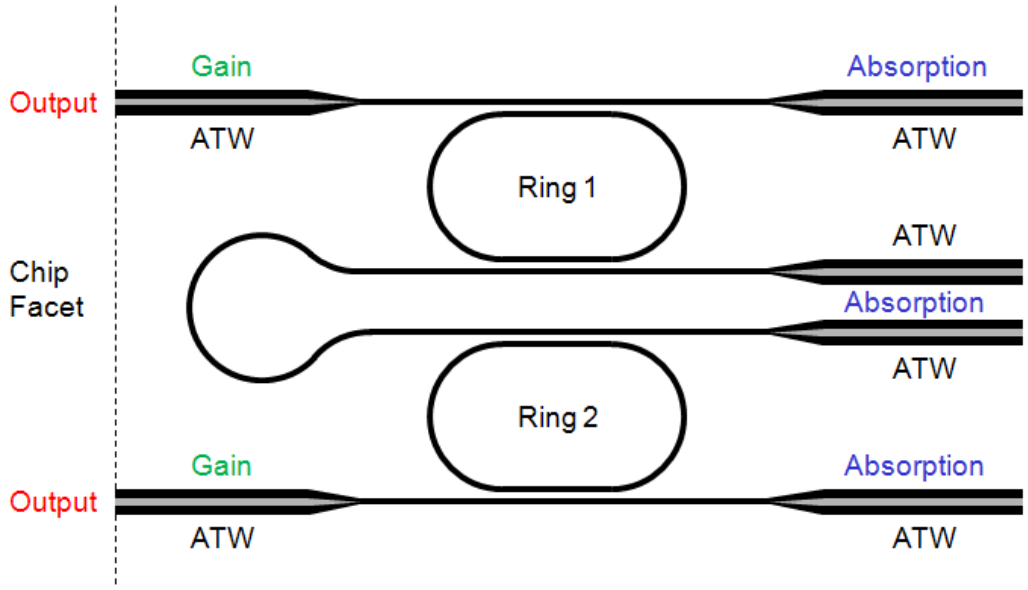

Figure 5-5: A design of the double ring resonator-coupled laser employing asymmetric twin waveguides (ATWs). The black waveguides are passive waveguides residing on the lower waveguide plane, while the grey waveguides are active waveguides located on the upper waveguide plane.

consideration in the design was made for the characterization of the devices. From the point of view of materials and device research, this prioritization makes sense. However, there are some structures that can be incorporated into the device design that can considerably steamline the fabrication and testing processes. One of these is the vertical grating coupler that has been developed by researchers to provide efficient coupling of light from a horizontal waveguide to a fiber oriented above the plane of the sample [124].

A side-view schematic of the grating coupler is shown in Figure 5-6. The output coupling angle θ is generally designed to be close to 10° to avoid the unwanted second order reflection of the light from the grating back into the waveguide. Several parameters need to be designed and modeled, including the grating period, fill factor, and etch depth. A cladding layer is typically used above the grating to increase the upward coupling efficiency [125]. For better mode-matching to the fiber, the mode is expanded horizontally in the direction orthogonal to the plane of the paper in Figure 5-6. Adiabatic tapers as well as MMI-based spot-size converters have been employed

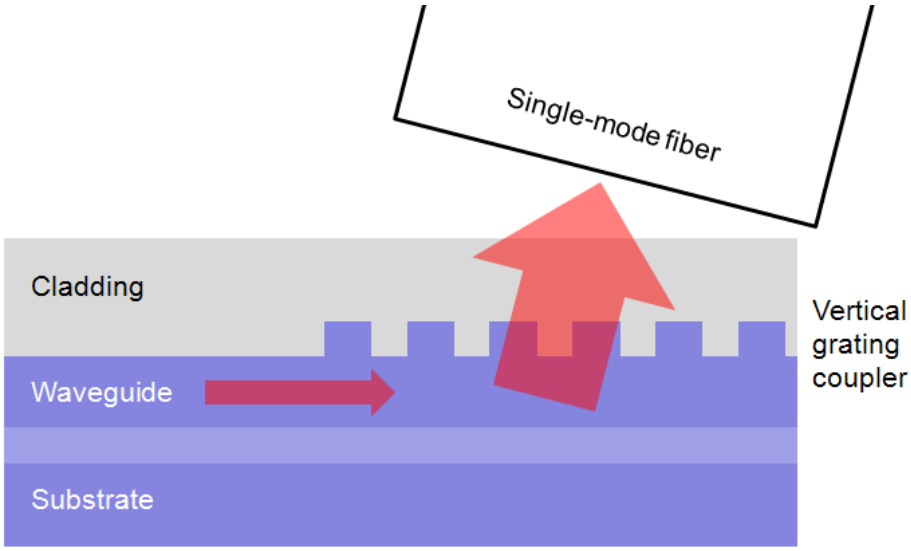

Figure 5-6: Side-view schematic of a vertical grating coupler. The optical mode propagating from the waveguide is coupled upward into the single-mode fiber. The mode is expanded in the horizontal direction orthogonal to the plane of the paper via a waveguide spot-size converter.

for this purpose [14]. Coupling efficiencies of 30% are typical for grating couplers that are designed in silicon-on-insulator [125]. Due to the smaller vertical index contrast available in the InP material system, the design of high-efficiency vertical grating couplers may be more challenging. InP-based membrane vertical couplers have been fabricated with 47% coupling efficiency [132].

Incorporating vertical couplers into the laser structure would require the construction of a new testing setup to accommodate the vertical orientation of output light. However, with vertical couplers, the dies would not need to be cleaved to have optical-quality facets, and so the time consuming procedures of wafer thinning, scribing/cleaving, and mounting extremely fragile samples can be potentially eliminated (lapping the wafer does also provide benefits for heat dissipation and electrical resistance, however). Figure 5-7 shows the design of a double ring resonator-coupled laser in which the cavity is made to turn in on itself rather than having the mirror facets. A vertical coupler is used to couple light upward, so no cleaving would be required at all. Vertical couplers would also allow for in-line testing of optical components. Without having to complete the fabrication process, metrology can be used to help

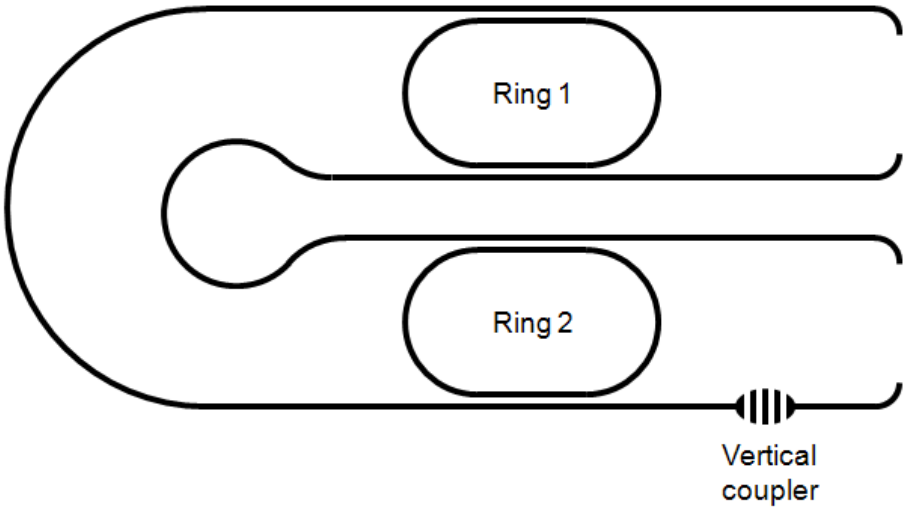

Figure 5-7: Schematic of a double ring resonator-coupled laser that employs vertical couplers fabricated entirely in active material and does not require cleaving. After metalization, the chip can be moved to testing without the need for lapping and cleaving.

estimate the final performance of the device if vertical couplers are present [83].

5.3 Conclusions

A natural extension of the work that was presented in this thesis includes the exploration of new III-V materials and new waveguide structures. In this chapter, the GaSb material system and waveguide-based vertical couplers were presented as potential research avenues. Future work can also include longer-term initiatives such as the construction of a tunable diode laser absorption spectroscopy (TDLAS) system for trace gas sensing, which will require expertise from areas beyond materials and devices. A good start would include research into the optimization of the manufacturing process for yield, specifically in terms of the packaging of the devices. Furthermore, certain TDLAS applications require lasers with high operational temperature and low threshold current. In Chapter 4, these specifications were not directly incorporated into the laser design, but can be considered in the future for the appropriate application. The author, as an engineer, hopes that the research included here will be used

as a basis for the future development of real-world systems that pushes the forefront of human technology.

Appendix A

Modeling Techniques Used in this Thesis

A.1 Beam Propagation Method

The Beam Propagation Method (BPM) is a useful technique for simulating waveguide propagation and calculating waveguide modes. BPM is an iterative solution based on a simplified form of the scalar Helmholtz Equation for electromagnetic wave propagation [29]. The simplification that is applied is known as the paraxial approximation and breaks down for large propagation angles, which are measured from the main axis of propagation (usually denoted as the z axis).

The Helmholtz equation is given by

$$\left[\nabla^2_{x,y,z} + k(x,y,z)^2\right] E(x,y,z)e^{j\omega t} = 0 \tag{A.1}$$

where $k(x,y,z) = k_0 n(x,y,z)$ is the spatially-dependent wave vector due to a spatially-dependent index of refraction distribution.

The spatial component of the electric field can be written as the product of a slowly varying field u and a rapidly varying oscillation in the z axis (axis of propagation) with propagation constant β.

$$E(x, y, z) = u(x, y, z)e^{-j\beta z} \tag{A.2}$$

Plugging in the form of E in Equation A.2, we obtain from Equation A.1,

$$\left[\nabla^2_{x,y,z} - 2j\beta\frac{\partial u}{\partial z} + (k^2 - \beta^2)\right] u = 0 \tag{A.3}$$

Notice that this differential equation has a second derivative in the propagation direction z, making it difficult to solve. The paraxial or parabolic approximation, also known as the slowly-varying envelope approximation, helps to simplify equation A.3 by considering the case where u varies slowly with respect to z, such that $\frac{\partial u}{\partial z} \gg \frac{\partial^2 u}{\partial z^2}$. After the paraxial approximation is applied, Equation A.3 becomes

$$\left[\nabla^2_{x,y} - 2j\beta\frac{\partial u}{\partial z} + (k^2 - \beta^2)\right] u = 0 \tag{A.4}$$

$$-\frac{j}{2\beta}\left[\nabla^2_{x,y} + (k^2 - \beta^2)\right] u = \frac{\partial u}{\partial z} \tag{A.5}$$

Notice the absence of the z component in the ∇^2 operator. Equation A.5 is the basis for BPM. There are two general methods for solving Equation A.5: (1) the Fourier transform method, and (2) the finite difference method [101].

A.1.1 Fourier Transform BPM

The Fourier transform BPM, also called split-step BPM, breaks down the iterative solution of u into two steps. In the first step, the Fourier transform of u is propagated in the spatial frequency domain a distance dz, with the approximation that the index distribution is a constant in space. An average value of refractive index, $\bar{n}$, is commonly used for the approximation. In the second step, the nonuniformity of $n(x, y, z)$ is applied by "correcting" for the phase of u in the spatial domain. The conversion

between the spatial domain and the spatial frequency domain is easily achieved via the fast Fourier transform (FFT).

To illustrate the intuition of the Fourier transform BPM technique, the author has provided a split-step BPM routine in Matlab below. Because of the approximation errors of Fourier transform BPM, similar methods that yield more accurate results, such as the wave propagation method, have been developed, but are not widely utilized [15].

```
%Set simulation domain
X=200e-6; dx=X/1000; x=-X/2:dx:X/2-dx; Fx=1/dx; dfx=1/X;
kx=2*pi*(-Fx/2:dfx:Fx/2-dfx);
Z=400e-6; dz=Z/10; z=0:dz:Z;

%Set initial conditions
lambda=1.55e-6; k0=2*pi/lambda;
u4{1}=exp(-(x/10e-6).^2);       %Gaussian wavefront

%Can change this section to more complicated index distributions
n_bar=1; dn=zeros(1,length(x));          %Free space propagation
prop_const = exp(-i*( (1/(2*n_bar*k0))*(kx.^2) )*dz);

%Propagate in z using FFT BPM
for m=1:length(z),
    u1 = prop_const .* fftshift(fft(fftshift(u4{m})));
    u4{m+1} = exp(+i*k0*dn*dz) .* fftshift(ifft(fftshift(u1)));
end
```

A.1.2 Finite Difference BPM

The other way to solve Equation A.5 is the finite difference BPM, which has been shown to yield more accurate and faster results than the Fourier-transform BPM

[101]. The finite difference BPM relies on a discretization of Equation A.5

$$\frac{u_i^{m+1} - u_i^m}{dz} = \frac{i}{2k_0\bar{n}} \left(\frac{\partial^2}{dx^2} + (k^2 - (k_0\bar{n})^2) \right) \frac{u_i^{m+1} + u_i^m}{2} \tag{A.6}$$

where i denotes the grid point in x, m denotes the grid plane in z, and ∂^2 is the second order difference operator, $\partial^2 u_i = u_{i+1} + u_{i-1} - 2u_i$. Equation A.6 can be rearranged into the form of a standard tridiagonal matrix equation that can be solved efficiently [101]. Though less intuitive, the BPM solver that is used to make the calculations in this thesis employ the finite difference method due to its increased speed and accuracy. Improvements to the finite difference BPM technique include vectoral BPM, bi-directional BPM, and wide-angle BPM [40, 93, 34].

A.1.3 Mode Solving with BPM

A useful analytical method for understanding the behavior of light inside a waveguide is mode theory. The modes of a waveguide form an orthogonal basis for any optical excitation in the waveguide. That is to say, any optical excitation within a waveguide can be decomposed into a weighted sum of the modes of the waveguide. Some of these modes may be guided and some may be unguided. Most often, the modes of interest are the guided modes. The propagation of an optical field in a waveguide can be expressed by

$$u(z) = \sum_p c_p \phi_p e^{-j\beta_p z} \tag{A.7}$$

where ϕ_p is the field distribution of the p-th mode, β_p is the propagation constant of the p-th mode, and c_p is the weight of the p-th mode in the construction of u.

One of the most useful features of BPM is the capability of solving for the modes of an arbitrary waveguide, and there are several ways to do it. The most straightforward method is to simply propagate light down a waveguide. For example, if the

waveguide of interest supports either one or two modes, then launching an arbitrary field excitation that is symmetric will yield the fundamental mode after a sufficient propagation distance, because the first excited mode is anti-symmetric and the higher order modes are unguided. An arbitrary field excitation that is not symmetric, with its fundamental mode contribution removed by an orthogonalization, can be launched to obtain the first excited mode.

There are faster approaches to mode solving that are not limited to solving for one or two modes, including the (1) the correlation method, and (2) the imaginary distance BPM. The correlation method calculates the correlation $C(z)$ between the input field and the propagating field.

$$\begin{aligned} C(z) &= \int u^*(0)u(z)dx && \text{(A.8)} \\ &= \int \left(\sum_c c_p^* \phi_p^*\right)\left(\sum_c c_p \phi_p e^{-j\beta_p z}\right) dx && \text{(A.9)} \\ &= \sum_c |c_p|^2 e^{-j\beta_p z} && \text{(A.10)} \end{aligned}$$

The Fourier transform of $C(z)$ will peak at every value of β_p for which a mode exists. Once the values of the propagation constants β_p are known, the modes can be solved via

$$\phi_m = \frac{1}{L}\int_0^L u(z)e^{-j\beta_p z} \qquad \text{(A.11)}$$

The imaginary distance BPM works as if the light is propagating through imaginary space. Replacing z with $z' = jz$ in Equation A.7, the complex exponential becomes an exponential growth term. By launching an arbitrary field excitation into the waveguide, the lowest order mode (which has the largest β) will grow the fastest, quickly dominating the field distribution in the waveguide. An orthogonalization method can be used to remove the mode from the launch field, and the process can

be repeated to calculate the higher-order modes.

A.2 Coupled-mode Analysis

Couple-mode theory is a useful method for understanding the behavior of a system of waveguides. For simplicity, the analysis in this section will be performed for single-mode waveguides. Every mode of a waveguide has a different propagation constant β, hence single-mode waveguides are often desired to avoid the effects of beating between multiple modes that can cause the guided light to "bounce" around as it propagates. Any light that is coupled into a single-mode waveguide can be decomposed into a weighted sum of the one guided mode with many unguided modes. After a sufficient propagation distance, the light inside the waveguide will consist only of the one guided mode.

A.2.1 Directional Couplers

Figure A-1 shows two single-mode waveguides situated next to each other. If they are brought close to each other, the fields of the mode in one waveguide will begin to overlap with the other waveguide. In fact, the light that is launched into Waveguide 1 will be coupled into Waveguide 2. The distance required to couple light from one waveguide to the other is called L_π. One way to think about the phenomenon is to realize that as the two waveguides are brought into proximity, they can no longer be analyzed separately from each other. Together, they form a "super" waveguide. This "super" waveguide has two so-called "super" modes–a symmetric and an anti-symmetric supermode. Launching light only into Waveguide 1 will excite both supermodes, and hence the light "bounces" between the two waveguides with a beat length L_π that is dependent on the difference in the β of the supermodes. This structure is often called a directional coupler.

Consider the fundamental modes of Waveguide 1 and Waveguide 2, which will have excitation amplitudes E_1 and E_2, respectively. As they propagate, each mode not only undergoes a phase shift, but is also gradually coupled into the other mode.

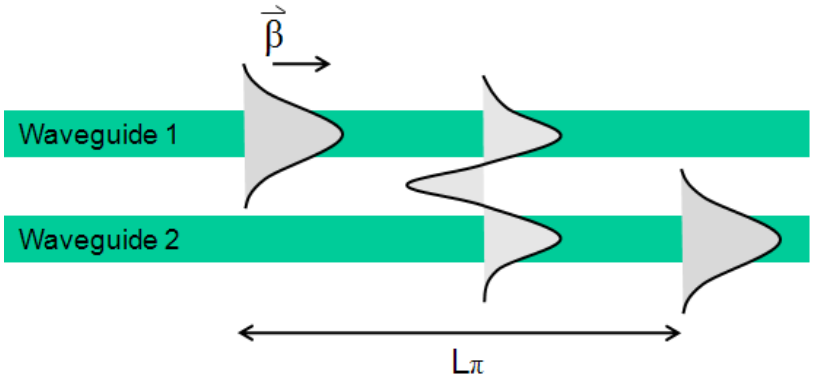

Figure A-1: Two single-mode waveguides brought into proximity, such that the light is coupled between them. Light that is launched into Waveguide 1 is completely coupled to Waveguide 2 after a propagation distance of L_π.

This can be represented by

$$\frac{dE_1(z)}{dz} = -j\beta_1 E_1(z) - jc_{12}E_2(z) \tag{A.12}$$

$$\frac{dE_2(z)}{dz} = -j\beta_2 E_2(z) - jc_{21}E_1(z) \tag{A.13}$$

where c_{12} and c_{21} are the coupling constants, which are dependent on the waveguide properties. If the two waveguides are identical, then $|c_{12}| = |c_{21}|$ and $\beta_1 = \beta_2$, but in reality this is rarely the case. Conventionally, two variables are defined to describe this discrepancy.

$$\beta_0 = \frac{\beta_1 + \beta_2}{2} \tag{A.14}$$

$$\Delta\beta = \frac{\beta_1 - \beta_2}{2} \tag{A.15}$$

such that $\beta_{1/2} = \beta_0 \pm \Delta\beta$. Now, the slowly varying relative field amplitudes $\tilde{E}_1$ and $\tilde{E}_2$ are introduced,

$$\tilde{E}_1(z) = E_1(z)e^{j\beta_0 z} \quad (A.16)$$

$$\tilde{E}_2(z) = E_2(z)e^{j\beta_0 z} \quad (A.17)$$

which obey the following set of equations, modified from Equations A.12 and A.13:

$$\frac{d\tilde{E}_1(z)}{dz} = -j\Delta\beta\tilde{E}_1(z) - jc_{12}\tilde{E}_2(z) \quad (A.18)$$

$$\frac{d\tilde{E}_2(z)}{dz} = j\Delta\beta\tilde{E}_2(z) - jc_{21}\tilde{E}_1(z) \quad (A.19)$$

Additionally, the power conservation constraint requires that

$$\frac{d}{dz}(|\tilde{E}_1(z)|^2 + |\tilde{E}_1(z)|^2) = 0 \quad (A.20)$$

which means that $c_{12} = c_{21}*$.

Without loss of generality, assume that at $z = 0$, the fundamental mode is launched into Waveguide 1. That is,

$$\tilde{E}_1(0) \neq 0 \quad (A.21)$$

$$\tilde{E}_2(0) = 0 \quad (A.22)$$

Solving for $\tilde{E}_1(z)$ and $\tilde{E}_2(z)$ gives

$$\tilde{E}_1(z) = \tilde{E}_1(0)\left(\cos(\gamma z) - j\frac{\Delta\beta}{\gamma}\sin(\gamma z)\right) \quad (A.23)$$

$$\tilde{E}_2(z) = -j\tilde{E}_1(0)\frac{\kappa_{21}}{\gamma}\sin(\gamma z) \quad (A.24)$$

where $\gamma = \sqrt{\Delta\beta^2 + |c_{12}|^2}$.

The optical power $P(z)$ is proportional to the magnitude squared of the electric field, so

$$P_1(z) = P_1(0)\left(\cos^2(\gamma z) + \left(\frac{\Delta\beta}{\gamma}\right)^2 \sin^2(\gamma z)\right) \quad \text{(A.25)}$$

$$P_2(z) = -jP_1(0)\left(\frac{|c_{21}|}{\gamma}\right)^2 \sin^2(\gamma z) \quad \text{(A.26)}$$

If the waveguides are identical, i.e. $\Delta\beta = 0$, then Equations A.25 and A.26 would take on the form

$$P_1(z) = P_1(0)\cos^2(\gamma z) \quad \text{(A.27)}$$

$$P_2(z) = P_1(0)\sin^2(\gamma z) \quad \text{(A.28)}$$

If the waveguides are identical, the coupling length z can be set to obtain anywhere between 0% and 100% power coupling between the waveguides. To obtain 100% power transmission from Waveguide 1 to Waveguide 2, a length of $z = L_\pi = \frac{\pi}{2|c_{12}|}$ is required.

A.2.2 Waveguide-coupled Ring Resonators

The situation is made more interesting if Waveguide 2 loops back onto itself, forming a ring or racetrack, such as the one shown in Figure A-2. In this situation, the power coupled into Waveguide 2 (now a ring/racetrack) comes back around and is coupled back into itself and Waveguide 1, continuing until a steady state is reached. Consider the configuration of Figure A-2, in which two straight waveguides are coupled to a single racetrack. The excitation amplitudes of the inputs and outputs, along with amplitude transmission coefficient t and amplitude coupling coefficient κ of the directional couplers are given. The coefficients t and κ are lumped quantities that describe the entire directional coupler and can be calculated via the coupled-mode theory ex-

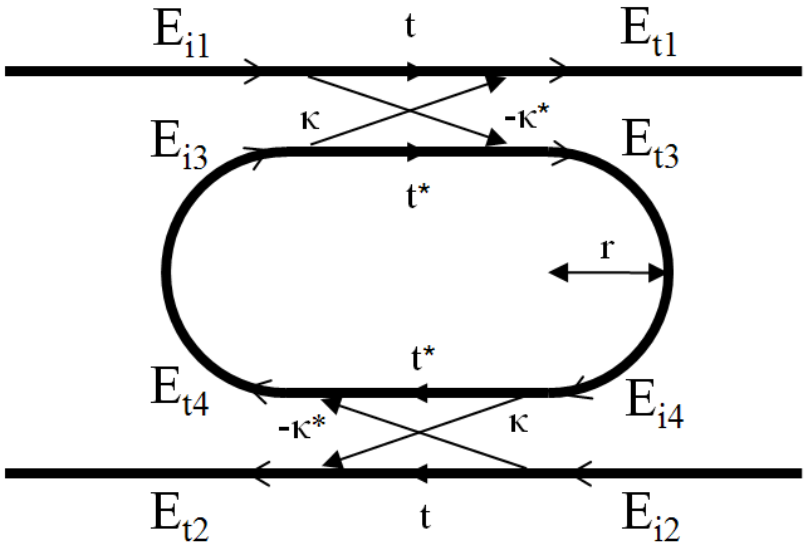

Figure A-2: A coupled system of a racetrack and two waveguides. The straight sections of the racetrack are directional couplers that have amplitude transmission coefficients t and amplitude coupling coefficients κ. The excitation amplitudes of the inputs and outputs are indicated.

plored in Section A.2.1. The coefficients t and κ are complex in general: there is an amplitude and phase change associated with either output of the directional coupler. For a lossless directional coupler, $|\kappa|^2 + |t|^2 = 1$. In general, there will be some scattering losses associated with the directional coupler, making $|\kappa|^2 + |t|^2 < 1$.

By inspection of Figure A-2, the following matrix equations can be formulated:

$$\begin{pmatrix} E_{t1} \\ E_{t3} \end{pmatrix} = \begin{pmatrix} t & \kappa \\ -\kappa* & t* \end{pmatrix} \times \begin{pmatrix} E_{i1} \\ E_{i3} \end{pmatrix} \tag{A.29}$$

$$\begin{pmatrix} E_{t2} \\ E_{t4} \end{pmatrix} = \begin{pmatrix} t & \kappa \\ -\kappa* & t* \end{pmatrix} \times \begin{pmatrix} E_{i2} \\ E_{i4} \end{pmatrix} \tag{A.30}$$

and the relations

$$E_{i4} = e^{j\tilde{\theta}/2} E_{t3} \tag{A.31}$$

$$E_{i3} = e^{j\tilde{\theta}/2} E_{t4} \tag{A.32}$$

where $\tilde{\theta} = \tilde{n}_{eff}\frac{4\pi^2 r}{\lambda}$ and $\tilde{n}_{eff} = n_{eff} + j\alpha/2$ is the complex effective refractive index. The term α is the power loss of the waveguide per unit length. Without loss of generality, only one nonzero input will be assumed. That is,

$$E_{i1} \neq 0 \tag{A.33}$$

$$E_{i2} = 0 \tag{A.34}$$

Solving for the outputs will result in:

$$E_{t1}/E_{i1} = \frac{t - t^* e^{j\tilde{\theta}/2}}{1 - e^{j\tilde{\theta}}(t^*)^2} \tag{A.35}$$

$$E_{t2}/E_{i1} = \frac{-|\kappa|^2 e^{j\tilde{\theta}/2}}{1 - (t^*)^2 e^{j\tilde{\theta}}} \tag{A.36}$$

The power transmission coefficients are equal to the square of the amplitude coefficients:

$$P_{t1}/P_{i1} = \left|\frac{t - t^* e^{j\tilde{\theta}/2}}{1 - e^{j\tilde{\theta}}(t^*)^2}\right|^2 \tag{A.37}$$

$$P_{t2}/P_{i1} = \left|\frac{-|\kappa|^2 e^{j\tilde{\theta}/2}}{1 - (t^*)^2 e^{j\tilde{\theta}}}\right|^2 \tag{A.38}$$

Notice that the transmission coefficients are wavelength-dependent because $\tilde{\theta}$ is wavelength-dependent. The terms P_{t1}/P_{i1} and P_{t2}/P_{i1} are periodic with wavelength, because the resonances of the ring are periodic with wavelength. The free spectral range (FSR) and the full-width at half maximum (FWHM) of the resonances can be given by

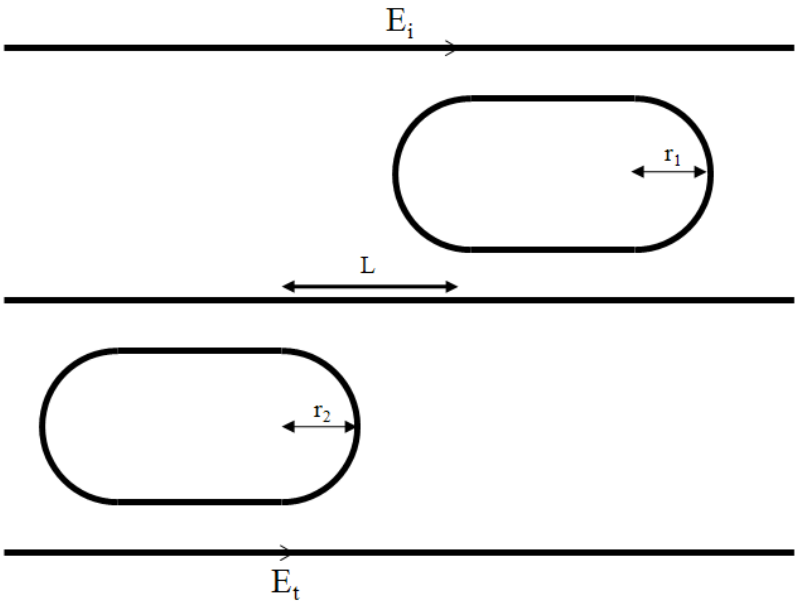

Figure A-3: Two racetracks with slightly different circumferences are cascaded together. The FSR of the dual-racetrack configuration is increased from the single-racetrack configuration due to the Vernier effect. The transmission is given by Equations A.41 and A.42.

$$FSR = \frac{\lambda^2}{n_{eff} 2\pi r} \tag{A.39}$$

$$FWHM = \frac{\kappa^2 \lambda^2}{2\pi^2 r n_{eff}} \tag{A.40}$$

Figure A-3 shows an image of two cascaded racetracks similar to the one analyzed in Chapter 4. The amplitude and power transmission through two rings can be derived by inspection from Equation A.36.

$$E_t/E_i = \frac{|\kappa|^4 e^{j\tilde{\theta}_1/2} e^{j\tilde{\theta}_2/2} e^{j\tilde{\theta}_L/2}}{(1-(t^*)^2 e^{j\tilde{\theta}_1})(1-(t^*)^2 e^{j\tilde{\theta}_2})} \tag{A.41}$$

$$P_t/P_i = \left| \frac{|\kappa|^4 e^{j\tilde{\theta}_1/2} e^{j\tilde{\theta}_2/2} e^{j\tilde{\theta}_L/2}}{(1-(t^*)^2 e^{j\tilde{\theta}_1})(1-(t^*)^2 e^{j\tilde{\theta}_2})} \right|^2 \tag{A.42}$$

where $\tilde{\theta}_L = \tilde{n}_{eff} \frac{2\pi L}{\lambda}$ is the phase accumulated from the middle waveguide.

Only the wavelengths that are resonant with both racetracks will exhibit transmission peaks. If the two racetracks can be made to be different in circumference–and hence have different FSRs, the total FSR will be equal to the least common multiplier of the FSRs of the individual rings [45]. More complicated designs have been created that utilize more than two rings to achieve a wide range of desired transmission responses, *e.g.* for the application of wavelength division multiplexed add/drop filters [60, 89].

Appendix B

Fabrication Techniques Used in this Thesis

B.1 Photolithography

Photolithography is the use of light to transfer patterns into a photosensitive material. In its most common form, a photosensitive polymer, known as the photoresist (resist for short), is illuminated with light ("exposed") in certain areas, which causes those areas to become soluble in the developer. By changing the illumination pattern, different features can be "written" into the photoresist. There are two tones of photoresist: (1) a positive photoresist is one in which the areas exposed to light become soluble in the developer, and (2) a negative photoresist is nominally soluble in the developer and the areas illuminated with light become insoluble.

Photoresists are generally applied using the spin-coating technique at speeds of 2–5 krpm. The resists that are used in this thesis are sensitive to photons of the mercury i-line (365 nm). The total amount of light imparted on the resist is referred to as the dose and is measured in Joules / cm^2. Contrary to what one may think, photoresists are generally quite transparent to their exposure wavelength. This ensures that the lower part of the photoresist experiences a similar dose as the top surface.

Contact lithography is a form of photolithography whereby the desired illumination pattern is obtained by transmitting the light through a patterned photomask

that is in direct contact with the substrate coated with photoresist. The photomask is a glass plate that is patterned with metal (generally chromium). The pattern on the photomask can be fabricated using electron beam lithography or a direct-write lithography system. Areas where there is metal will block the light so that the photoresist does not become exposed there. The fidelity of the photolithographically written pattern is strongly correlated to the fidelity of the pattern on the mask. Therefore, an examination of the photomask for defects or other non-idealities such as line-edge roughness is important prior to processing. When more than one photolithography step is required, the different photomasks will need to have alignment marks to facilitate the alignment of the patterns that need to be written at different steps of the fabrication process.

The resolution of contact lithography is determined by the combination of a number of factors. The wavelength of the exposure tool, generally a mask aligner, will set the smallest theoretical resolution. However, the resolution of a contact lithography system is most often determined by other factors, such as the photomask resolution, the photoresist contrast, properties of the developer, and the quality of the contact between the photomask and the resist. The contact quality is probably the most variable from a practical point of view. Any non-uniformity in the photoresist layer or particulates that land on top of the photoresist can create gaps between the photomask and the photoresist, which will degrade the resolution of the system and produce inconsistent results.

Photolithography can also be performed using a direct-write system in which a laser is rastered across the sample to expose the desired areas. Direct-write photolithography is advantageous to contact lithography because it is less affected by particulates on the wafer, and also does not require a photomask, making it dynamically programmable. However, it requires a longer exposure time in general, because the areas are exposed sequentially, rather than in parallel. Furthermore, because the light source is coherent, direct-write photolithography is more susceptible to scalloping from substrate back-reflection. This can be remedied by placing an anti-reflective coating layer below the photoresist.

B.2 Electron Beam Lithography

Electron beam (e-beam) lithography is a direct-write lithography method that involves the use of electrons, rather than photons, to expose the resist. Because the wavelength of electrons are on the order of an x-ray photon, e-beam lithography systems can achieve sub-10-nanometer resolution [63]. However, because of the extended time required to write a pattern using e-beam lithography, photolithography is still the workhorse of the IC industry. E-beam lithograpy is often used to pattern the photomasks that are used in photolithography systems.

E-beam resists can be categorized into positive and negative resists just like photoresists. Analogously, the total number of electrons imparted into the resist is referred to as the dose, usually measured in Coulombs / cm^2. The acceleration energy of the electrons are an important parameter in e-beam lithography. Higher energy electrons move faster and interact less with the resist than lower energy electrons. Thus, exposing with higher electron energies requires higher doses to provide the same exposure levels as exposing with lower energy electrons. However, higher energy electrons are necessary when thicker e-beam resist layers are used, to ensure that the dose at the top of the resist is similar to the dose at the bottom of the resist layer.

Because electrons are charged particles, the wafer must provide a path to ground to avoid charge build-up in the resist layer. The substrate should be conductive, and sometimes a thin layer of metal or conducting polymer (e.g. E-spacer or Aquasave) can be used to provide a ground plane for the electron beam, thus decreasing any pattern-dependent beam errors due to charging.

The resolution of the e-beam system is not simply determined by the spot size of the electron beam. Electrons that travel through the resist on the first pass can be back-scattered from the substrate and expose resist in the proximity of the electron beam spot. This is known as the proximity effect. The exposure point spread function is often modeled to first order as a double Gaussian; a number of correction terms can be introduced [96]. When a desired pattern contains regions of varying density, proximity effect correction (PEC) will need to be applied. There is PEC software that

can calculate the requisite doses at different areas so that the exposure level remains uniform over the entire pattern.

B.3 Etching

Etching, the removal of material, is one of the key components in the fabrication toolbox. Etching processes can be divided into two categories: (1) wet etching, and (2) dry etching. In an etch process, an etchmask or hardmask is used to protect the areas that are not desired to be etched. The selection of the proper etchant and etch parameters, along with the appropriate etchmask is an important part of process design. The ratio of the etch rate of the material to be etched to the etchmask is called the etch selectivity. A compilation of etchrates for many commonly used materials and their wet/dry etchants can be found in the literature [139, 140].

Wet etching is a chemical process, usually involving an acidic or basic solution. For example, SiO_2 can be etched by hydrofluoric acid (HF). Because wet etching is a chemical process, the dilution of the etchant will normally be directly proportional to the etch rate. Wet etch processes can achieve selectivities of greater than 10^6. Wet etching is isotropic, meaning that the etch rate is the same in every direction. Therefore, wet etching results in round etch profiles that are often unsuitable for photonics applications, and is rarely used in the processing of photonic devices except when used to remove material universally over the entire wafer such as in a lift-off or etchmask removal step.

Most often, photonic features are defined using dry etching, because dry etch processes can be made to be much more anisotropic than wet etching. A common dry etching method is reactive ion etching (RIE). A conventional reactive ion etcher consists of a chamber with two parallel electrodes. The sample to be etched is placed on one electrode. The other electrode is grounded. The chamber is brought under vacuum and etch gases are introduced into the chamber. A radio frequency (RF) voltage is capacitively coupled to the non-grounded electrode, ionizing the gas molecules and creating a plasma. The radicals and ions of the plasma chemically etch the sample.

The RF fields in the chamber change direction with each cycle of the RF signal, causing the ions and electrons to experience a force towards one electrode and then the other. The electrons are accelerated into the electrodes, while the ions do not experience as much motion due to their heavier masses. The non-grounded electrode builds a negative charge due to the absorbed electrons, and an equilibrium DC bias voltage is created between the positive ions in the plasma and the negative electrode. The DC bias causes the positive ions to accelerate toward the sample. Reactive ion etching is the combination of chemical etching by the reactive species in the plasma and ion bombardment, which not only enhances the chemical etching, but also sputters away material [21]. Materials that are not etched chemically in the RIE can still be etched by ion bombardment alone, or sputter etching. Typical sputtering rates are much slower than RIE etch rates because of the lack of chemical etching. A well-designed RIE hardmask is sputtered and not chemically etched. Dry etch processes generally have selectivities below 50.

There are several RIE parameters that can be adjusted to optimize a particular etch. The parameters are as follows: (1) gas flow, (2) RF power or DC bias voltage/power, (3) chamber pressure, (4) temperature, and (5) etch time. The flow rate of each gas determines its relative fraction in the mixture of gases present in the chamber. The flow rate needs to be high enough to ensure that the reactive agents are replenished faster than they are depleted through the chemical reactions. The chamber pressure indicates the density of reactive species in the plasma that will be available for etching. There is a trade-off however, because increasing the pressure also increases the particle collision rate, which makes the etching more isotropic. Changing the RF power also changes the number of reactive species available for chemical etching. A trade-off exists with respect to the DC bias voltage: a lower DC bias voltage is required to reduce the sputter-etching of the mask, while a larger DC bias is desired to increase the anisotropy. In a conventional RIE, one can control the RF power or the DC voltage, but not both. An inductively-coupled plasma (ICP) RIE system (as opposed to the conventional "capacitively-coupled plasma") allows the bias voltage and the RF power to be set independently from each other. The

expanded parameter space of the ICP RIE allows for better etch optimization.

B.4 Planarization

For photonics applications, etching is generally used to create some sort of waveguide or confining structure. After etching, planarization is often performed for two purposes: (1) to passivate the sidewalls of the device and (2) to make the surface of the sample planar to assist in further processing. Unpassivated sidewalls may be a source of mid-gap states that increase the non-radiative recombination rate. If left unpassivated, the sidewalls may also form conductive paths, such as from the oxidation of indium in InP-based devices [110]. In the case that no further top-side processing is required, the planarization process does not need to make the substrate surface completely flat.

Attributes that planarization materials for photonics applications should exhibit include the following:

(a) Low index of refraction

(b) Transparent to the wavelength of operation

(c) Good adhesion to the substrate

(d) Easy to apply

Common planarization materials include SiO_2, and spin-on dielectrics such as hydrogen silsesquioxane (HSQ) or benzocyclobutene (BCB). For the devices described in this thesis, BCB is used for its ease of processing [147]. Along with a low index of refraction (≈ 1.5), BCB has a low curing temperature (250°C), good planarization, and fast etch-back using fluorine-based RIE. After etchback, BCB can exhibit a small degree of surface roughness, which facilitates the adhesion of metal contacts, which are usually applied after the planarization step.

B.5 Metalization

Active photonic devices that utilize electrostatic biasing or carrier injection require metal contacts. If metalized properly, a device should exhibit low contact resistance, leading to lower levels of Joule heating and higher carrier injection efficiency (for carrier injection devices). For a more comprehensive treatment of contact resistance, please refer to Appendix D. The metal-semiconductor contact can be a challenging aspect of process development. There are many different metal stacks that can be used to achieve ohmic contacts with low contact resistance to different n-type and p-type semiconductors, provided that the semiconductor layers are doped to an adequate level [108]. For example, for p+ doped InGaAs, the contact metal stack most commonly used is Ti/Pt/Au annealed at 400-450°C for 30-60 seconds [44].

Care must be taken not to damage the p-type semiconductor that makes contact to the metal. Ion bombardment damaged caused by reactive ion etching or plasma-enhanced chemical vapor deposition processes have been shown to damage the semiconductor layer, making it difficult to fabricate ohmic contacts with low contact resistance [8]. Because the p-contact is so much smaller than the n-contact, the p-contact is normally the factor limiting the diode resistance of the device.

Metal pads also facilitate heat dissipation. Figure B-1 shows the side view of a ridge that is experiencing resistive heating. Heat is dissipated from the waveguide upward to the metal pad, and downward through the substrate. The semiconductor thermal conductivity is generally smaller than that of the metal, and the planarization

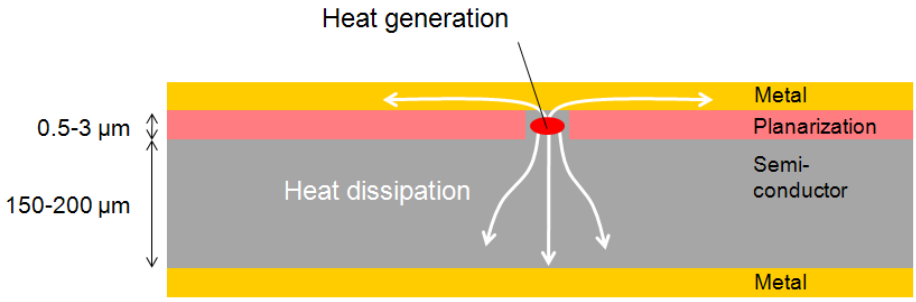

Figure B-1: A qualitative visualization of the heat dissipation pathways for a ridge laser.

layer will be thermally insulating. For example, indium phosphide has a thermal conductivity of 68 W/m·K, compared to 318 W/m·K for gold and 0.29 W/m·K for BCB. Often, one of the metal pads will be connected to a thermoelectric cooler serving as a heat sink. Good metal contacts not only minimize resistive heating, but also facilitates in heat dissipation.

Thin layers of metal can be deposited using e-beam evaporation or sputtering. E-beam evaporation is a form of direction deposition, meaning that the sidewalls of any topography on the surface of the wafer will not be coated. Sputtering is a form of conformal deposition that covers the sidewalls and is undesirable if the metal contacts are to be patterned with a lift-off step. The thicknesses of e-beam evaporated or sputtered metal layers can both be controlled to within a few nanometers. However, the deposition rates are often too slow to make contacts much thicker than 0.5 μm. To make thicker contacts, electroplating is a time-tested industrial standard. Often the metal stack at the metal-semiconductor interface is evaporated to precise thicknesses, and then electroplating, which does not have the same thickness control, is used to make the contacts thicker (a few microns).

Appendix C

Fabrication Process Details

C.1 Heterostructures

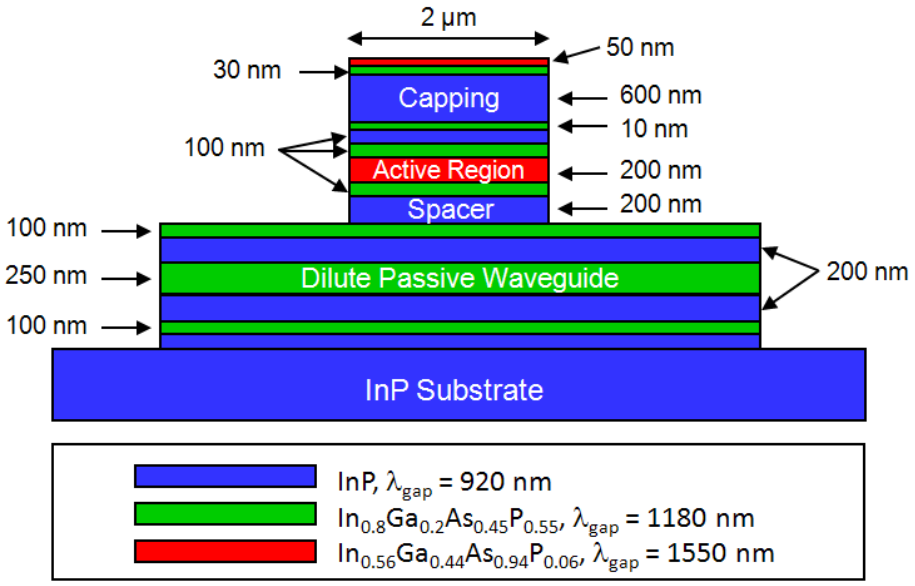

Figure C-1: The heterostructure for the all-optical logic devices of Chapter 2. The top layers form the active SOA, and the bottom layers form the passive waveguide.

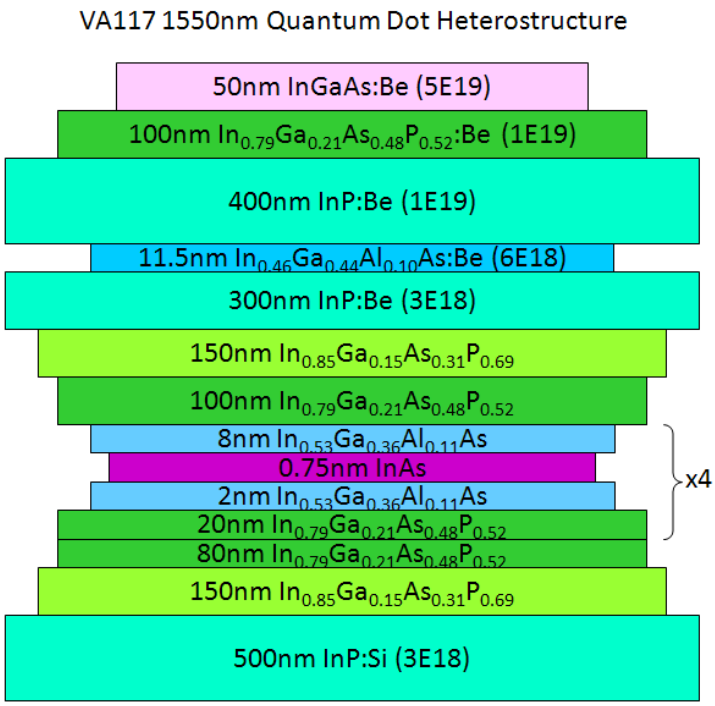

Figure C-2: The InAs quantum dot 1550 nm laser structure investigated in Section 3.1.

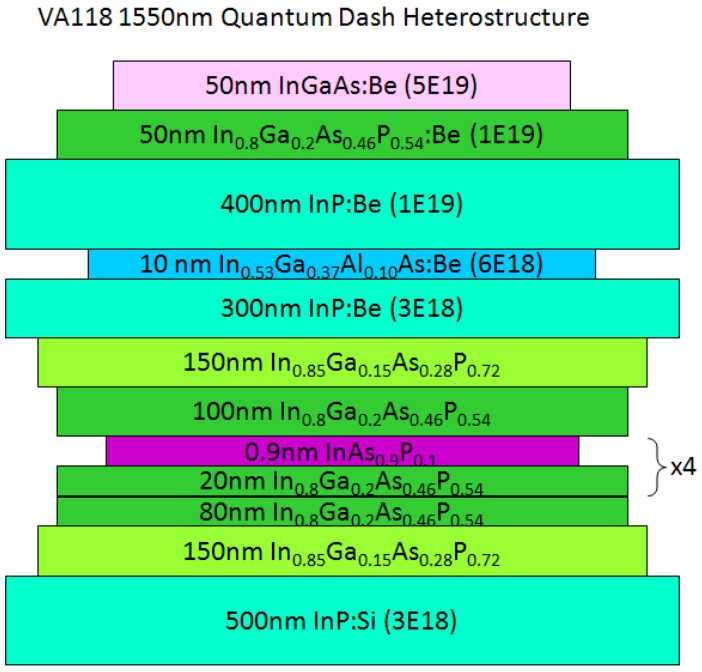

Figure C-3: The InAs quantum dash 1550 nm laser structure investigated in Section 3.1.

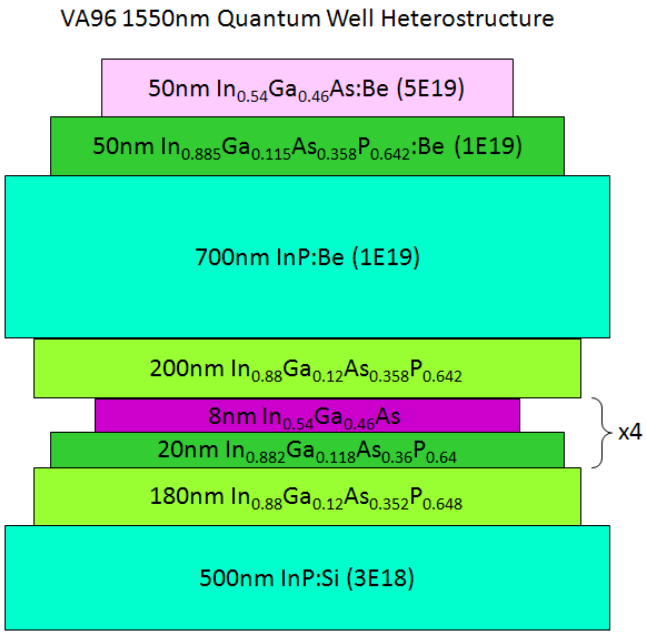

Figure C-4: The InGaAs quantum well 1550 nm laser structure investigated in Section 3.1.

Figure C-5: The layer structure for VA159, one of the strained InGaAs quantum well laser structures investigated in Section 3.2 and Chapter 4.

C.2 Process Flows

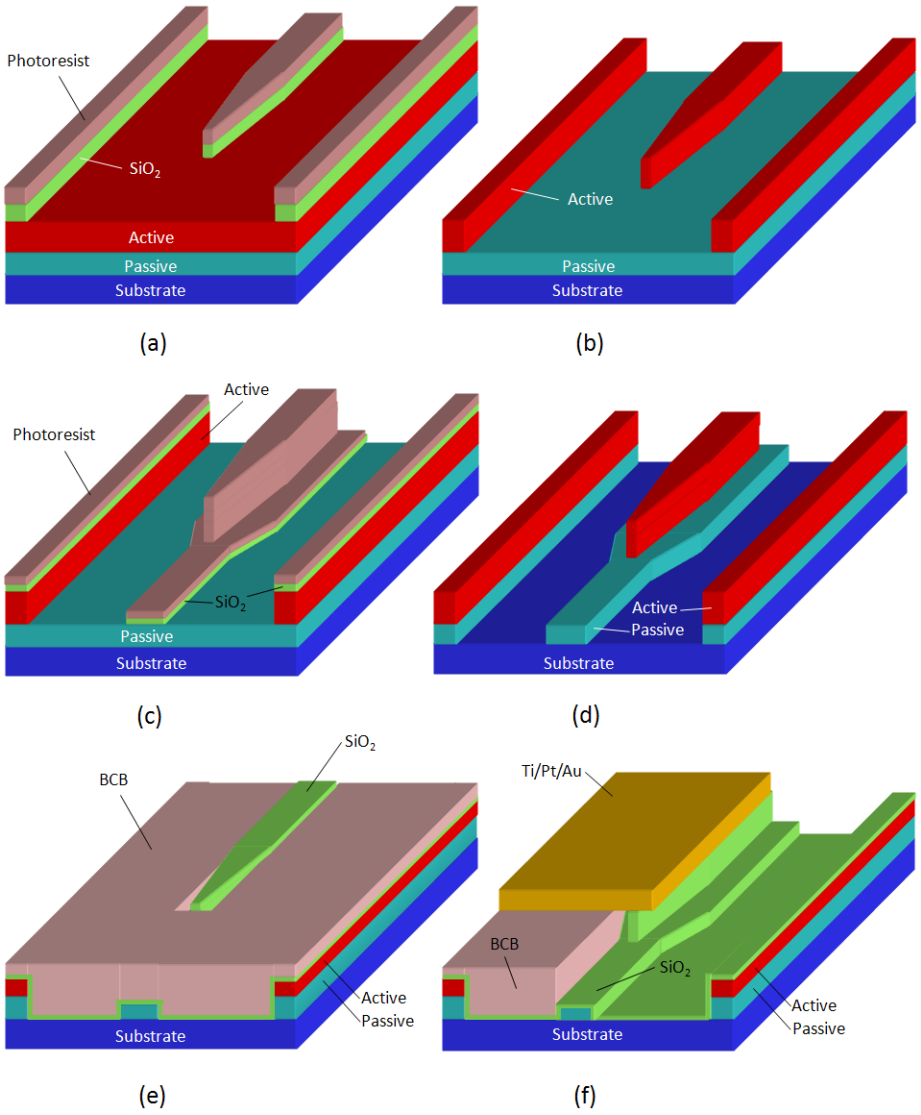

Figure C-6: Process flow for the all-optical logic gates investigated in Chapter 2. (a) 200 nm of SiO_2 is deposited (PECVD), followed by a photolithography step to define the active waveguides and trenches. (b) The resist is removed and the active region is etched using ICP RIE. (c) A layer of 200 nm SiO_2 is deposited (PECVD), followed by a 2nd photolithography step to define the passive waveguides. (d) The resist is removed and the passive waveguides are etched using ICP RIE. (e) BCB is applied and etched back in RIE to expose the SiO_2 on the active ridge. (f) The SiO_2 is removed in HF. A photolithography step is implemented to define the contact pads, and Ti/Pt/Au contacts are deposited by e-beam evaporation, followed by lift-off. The wafer is lapped to 160 μm, followed by backside e-beam evaporation of Ge/Au/Ni/Au. The metal is annealed at 450°C for 30 s to obtain ohmic contacts.

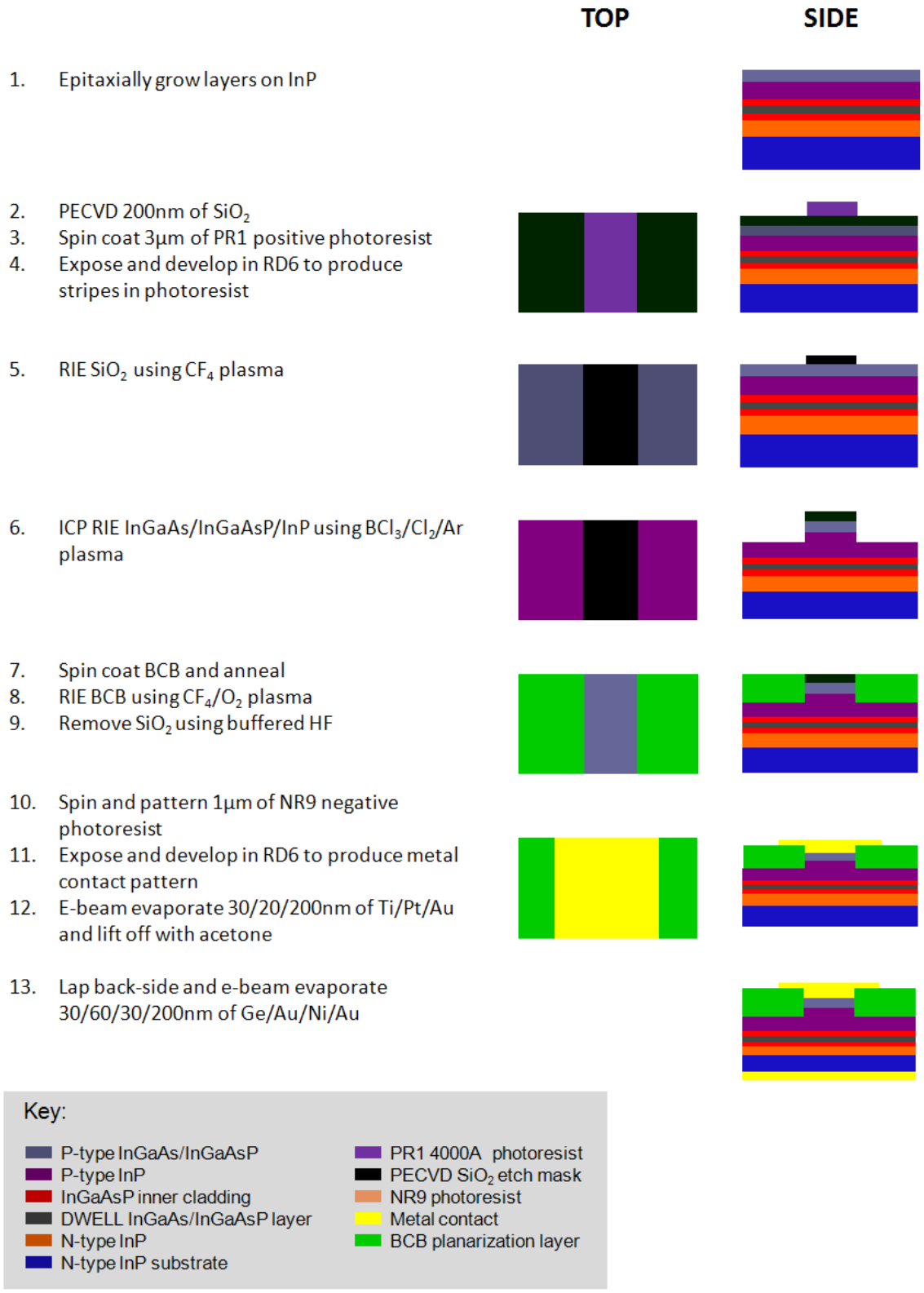

Figure C-7: Process flow for the quantum dot and quantum dash ridge lasers investigated in Section 3.1.

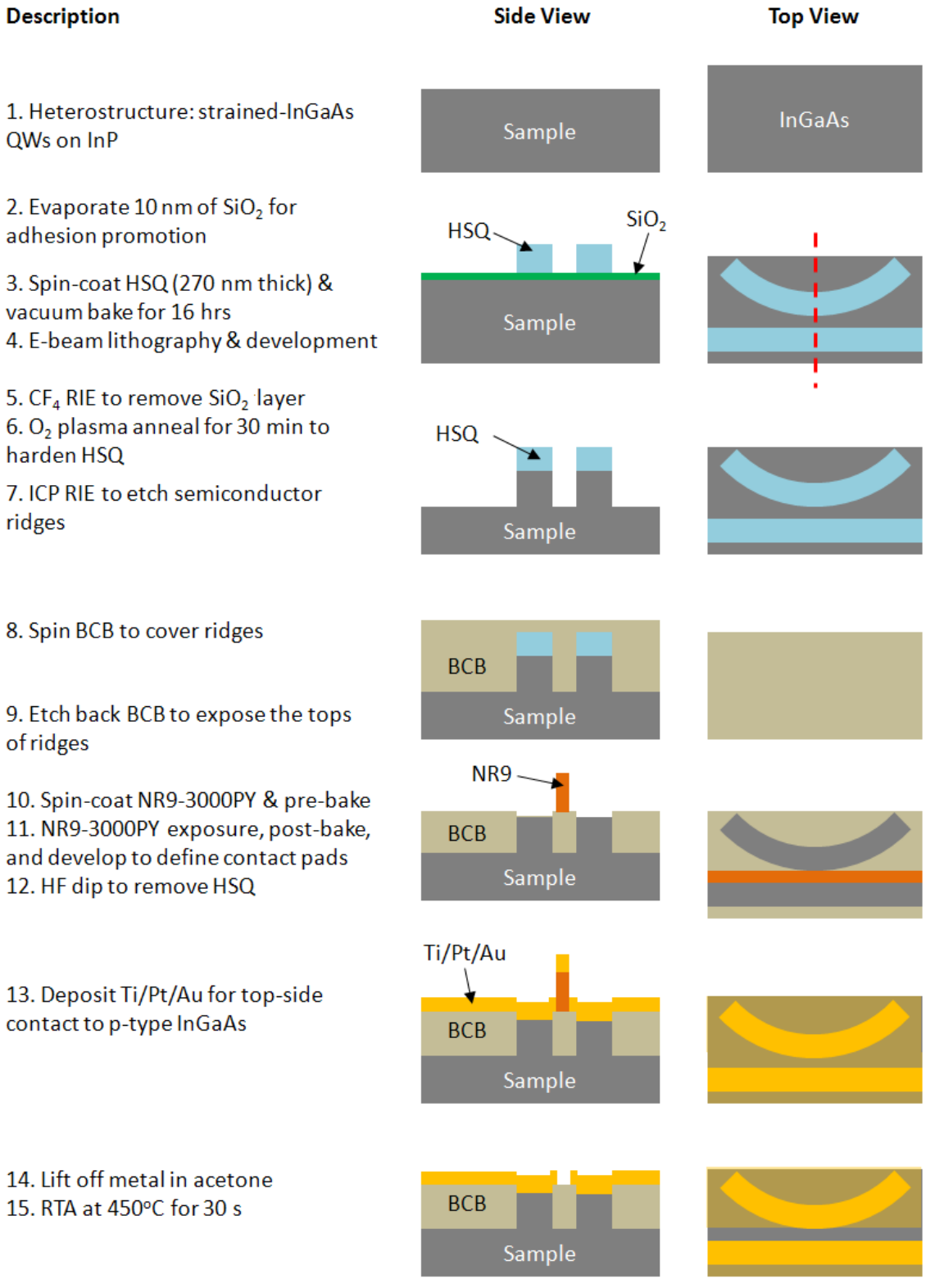

Figure C-8: Process flow for the single-facet and ring resonator-coupled lasers presented in Chapter 4.

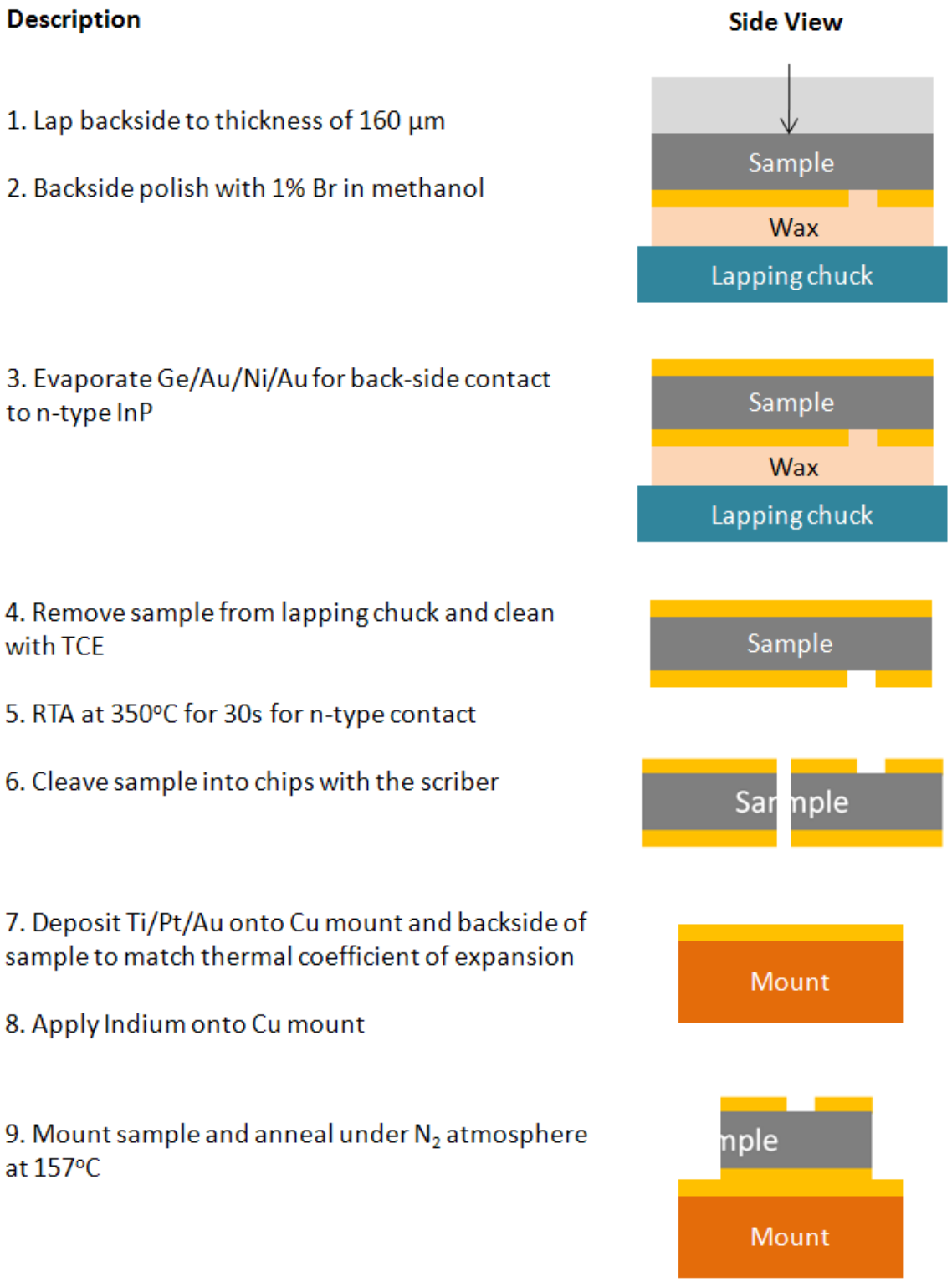

Figure C-9: Procedure for the post-processing of InP-based chips and devices.

C.3 Masks and Device Layouts

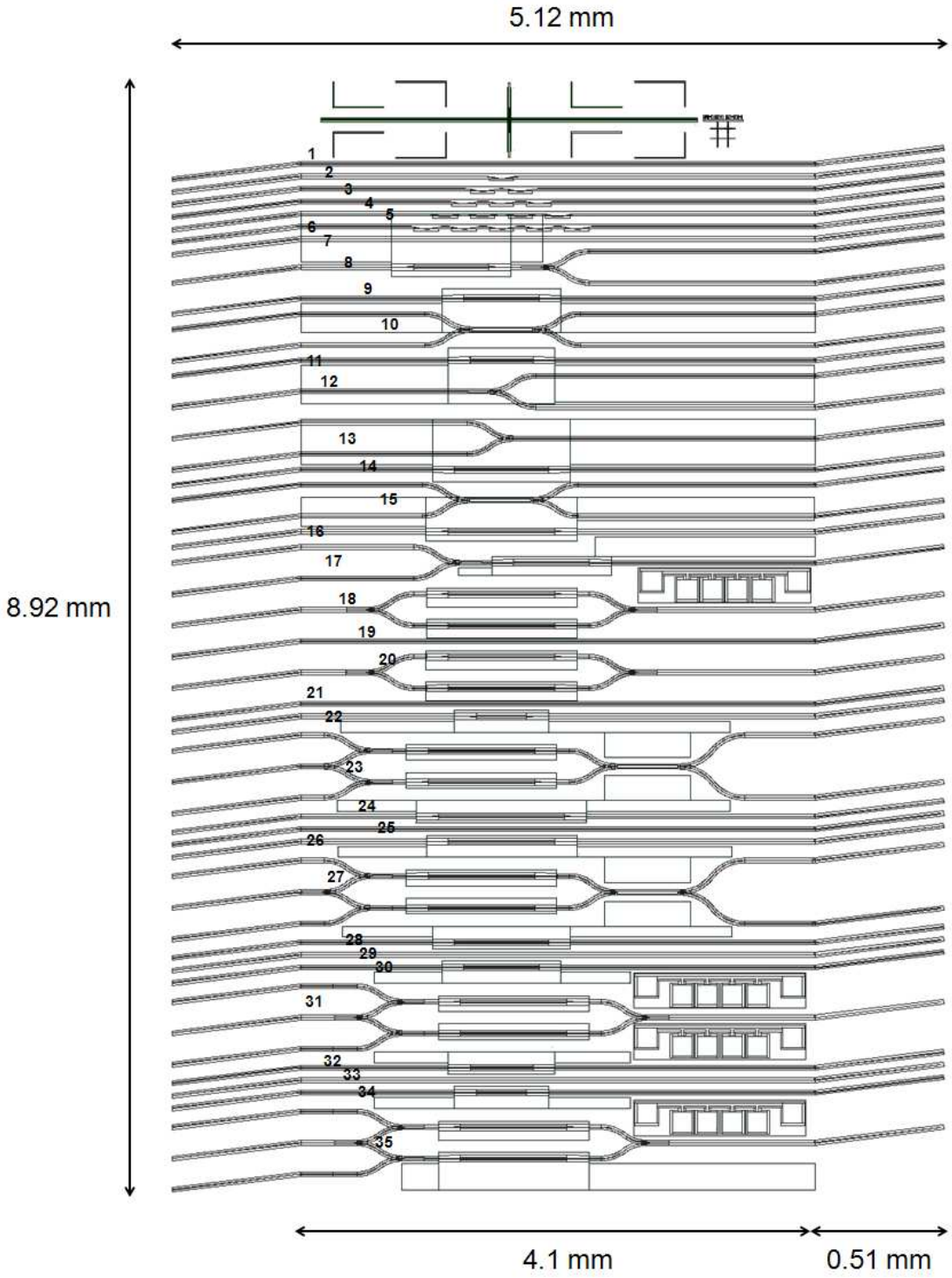

Figure C-10: Three-mask layout of the all-optical logic chip from Chapter 2. The devices are numbered in reference to Table C.1.

Table C.1: Devices on the all-optical logic chip adapted from [141].

Device	Description	SOA Length (μm)	SOA Width (μm)
1	Passive waveguide	-	-
2	Passive w/ 2 bends	-	-
3	Passive w/ 4 bends	-	-
4	Passive w/ 6 bends	-	-
5	Passive w/ 8 bends	-	-
6	Passive w/ 10 bends	-	-
7	Passive waveguide	-	-
8	SOA with 1×2 MMI	600	4
9	Straight SOA	600	4
10	2×2 MMI	-	-
11	Straight SOA	500	4
12	1×2 MMI	-	-
13	2×1 MMI	-	-
14	Straight SOA	750	4
15	2×2 MMI	-	-
16	Straight SOA	850	4
17	SOA with 1×2 MMI	600	2
18	Simple MZI	850	2
19	Passive waveguide	-	-
20	Simple MZI	850	4
21	Passive waveguide	-	-
22	Straight SOA	400	4
23	AOL unit cell	850	2
24	Straight SOA	1000	2
25	Passive waveguide	-	-
26	Straight SOA	850	2
27	AOL unit cell	850	4
28	Straight SOA	750	2
29	Passive waveguide	-	-
30	Straight SOA	600	2
31	Wavelength converter	850	2
32	Straight SOA	500	2
33	Passive waveguide	-	-
34	Straight SOA	400	2
35	Wavelength converter	850	4

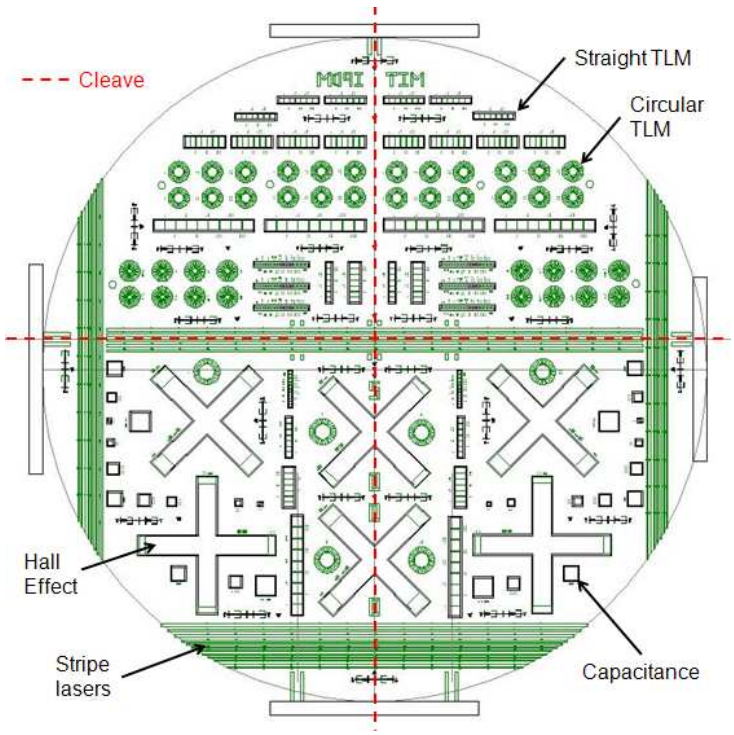

Figure C-11: Two-mask layout of diagnostic devices, including contact resistance TLM structures.

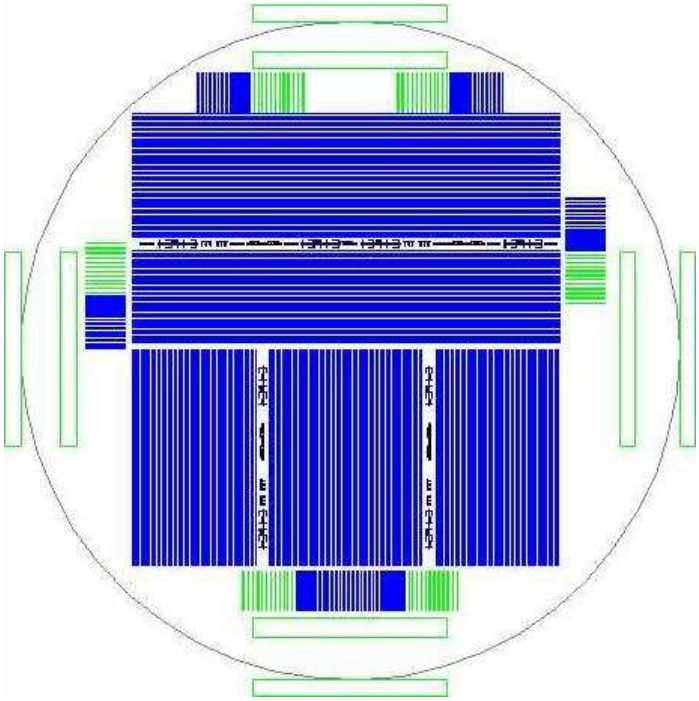

Figure C-12: Two-mask layout of the ridge lasers (ranging from 1 μm to 30 μm wide) that are investigated in Section 3.1.

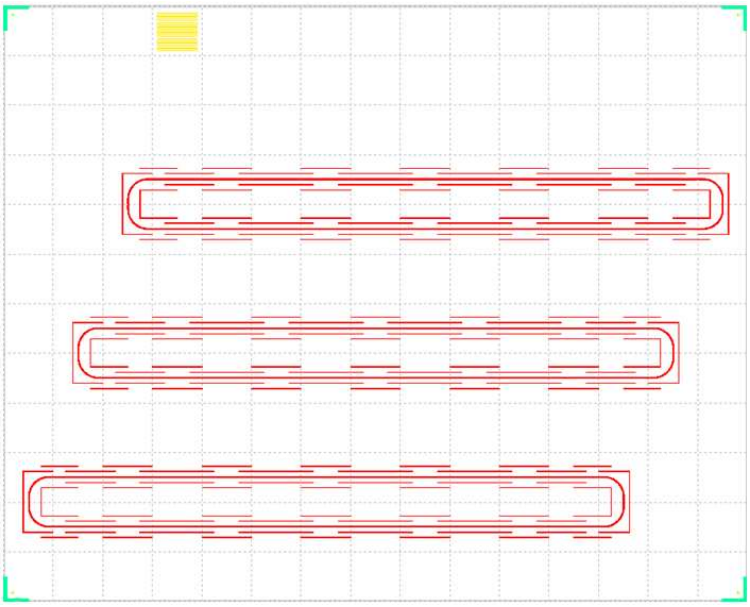

Figure C-13: Electron beam lithography layout of single-facet lasers with fences. The die is intended to be cleaved 600 μm from the left edge to yield 6 single-facet lasers with different cavity lengths. The square grids delineate the boundaries between the (100 μm)^2 write fields. The grating is patterned to facilitate the act of locating the die on the wafer with the naked eye.

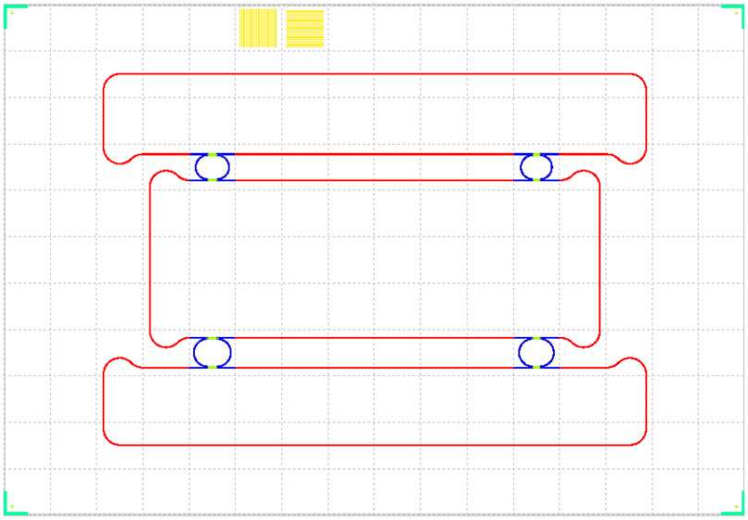

Figure C-14: Electron beam lithography layout of double ring resonator-coupled lasers. The die is intended to be cleaved down the middle to yield 2 double ring resonator-coupled lasers. The two rings in each laser are detuned to yield 40 nm of total FSR. Multiple contacts were fabricated to bias different sections of the lasers with different injection currents. In particular, the rings were designed to be biased separately from the straight waveguide sections.

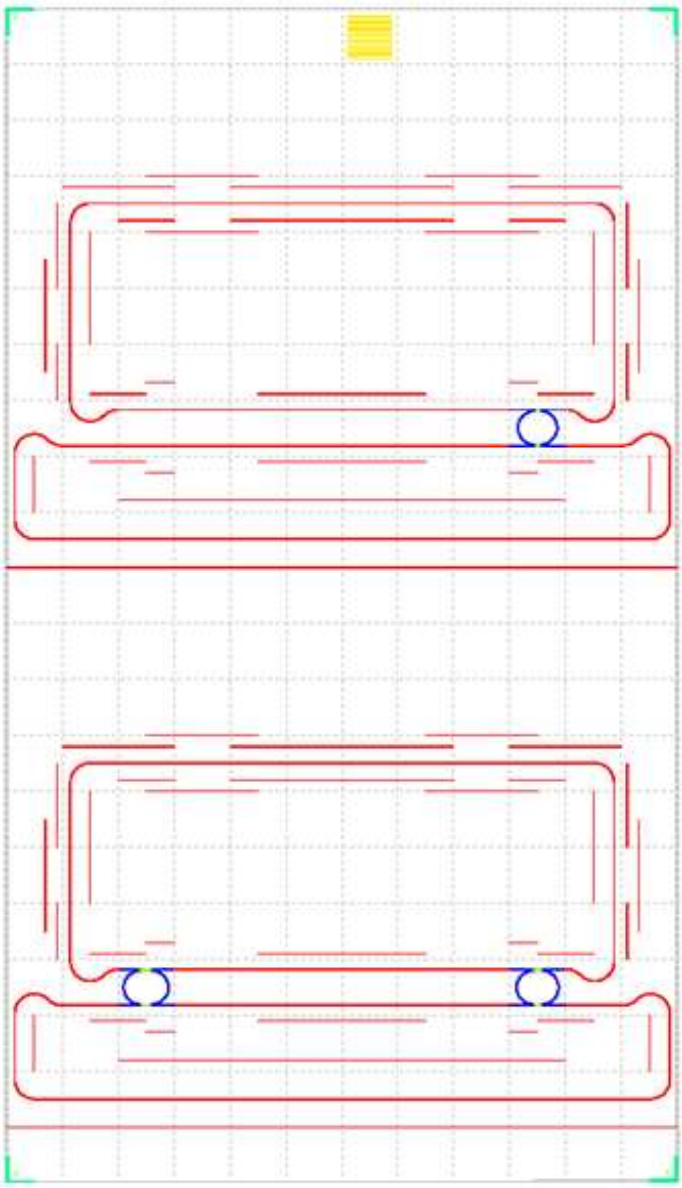

Figure C-15: Electron beam lithography layout of single ring resonator-coupled lasers with fences. The die is intended to be cleaved down the middle to yield 3 single ring resonator-coupled lasers. The top left pair of single-facet lasers is used for diagnostic purposes. Multiple contacts were fabricated to bias different sections of the lasers with different injection currents. In particular, the rings were designed to be biased separately from the straight waveguide sections. Adjacent contact pads were separated by 10 μm.

C.4 Tables and Figures

C.4.1 Lithography

Table C.2: Photolithography parameters.

Parameter	AZ5214 Image Reversal	AZ5213 Positive	PR1-4000A	NR9-1000PY/ NR9-3000PY
Spin [krpm]	4	4	5	3
Pre-bake	30 min, 90°C	30 min, 90°C	15 min, 100°C	3 min, 90°C
Exposure Tool	Elec. Visions EV620	Elec. Visions EV620	Elec. Visions EV620	Heidelberg μPG
Exposure	15 mJ/cm^2	100 mJ/cm^2	125 mJ/cm^2	18 mW (4x)
Post-bake	30 min, 90°C	-	-	2 min, 90°C
Flood Expose	600 mJ/cm^2	-	-	-
Developer	AZ422	AZ422	RD6	RD6
Development [s]	90	90	50	16

Table C.3: Electron beam lithography parameters for writing 1 μm wide waveguides.

Parameter	FOx-14 HSQ	FOx-22 HSQ	E-spacer (Aquasave)
Spin Speed [krpm]	3	2	4
Thickness [nm]	265	270	5
Dose InP sub [μC/cm^2]	450	600	-
Dose GaSb sub [μC/cm^2]	-	450	-
Developer	25% TMAH	25% TMAH	Remove w/ H_2O
Development time [s]	100	40	-

Table C.4: Plasma asher HSQ anneal parameters.

Gases	Pressure (mT)	Power (W)	Time (min)
He+20% O_2	100	100	30

C.4.2 Deposition

Table C.5: Plasma enhanced chemical vapor deposition (PECVD) parameters.

Parameter	Low-stress Silicon Dioxide	Low-n Silicon Nitride	High-n Silicon Nitride
Pressure [mT]	900	900	900
Temperature [°C]	300	300	300
N_2O [sccm]	1490	0	0
N_2 [sccm]	392	1960	1960
SiH_4 [sccm]	10	40	40
NH_3 [sccm]	0	40	10
RF	13.56 MHz (50W)	20% 380kHz / 80% 13.56 MHz (25W)	20% 380kHz / 80% 13.56 MHz (25W)
Dep Rate [nm/min]	0.6	0.24	0.20
Etch Rate (BHF) [nm/s]	360–390	69	16
n	1.5	1.87	2.3

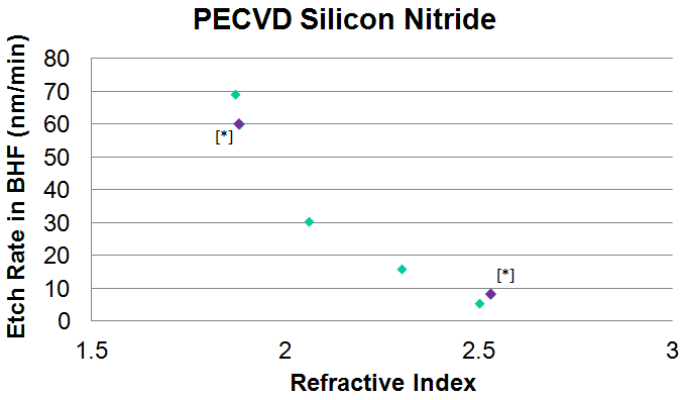

Figure C-16: The measured etch rate of PECVD silicon nitride in buffered HF as a function of the refractive index of the silicon nitride layer. The asterisked data points are from [139].

C.4.3 Etching

Table C.6: Plasma Therm reactive ion etching parameters. (The addition of a glass slide in the Plasma Therm increases the capacitance of the system. Functionally, this allows for lower voltages at the same power.)

Parameter	PECVD SiO_2	PECVD high-n Silicon Nitride	BCB
Gas(es)	CF_4	CF_4/O_2	CF_4/O_2
Flow (sccm)	15	8/16	8/16
Pressure (mT)	10	10	10
Power (W)	150	300	300
Voltage (V)	310	200	340
Etch Rate (nm/min)	20	20	200
Glass slide	No	Yes	Yes

Table C.7: Samco inductively-coupled plasma reactive ion etching parameters.

Parameter	InP	InP	GaSb	GaSb-based Laser
Gas(es)	$SiCl_4/Cl_2/Ar$	$BCl_3/Cl_2/Ar$	$SiCl_4/Cl_2/Ar$	$SiCl_4/Cl_2/Ar$
Flow (sccm)	2/0.5/10	2/2/16	10/0.5/50	10/0.5/50
Pressure (Pa)	0.6	0.25	0.4	0.4
ICP Power (W)	250	250	100	100
Bias Power (W)	160	100	50	80
Temp (°C)	220	220	100	100
Etch Rate (nm/min)	1020	730	1700	540

Table C.8: Wet etching parameters.

Parameter	PECVD SiO_2	HSQ	PECVD High-n Si Nitride	InGaAs Surface Clean
Etchant	Transene BHF	BHF	BHF	1:10 HCl:H_2O
Etch Rate (nm/min)	360-390	360-390	16	-

C.4.4 Planarization and Metalization

Table C.9: BCB process overview.

Step	Details
Spin-coat adhesion promotor	2.5krpm, 20s
Hot plate bake	100°C, 5:00
Spin-coat BCB	1–5 krpm, 30s
Hot plate bake	100°C, 1:00
Anneal in N_2	Refer to Table C.10
Etch back	Refer to Table C.6

Table C.10: BCB anneal process.

Step	Details
Place sample on smaller Si piece	Don't overlap edges
Load boat into furnace	
Flow N_2 at room T	20 scfh, 30 min
Increase T to 100°C	5 scfh, 10 min soak
Increase T to 150°C	5 scfh, 20 min soak
Increase T to 200°C	5 scfh, 10 min soak
Increase T to 250°C	5 scfh, 120 min anneal
T free fall to < 100°C	5 scfh, 60 min

Table C.11: Metal evaporation parameters.

Semiconductor	Metal Stack	Thicknesses [nm]	Anneal
p-type InGaAs(P)	Ti/Pt/Au	30/20/450	450°C, 30 s
n-type InP	Ge/Au/Ni/Au	20/60/30/200	350°C, 30 s

Table C.12: Electroplating process overview.

Step	Procedure	Details
1	Deposit seed layer	80nm Au
2	Set up beaker with anode/cathode	Orotemp 24C RTU (65°C)
3	Turn on power supply (forward pulse)	2ms/4ms (on/off)
4	Plate for 5 min (1 μm Au)	13-15 mA, 0.5V
5	Remove seed layer	Fast dip in Au etchant

Appendix D

Contact Resistance

D.1 Introduction

This short tutorial on contact resistance is intended to be a starting point for understanding how to make contact resistance measurements accurately and correctly. It is the author's experience that the literature is often superficial about describing contact resistance measurements and can present derivations in inadequate detail.

D.1.1 Terminology

1. Contact pad: the layer of metal that interfaces with the semiconductor.

2. Specific contact resistance, ρ_c: the resistance for a unit area of contact pad, normally with units of $\Omega \cdot \text{cm}^2$. The resistance of the metal-semiconductor interface for a contact pad of area A is $R_c = \rho_c/A$.

3. Transmission line model (TLM): one of the commonly used models that are used to extract the contact resistance of a contact-semiconductor interface from current and voltage measurements. Details are in Appendix Section D.2

4. TLM test structure: a test structure on a chip consisting of an array metal contact pads, from which the specific contact resistance ρ_c can be measured utilizing the transmission line model. See Figure D-1.

D.1.2 Contact Resistance Measurement

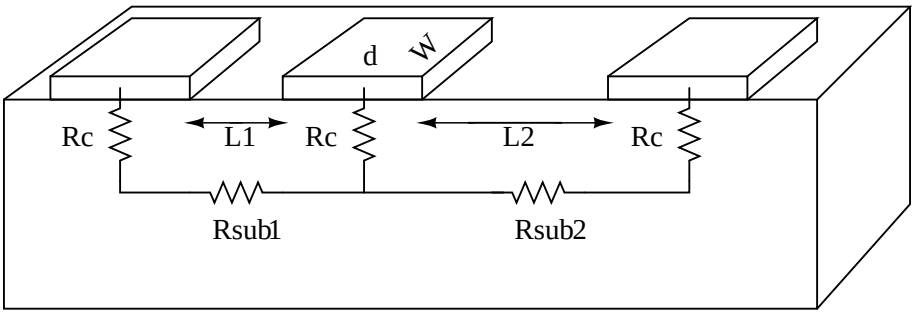

Figure D-1: A TLM test structure consisting of three contact pads on a semiconductor substrate. Depicted are the resistances of the substrate between the contact pads R_{sub}, along with the resistance R_c, whose value can be used to find the specific contact resistance.

Consider Figure D-1, which portrays three contact pads on a substrate separated from each other by distances L_1 and L_2. The contact pads have dimensions of $d \times W$. Also shown are the different resistances: R_{sub1} and R_{sub2}, which are the resistances of the substrate between the pads, and R_c, whose value can be used to determine the specific contact resistance. R_c is depicted as a resistor at the interface of the metal and the semiconductor.

Neglecting fringe currents, the resistance between the left-most two contact pads is

$$R = 2R_c + R_{sub1} = 2R_c + \frac{R_{s1}L_1}{W} \tag{D.1}$$

where R_{s1} is the sheet resistance of the bulk semiconductor. Measuring the resistance between contact pads separated by different values of L will generate a plot similar to Figure D-2.

The slope of the line is seen to be $\frac{R_{s1}}{W}$. The y-intercept, $2R_c$, is the part of the total resistance that is not related to the substrate resistance R_{sub}. $2R_c$ is everything that is "left-over" from the total resistance when the contribution of the substrate resistance is removed.

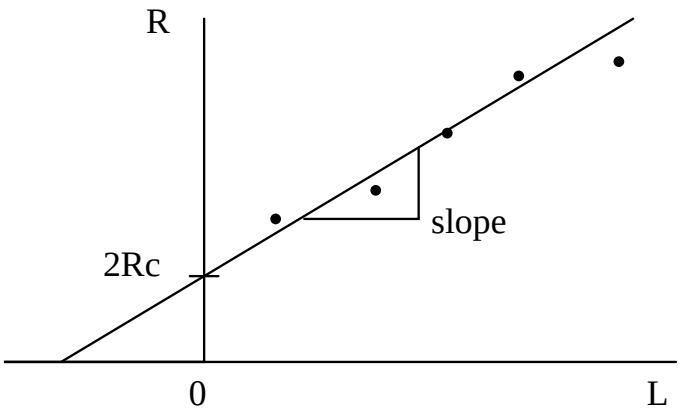

Figure D-2: A typical plot of a series of resistance measurements using a TLM test structure. The slope is equal to $\frac{R_{s1}}{W}$ and the y-intercept is $2R_c$.

D.1.3 Lumped Model

The lumped model is the simplest model used to determine ρ_c given that R_c is measured. The lumped model assumes that R_c is due entirely to the interface resistance, or specific contact resistance. That is,

$$\rho_c = R_c W d \tag{D.2}$$

Because current flow is more complicated than the lumped model implies, the lumped model is only useful for an order of magnitude estimate of ρ_c. The lumped model fails to consider the lateral current flow in the region beneath the contact pads.

D.2 Transmission Line Model

The transmission line model is a 1D model of contact resistance that has been shown to provide relatively accurate results as compared to 2D and 3D models [62]. As its name would suggest, the TLM describes the metal-semiconductor interface as a transmission line, as shown in Figure D-3, in which the metal-semiconductor interface is exaggerated in order to show the interface contact resistance.

Consider the current I that flows from a contact pad at the left (not shown), rightward through the substrate, into contact pad shown in Figure D-3. As I reaches

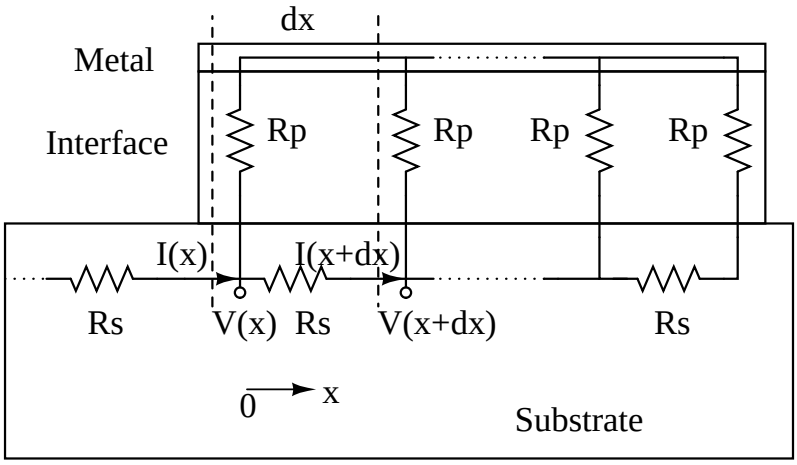

Figure D-3: The TLM with relevant resistances, currents, voltages as a function of x, which is zero at the left-most region of the contact and increases toward the right. The thickness of the interface between the metal and semiconductor is exaggerated to depict the metal-semiconductor interface resistance R_p and the substrate resistance R_s for a section dx.

the contact pad at $x = 0$, the current will gradually flow upward along the length of the contact. The resistors R_p and R_s represent the resistance of the interface and the resistance of the substrate, respectively, for a small length dx. R_c is given by $V(x = 0)/I(x = 0)$, since it is the "left-over" resistance when the contribution of the substrate is removed. The mathematical analysis of this structure is derived in [37, 94] and reproduced, with additional mathematical clarifications and simplifications, below.

The interface is divided into sections of length dx in Figure D-3. If the metal pad has dimensions $d \times W$ as in Figure D-1, then

$$R_\rho = \frac{\rho_c}{W \cdot dx} \tag{D.3}$$

$$R_s = R_{s1}\frac{dx}{W} \tag{D.4}$$

The drop in voltage in the substrate under the contact pad over a distance dx is given by

$$
\begin{aligned}
dV &= -I(x)R_s && \text{(D.5)}\\
&= -I(x)R_{s1}\frac{dx}{W} && \text{(D.6)}\\
\frac{dV}{dx} &= -I(x)\frac{R_{s1}}{W} && \text{(D.7)}
\end{aligned}
$$

The drop in current in the substrate under the contact pad over a distance dx is

$$
\begin{aligned}
dI &= -V(x)/R_\rho && \text{(D.8)}\\
&= -V(x)\frac{W\cdot dx}{\rho_c} && \text{(D.9)}\\
\frac{dI}{dx} &= -V(x)\frac{W}{\rho_c} && \text{(D.10)}
\end{aligned}
$$

Equations D.7 and D.10 can be used to arrive at the following differential equation and its solutions,

$$
\begin{aligned}
\frac{d^2V}{dx^2} &= -\frac{dI}{dx}\frac{R_{s1}}{W} && \text{(D.11)}\\
&= V(x)\frac{W}{\rho_c}\frac{R_{s1}}{W} = V(x)\frac{R_{s1}}{\rho_c} && \text{(D.12)}\\
\Rightarrow V(x) &= A_1 e^{\sqrt{R_{s1}/\rho_c}x} + A_2 e^{-\sqrt{R_{s1}/\rho_c}x} && \text{(D.13)}\\
I(x) &= -\frac{W}{R_{s1}}\frac{dV}{dx} && \text{(D.14)}\\
&= -\frac{W}{R_{s1}}\sqrt{R_{s1}/\rho_c}\left(A_1 e^{\sqrt{R_{s1}/\rho_c}x} - A_2 e^{-\sqrt{R_{s1}/\rho_c}x}\right) && \text{(D.15)}
\end{aligned}
$$

The convention is to define a transfer length $L_T = \sqrt{\frac{\rho_c}{R_{s1}}}$, so that

$$
\begin{aligned}
V(x) &= A_1 e^{x/L_T} + A_2 e^{-x/L_T} && \text{(D.16)}\\
I(x) &= -\frac{W}{R_{s1}L_T}\left(A_1 e^{x/L_T} - A_2 e^{-x/L_T}\right) && \text{(D.17)}
\end{aligned}
$$

At the boundary $x = d$, the right-most edge of the contact pad, the current is zero, so

$$I(d) = -\frac{W}{R_{s1}L_T}\left(A_1 e^{d/L_T} - A_2 e^{-d/L_T}\right) = 0 \tag{D.18}$$

$$A_1 = A_2 e^{-2d/L_T} \tag{D.19}$$

Then R_c can be found to be

$$R_c = \frac{V(0)}{I(0)} = \frac{A_2 e^{-2d/L_T} + A_2}{-\frac{W}{R_{s1}L_T}\left(A_2 e^{-2d/L_T} - A_2\right)} \tag{D.20}$$

$$= \frac{R_{s1}L_T}{W}\left(\frac{1 + e^{-2d/L_T}}{1 - e^{-2d/L_T}}\right) \tag{D.21}$$

$$= \frac{R_{s1}L_T}{W}\left(\frac{e^{d/L_T} + e^{-d/L_T}}{e^{d/L_T} - e^{-d/L_T}}\right) \tag{D.22}$$

$$= \frac{R_{s1}L_T}{W}\left(\frac{1}{\tanh(d/L_T)}\right) \tag{D.23}$$

$$= \frac{\sqrt{R_{s1}\rho_c}}{W}\left(\coth\left(d\sqrt{\frac{R_{s1}}{\rho_c}}\right)\right) \tag{D.24}$$

Equation D.24 is a transcendental equation that can be used to calculate ρ_c from R_c and the other parameters. W and d are measured from the physical dimensions of the contact pad; R_{s1} and R_c are obtained from the slope and intercept of the contact resistance measurement.

D.2.1 Intuition

The specific contact resistance, ρ_c, has units of $\Omega \cdot \text{cm}^2$ whereas resistivity, ρ_s, has units of $\Omega \cdot \text{cm}$. Recall that resistance is related to the resistivity by

$$R = \frac{\rho_s L}{A} \tag{D.25}$$

where L is the length of the resistor and A is the cross-sectional area. The metal-

semiconductor interface can be thought of as an infinitely thin resistor that has finite resistance. The length is not a geometrical factor that the contact resistance possesses, so the resistance is simply related to the specific contact resistance by the area A.

$$R_c = \frac{\rho_c}{A} \tag{D.26}$$

The lumped model does not take into account the lateral flow of current underneath the contact pad. Thus, the TLM should converge to the lumped model if the contact pad is very short, $d \ll L_T = \sqrt{\frac{\rho_c}{R_{s1}}}$. In this limit,

$$\begin{aligned} R_c &= \frac{R_{s1}L_T}{W}\left(\frac{1}{\tanh(d_{short}/L_T)}\right) && \text{(D.27)} \\ &\approx \frac{R_{s1}L_T}{W}\left(\frac{L_T}{d}\right) = \frac{\rho_c}{Wd} && \text{(D.28)} \end{aligned}$$

Where Equation D.28 is obtained by taking the linear Taylor series term of the hyperbolic tangent function.

The other limit one could take is $d \gg L_T = \sqrt{\frac{\rho_c}{R_{s1}}}$. In this limit

$$\begin{aligned} R_c &= \frac{R_{s1}L_T}{W}\left(\frac{1}{\tanh(d_{long}/L_T)}\right) && \text{(D.29)} \\ &\approx \frac{R_{s1}L_T}{W} && \text{(D.30)} \end{aligned}$$

Notice that if R_c had the same sheet resistance as the bulk semiconductor R_{s1}, the contact pad would have a length equal to the transfer length L_T. This limit of d_{long} is the simplification that Shockley made in his original proposition of the TLM in 1964 [109]. In this limit, d is no longer a relevant parameter.

In a practical lab setting, one should estimate a typical value for L_T to determine which limit, if any, applies to the particular contact pads in question. As an example, InP doped to p+ at 10^{19} cm^{-3} will have a sheet resistance, assuming the current flows at a depth of 0.1 μm, of approximately 300 Ω. A good specific contact resistance is

Table D.1: Values of $\tanh(d/L_T)$ for different values of d/L_T.

d/L_T	0.1	0.2	1	2	10	20	100	200
$\tanh(d/L_T)$	0.09967	0.19738	0.76159	0.96403	1.00000	1	1	1

on the order of $\rho_c = 10^{-6}\ \Omega \cdot \mathrm{cm}^2$. The transfer length is then

$$L_T = \sqrt{\frac{\rho_c}{R_{s1}}} = 0.6\ \mu\mathrm{m} \tag{D.31}$$

It would be difficult to probe a contact pad with $d \ll L_T$. In fact, d is most probably large enough to use the simplified form of R_c in the limit of $d \gg L_T$. Table D.1 presents values of $\tanh(d/L_T)$ as a function of d/L_T. Depending on the desired accuracy, the table can be used to decide whether this simplified form of R_c would be appropriate.

D.2.2 Anneal Process Changes to the TLM

The metalization process usually involves an anneal to improve the contact resistance of the metal-semiconductor interface. For example, a Ti/Pt/Au contact to InGaAs requires an anneal at 450°C for 30 s. Diffusion and phase separation can occur during this high-temperature step, and there is no reason to believe that the semiconductor sheet resistance under the contact pad will remain the same as the sheet resistance of the bulk semiconductor, R_{s1}. If the sheet resistance of the semiconductor under the contact pad is denoted as R_{s2}, all of the previous analysis remains the same, with R_{s2} replacing R_{s1}.

$$R_c = \frac{\sqrt{R_{s2}\rho_c}}{W}\left(\coth\left(d\sqrt{\frac{R_{s2}}{\rho_c}}\right)\right) \tag{D.32}$$

The issue now is that R_{s2} is unknown, whereas R_{s1} was known. Another type of measurement needs to be made here: the so-called "contact end resistance" measurement. The contact end resistance R_e is defined as $V(d)/I(0)$.

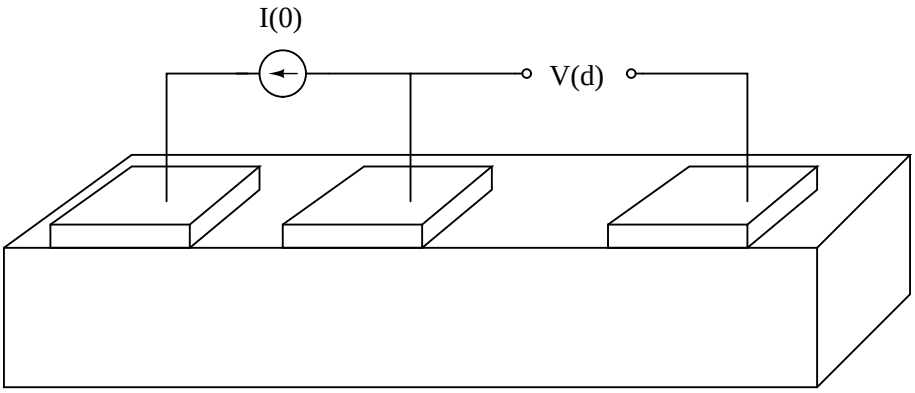

Figure D-4: Measuring the contact end resistance: apply current $I(0)$ and measure the voltage $V(d)$.

$$R_e = \frac{V(d)}{I(0)} = \frac{A_2 e^{-2d/L_T} e^{d/L_T} + A_2 e^{-d/L_T}}{-\frac{W}{R_{s2} L_T}\left(A_2 e^{-2d/L_T} - A_2\right)} \tag{D.33}$$

$$= \frac{R_{s2} L_T}{W}\left(\frac{e^{-d/L_T} + e^{-d/L_T}}{1 - e^{-2d/L_T}}\right) \tag{D.34}$$

$$= \frac{R_{s2} L_T}{W}\left(\frac{2}{e^{d/L_T} - e^{-d/L_T}}\right) \tag{D.35}$$

$$= \frac{R_{s2} L_T}{W}\left(\frac{1}{\sinh(d/L_T)}\right) \tag{D.36}$$

$$= \frac{\sqrt{R_{s2}\rho_c}}{W}\left(\frac{1}{\sinh\left(d\sqrt{\frac{R_{s2}}{\rho_c}}\right)}\right) \tag{D.37}$$

To measure the contact end resistance, apply current $I(0)$ and measure the voltage $V(d)$, as shown in Figure D-4.

Notice also that

$$\frac{R_c}{R_e} = \cosh\left(d\sqrt{\frac{R_{s2}}{\rho_c}}\right) \tag{D.38}$$

D.2.3 Fringe Currents

Thus far, rectangular TLM contacts in one dimension have been considered. However, in reality, the contact pads will have some finite W, causing the 1D treatment to break

down at the pad edges where there are fringe currents that do not behave as the 1D TLM model describes. One solution that is often pursued is to etch away the doped semiconductor around the TLM contact pads, forcing the current to remain within the confines of the pad W. Most often the doped semiconductor is grown on semi-insulating substrates.

D.2.4 Circular Contact Structures

Another way to prevent fringe currents is to use circular TLM contacts, as shown in Figure D-5. The circular symmetry eliminates the presence of fringe currents. Circular TLM structures consist of an inner circular contact with radius a and an outer ring contact with inner and outer radii a_1 and a_2, respectively. The transmission line model can be used as above; the only difference is that the resistances change along the transmission line (because the circumference changes). The current flows radially, so the resistance at any point must depend on r. In cylindrical coordinates,

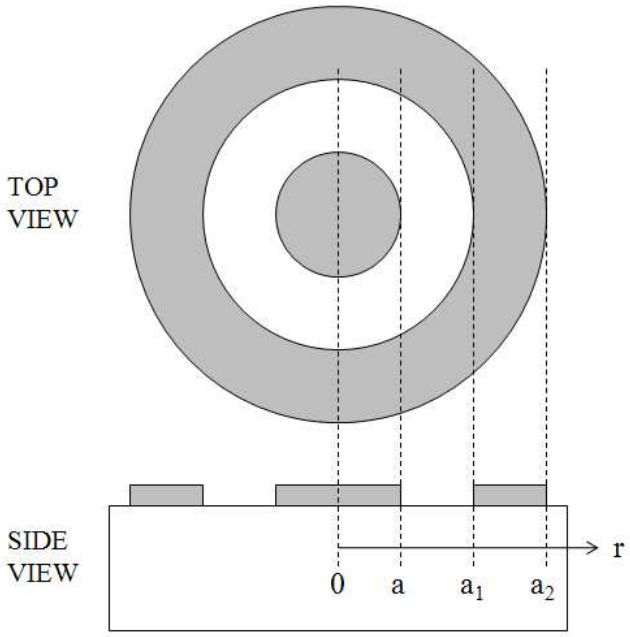

Figure D-5: The top and side views of a circular TLM contact resistance structure. Circular TLM structures do not suffer from fringe currents.

$$dV(r) = I(r)R_{s1}\left[\frac{dr}{2\pi r}\right] \tag{D.39}$$

$$dI(r) = \frac{V(r)}{\rho_c}2\pi r dr \tag{D.40}$$

which produces the differential equations

$$\frac{dV(r)}{dr} = I(r)R_{s1}\left[\frac{1}{2\pi r}\right] \tag{D.41}$$

$$\frac{dI(r)}{dr} = \frac{V(r)}{\rho_c}2\pi r \tag{D.42}$$

Equations D.41 and D.42 can be used to arrive at the following differential equation and its solutions,

$$\frac{d^2V(r)}{dr^2} = \frac{dI(r)}{dr}R_{s1}\frac{1}{2\pi r} - I(r)R_{s1}\frac{1}{2\pi r^2} \tag{D.43}$$

$$= \left(\frac{V(r)}{\rho_c}2\pi r\right)R_{s1}\frac{1}{2\pi r} - \left(\frac{dV(r)}{dr}\frac{2\pi r}{R_{s1}}\right)R_{s1}\frac{1}{2\pi r^2} \tag{D.44}$$

$$= V(r)\frac{R_{s1}}{\rho_c} - \frac{dV(r)}{dr}\frac{1}{r} \tag{D.45}$$

$$\Rightarrow \quad 0 = r^2\frac{d^2V(r)}{dr^2} + r\frac{dV(r)}{dr} - \frac{1}{L_T^2}r^2V(r) \tag{D.46}$$

As before, it is conventional to define the transfer length

$$L_T = \sqrt{\frac{\rho_c}{R_{s1}}} \tag{D.47}$$

It will also be useful to define $U(r/L_T) = V(r)$, then

$$
\begin{aligned}
0 &= r^2\frac{d^2V(r)}{dr^2} + r\frac{dV(r)}{dr} - \frac{1}{L_T^2}r^2V(r) && \text{(D.48)}\\
&= r^2\frac{d^2U(r/L_T)}{dr^2} + r\frac{dU(r/L_T)}{dr} - \frac{1}{L_T^2}r^2U(r/L_T) && \text{(D.49)}\\
&= \frac{r^2}{L_T^2}\frac{d^2U(r/L_T)}{d(r/L_T)^2} + \frac{r}{L_T}\frac{dU(r/L_T)}{d(r/L_T)} - \frac{r^2}{L_T^2}U(r/L_T) && \text{(D.50)}\\
&= r'^2\frac{d^2U(r')}{dr'^2} + r'\frac{dU(r')}{dr'} - r'^2U(r') && \text{(D.51)}
\end{aligned}
$$

Equation D.51 follows from the change of variable $r' = r/L_T$, and is actually the modified Bessel differential equation of zeroth order, for which the solutions are the modified Bessel functions of zeroth order:

$$V(r) = C_1 I_o(r/L_T) + C_2 K_o(r/L_T) \tag{D.52}$$

where I_o and K_o are the zeroth-order modified Bessel functions of the first and second kind, respectively. For a circular contact, the boundary conditions are $I(0) = 0$ and $I(a) = i_o$; for an annular contact the boundary conditions are $I(a_1) = i_o$ and $I(a_2) = 0$ [79]. For the inner (circular) contact

$$R_{inner} = \frac{R_{s1}L_T}{2\pi a}\frac{I_o(a/L_T)}{I_1(a/L_T)} \tag{D.53}$$

and for the outer (annular) contact

$$R_{outer} = \frac{R_{s1}L_T}{2\pi a_1}\left[\frac{K_1(a_2/L_T)I_o(a_1/L_T) + I_1(a_2/L_T)K_o(a_1/L_T)}{K_1(a_1/L_T)I_1(a_2/L_T) - K_1(a_2/L_T)I_1(a_1/L_T)}\right] \tag{D.54}$$

Note here that I_1 and K_1 are first-order modified Bessel functions of the first and second kind, respectively. They arise when the derivatives of the Bessel functions are taken, due to the relationship described by Equations D.56 and D.56.

Table D.2: Values of $I_1(a_2/L_T)$ and $K_1(a_2/L_T)$ as a function of a_2/L_T.

a_2/L_T	0	0.1	0.2	1	2	9.9
$I_1(a_2/L_T)$	0	0.0501	0.1005	0.5652	1.591	2428
$K_1(a_2/L_T)$	∞	9.8538	4.7760	0.6019	0.1399	0.00002072

$$\frac{d}{dx}I_o(x) = I_1(x) \tag{D.55}$$

$$\frac{d}{dx}K_o(x) = -K_1(x) \tag{D.56}$$

An interesting issue arises for circular TLM structures: the plot of total resistance versus gap spacing is nonlinear because the resistance due to the semiconductor is dependent on r [66]. The y-intercept $2R_c$ is equal to $R_{inner} + R_{outer}$. Normally, the limit of $a_2 \gg L_T$ is taken for simplicity. Table D.2 gives some values of I_1 and K_1 for values of a_2/L_T.

In the limit of of $a_2 \gg L_T$, then

$$R_{outer} = \frac{R_{s1}L_T}{2\pi a_1}\left[\frac{K_o(a_1/L_T)}{K_1(a_1/L_T)}\right] \tag{D.57}$$

The parameter a_2 is no longer relevant.

Now consider the semiconductor resistance in the gap $g = a_1 - a$. The voltage drop ΔV_{semi} is

$$\Delta V_{semi} = i_o \int_a^{a_1} \frac{R_{s1}dr}{2\pi r} = i_o \frac{R_{s1}}{2\pi}\ln\left(\frac{a_1}{a}\right) \tag{D.58}$$

The total voltage drop is then

$$\Delta V = i_o R_{inner} + \Delta V_{semi} + i_o R_{outer} \tag{D.59}$$

$$= \frac{i_o R_{s1}}{2\pi}\left[\ln\left(\frac{a_1}{a}\right) + \frac{L_T}{a}\frac{I_o(a/L_T)}{I_1(a/L_T)} + \frac{L_T}{a_1}\frac{K_o(a_1/L_T)}{K_1(a_1/L_T)}\right] \tag{D.60}$$

Table D.3: Values of $I_o(x)/I_1(x)$ and $K_o(x)/K_1(x)$ as a function of x.

x	1	2	5	9.9
$I_o(x)/I_1(x)$	2.240	1.433	1.119	1.055
$K_o(x)/K_1(x)$	0.6998	0.8142	0.9125	0.9532

As described above, the resistance is not linear with the gap spacing. Often, it is assumed that for the region of operation, $a \gg L_T$ and $a_1 \gg L_T$, in which case $\frac{I_o(a/L_T)}{I_1(a/L_T)} \rightarrow 1$ and $\frac{K_o(a_1/L_T)}{K_1(a_1/L_T)} \rightarrow 1$. Table D.3 helps put the approximation into perspective.

The asymtotic behavior of this approximation is slower than the previous approximations. From Table D.3, when a and a_1 are about 10 times larger than L_T, then

$$\Delta V = \frac{i_o R_{s1}}{2\pi}\left[\ln\left(\frac{a_1}{a}\right) + \frac{L_T}{a} + \frac{L_T}{a_1}\right] \tag{D.61}$$

$$\Delta V = \frac{i_o R_{s1}}{2\pi}\left[\ln\left(\frac{a_1}{a_1 - g}\right) + L_T\left(\frac{1}{a_1} + \frac{1}{a_1 - g}\right)\right] \tag{D.62}$$

$$\Rightarrow \quad R = \frac{R_{s1}}{2\pi}\left[\ln\left(\frac{a_1}{a_1 - g}\right) + L_T\left(\frac{1}{a_1} + \frac{1}{a_1 - g}\right)\right] \tag{D.63}$$

where g is the gap spacing. Researchers often start with Equation D.63 when analyzing circular TLM structures [50]. However, if $a_1 \gg d$ is assumed, then Equation D.63 becomes linear:

$$R = R_{s1}\left(\frac{g}{2\pi a} + \frac{L_T}{\pi a_1}\right) \tag{D.64}$$

Keep in mind that Equation D.64 describes the total resistance.

D.3 Conclusion

In an experimental setting, measuring the contact resistance to a degree of accuracy beyond what is needed to determine that the contact resistance will not be obstruc-

tive to device performance is often unnecessary. However, accurate contact resistance measurements may be needed in the characterization new semiconductor materials or metal stacks for making contact. To perform rigorous contact resistance measurements, factors that are beyond this Appendix, such as taking into account the sheet resistance of the metal, may require consideration [66]. The contact resistance of an active device is a very important parameter to understand. Contact resistance that is too high causes the device to be inefficient, and the heat generated can damage the device. Rectangular and circular TLM structures are commonly used to measure the contact resistance: rectangular TLM structures are more straightforward to understand but require an extra etch step in the fabrication process, while circular TLM structures are easier to fabricate but theoretically more complicated.

References

[1] S. Adachi. Model dielectric constants of GaP, GaAs, GaSb, InP, InAs, and InSb. *Phys. Rev. B*, 35:7454–7463, May 1987.

[2] S. Adachi. *Physical properties of III-V semiconductor compounds: InP, InAs, GaAs, GaP, InGaAs, and InGaAsP*. Wiley, 1992.

[3] G. P. Agrawal. *Fiber-Optic Communication Systems*. Wiley-Interscience, 3rd edition, 2002.

[4] Hamad A. Albrithen, Gale S. Petrich, Leslie A. Kolodziejski, Abdelmajid Salhi, and Abdulrahman A. Almuhanna. Investigating GaSb(001) dry etching by ICP-RIE on a non-silicon containing sample holder with no organic gases. In *Mater. Res. Soc. Symp. Proc.*, volume 1396, 2004.

[5] C. Alibert, M. Skouri, A. Joullie, M. Benouna, and S. Sadiq. Refractive indices of AlSb and GaSb-lattice-matched $Al_xGa_{1-x}As_ySb_{1-y}$ in the transparent wavelength region. *Journal of Applied Physics*, 69(5):3208–3211, 1991.

[6] B. Alloing, C. Zinoni, V. Zwiller, L. H. Li, C. Monat, M. Gobet, G. Buchs, A. Fiore, E. Pelucchi, and E. Kapon. Growth and characterization of single quantum dots emitting at 1300 nm. *Applied Physics Letters*, 86(10):101908, 2005.

[7] S. Anantathanasarn, R. Ntzel, P. J. van Veldhoven, F. W. M. van Otten, Y. Barbarin, G. Servanton, T. de Vries, E. Smalbrugge, E. J. Geluk, T. J. Eijkemans, E. A. J. M. Bente, Y. S. Oei, M. K. Smit, and J. H. Wolter. Lasing of wavelength-tunable (1.55 μm region) InAs/InGaAsP/InP (100) quantum dots grown by metal organic vapor-phase epitaxy. *Applied Physics Letters*, 89(7):073115, 2006.

[8] R. Audino, G. Autore, D. Dovio, and A. Piccirillo. Rectifying effects on TiPtAu/p-InGaAsP contacts induced by plasma processes. *Electronics Letters*, 27(25):2359–2360, Dec 1991.

[9] A. G. Baca, F. Ren, J. C. Zolper, R. D. Briggs, and S. J. Pearton. A survey of ohmic contacts to III-V compound semiconductors. *Thin Solid Films*, 308:599–606, 1997.

[10] Tymon Barwicz. *Accurate Nanofabrication Techniques for High-Index-Contrast Microphotonic Devices*. PhD thesis, Massachusetts Institute of Technology, Cambridge, MA, 2005.

[11] Tymon Barwicz, Miloš A. Popović, Michael R. Watts, Peter T. Rakich, Erich P. Ippen, and Henry I. Smith. Fabrication of add-drop filters based on frequency-matched microring resonators. *J. Lightwave Technol.*, 24(5):2207, May 2006.

[12] W. W. Bewley, I. Vurgaftman, C. S. Kim, M. Kim, C. L. Canedy, J. R. Meyer, J. D. Bruno, and F. J. Towner. Room-temperature "W" diode lasers emitting at $\lambda \approx 4.0$ μm. *Applied Physics Letters*, 85(23):5544–5546, 2004.

[13] D. Bimberg, M. Grundmann, and N. N. Ledentsov. *Quantum-Dot Heterostructures*. Wiley, 1999.

[14] W. Bogaerts, D. Taillaert, B. Luyssaert, P. Dumon, J. Van Campenhout, P. Bienstman, D. Van Thourhout, R. Baets, V. Wiaux, and S. Beckx. Basic structures for photonic integrated circuits in silicon-on-insulator. *Opt. Express*, 12(8):1583–1591, Apr 2004.

[15] K.-H. Brenner and W. Singer. Light propagation through microlenses: a new simulation method. *Appl. Opt.*, 32(26):4984–4988, Sep 1993.

[16] J. Campbell and D. Bellavance. Monolithic laser/waveguide coupling by evanescent fields. *Quantum Electronics, IEEE Journal of*, 13(4):253–255, Apr 1977.

[17] Warren C. W. Chan, Dustin J. Maxwell, Xiaohu Gao, Robert E. Bailey, Mingyong Han, and Shuming Nie. Luminescent quantum dots for multiplexed biological detection and imaging. *Current Opinion in Biotechnology*, 13(1):40–46, 2002.

[18] C. J. Chang-Hasnain. Tunable VCSEL. *Selected Topics in Quantum Electronics, IEEE Journal of*, 6(6):978–987, Nov/Dec 2000.

[19] C.-H. Chen, D. Wolfson, L.A. Johansson, D.J. Blumenthal, and L.A. Coldren. Demonstration of 40 Gbit/s optical packet synchronisation using fibre bragg gratings and fast-tunable wavelength converters. *Electronics Letters*, 42(6):367–369, March 2006.

[20] Pei-Chun Chi. *Growth and Characterization of Mid-Infrared Phosphide-Based Semiconductor Diode Lasers*. PhD thesis, Massachusetts Institute of Technology, Cambridge, MA, 2010.

[21] J. W. Coburn. *Plasma Etching and Reactive Ion Etching*. American Institute of Physics, 1982.

[22] L. A. Coldren and S. W. Corzine. *Diode Lasers and Photonic Integrated Circuits*. Wiley-Interscience, 1995.

[23] L.A. Coldren. Monolithic tunable diode lasers. *Selected Topics in Quantum Electronics, IEEE Journal of*, 6(6):988–999, Nov/Dec 2000.

[24] Larry A. Coldren, G. A. Fish, Y. Akulova, J. S. Barton, L. Johansson, and C. W. Coldren. Tunable semiconductor lasers: A tutorial. *J. Lightwave Technol.*, 22(1):193, Jan 2004.

[25] D. Cotter, R. J. Manning, K. J. Blow, A. D. Ellis, A. E. Kelly, D. Nesset, I. D. Phillips, A. J. Poustie, and D. C. Rogers. Nonlinear optics for high-speed digital information processing. *Science*, 286(5444):1523–1528, 1999.

[26] Y. Deki, T. Hatanaka, M. Takahashi, T. Takeuchi, S. Watanabe, S. Takaesu, T. Miyazaki, M. Horie, and H. Yamazaki. Wide-wavelength tunable lasers with 100 GHz FSR ring resonators. *Electronics Letters*, 43(4):225–226, 15 2007.

[27] Gregory C. DeSalvo, Wen F. Tseng, and James Comas. Etch rates and selectivities of citric acid/hydrogen peroxide on GaAs, $Al_{0.3}Ga_{0.7}As$, $In_{0.2}Ga_{0.8}As$, $In_{0.53}Ga_{0.47}As$, $In_{0.52}Al_{0.48}As$, and InP. *Journal of the Electrochemical Society*, 139(3):831–835, 1992.

[28] N. J. Doran and D. Wood. Nonlinear-optical loop mirror. *Opt. Lett*, 13(1):56–58, 1988.

[29] J. Fleck, J. Morris, and M. Feit. Time-dependent propagation of high energy laser beams through the atmosphere. *Applied Physics A: Materials Science and Processing*, 10:129–160, 1976.

[30] Tom Geballe. IR transmission spectra. http://www.gemini.edu/sciops/telescopes-and-sites/observing-condition-constraints/ir-transmission-spectra. Accessed: 21/07/2011.

[31] S. Gehrsitz, F. K. Reinhart, C. Gourgon, N. Herres, A. Vonlanthen, and H. Sigg. The refractive index of $Al_xGa_{1-x}As$ below the band gap: Accurate determination and empirical modeling. *Journal of Applied Physics*, 87(11):7825–7837, 2000.

[32] P. E. Green. Fiber to the home: the next big broadband thing. *Communications Magazine, IEEE*, 42(9):100–106, Sept 2004.

[33] G. Griffel, J. H. Abeles, R. J. Menna, A. M. Braun, J. C. Connolly, and M. King. Low-threshold InGaAsP ring lasers fabricated using bi-level dry etching. *Photonics Technology Letters, IEEE*, 12(2):146–148, Feb 2000.

[34] G. Ronald Hadley. Wide-angle beam propagation using Padé approximant operators. *Opt. Lett.*, 17(20):1426–1428, Oct 1992.

[35] Basil W. Hakki and Thomas L. Paoli. CW degradation at 300 K of GaAs double heterostructure junction lasers. II. Electronic gain. *Journal of Applied Physics*, 44(9):4113–4119, Sep 1973.

[36] K. L. Hall and K. A. Rauschenbach. 100-Gbit/s bitwise logic. *Optics Letters*, 23(16):1271–1273, 1998.

[37] H. B. Harrison. *Characterizing Metal Semiconductor Ohmic Contacts*. Internal report. Royal Melbourne Institute of Technology.

[38] K. Hjort. Sacrificial etching of III - V compounds for micromechanical devices. *Journal of Micromechanics and Microengineering*, 6:370–375, December 1996.

[39] Charles W. Holzwarth. *Material Selection and Nanofabrication Techniques for Electronic Photonic Integrated Circuits*. PhD thesis, Massachusetts Institute of Technology, Cambridge, MA, 2009.

[40] W. P. Huang and C. L. Xu. Simulation of three-dimensional optical waveguides by a full-vector beam propagation method. *Quantum Electronics, IEEE Journal of*, 29(10):2639–2649, Oct 1993.

[41] H. Ishio, J. Minowa, and K. Nosu. Review and status of wavelength-division-multiplexing technology and its application. *Lightwave Technology, Journal of*, 2(4):448–463, Aug 1984.

[42] B. Jensen and A. Torabi. Refractive index of quaternary $In_{1-x}Ga_xAs_yP_{1-y}$ lattice matched to InP. *Journal of Applied Physics*, 54(6):3623–3625, Jun 1983.

[43] A. Kapsalis, D. Syvridis, M. Hamacher, and H. Heidrich. Broadly tunable laser using double-rings vertically coupled to a passive waveguide. *Quantum Electronics, IEEE Journal of*, 46(3):306–312, Mar 2010.

[44] A. Katz, P. M. Thomas, S. N. G. Chu, W. C. Dautremont-Smith, R. G. Sobers, and S. G. Napholtz. Pt/Ti Ohmic contact to p-InGaAsP (1.3 μm) formed by rapid thermal processing. *Journal of Applied Physics*, 67:884, 1990.

[45] Doo Gun Kim and Young-Wan Choi. Wide tuning characteristics of double-ring coupled lasers. *Optics Communications*, 282(13):2516–2523, 2009.

[46] J. G. Kim, L. Shterengas, R. U. Martinelli, G. L. Belenky, D. Z. Garbuzov, and W. K. Chan. Room-temperature 2.5 μm InGaAsSb/AlGaAsSb diode lasers emitting 1 W continuous waves. *Applied Physics Letters*, 81(17):3146–3148, 2002.

[47] J. S. Kim, J. H. Lee, S. U. Hong, W. S. Han, H.-S. Kwack, C. W. Lee, D. K. Oh, J. S. Kim, J. H. Lee, S. U. Hong, W. S. Han, H.-S. Kwack, C. W. Lee, and D. K. Oh. Room-temperature operation of InP-based InAs quantum dot laser. *IEEE Photonics Technology Letters*, 16:1607–1609, July 2004.

[48] M. Kim, W. W. Bewley, J. R. Lindle, C. S. Kim, I. Vurgaftman, J. R. Meyer, J. G. Kim, and R. U. Martinelli. Midinfrared "W" diode lasers with improved electrical characteristics. *Applied Physics Letters*, 83(26):5374–5376, 2003.

[49] Su-Hyun Kim, Young-Tae Byun, Doo-Gun Kim, Nadir Dagli, and Young-Chul Chung. Widely tunable coupled-ring reflector laser diode consisting of square ring resonators. *J. Opt. Soc. Korea*, 14(1):38–41, Mar 2010.

[50] J. H. Klootwijk and C. E. Timmering. Merits and limitations of circular TLM structures for contact resistance determination for novel III-V HBTs. *Microelectronic Test Structures, 2004. Proceedings. ICMTS'04. The International Conference on*, pages 247–252, 2004.

[51] K. J. Knopp, D. Vakhshoori, P. D. Wang, M. Azimi, M. Jiang, P. Chen, Y. Matsui, K. McCallion, A. Baliga, F. Sakhitab, M. Letsch, B. Johnson, R. Huang, A. Jean, B. DeLargy, C. Pinzone, F. Fan, J. Liu, C. Lu, J. Zhou, H. Zhu, R. Gurjar, P. Tayebati, D. MacDaniel, R. Baorui, R. Waterson, and G. Vander-Rhodes. High power MEMs-tunable vertical-cavity surface-emitting lasers. In *Advanced Semiconductor Lasers and Applications/Ultraviolet and Blue Lasers and Their Applications/Ultralong Haul DWDM Transmission and Networking/WDM Components, 2001. Digest of the LEOS Summer Topica*, page 2, 2001.

[52] T. L. Koch, U. Koren, R. P. Gnall, C. A. Burrus, and B. I. Miller. Continuously tunable 1.5 μm multiple-quantum-well GaInAs/GaInAsP distributed-Bragg-reflector lasers. *Electronics Letters*, 24(23):1431–1433, Nov 1988.

[53] A. Krier. *Mid-infrared Semiconductor Optoelectronics*. Springer, 2006.

[54] G. K. Kuang, G. Bohm, N. Graf, M. Grau, G. Rosel, R. Meyer, and M.-C. Amann. Long wavelength InGaAs-InGaAlAs-InP diode lasers grown by solid-source molecular-beam epitaxy. *Electronics Letters*, 36(22):1849–1851, Oct 2000.

[55] F. Lelarge, B. Rousseau, B. Dagens, F. Poingt, F. Pommereau, and A. Accard. Room temperature continuous-wave operation of buried ridge stripe lasers using InAs-InP (100) quantum dots as active core. *IEEE Photonics Technology Letters*, 17:1369–1371, July 2005.

[56] Franois Lelarge, Batrice Dagens, Jeremie Renaudier, R. Brenot, Alain Accard, Frdric van Dijk, Dalila Make, Odile Le Gouezigou, Jean-Guy Provost, Francis Poingt, Jean Landreau, Olivier Drisse, Estelle Derouin, Benjamin Rousseau, Frdric Pommereau, and Guang-Hua Duan. Recent advances on InAs/InP quantum dash based semiconductor lasers and optical amplifiers operating at 1.55 μm. *Selected Topics in Quantum Electronics, IEEE Journal of*, 13(1):111–124, Jan-Feb 2007.

[57] S. G. Li, Q. Gong, Y. F. Lao, K. He, J. Li, Y. G. Zhang, S. L. Feng, and H. L. Wang. Room temperature continuous-wave operation of InAs/InP(100) quantum dot lasers grown by gas-source molecular-beam epitaxy. *Applied Physics Letters*, 93(11):111109, September 2008.

[58] W. Li, J. B. Hroux, H. Shao, and W. I. Wang. Strain-compensated InGaAsSb/AlGaAsSb mid-infrared quantum-well lasers. *Applied Physics Letters*, 84(12):2016–2018, 2004.

[59] C. Lin, M. Grau, O. Dier, and M.-C. Amann. Low threshold room-temperature continuous-wave operation of 2.24 μm-3.04 μm GaInAsSb/AlGaAsSb quantum-well lasers. *Applied Physics Letters*, 84(25):5088–5090, Jun 2004.

[60] B. E. Little, S. T. Chu, H. A. Haus, J. Foresi, and J.-P. Laine. Microring resonator channel dropping filters. *Lightwave Technology, Journal of*, 15(6):998–1005, Jun 1997.

[61] B. Liu, A. Shakouri, and J. E. Bowers. Wide tunable double ring resonator coupled lasers. *Photonics Technology Letters, IEEE*, 14(5):600–602, May 2002.

[62] W. M. Loh, S. E. Swirhun, T. A. Schreyer, R. M. Swanson, and K. C. Saraswat. Modeling and measurement of contact resistances. *Electron Devices, IEEE Transactions on*, 34(3):512–524, Mar 1987.

[63] Bernd E. Maile, Wolfgang Henschel, Heinrich Kurz, Bert Rienks, Roelof Polman, and Piet Kaars. Sub-10 nm linewidth and overlay performance achieved with a fine-tuned EBPG-5000 TFE electron beam lithography system. *Japanese Journal of Applied Physics*, 39(Part 1, No. 12B):6836–6842, 2000.

[64] R. J. Manning, A. D. Ellis, A. J. Poustie, and K. J. Blow. Semiconductor laser amplifiers for ultrafast all-optical signal processing. *Journal of the Optical Society of America B*, 14(11):3204–3216, 1997.

[65] Aleksandra Markina. *Design and Simulation for the Fabrication of Integrated Semiconductor Optical Logic Gates*. PhD thesis, Massachusetts Institute of Technology, Cambridge, MA, 2005.

[66] G. S. Marlow and M. B. Das. The effects of contact size and non-zero metal resistance on the determination of specific contact resistance. *Solid-State Electron*, 25(2):91–94, 1982.

[67] B. Mason, J. Barton, G. A. Fish, L. A. Coldren, and S. P. Denbaars. Design of sampled grating DBR lasers with integrated semiconductor optical amplifiers. *Photonics Technology Letters, IEEE*, 12(7):762–764, Jul 2000.

[68] Takashi Matsumoto, Akira Suzuki, Morio Takahashi, Shinya Watanabe, Satoru Ishii, Kouichi Suzuki, Taro Kaneko, Hiroyuki Yamazaki, and Naoki Sakuma. Narrow spectral linewidth full band tunable laser based on waveguide ring resonators with low power consumption. In *Optical Fiber Communication Conference*, page OThQ5. Optical Society of America, 2010.

[69] S. Matsuo and T. Segawa. Microring-resonator-based widely tunable lasers. *Selected Topics in Quantum Electronics, IEEE Journal of*, 15(3):545–554, May-June 2009.

[70] V. M. Menon, F. Xia, and S. R. Forrest. Photonic integration using asymmetric twin-waveguide (ATG) technology: part II-devices. *Selected Topics in Quantum Electronics, IEEE Journal of*, 11(1):30–42, 2005.

[71] A. Michon, G. Patriarche, G. Beaudoin, G. Saint-Girons, N. Gogneau, and I. Sagnes. Density of InAs/InP(001) quantum dots grown by metal-organic vapor phase epitaxy: Independent effects of InAs and cap-layer growth rates. *Applied Physics Letters*, 91(10):102107, 2007.

[72] D. A. B. Miller. Rationale and challenges for optical interconnects to electronic chips. *Proceedings of the IEEE*, 88(6):728–749, Jun 2000.

[73] I. Moerman, P. P. Van Daele, and P. M. Demeester. A review on fabrication technologies for the monolithic integration of tapers with III-V semiconductor devices. *Selected Topics in Quantum Electronics, IEEE Journal of*, 3(6):1308–1320, 1998.

[74] J. Mork, M. L. Nielsen, and T. W. Berg. The dynamics of semiconductor optical amplifiers: Modelling and applications. *Optics and photonics news*, 14(7):42–48, 2003.

[75] M. Munoz Uribe, C. E. M. de Oliveira, J. H. Clerice, R. S. Miranda, M. B. Zakia, M. M. G. de Carvalho, and N. B. Patel. Measurement of refractive index of GaSb (1.8 to 2.56 μm) using a prism. *Electronics Letters*, 32(3):262–264, Feb 1996.

[76] Manfred Murtz and Peter Hering. Online monitoring of exhaled breath using mid-infrared laser spectroscopy. In *Mid-Infrared Coherent Sources and Applications*, NATO Science for Peace and Security Series B: Physics and Biophysics, pages 535–555. Springer Netherlands, 2008.

[77] R. Nagarajan, M. Kato, V. G. Dominic, C. H. Joyner, R. P. Schneider, A. G. Dentai, T. Desikan, P. W. Evans, M. Kauffman, D. J. H. Lambert, et al. 400 Gbit/s (10 channel $\times$ 40 Gbit/s) DWDM photonic integrated circuits. *Electronics Letters*, 41(6):347–349, 2005.

[78] S. Nakamura, Y. Ueno, and K. Tajima. Error-free all-optical demultiplexing at 336 Gb/s with a hybrid-integrated symmetric-Mach-Zehnder switch. In *Optical Fiber Communication Conference and Exhibit, 2002. OFC 2002*, 2002.

[79] V. Y. Niskov and G. A. Kubetsky. Resistance of ohmic contacts between metals and semiconductor films. *Sov Phys Semiconductors*, 4(9):1553–1554, 1971.

[80] Yoshitomo Okawachi, Mark Foster, Jay Sharping, Alexander Gaeta, Qianfan Xu, and Michal Lipson. All-optical slow-light on a photonic chip. *Opt. Express*, 14(6):2317–2322, Mar 2006.

[81] D. Olego, T. Y. Chang, E. Silberg, E. A. Caridi, and A. Pinczuk. Compositional dependence of band-gap energy and conduction-band effective mass of $In_{1-x-y}Ga_xAl_yAs$ lattice matched to InP. *Applied Physics Letters*, 41(5):476–478, Sep 1982.

[82] M. H. Paek, P. H. Hao, and L. C. Wang. Anomalous lateral Zn surface diffusion in InP caused by Zn-contained metallization. *Journal of Electronic Materials*, 26(1):25–29, 1997.

[83] Mario Paniccia, Mike Morse, and Michael Salib. Integrated photonics. In *Silicon Photonics*, volume 94 of *Topics in Applied Physics*, page 1999. Springer Berlin / Heidelberg, 2004.

[84] Seoijin Park, Seong-Soo Kim, Liwei Wang, and Seng-Tiong Ho. Single-mode lasing operation using a microring resonator as a wavelength selector. *Quantum Electronics, IEEE Journal of*, 38(3):270–273, Mar 2002.

[85] N. S. Patel, K. L. Hall, and K. A. Rauschenbach. Interferometric all-optical switches for ultrafast signal processing. *Appl. Opt*, 37(14):2831–2842, 1998.

[86] N. S. Patel, K. A. Rauschenbach, and K. L. Hall. 40-Gb/s demultiplexing using an ultrafast nonlinear interferometer (UNI). *Photonics Technology Letters, IEEE*, 8(12):1695–1697, 1996.

[87] J. Piprek, P. Abraham, and J. E. Bowers. Self-consistent analysis of high-temperature effects on strained-layer multiquantum-well InGaAsP-InP lasers. *Quantum Electronics, IEEE Journal of*, 36(3):366–374, Mar 2000.

[88] M. Popovic. *Theory and Design of High-Index-Contrast Microphotonic Circuits*. PhD thesis, Massachusetts Institute of Technology, Cambridge, MA, 2008.

[89] Miloš A. Popovíc, Tymon Barwicz, Michael R. Watts, Peter T. Rakich, Luciano Socci, Erich P. Ippen, Franz X. Kärtner, and Henry I. Smith. Multistage high-order microring-resonator add-drop filters. *Opt. Lett.*, 31(17):2571–2573, Sep 2006.

[90] D. G. Rabus. *Integrated ring resonators : the compendium*. Springer, 2007.

[91] D. G. Rabus, Zhixi Bian, and A. Shakouri. A GaInAsP-InP double-ring resonator coupled laser. *Photonics Technology Letters, IEEE*, 17(9):1770–1772, Sept 2005.

[92] D. G. Rabus, Zhixi Bian, and A. Shakouri. Ring resonator lasers using passive waveguides and integrated semiconductor optical amplifiers. *Selected Topics in Quantum Electronics, IEEE Journal of*, 13(5):1249–1256, Sept-Oct 2007.

[93] Hongling Rao, R. Scarmozzino, and R. M. Osgood, Jr. A bidirectional beam propagation method for multiple dielectric interfaces. *Photonics Technology Letters, IEEE*, 11(7):830–832, Jul 1999.

[94] G. K. Reeves and H. B. Harrison. Obtaining the specific contact resistance from transmission line model measurements. *Electron Device Letters, IEEE*, 3(5):111–113, 1982.

[95] P. Ressel, P. H. Hao, M. H. Park, Z. C. Yang, L. C. Wang, W. Österle, P. Kurpas, E. Richter, E. Kuphal, and H. L. Hartnagel. Pd/Sb (Zn) and Pd/Ge (Zn) ohmic contacts on p-type indium gallium arsenide: The employment of the solid phase regrowth principle to achieve optimum electrical and metallurgical properties. *Journal of Electronic Materials*, 29(7):964–972, 2000.

[96] S. A. Rishton and D. P. Kern. Point exposure distribution measurements for proximity correction in electron beam lithography on a sub-10 nm scale. *Journal of Vacuum Science Technology B: Microelectronics and Nanometer Structures*, 5(1):135–141, Jan 1987.

[97] John A. Rogers, Kateri E. Paul, Rebecca J. Jackman, and George M. Whitesides. Using an elastomeric phase mask for sub-100 nm photolithography in the optical near field. *Applied Physics Letters*, 70(20):2658–2660, 1997.

[98] Hideaki Saito, Kenichi Nishi, and Shigeo Sugou. Influence of GaAs capping on the optical properties of InGaAs/GaAs surface quantum dots with 1.5 μm emission. *Applied Physics Letters*, 73(19):2742–2744, 1998.

[99] Hideaki Saito, Kenichi Nishi, and Sigeo Sugou. Ground-state lasing at room temperature in long-wavelength InAs quantum-dot lasers on InP(311)B substrates. *Applied Physics Letters*, 78(3):267–269, 2001.

[100] B. E. A. Saleh and M. C. Teich. *Fundamentals of Photonics*. John Wiley and Sons, 1991.

[101] R. Scarmozzino and R. M. Osgood, Jr. Comparison of finite-difference and fourier-transform solutions of the parabolic wave equation with emphasis on integrated-optics applications. *J. Opt. Soc. Am. A*, 8(5):724–731, May 1991.

[102] R. R. Schaller. Moore's law: past, present and future. *Spectrum, IEEE*, 34(6):52–59, Jun 1997.

[103] E. F. Schubert. *Light Emitting Diodes*. Cambridge University Press, 2003.

[104] C. Seassal, J. L. Leclercq, and P. Viktorovitch. Fabrication of InP-based free-standing microstructures by selective surface micromachining. *Journal of Micromechanics and Microengineering*, 6:261–265, June 1996.

[105] T. Segawa, S. Matsuo, T. Kakitsuka, T. Sato, Y. Kondo, and H. Suzuki. Full C-band tuning operation of semiconductor double-ring resonator-coupled laser with low tuning current. *Photonics Technology Letters, IEEE*, 19(17):1322–1324, Sept, 2007.

[106] W. Sellmeier. Zur Erklärung der abnormen Farbenfolge im Spectrum einiger Substanzen. *Annalen der Physik und Chemie*, 219(6):272–282, 1871.

[107] R. J. Shapiro. The internet's capacity to handle fast-rising demand for bandwidth. *US Internet Industry Association*, 2007.

[108] T. C. Shen, G. B. Gao, and H. Morkoç. Recent developments in ohmic contacts for III-V compound semiconductors. *Journal of Vacuum Science Technology B: Microelectronics and Nanometer Structures*, 10(5):2113–2132, 1992.

[109] W. Shockley. Research and investigation of inverse epitaxial UHF power transistors. *Air Force Atomic Laboratory, Wright-Patterson Air Force Base, Rep. No. AL-TDR-64-207, Sept*, 1964.

[110] S. Sloan. Processing and passivation techniques for fabrication of high-speed InP/InGaAs mesa photodetectors. *Hewlett Packard Journal*, pages 69–75, Oct 1989.

[111] L. B. Soldano and E. C. M. Pennings. Optical multi-mode interference devices based on self-imaging: principles and applications. *Lightwave Technology, Journal of*, 13(4):615–627, Apr 1995.

[112] M. Sopanen, H. P. Xin, and C. W. Tu. Self-assembled GaInNAs quantum dots for 1.3 and 1.55 μm emission on GaAs. *Applied Physics Letters*, 76(8):994–996, 2000.

[113] Evgeni Sorokin. Ultrabroadband solid-state lasers in trace gas sensing. In *Mid-Infrared Coherent Sources and Applications*, NATO Science for Peace and Security Series B: Physics and Biophysics, pages 557–574. Springer Netherlands, 2008.

[114] Rudolf Steiner. Medical applications of mid-IR solid-state lasers. In *Mid-Infrared Coherent Sources and Applications*, NATO Science for Peace and Security Series B: Physics and Biophysics, pages 575–588. Springer Netherlands, 2008.

[115] K. E. Stubkjaer. Semiconductor optical amplifier-based all-optical gates for high-speed optical processing. *Selected Topics in Quantum Electronics, IEEE Journal of*, 6(6):1428–1435, 2000.

[116] P. V. Studenkov, M. R. Gokhale, and S. R. Forrest. Efficient coupling in integrated twin-waveguide lasers using waveguide tapers. *Photonics Technology Letters, IEEE*, 11(9):1096–1098, 1999.

[117] P. V. Studenkov, M. R. Gokhale, W. Lin, I. Glesk, P. R. Prucnal, and S. R. Forrest. Monolithic integration of an all-optical Mach-Zehnder demultiplexer using an asymmetric twin-waveguide structure. *Photonics Technology Letters, IEEE*, 13(6):600–602, 2001.

[118] Pavel V. Studenkov. *Photonic Integration Using Asymmetric Twin-Waveguides*. PhD thesis, Princeton University, Princeton, NJ, 2001.

[119] Y. Suematsu, M. Yamada, and K. Hayashi. Integrated twin-guide AlGaAs laser with multiheterostructure. *Quantum Electronics, IEEE Journal of*, 11(7):457–460, Jul 1975.

[120] M. Sugawara, T. Akiyama, N. Hatori, Y. Nakata, H. Ebe, and H. Ishikawa. Quantum-dot semiconductor optical amplifiers for high-bit-rate signal processing up to 160 Gb/s and a new scheme of 3 R regenerators. *Measurement Science and Technology*, 13(11):1683–1691, 2002.

[121] M. Sugawara, K. Mukai, Y. Nakata, K. Otsubo, and H. Ishilkawa. Performance and physics of quantum-dot lasers with self-assembled columnar-shaped and 1.3-μm emitting InGaAs quantum dots. *Selected Topics in Quantum Electronics, IEEE Journal of*, 6(3):462–474, May/Jun 2000.

[122] Yun Sun, Piero Pianetta, Po-Ta Chen, Masaharu Kobayashi, Yoshio Nishi, Niti Goel, Michael Garner, and Wilman Tsai. Arsenic-dominated chemistry in the acid cleaning of InGaAs and InAlAs surfaces. *Applied Physics Letters*, 93(19):194103, 2008.

[123] K. Suzuki, K. Iwatsuki, S. Nishi, and M. Saruwatari. Error-free demultiplexing of 160 Gbit/s pulse signal using optical loop mirror including semiconductor laser amplifier. *Electronics Letters*, 30(18):1501–1503, 1994.

[124] D. Taillaert, W. Bogaerts, P. Bienstman, T. F. Krauss, P. Van Daele, I. Moerman, S. Verstuyft, K. De Mesel, and R. Baets. An out-of-plane grating coupler for efficient butt-coupling between compact planar waveguides and single-mode fibers. *Quantum Electronics, IEEE Journal of*, 38(7):949–955, Jul 2002.

[125] Dirk Taillaert, Frederik Van Laere, Melanie Ayre, Wim Bogaerts, Dries Van Thourhout, Peter Bienstman, and Roel Baets. Grating couplers for coupling between optical fibers and nanophotonic waveguides. *Japanese Journal of Applied Physics*, 45(8A):6071–6077, 2006.

[126] Jun Tatebayashi, Masao Nishioka, and Yasuhiko Arakawa. Over 1.5 μm light emission from InAs quantum dots embedded in InGaAs strain-reducing layer grown by metalorganic chemical vapor deposition. *Applied Physics Letters*, 78(22):3469–3471, 2001.

[127] TeleGeography.com. *TeleGeography Report*. 2007.

[128] F. K. Tittel, G. Wysocki, A. Kosterev, and Y. Bakhirkin. Semiconductor laser based trace gas sensor technology: Recent advances and applications. In *Mid-Infrared Coherent Sources and Applications*, NATO Science for Peace and Security Series B: Physics and Biophysics, pages 467–493. Springer Netherlands, 2008.

[129] Y. Ueno, S. Nakamura, H. Hatakeyama, T. Tamanuki, T. Sasaki, and K. Tajima. 168 Gb/s OTDM wavelength conversion using an SMZ-type all-optical switch. *Proceedings of ECOC*, 1:13–14, 2000.

[130] A. V. Uskov, E. P. O'Reilly, R. J. Manning, R. P. Webb, D. Cotter, M. Laemmlin, N. N. Ledentsov, and D. Bimberg. On ultrafast optical switching based on quantum-dot semiconductor optical amplifiers in nonlinear interferometers. *IEEE Photonics Technology Letters*, 16(5):1265–1267, 2004.

[131] F. Van Laere, G. Roelkens, M. Ayre, J. Schrauwen, D. Taillaert, D. Van Thourhout, T.F. Krauss, and R. Baets. Compact and highly efficient grating couplers between optical fiber and nanophotonic waveguides. *Lightwave Technology, Journal of*, 25(1):151–156, Jan 2007.

[132] F. Van Laere, T. Stomeo, D. Taillaert, G. Roelkens, D. Van Thourhout, T. F. Krauss, and R. Baets. Efficient polarization diversity grating couplers in bonded InP-membrane. *Photonics Technology Letters, IEEE*, 20(4):318–320, Feb 2008.

[133] A. Vicet, D. A. Yarekha, A. Ouvrard, R. Teissier, C. Alibert, and A. N. Baranov. Tunability of antimonide-based semiconductor lasers diodes and experimental evaluation of the thermal resistance. *Optoelectronics, IEE Proceedings*, 150(4):310–313, Aug 2003.

[134] Kristijonas Vizbaras and Markus-Christian Amann. Room-temperature 3.73 μm GaSb-based type-I quantum-well lasers with quinternary barriers. *Semiconductor Science and Technology*, 27(3):032001, 2012.

[135] I. Vurgaftman, J. R. Meyer, and L. R. Ram-Mohan. Band parameters for III-V compound semiconductors and their alloys. 89(11):5815–5875, 2001.

[136] J. P. Wang, B. S. Robinson, S. A. Hamilton, and E. P. Ippen. Demonstration of 40-Gb/s packet routing using all-optical header processing. *Photonics Technology Letters, IEEE*, 18(21):2275–2277, 2006.

[137] Jade Wang. *Demonstrating Effective All-Optical Processing in Ultrafast Data Networks Using Semiconductor Optical Amplifiers*. PhD thesis, Massachusetts Institute of Technology, Cambridge, MA, 2008.

[138] Y. Wang, C. Yu, L. Yan, A. E. Willner, R. Roussev, C. Langrock, M. M. Fejer, J. E. Sharping, and A. L. Gaeta. 44-ns continuously tunable dispersionless optical delay element using a PPLN waveguide with two-pump configuration, DCF, and a dispersion compensator. *Photonics Technology Letters, IEEE*, 19(11):861–863, June 2007.

[139] K. R. Williams, K. Gupta, and M. Wasilik. Etch rates for micromachining processing-part II. *Microelectromechanical Systems, Journal of*, 12(6):761–778, Dec 2003.

[140] K. R. Williams and R. S. Muller. Etch rates for micromachining processing. *Microelectromechanical Systems, Journal of*, 5(4):256–269, Dec 1996.

[141] Ryan D. Williams. *Photonic Integrated Circuits for Optical Logic Applications*. PhD thesis, Massachusetts Institute of Technology, Cambridge, MA, 2007.

[142] F. Xia, V. M. Menon, and S. R. Forrest. Photonic integration using asymmetric twin-waveguide (ATG) technology: part I-concepts and theory. *Selected Topics in Quantum Electronics, IEEE Journal of*, 11(1):17–29, 2005.

[143] Q. Xu and M. Lipson. All-optical logic based on silicon micro-ring resonators. *Optics Express*, 15(3):924–929, 2007.

[144] Mehmet Fatih Yanik and Shanhui Fan. Stopping light all optically. *Phys. Rev. Lett.*, 92(8):083901, Feb 2004.

[145] M. Zegaoui, J. Harari, N. Choueib, V. Magnin, and D. Decoster. Quick planarisation based on hydrogen silsesquioxane (HSQ) for deep etched InP based structures. *Electronics Letters*, 43(22), 2007.

[146] T. Zhang, C. Zhang, G. Fu, Y. Li, L. Gu, G. Zhang, QW Song, B. Parsons, and R. R. Birge. All-optical logic gates using bacteriorhodopsin films. *Optical Engineering*, 39:527, 2000.

[147] J.-F. Zheng, P. J. Hanberg, H. V. Demir, V. A. Sabnis, O. Fidaner, J. S. Harris, Jr., and D. A. B. Miller. Novel planarization and passivation in the integration of III-V semiconductor devices. In *Society of Photo-Optical Instrumentation Engineers (SPIE) Conference Series*, volume 5356 of *Society of Photo-Optical Instrumentation Engineers (SPIE) Conference Series*, pages 81–91, June 2004.

[148] A. J. Zilkie, J. Meier, P. W. E. Smith, M. Mojahedi, J. S. Aitchison, P. J. Poole, C. N. Allen, P. Barrios, and D. Poitras. Femtosecond gain and index dynamics in an InAs/InGaAsP quantum dot amplifier operating at 1.55 μm. *Optics Express*, 14(23):11453–11459, 2006.